Development and evaluation of a library of novel 18F-labelled PET tracers targeting the P2X7 receptor

Fantoni, Enrico Raffaele

Awarding institution:
King's College London

Development and evaluation of a library of novel ^{18}F-labelled PET tracers targeting the P2X7 receptor

Enrico Raffaele Fantoni

Student ID: 1257251

Submitted in partial fulfilment of the requirements for the degree of Doctor of Philosophy in Nuclear Imaging Sciences

Department of Imaging Sciences and Biomedical Engineering

King's College London

Supervisors: Antony Gee and Simon Lovestone

April 2016

Abstract

Inflammation imaging is central to the diagnosis and monitoring of the progression of a vast range of diseases. As is suggested by the strong upregulation in the presence of biological insults, the P2X7 receptor plays a fundamental role in the inflammatory cascade. In this context, the development of a centrally acting Positron Emission Tomography (PET) tracer is a promising step towards harnessing the therapeutic and diagnostic potential offered by this target.

In this work, inspired by the known antagonist A-804598, a set of four novel ^{18}F-labelled PET ligands were designed, synthesised and evaluated in *in vitro* and *in vivo* models of neuroinflammation. The tracers were synthesised *via* novel trisubstituted guanidine and copper alkyne-azide cyclised intermediates. Multi-step radiofluorinations were carried out with the use of the [^{18}F]fluorobenzyl amine synthon and "click" radiochemical techniques employing [^{18}F]fluoroethyl amine. The compounds were evaluated *in vitro* with radioligand binding and calcium influx assays. Further validation was carried out in a hypoxic ischaemic mouse tissue model of neuroinflammation and in lipopolysaccharide-injected rats.

This work generated four novel PET tracers, including one able to recognise inflamed tissues *in vivo*. These developments could form an important part of a drug discovery programme and may lead to an improved understanding of neuroinflammatory diseases and the treatment thereof.

Contents

Table of figures

Table of tables

Acknowledgements

A lot of time and effort has gone into making this dissertation into what is its final version. All this would not have been possible without my wonderful parents, sister and extended family that have supported me throughout this endeavour. A special thank you also goes to all my friends who have helped me stay sane and grow in many other areas of my life throughout these years.

Furthermore, the Imaging Sciences Division at King's College London has played a crucial role in the success of this project. First of all, my supervisors Tony Gee and Simon Lovestone, who have provided invaluable support and advice throughout these years, as well as giving me peace of mind regarding the financing of this project, entirely subsidized by Biomedical Research Council grants (NIHR BRC). My gratitude is extended towards Chantal Bazenet, Ran Yan, Federico Turkheimer and Philip Blower, while the work done by the collaborators Diego Dal Ben (Univeristy of Camerino, Italy), Francesco Di Virgilio and Simonetta Falzoni (University of Ferrara) was instrumental to the completion of this work.

Furthermore, I would like to thank Bobbi Fleiss and the perinatal imaging group. Bobbi has dedicated a huge amount of time and effort in making me practiced in biology and in the planning of the experiments, while making the whole experience enjoyable. Also, thanks to Robin Fortt, Michelle Ma, Brett Patterson, Zilin Yu, Sam Terry, Sara Lacerda, Julia Baguña Torres, Simona De Robertis, Salvatore Bongarzone, Diana Cash, Camilla Simmons, Julia Blower and especially to Nisha Singh, all of whom have given a helping hand at multiple stages of the project, have proof-read my thesis and offered advice.

The work at St Thomas' would also not be possible without the fantastic support team that ensures the smooth running of the department's facilities. As such I would like to thank David Thakor, Barry Crook, Kavitha Sunassee, Nisha Kuzhuppilly Ramakrishnan, all the St Thomas' PET centre staff and the Rayne Institute BSU staff.

Finally, many fellow students and researchers have made this experience more than just a step in my professional education, and I am glad I could share with you all, too many to name individually here, a laugh, an interesting thought and life's events.

Abbreviations

(D)PBS: Dulbecco's Phosphate-Buffered Saline

(m)RNA: (Messenger) ribonucleic acid

(T)PSA: (Topological) Polar Surface Area

Ab: Antibody

AcOH: Acetic acid

ADME(T): Absorption, distribution, metabolism, excretion (and toxicity)

ANOVA: Analysis of variance

ATP: Adenosine triphosphate

AUC: Area under the curve

BBB: Blood-brain barrier

BBG: Brilliant blue G

BPDS: bathophenanthroline disulfonic acid disodium salt hydrate

BSA: Bovine serum albumin

Bz-ATP: 2'(3')-O-(4-Benzoylbenzoyl)adenosine-5'-triphosphate tri(triethylammonium) salt

C18: Octadecyl carbon chain

Calcd.: Calculated

$CDCl_3$: Deuterated chloroform

cDNA: Complementary desossiribonucleic acid

CNS: Central nervous system

Cps: Counts per seconds

CT: Computed tomography

D_2O: Deuterated water

DAPI: 4',6-diamidino-2-phenylindole

DCM: Dichloromethane

DMEM: Dulbecco's Modified Eagle Medium

DMF: Dimethyl formamide

DMSO: Dimethylsulfoxide

EC_{50}: Half maximal effective concentration

EDTA: Ethylenediaminetetraacetic acid

Eq.: Equivalents

ESI: Electrospray ionisation

EtOAc: Ethyl acetate

FACS: Fluorescence-assisted cell sorting

FBS: Foetal bovine serum

FCC: Flash column chromatography

FDG: 2-Deoxy-2-fluoroglucose

FITC: Fluorescein isothiocyanate

FL1: Fluorescence emission

FSC: Front scatter

FT-IR: Fourier transform-infrared

GAPDH: Glyceraldehyde 3-phosphate dehydrogenase

GOI: Gene of interest

Hex: Hexane

HI: Hypoxic ischemic

HLB: hydrophilic lipophilic bonding

hP2X7: Human P2X7

HPLC: High-performance liquid chromatography

I/P: Intraperitoneal

I/V: Intravenous

IC_{50}: Half maximal inhibitory concentration

ICC: Immunocytochemistry

ID: Injected dose

IHC: Immunohistochemistry

IL-4, IL-1β: Interleukin-4, interleukin-1β

ITLC: Radioactive thin-layer chromatography

J: Coupling constant

K_d: Dissociation constant

LC/MS: Liquid chromatography/mass spectrometry

LHS: Left hand-side

LogP: Partition coefficient

LPS: Lipopolysaccharide

mAU: Milli atomic units

MeCN: Acetonitrile

MeOD: Deuterated methanol

MeOH: Methanol

mP2X7: Mouse P2X7

MRI: Magnetic resonance imaging

MS: Mass spectrometry

MTT: 3-(4,5-Dimethylthiazol-2-yl-)-2,5-diphenyl-2H-tetrazolium bromide

MW: Microwave

NADPH: Nicotinamide adenine dinucleotide phosphate

NLRP3: NACHT, LRR and PYD domains-containing protein 3

NMR: Nuclear Magnetic resonance

NSB: Non-specific binding

P2(R)X7: ATP-activated purinergic receptor 2, subtype X, subunit 7

pE: positron energy

PET: Positron emission tomography

PPTS: Pyrodonium *p*-toluenesulfonate

PFA: Paraformaldehyde

PTFE: Polytetrafluoroethylene

QC: Quality control

Q-TOF: Quadrupole-time of flight

R_f: Retention factor

RHS: Right hand-side

RIPA: Radioimmunoprecipitation assay buffer

R_n: Normalized reporter value

ROI: Region of interest

rP2X7: Rat P2X7

rpm: rate per minute

RPMI: Roswell Park Memorial Institute medium

R_t: Retention time

rt: Room temperature

RT-PCR: Reverse transcriptase polymerase chain reaction

SA: Specific activity

SB: Self-block

SD: Standard deviation

SEM: Standard error of the mean

SNPs: Single nucleotide polymorphisms

SPE: solid phase extraction

SPECT: Single photon emission computed tomography

SSC: Side scatter

$t_{1/2}$: Half life

^{t}BuOH: Tert-butanol

TBAF: Tetrabutyammonium fluoride

TEA: Triethylamine

TFA: Trifluoroacetic acid

THF: Tetrahydrofuran

TLC: Thin-layer chromatography

UB: Unblocked

UV: Ultra-violet

WT: Wild-type

Nil sine magno vita labore dedit mortalibus.
Life grants nothing to us mortals without hard work.

Horatius, *“Satires”*, 1.9, 59-60

Chapter 1

Introduction

Introduction

1.2 The P2X7 receptor

1.2.1 The discovery of P2X7's structure

Ever since the isolation of adenosine triphosphate (ATP) in the first half of the last century, it was known that this molecule was fundamental at a pharmacological and biological level.[1] Nonetheless, it took half a century for ATP-activated receptors to be discovered, named purinergic receptors and subdivided into P1 and P2 subtypes. P2 receptors were the most potently activated by ATP>ADP>AMP>adenosine, whereas P1 receptors followed the opposite trend.[2] In the 80s, further subtypes where recognised; P2X receptors represented all ATP activated ligand-gated cation channels, whereas P2Y purinoceptors included all G protein-coupled receptors. The subtypes included also P2T receptors (found to mediate aggregation on platelets), P2U receptors (activated by uracil), P2D receptors (mediators of adenine dinucleotides extracellular functions).[3, 4]. Furthermore, P2Z receptors were identified as key mediators of degranulation on hematopoietic cells.[5] It was not until 1996 that this receptor was renamed P2X7 in recognition of its role, akin to other P2X receptors, in gating the flux of small cations.[6]

The P2X7 receptor is now relatively well characterised. Cloning has enabled its structural characterisation as a 69 kDa, 595 amino acid polypeptide. P2X7 is a homotrimeric ligand-gated cation channel that sits on the outer cell membrane. It contains two-transmembrane (2TM) motifs with intracellular termini[7] and an often N-glycosylated extracellular loop.[7] The C-terminal domain is particularly long and features a tumour necrosis factor receptor-1 region, as well as a lipopolysaccharide (LPS) binding motif.[8] In fact, the majority of the downstream signalling is thought to be carried out *via* this terminus.[9, 10] In the extracellular loop, the P2X7 amino acid sequence includes a series of lysine and phenylalanine residues crucial for ATP binding[11] and an abundance of disulfide-bound cysteines that hold the extracellular domain in place (Figure 1).[12, 13]

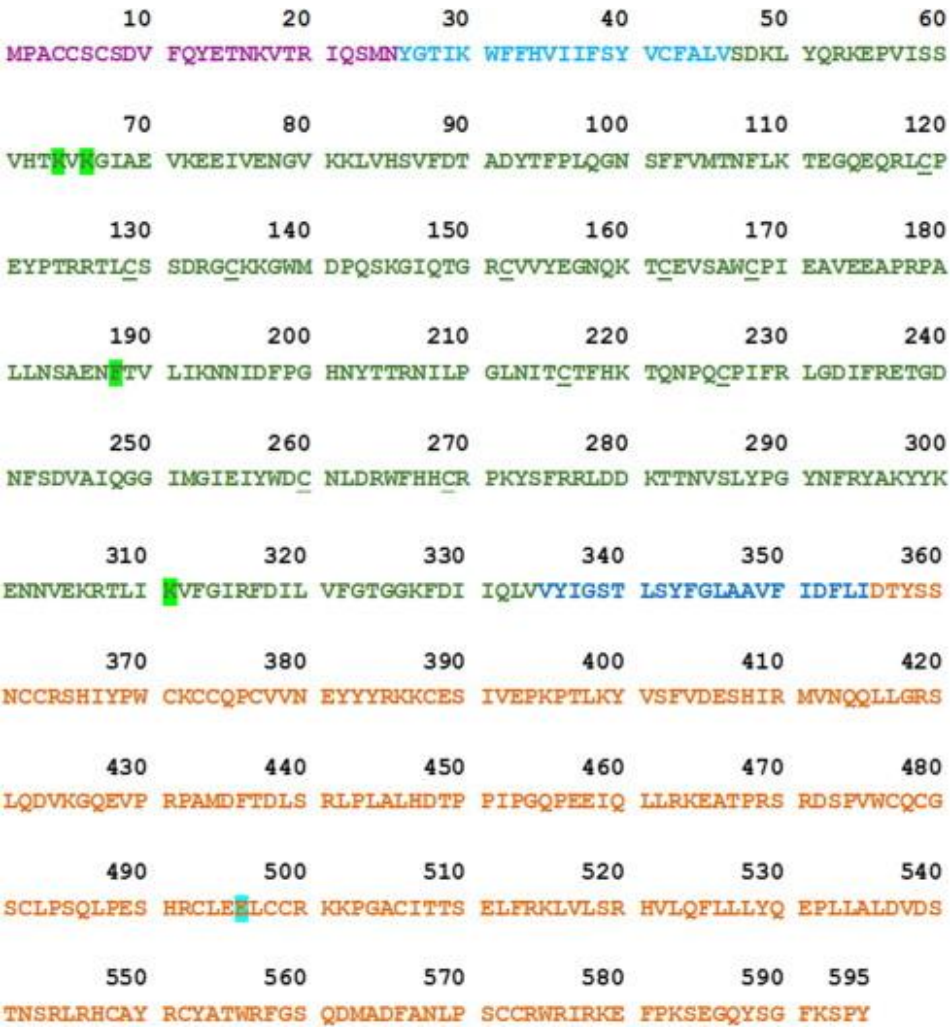

Figure 1 P2X7 amino acid sequence from N-to-C terminus

Brief activation (<10 s) of the P2X7 receptor results in a rapid, reversible membrane depolarization with bidirectional flux of Na^+ and Ca^{2+} (inwards) and K^+ (outwards).[14] Upon prolonged exposure to ATP or other agonists, the P2X7 receptor converts to a nonselective pore that is permeable to small molecules of molecular weight up to 900 Da, such as Yo-Pro and ethidium, both routinely used to measure the switch to pore-like behaviour of P2X7.[15] Interestingly, deletion of the C-terminal domain showed that it is crucial to the formation of a pore: of its 240 amino acids, 177 are necessary to induce pore formation.[6] However, it is still a matter of debate whether ATP alone is responsible for the switch to pore-like properties. It has been suggested that allosteric modulators or other proteins such as the pannexin-1 pore might be crucially involved.[16-18] Moreover, pannexin-1 peptide mimics have been effective at blocking the initial stages of pore formation without affecting the ion flux.[19]

Recently, the crystal structure of the zebrafish P2X4 receptor (zP2X4) in the open and ATP-bound form[20, 21] has led to some insight into the conformation of P2X7 by homology modelling (Figure 2).[22, 23]

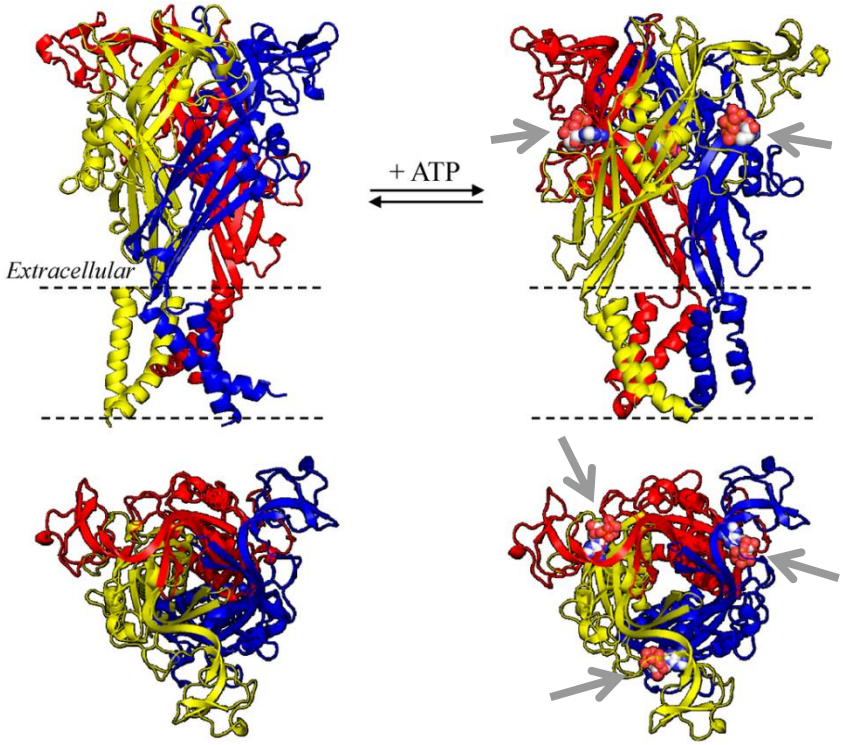

Figure 2 Structural homology models of the trimeric human P2X7 receptor

The key observation is the fact that three ATP molecules are able to fit the receptor and promote the opening of a pore transversal to the membrane *via* a concerted jaw-like movement of the three subunits, further stabilised by extracellular zinc bridges (Figure 3).[20, 24] The transmembrane domains usually lie in an oblique angle to the membrane. Upon ATP activation, they are thought to shift to a perpendicular angle, whereby opening a gap that initially allows cation fluxes. Upon prolonged agonist stimulation, larger molecules are able to permeate. This validates the hypothesis suggested by non-denaturing protein electrophoresis that three receptor subunits act in synchrony enabling P2X7 function.[24, 25]

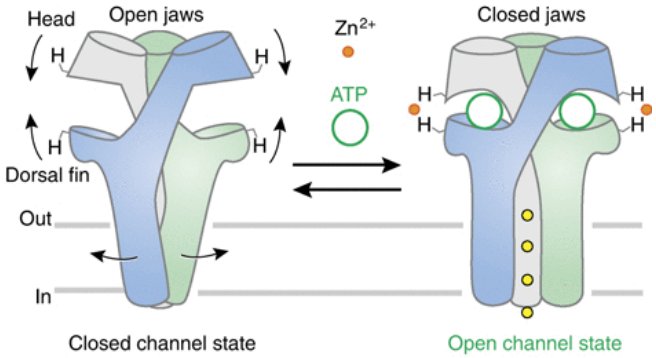

Figure 3 Schematic representation of a plausible activation mechanism of P2X receptors

Furthermore, a minimum of 11 receptor polymorphisms (Figure 4) are known to occur albeit with <5% frequency. At least 5 of them can affect the cationic fluxes and overall receptor function,[26-30] although it has not been entirely elucidated whether these effects are dependent on modifications to the receptor structure or to its conductance. Association to human disease has been found for several of these single nucleotide polymorphisms (SNPs)..[31, 32] The non-synonymous SNP rs2230912 coding for Arg[460] instead of Gln has been linked to mood disorders in three large-cohort studies.[33-35] Moreover, the A348T mutation induces increased ionic fluxes through P2X7 and is associated with anxiety disorders and with protection against symptomatic toxoplasmosis.[36] Finally, the loss-of-function SNP rs3751143 coding for Ala[496] over Glu confers decreased protection from *Mycobacterium tuberculosis* infections.[37, 38]

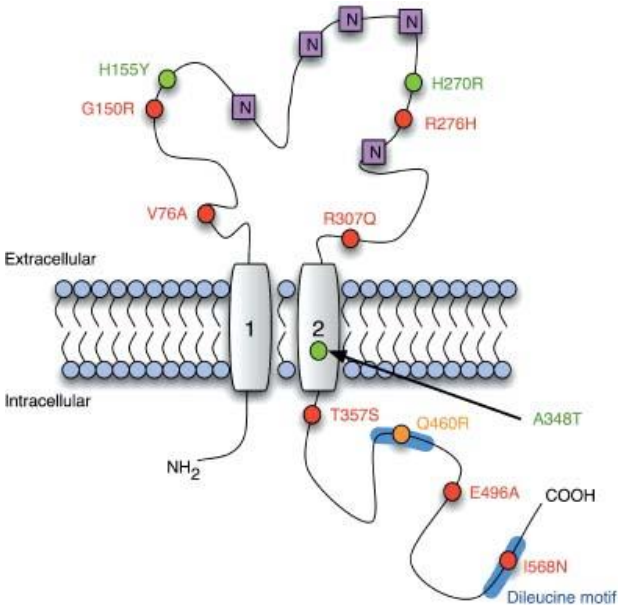

Figure 4 P2X7 polymorphic residues

1.2.2 Distribution of P2X7

A variety of techniques have been used to ascertain the distribution of the P2X7 receptor: electrophysiology, reverse transcription polymerase chain reaction (RT-PCR) of mRNA and in situ hybridised mRNA, immunostaining, immunoblotting, radioligand assays, as well as genetic manipulations.[39, 40] In healthy subjects it's been found to be a ubiquitous receptor, present predominantly on cells of hematopoietic origin, such as glia, granulocytes, monocytes, macrophages, lymphocytes, dendritic cells and platelets.[41] Moreover, it has been found in lower yet conspicuous amounts on epithelial and muscle cells.[39] Depending on the cell line and organ

expressing P2X7, its calcium permeability can regulate cardiorespiratory reflexes,[42, 43] membrane polarisation[44] and conductance,[45] substance secretion,[46, 47] muscle[48, 49] and ciliary contractions,[50, 51] apoptotic,[52-55] necrotic[56, 57] and proliferative stimuli,[58-62] clearance of dead cells[63] and intercellular signalling.[64-66]

In the central nervous system (CNS), predominant P2X7 expression has been found on murine and human spinal cord and hippocampus. P2X7 is also abundant in the area postrema, nucleus tractus, brain stem, medulla, hypothalamus, cerebellum, striatum, cortex and on enteric and retinal neurons.[39] *In vitro* autoradiography of mouse brain slices with the tritiated P2X7-selective antagonist [^{3}H]A-804598 has shown binding throughout the brain and spinal cord, with highest uptake in the thalamic and hypothalamic nuclei, hippocampus, spinal trigeminal tract and nucleus, the cortex, cerebellum and caudate putamen.[67]

At a CNS cellular level, P2X7 has been abundantly observed on microglia,[68] astrocytes,[69] olygodendrocytes,[70] Schwann cells[71] and other glial cells. Neuronal expression appears slightly less widespread; indeed some receptor detection techniques have failed to pick it up.[40] On excitatory neurons, P2X7 has been observed presynaptically,[72] as well as on neuronal terminals [73, 74] and the nuclear envelope of hippocampal nuclei.[75] Troublingly, disagreement over the specificity of P2X7 antibodies employed to track the receptor expression has arose due to positive staining in P2X7$^{-/-}$ mice.[76] This could be explained by incomplete receptor knockout in these transgenic models.[77] Nevertheless, controversy over the reliability of current P2X7 neuronal immunostaining studies remains, as a thorough comparison of all available antibodies has found numerous staining inconsistencies.[78] These contradictory patterns could also be cautiously interpreted as being vulnerable to diverse experimental condition variations which impact the receptor expression itself.

Aside from healthy cells, P2X7 has also been found to be strongly expressed on several tumour cell lines, notably neuroblastoma cells, prostate cancer cells, epidermal carcinomas, osteosarcomas and osteoclastomas.[79-81]

Despite P2X7's diverse role, it has been shown to be outstandingly upregulated in disease both at a genetic as well as at a receptor level.[82] Even if P2X7 has a significant epithelial expression, it remains low compared to the receptor's expression in CNS cells, providing low risks in terms of substrate bioavailability.[39]

1.2.3 P2X7 functions

A large body of literature exists on the function of P2X7 at a physiological level. Many factors point to a key role of the receptor in regulating the inflammatory cascade,[83] as indicated by the following observations pertaining P2X7's diverse functions.

Firstly, *in vitro* and *in vivo* P2X7 blocking or genetic knock out models have shown that the receptor plays a central role in the release of cytokines, particularly IL-1β, from microglia and macrophages.[84] In fact, the activation and externalisation of pro-IL-1β is abolished in P2X7-deficient compared to wild-type macrophages, while the production of IL-1 and IL-1β is arrested only in $P2X7^{-/-}$ LPS-injected, ATP-stimulated mice and not in wild type mice.[85, 86] Likewise, P2X7 blockade in wild type mice halts IL-1β release.[86]

Secondly, P2X7 is key in recovery following treatment with a lipopolysaccharide (LPS) inflammatory insult.[87-90] It is also well established that P2X7 is involved in the generation of reactive oxygen species (ROS) in macrophages and microglia. This is suggested in particular by the fact that ATP-stimulated primary rat microglia show remarkable increases in the production of ROS, an effect which is largely abolished with P2X7 blockade.[91] ROS production may be linked to activation of the pathogen recognition receptor NLRP3 by P2X7.[92] However, others reported that P2X7 or ATP could induce the activation of the NLRP3 inflammasome *via* routes extraneous to ROS.[93, 94]

Fourthly, membrane blebbing and other morphological changes can be halted upon P2X7 deletion or blockade.[83] Similarly, the release of cathepsins and other lysosomal proteases is dependent on the endocellular permeability of P2X7 to calcium[95, 96] and can be halted with P2X7 blocking.[97] Additionally, it is involved in the regulation of phagocytosis, as suggested by the acquired ability of HEK293 cells to take up fluorescently labelled bacteria or latex beads upon transfection with P2X7, albeit only in the absence of ATP stimulation.[98]

Finally, P2X7 plays a role in the excretion of inflammatory prostaglandin [99] and glutamate.[100-102] It can directly activate the transcription of inflammatory and cell metabolism genes through interaction with the nuclear factor-κB[103, 104] and it is involved in the induction of apoptosis.[105, 106] Conversely, in certain P2X7 splice variants expressed in microglia and T-cells the receptor appears to have the opposite role of promoting cell proliferation,[60, 107-109] suggesting that subtle

differences in receptor activation may induce drastically different downstream effects. This effect hints that P2X7 could be sitting at the interface between pro-inflammatory and anti-inflammatory immune responses.[110-112]

1.2.4 The P2X7 inflammatory pathway

Despite its exact mechanism of action is yet only partly understood due to its complexity, several models have been able to depict in broad terms the way P2X7 is involved in the initiation and maintenance of a chronic inflammatory cascade, particularly in the brain, where its expression is highest.

The P2X7 dilation model by Pelegrin describes the receptor as a gradually permeable transmembrane protein acting in synchrony with pannexin-1.[113] Exposure of P2X7 to ATP leads to sequential distortion of the symmetrical trimeric structure, thus reducing the affinity of the remaining binding sites for ATP. Higher ATP concentrations dilate the pore rendering it permeable to small cations. However, it is only upon binding of the third agonist molecule, at high ATP concentrations, that the receptor allows full cation permeation, that the previously P2X7-associated pannexin-1 pore detaches and that downstream inflammatory signalling commences.

This model is pleasingly complemented by the Sperlágh P2X7-centric neuroinflammatory model (Figure 5).[77] According to the latter, neuronal depolarisation signals produce an initial synaptic release of ATP capable of reaching pre- and post-synaptic P2X7 receptors (Figure 5A). This is a state consistent with normal functioning of P2X7 receptors as described in section 1.2.2.

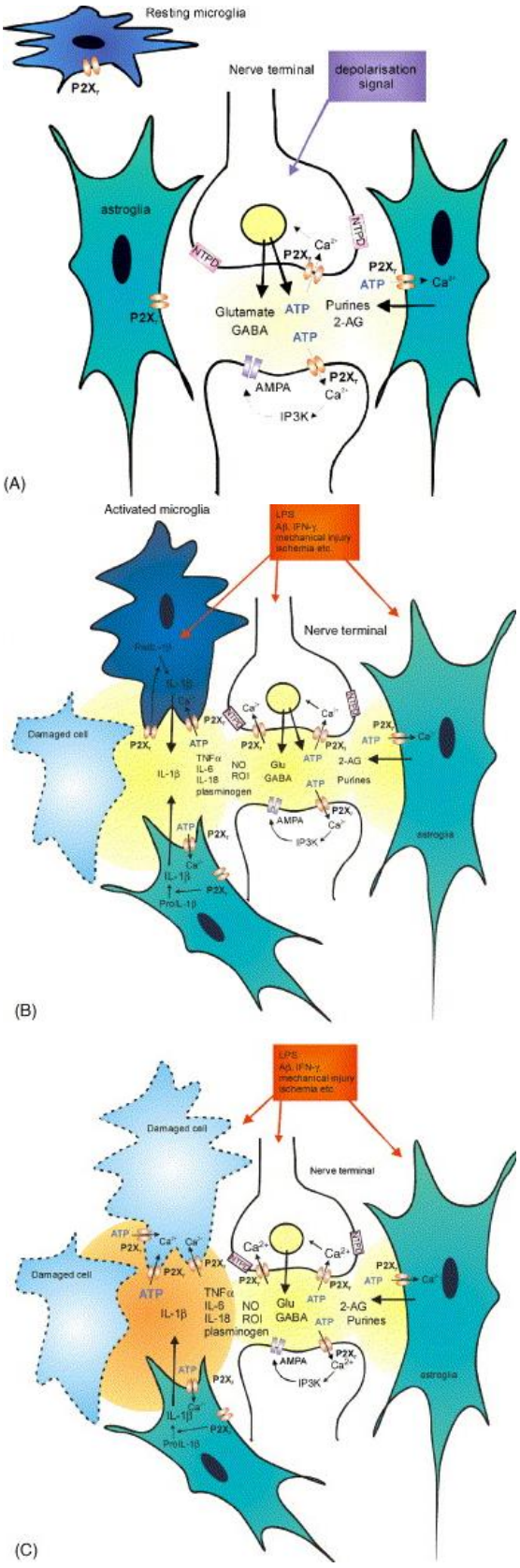

Figure 5 Sperlágh hypothetical pathway model of P2X7 activation in the brain

Neuroinflammatory cells, instead, become activated in consequence to further ATP release following LPS, mechanical, metabolic or inflammatory stress, cellular injury as well as changes

in the ionic environment (Figure 5B). In these conditions ATP initiates an inflammatory cytokine and chemokine release sufficient to deliver an acute inflammatory response to an insult. Full blown inflammation instead commences when cell apoptosis and necrosis start occurring (Figure 5C). This induces large bursts of ATP which fully open the P2X7 channel and exacerbate the inflammatory response turning it into a chronic condition.

The way P2X7 receptors mediate neuroinflammation is known with a certain level of detail (Figure 6). Insults activate neuroinflammatory cells *via* the mediation of Toll-like receptors (TLRs, 1).[114] The process is also gated by lipopolysaccharide (LPS) chains that prime the inflammatory cells enabling cytoplasmic signalling. This directly involves P2X7 *via* its C-terminal intracellular LPS-binding motif.[115, 116] Downstream signalling triggers the activation of the nuclear factor (NF)-κB signal transduction pathway.[117] This is a gene expression regulator that enables the transcription of pro-IL-1β and other cytokines.[118] Pro-IL-1β must be activated and converted into mature IL-1β before being released extracellularly *via* exocytosis.[119] Instead, IL-18 is transcribed, translated and secreted integrally.[120] NF-κB also indirectly triggers the release of neurotoxins such as reactive oxygen species (ROS) and nitric oxide species (NO), which in turn feedback to NF-κB in a manner that is largely still a matter of intense debate.[121-125]

Altogether, the cytokines and neurotoxic factors act in a dual manner; on one hand some induce phagocytosis and clearance of the inflammatory stimulus, thus aiding neuronal survival (2).[126, 127] On the other hand, some are detrimental to neurons (3).[128, 129] Meanwhile, a contrasting effect is exerted by neuroprotective (M2) microglia. These promote insult clearance (4) so as to lead to an overall homeostatic balance.[130]

Neuronal death results in an abundant release of extracellular ATP, which signals to the P2X7 receptor (5) the secretion of an assortment of proteins (secretome), notably pro-caspase-1, later activated to caspase-1.[131] The secretome composition considerably varies depending on the type and strength of stimulus, thus enforcing distinct pro- or anti-inflammatory cellular profiles.[112] Catalysis by caspase-1 and the NLRP3 inflammasome leads to the release of further cytokines,[132-134] which are responsible for an amplification of the inflammatory cascade and resulting in chronic inflammation.[135]

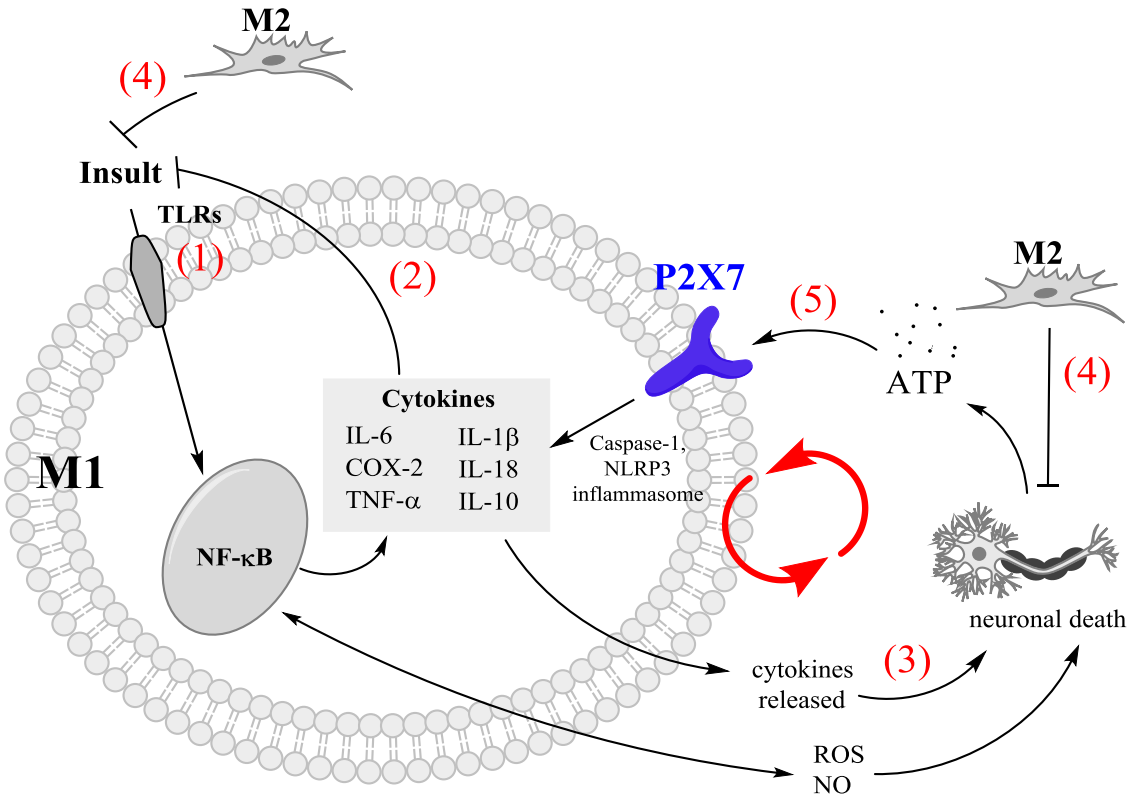

Figure 6 Simplified scheme representing the role of P2X7 in microglial activity

1.2.5 P2X7's involvement in disease

The inflammatory response regulated by P2X7 is the leading or accompanying cause of many diseases.[137] This section focuses on the most relevant cases in which P2X7's involvement has been found to have a most crucial role.

Alzheimer's disease

A growing number of reports discuss the role of P2X7 in relation to the formation of amyloid-β (Aβ) plaques in Alzheimer's disease (AD) and related CNS diseases characterised by the presence of misfolded proteins. P2X7 presents significantly increased expression in human AD primary microglial cultures, Aβ-exposed foetal microglia, intracranially Aβ-injected rat hippocampi[138] and in a transgenic mouse model of Alzheimer's disease (Tg2576).[91] Moreover, in primary microglial cultures treated with Aβ as well as in live mice intracranially injected with Aβ, P2X7 deletion abolishes IL-1β secretion, a common biomarker for neuroinflammation.[127] Regarding the potential therapeutic and diagnostic potential of P2X7 targeting in relation to Alzheimer's disease, microglial P2X7 receptor expression has been shown to precede Aβ

plaque formation and it is accompanied by ROS production and extensive neuronal damage in the cerebral cortex in APPswe/PS1dE9 transgenic mouse models of AD.[139] *In vitro* inhibition of P2X7 in P2X7-transfected HEK293 cells and neuroblastoma N2a cells favours the non-pathogenic processing of the amyloid-precursor protein (APP) *via* α-secretase rather than β-secretase. Likewise, *in vivo* inhibition of the receptor in the human APP TgJ20 mice significantly reduced the amyloid plaque burden in the hippocampus.[140] Given this picture, P2X7 among other inflammatory markers appears crucial at the early stages of AD and could be a viable marker for onset of the disease.[141-144]

Other misfolded protein diseases

In other misfolded protein diseases, targeting P2X7 has proven equally promising. In the R6/1 transgenic model of Huntington's disease (HD) where P2X7 shows an increased expression, P2X7 pharmacological blockade prevents weight loss and ameliorates cognitive and motor functions. Additionally, mutant huntingtin-expressing neurons show increased apoptosis when P2X7 is stimulated.[145] In the unilateral 6-oxidopamine rat model of Parkinson's disease (PD), P2X7 blockade significantly prevents striatal dopaminergic depletion.[146] In prion protein cell and mice models of Prion disease, treatment with a P2X7 blocker significantly reduces prion protein accumulation, although it does not halt the disease progression.[147] Finally, in the SOD1-G93A microglia mouse model of amyotrophic lateral sclerosis (ALS) P2X7 activity and expression dysregulates the NADPH oxidase 2 (NOX2) pathway,[148] while P2X7 blockade improves motor function in both sexes but not survival in male mice.[149]

Depression

Another CNS disease which P2X7 displays strong links to is depression.[150] It is well established that depressed individuals suffer from an increase in brain inflammation which is worsened during major depressive episodes.[151] P2X7 appears in particular to be crucial in its role as regulator of inflammatory cytokines, which in turn correlate with the severity and occurrence of depression.[152-154] Inflammatory cytokines can influence neurotransmitter metabolism, neuroendocrine function and regional brain activity. Additionally, depression-linked psychosocial stress can induce neuroinflammatory processes.[155, 156] P2X7 knock-out and pharmacological

blockade in mice models of depression has resulted in an anti-depressant-like profile and supports neurochemical changes in the hippocampus.[157-159] Furthermore, large-cohort, non-synonymous single nucleotide polymorphisms (SNPs) of the human *P2RX7* gene supported by *in vitro* data have been associated to mood disorders.[34, 160]

Epilepsy

Epileptic seizures are strongly entwined with neuroinflammation.[161] P2X7 activation has in particular been shown to strongly modulate hippocampal mossy fibre excitability, leading to synaptic depression, while P2X7 blockade can halt this effect.[162] Also, the severity of seizures increases with P2X7 activation and blockade reduces seizure-induced hippocampal damage.[163] The upregulation of hippocampal P2X7 receptors (and only P2X7 out of all P2X receptors) correlates strongly with seizure induction in rodent models of epilepsy.[164, 165] Finally, drug targeting of P2X7 has shown much needed seizure-suppressing and neuroprotective effects.[165]

CNS injuries

Traumatic brain injury (TBI) following percussion of the cranium is characterised by the ATP-induced activation of P2X7,[166] which has now become a priority target in TBI experimental therapy. In particular, P2X7 genetic deletion or blocking reduces cerebral oedema and long-term neurological injury in mice[167] and rats subject to cortical impact injury.[168] Recently, also radiation brain injury (RBI) was correlated with P2X7 *via* the production of extracellular ATP. Blockade or deletion of the receptor suppresses radiation-induced microglial activation and proliferation in the hippocampus, and restores the spatial memory of irradiated mice.[169] Similarly, ATP releases from peritraumatic regions following acute spinal cord injury (SCI) in rats activate P2X7,[170] although blocking did not corroborate the long-term beneficial outcomes when tested in contusion rat models of SCI.[171]

Neuronal scleroses

Also related to the P2X7 response to abnormal increases in extracellular ATP levels in the CNS are two forms of neuronal scleroses, amyotrophic lateral sclerosis (ALS) and multiple sclerosis (MS). In ALS, P2X7 impacts the cytokine release and oxidative damage following microglial,

astrocytic and neuronal P2X7 activation. It contributes to glutamate-induced excitotoxicity, mitochondrial dysfunction and apoptosis, RNA processing abnormalities, axonal trafficking defects, oligodendrocyte dysfunction, and, ultimately, muscle atrophy.[172, 173]

In MS, several P2X7 correlations have been found.[174] In experimental autoimmune encephalomyelitis (EAE) models of MS, Pfizer P2X7 knock-out mice[175] develop significantly worse symptomatology than wild type EAE mice.[176] However, the reverse occurs[177] when the Glaxo-Smith-Kline strain of P2X7-null mice[178] is used, pointing to a crucial role of the receptor in regulating lymphocyte production and that different P2X7 strains can lead to compensatory responses to P2X7 deficiency leading overall to beneficial effects on the disease pathogenesis.[177, 179] Moreover, a rare P2X7 variant with absent pore formation function has been recently found to protect against neuroinflammation in MS.[180]

Ischemia

P2X7 is also relevant to brain injuries in the form of ischemic strokes as well as to myocardial ischemias. Ischemia is a restriction in blood supply to tissues, causing the reduced availability or lack of glucose, oxygen and other molecules key to cell survival. Hypoxic ischemic strokes, in particular, are characterised by neuronal necrosis and extensive neuroinflammation.[181, 182] It is thought that P2X7 responds to ischemic insult-generated ATP, leading to oligodendrocyte precursor cell (OPC) damage and white matter loss.[183] It has been shown that oxygen-glucose deprived (OGD) BV-2 microglia can be rescued from death by pharmacological blockade of P2X7. Additionally, in OGD P2X7 knock-out mice, pharmacological blockade reduced cell death by half.[184] Conversely, in middle-cerebral artery occlusion (MCAO) mice models of cerebral ischemia P2X7 deletion or blockade did not reduce cell death, differently from IL-1 antagonism, suggesting a lack of direct link between P2X7 and neuronal death in this model.[185] However, in a different MCAO mice study P2X7 expression was shown as upregulated post-ischemically in the peri-infarct region[186] and similar observations were reported in OGD glial cells and neurons *in vitro*.[187, 188]

Ischemia can also occur in the myocardium, as demonstrated by the altered P2X7 expression in the isolated heart following ischemia/reperfusion injury.[189] Similarly, P2X7 antagonism in myocardial ischemic injury models inhibits the nociceptive signalling of the sympatho-excitatory

reflex induced by the ischemia, offering cardioprotection with the contribution of centrally-located P2X7.[190-192]

Neuropathic pain

Pain has the multiple purpose on one hand of protecting and repairing tissue injury by directly or indirectly activating the somatosensory system, while on the other hand it is a pathological consequence of an excessive release of nociceptive stimuli, otherwise known as neuropathic pain.[193] Such delicate balance is regulated by a complex "soup" of inflammatory mediators, which may target nociceptive receptors (nociceptors) directly, via complex cascades or may instead exploit low-threshold sensory fibres to elicit painful stimuli. This complex disease presents a range of potential CNS targets in the opioidergic, serotonergic, GABAergic, adrenergic and inflammatory systems, among which is COX-2, the target of many NSAIDs. The role of neuroinflammation in the induction and maintenance of chronic pain is gaining increasing interest.[194] Among the most attractive targets in this sense is P2X7, as suggested by the correlation with reduced pain upon receptor blockade.[195-198] P2X7 may act *via* IL-1β maturation,[178] cathepsin release,[97, 199] prostaglandin release,[99] and may work *via* the pore functionality of P2X7.[200] For example, the disruption of the P2X7 receptor gene is able to abolish neuropathic pain as measured by analysis of local and systemic cytokines.[135] Moreover, the loss of antihyperalgesic activity with P2X7 antagonism in IL-1*αβ* KO (lacking both IL-1α and IL-1β genes) compared to wild type mice, has suggested that P2X7 activity is mediated by IL-1β release.[201]

Non-CNS disorders

The role of the P2X7 receptor is not limited to the above-mentioned CNS disorders. In fact, it encompasses so many conditions that in this context, for sake of relevance, only just a mention of the implicated non-CNS diseases will be made.

Of widespread interest to the pharmaceutical community is its role in relation to rheumatic diseases such as rheumatoid arthritis, due to P2X7's mediatory role in the release of IL-1β and the activation of the NLRP3 inflammasome.[202] Moreover, it is a target for the treatment of renal diseases such as glomerulonephritis as its involvement in the response to abnormal levels of

ATP appears to exacerbate renal conditions.[203, 204] Similarly, P2X7 ATP-sensing ability and downstream signalling gives it a prominent role in respiratory diseases including asthma, chronic obstructive pulmonary disorder and pulmonary fibrosis.[205] Further, P2X7 is genetically and functionally associated to the innate immune response to intracellular pathogens. In particular this pertains tuberculosis, toxoplasmosis, chlamydia and HIV infections in the CNS (neuroAIDS).[32, 206]

On a different note, a non-functional conformation of P2X7 (nfP2X7) has recently been recognised as a novel and ubiquitous target specific to cancerous cells due to its role as a mediator of proliferation and cell death[206-210 207] This loss of ability to form an apoptotic pore but a calcium channel is induced by point mutations at residues K193 and K311.[208] In epithelial cancer cells, responsible for 80% of human tumours, including pancreatic, genital-urinary and bone cancers, the presence of nfP2X7 is particularly notable.[209]

Furthermore, P2X7 receptors are involved in the healthy functioning of the eye photoreceptor and rod bipolar cell responses as well as in the death of retinal neurons, making them an interesting target for ocular diseases such as glaucoma and optic nerve injury. In particular, the stimulation of P2X7 receptors is known to impact the health of retinal ganglion cells (RGCs).[210, 211] The role of P2X7 in eye health is particularly crucial in diabetic subjects, where increased vulnerability of retinal microvessels to the lethal effect of P2X7 can result in diabetic retinopathy.[212]

To further study the pathophysiological features of P2X7 in a living being often requires the use of molecular probes capable of reporting on abnormal biochemistry at the site of pathology. In this sense, non-invasive imaging is perfectly suited to probe the site of disease and report information helpful to devise therapy or prevention strategies. Molecular imaging is often the first of many steps towards a cure. It is key in the diagnosis of complex diseases and to the understanding of underlying biological dysfunctions at a molecular level. It is used to monitor the efficacy of clinical trials for novel drugs and to fast-track pharmaceutical development by aiding drug dosage trails, by clarifying the metabolic and excretory profile of molecules and by illustrating their kinetic behaviour in living systems. Additionally, some imaging techniques can directly provide avenues for therapy (see section 1.3.2).

1.2.6 P2X7 agonists and antagonists

Two broad compound classes have historically been the focus of much work on purinergic receptor pharmacology: ATP analogues and charged sulfonated dyes. Both classes do not conform to the typical physicochemical and pharmacological criteria used for selecting drug candidates as their high molecular weight and charged nature result in poor permeation through lipidic environment.[213] Additionally, both species are P2X7 activators, which clashes with the need to dampen P2X7 activity to tackle disease. However, ATP analogues have remained the standard for receptor activation. ATP itself as the endogenous agonist is poorly active at P2X7 receptors when compared to its aromatic derivative BzATP (Figure 7). The latter is thus used routinely in experimental settings, most often at its EC_{50} concentration (Table 1).

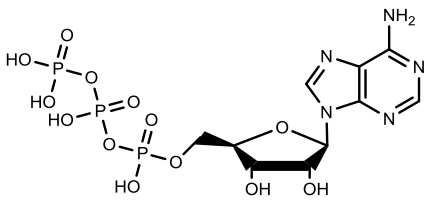

ATP

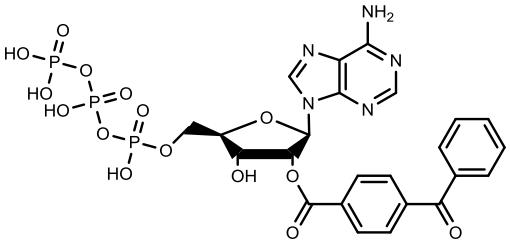

BzATP

Figure 7 Common P2X7 agonist structures.

Table 1 Agonist activity at P2X7

P2X7 Agonist	pEC_{50} at mP2X7 (M)	pEC_{50} at rP2X7 (M)	pEC_{50} at hP2X7 (M)	Refs
ATP	2.62±0.05	3.89±0.20	4.13±0.02	[214]
BzATP	3.99±0.06	5.01±0.04	5.33±0.05	[214]

Nanomolar potency antagonists have been identified since the early 2000's. A number of unselective antagonists are used to assess the physiology of purinergic receptors as a whole. However, many specific antagonists are now available as detailed in Table 2. Many efforts have been spent since to develop potent yet more orally bioavailable and metabolically stable molecules. Compound Brilliant Blue G (BBG) is widely employed as selective blocker for P2X7 in pharmacological assays.[215] Despite its high potency in murine models, however, it suffers from low affinity for the human P2X7 receptor despite the >80% sequence homology, making BBG unsuitable for clinical use. The latter is quite a common feature in P2X7 receptor

antagonists including KN-62, PPADS and oATP, which are not equally selective for all P2X7 homologues.[214] A large library of aryl amides was synthesised by AstraZeneca, resulting in a couple of adamantane-functionalised compounds with optimal properties yet excessively lipophilic. The library was later expanded by Evotec and Neurogen who achieved higher potencies by employing larger aromatics (quinolines, quinolones or benzimidazoles) compared to the original phenyl rings. Moreover, Pfizer entered clinical trials for rheumatoid arthritis with a cycloheptane arylamide of LogP 1-3. Yet, more promising structures have been uncovered meanwhile. Abbott's A-740003, A-804598 and A-438079 and GSK's GSK1482160 are all particularly strong leads. However, recently, A-740003 was shown to be poorly brain penetrant.[216] The cyanoguanidine compounds will be examined in greater detail in chapter 2. Another aspect of increasing potency is the largely consistent behaviour across the functional spectrum of P2X7 in the presence of potent antagonists. Hence, if calcium influx assays reveal high IC_{50}, assays relying on pore formation or IL-1β release are more likely to produce similar data. In Table 2 only the binding measured against the variation of calcium influx has been reported for conciseness.

Table 2 P2X7 receptor antagonists

Compound class	Antagonist	pIC_{50} at hP2X7 (M)	pIC_{50} at rP2X7 (M)	pIC_{50} at mP2X7 (M, BALB/c)	Selectivity	LogP	Refs
Unselective P2X antagonists	**PPADS**	5.49±0.03	5.08±0.02	4.39±0.07	Poor, active at other P2X and P2Y receptors	-3.43	[214,217]
	PPNDS	6.39±0.02	6.03±0.01	5.10±0.09	Poor, active at other P2X and P2Y receptors	-2.35	[214]
	Suramin	<2	<2	<2	Poor, active at other P2X and P2Y receptors		[214]
	NF279	4.70±0.05	<4	4.80±0.30	Poor, active at other P2X and P2Y receptors	-13.9	[214]
	oATP	<2	<2	<2	Poor, active at other P2X and P2Y receptors	-0.13	[214]
Isoquinolines	**KN-62**	4.97±0.12	<4	<4	Different affinity for human vs rodent P2X7 receptors.	4.8	[214,217]
	KN-04	4.26±0.19	<2	n/a	Different affinity for human vs rodent P2X7 receptors.	4.04	[217]
	Compound 18m	7.6±1.1	n/a	n/a	Good ADMET	4.51	[212]
Serendipitous hits	**BBG**	<4	5.09±0.06	<4	High, inactive at other P2 receptors	-3.7	[214]
	MRS 2159	5.76±0.03	5.33±0.04	4.80±0.05	Poor, active at other P2X and P2Y receptors	-1.43	[214]
Cyanoguanidines	**A-740003**	7.36±0.01	7.74±0.02	6.57±0.04	High, inactive at other P2 receptors	5.15	[196, 213, 216]
	A-804598	7.96	8.04±0.01	n/a	High, inactive at other P2 receptors, brain penetrant	4.37	[196, 213, 218]
Azoles	**A-438079**	6.91±0.01	6.51±0.03	6.01±0.12	High, inactive at other P2 receptors	3.3	[219, 220]
	Compound A	7.75±0.14	6.62±0.14	n/a	Brain penetrant	5.64	[219]
Cyclic imides	**AZ11645373**	8.15 (allosteric)	>4 (allosteric)	n/a	n/a	3.76	[221, 222]

Table 2

Compound class	Antagonist	pIC50 at hP2X7 (M)	pIC50 at rP2X7 (M)	pIC50 at mP2X7 (M, BALB/c)	Selectivity	LogP	Refs
Aryl amides	**Various**	Up to 8.4	n/a	n/a	n/a		[220]
	Compound 7	8.3±0.08	7.2±0.08	7.5±0.08	High, inactive at other P2 receptors	4.16	[223]
	Compound 8	7.7±0.07	7.8±0.1	7.1±0.2	Poor, high affinity for hSERT	4.35	[223]
Amidopyrrolidines	**GSK1482160**	8.5	6.6	n/a	n/a	1.88	[224, 225]
Dihydrotriazolopyrazinones	**Compound 11d**	9.2±3.9	7.1±3.5	n/a	Selective and brain-penetrant	2.44	[221-224]

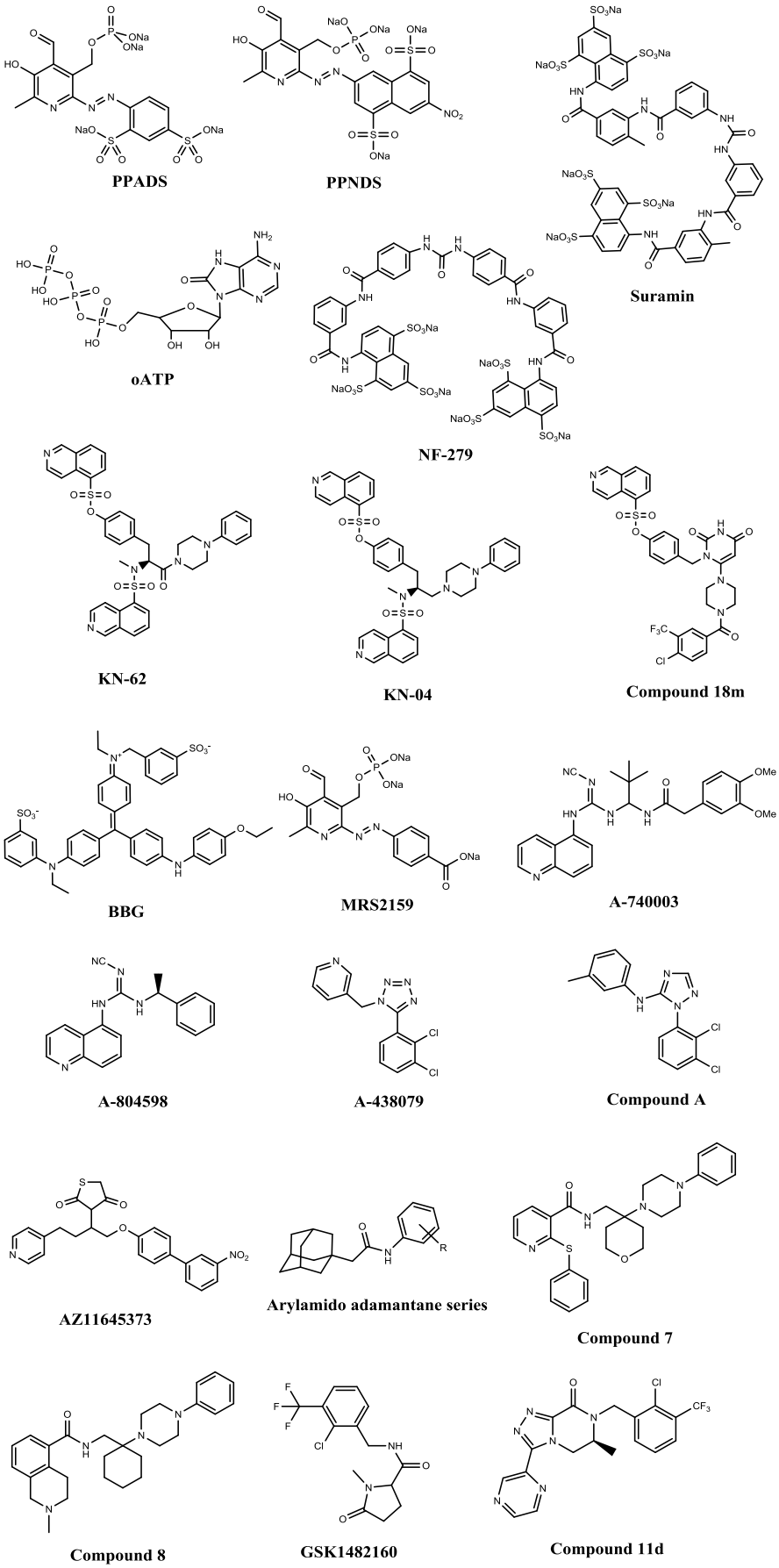

Figure 8 Selection of the best known P2X7 antagonists

1.2.7 Radiolabelled P2X7 imaging agents

Several tritiated P2X7 radioligands can be found in the literature. [^{3}H]Compound 13 is a KN62 analogue presenting an additional *ortho*-methyl group at the phenyl piperazine ring also presenting a tritium atom in the *para* position (Figure 9). The compound was employed for radioligand binding assays in HEK293 cells, indicating good affinity.[226]

It was not until 2007 that a second radiotracer, [^{3}H]Compound 17 was synthesised from its ethyl ester analogue by reduction with tritiated $LiAlH_4$. The tracer was evaluated in HEK293 and U-2 OS P2X7 transfected cell membranes and showed higher binding compared to wild type controls. It was then also used to show binding kinetics, competitiveness and the presence of cooperative binding in the presence of P2X7 receptor ligands ATP, decavanadate and by self-blockade.[222, 227, 228] In 2009, Donnelly-Roberts and co-workers at Abbott Laboratories released a third tritiated antagonist based on the structure of A-804598 (Figure 9). They reported radioligand binding data demonstrating high selectivity and affinity for rP2X7 expressed in recombinant 1321N1 cell membranes.[229] This radioligand was then taken forward by Able *et al.* at Pfizer for the study of the receptor occupancy in rat. Upon incubation of brain slices, they found widespread expression of the target receptor. However, only 60% specific binding was observed in homogenate assays at equilibrium. Finally, they showed *ex vivo* concentration-dependent inhibition of the binding upon incubation with triazole Compound A.[67] In 2014, others employed the tritiated ligand to assess the IC_{50} and K_i of a large panel of antagonists in 1321N1 cell membranes.[230] Recently, the new radioligand [^{3}H]JNJ-54232334 with rat pK_i of 9.3±0.1 was described. This compound improved on the specific binding of the previous tritiated compound as demonstrated by the reduced non-specific binding in P2X7$^{-/-}$ *in vitro* brain autoradiography. Also, the radiotracer showed homogenous binding, confirming the ubiquitousness of P2X7 observed in the same study by immunohistochemical staining, while retaining the ability to show more reliably than [^{3}H]A-804598 the *ex vivo* concentration-dependent receptor occupancy of P2X7 antagonist JNJ-54140515.[231]

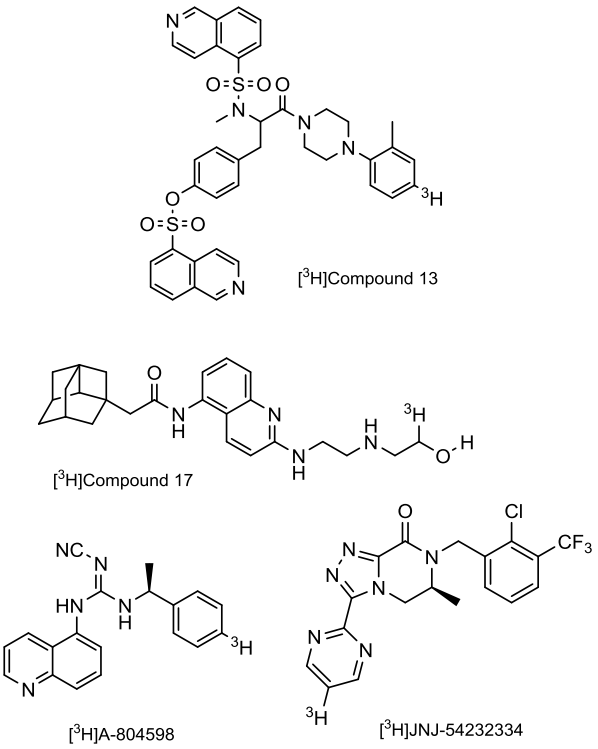

Figure 9 Chemical structures of selected P2X7 tritiated ligands.

In the last decade instead, a small library of P2X7 radioligands amenable for Positron Emission Tomography (PET) has become available (Figure 10). A radiofluorinated version of a derivative of compound A with nM affinity appeared in a patent in 2010. The latter included synthetic details of indirect radiolabelling by attachment of an [^{18}F]fluoroethyl fragment.[232] The binding of the cold tracer was tested in a Yo-Pro dye uptake-associated P2X7 pore formation assay. Upon inhibition by the non-selective P2X blocker PPADS, the tracer was inhibited by >69%, suggesting good affinity for P2X receptors. No further work with this compound has appeared in the literature since, possibly due to poor selectivity to a specific P2X receptor.

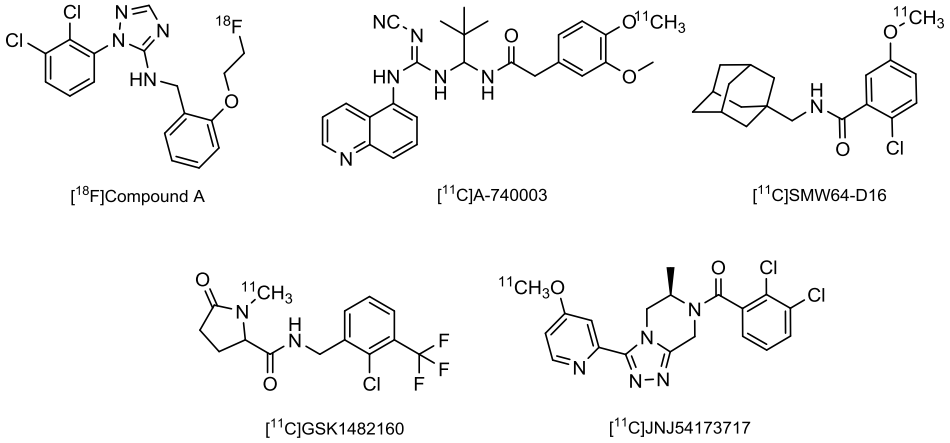

Figure 10 Chemical structures of selected P2X7 radiotracers.

In 2014, Janssen and co-workers at the VU University Medical Centre in Amsterdam reported the first radiolabelled P2X7 antagonist to be tested *in vivo*. Their compound, [^{11}C]A-740003, was radiolabelled by iodomethylation in the presence of base and heat. However, biodistribution studies in wild type rats showed low brain uptake, possibly due to low receptor distribution in this model, and low metabolic stability.[216] The tracer was shown to target the inflamed site when brain slices from two different rat models of neuroinflammation were incubated with [^{11}C]A-740003. Both models were injected intrastriatally with LPS or an adenoviral-associated viral vector expressing hP2X7R (AAV-hP2X7), respectively. Autoradiographic scanning revealed mildly increased striatal uptake in the AAV-hP2X7 model, but less than half in the LPS model, suggesting that different inflammation patterns might be generated in the two cases.[233] Moreover, the uptake of another P2X7 radiotracer developed by the Windhorst group at the VU University, [^{11}C]SMW64-D16, was very similar to that of [^{11}C]A-740003 in both models, but no significant brain binding was observed by PET. [233]

In 2015, Gao and co-workers at Indiana University published a new ^{11}C radiotracer,[234] based on the BBB penetrant hit GSK1482160, which possesses a 3 nM affinity for hP2X7.[224, 225, 235] The tracer was produced in just one synthetic and one radiosynthetic step with a 40-50% radiochemical yield and optimal radiochemical purity and specific activity. However, *in vivo* bioavailability and stability studies for the radiolabelled tracer have not been reported to date. Finally, at the time of submission of this thesis in 2016, Ory *et al.*[236] developed [^{11}C]JNJ-54173717 from its tritiated analogue [^{3}H]JNJ-54232334 (see above in this section). The tracer showed nanomolar affinity for P2X7, reversibility of binding, the ability to cross the BBB and an ideal lack of brain metabolites. Evaluation in a rat model intrastriatally-injected with a viral vector expressing fluorescent-labelled hP2X7 showed selective binding of the radiotracer with rapid washout from the non-injected control striatum. Additionally, [^{11}C]JNJ-54173717 binding in monkey brain was blocked with two distinct P2X7-selective antagonists. This is currently the most promising tracer available.

To the best of my knowledge, no further P2X7 radiotracers have been described, which leaves opportunity for the development of a novel ^{18}F-based P2X7 radiotracer.

1.3 Nuclear imaging with Positron Emission Tomography

1.3.1 Principles of Positron Emission Tomography

This work intends to investigate the P2X7 receptor and neuroinflammation by developing a tracer suitable for Positron Emission Tomography (PET) imaging. But why use PET?

PET is a non-invasive functional imaging technique which exploits radioactive decay as a means of signal detection. The related nuclear imaging technique of single photon emission computer tomography (SPECT) differs from PET in that it involves gamma (high energy photon) emitting radionuclides rather than the high energy beta emitters used in PET. Magnetic resonance imaging (MRI) is yet another non-invasive imaging technique, whose signal is generated by the relaxation of nuclear spins previously aligned to a strong magnetic field.

In PET, radionuclide decay results in the emission of positrons. These collide and annihilate with surrounding electrons (known as an “event”), generating two anti-parallel gamma rays of 511 keV along a so-called line-of-response (LOR) (Figure 11). Correlation of the two signals by coincident detection results in the 3D localisation of an event. Millions of signals need to be acquired for the signal-to-noise ratio (SNR) to reach adequate levels and for an image to be generated upon data processing and image reconstruction.

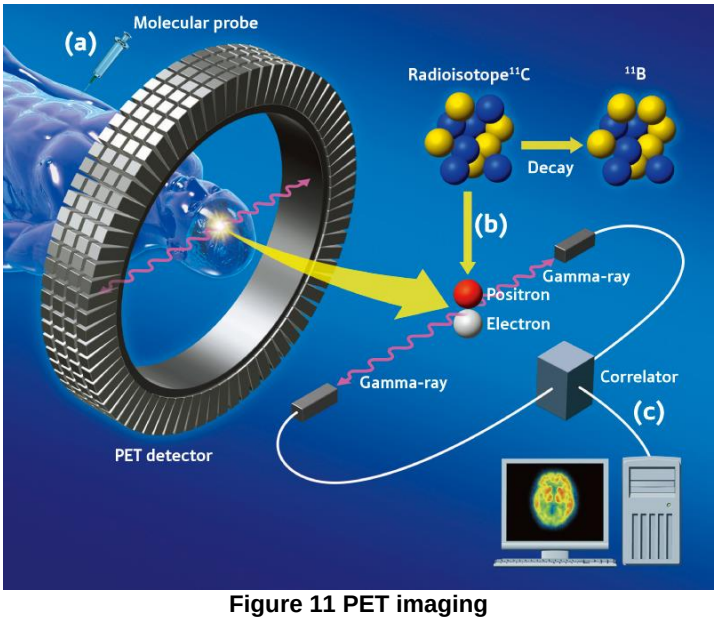

Figure 11 PET imaging

Coincidence detection of the antiparallel gamma rays enables resolutions of up to 1 mm, a limit set by the spatial resolution of the PET camera. This limit can lead to partial volume effect distortions in the measurements of true radioactivity concentration if the object of interest is smaller than about 10 mm.[238] The resolution value is also limited by the inherent distance

travelled by the positrons from the emitting nuclides before annihilation occurs. Positrons in fact have the same rest mass of electrons and as such the two experience extensive Coulomb interactions before the positron's kinetic energy is dissipated and annihilation can occur. The loss of resolution due to tissue-derived annihilations and scattering and varies according to the density of the tissues. Furthermore, variations in the momentum of the annihilating particles induce an angular deflection in the two antiparallel gamma rays generated, and are responsible for an inaccuracy of up to 3 mm. In contrast, SPECT relies on single photon emissions, meaning that coincidence events do not need to occur for a signal to be registered. Incident photons are only filtered by collimators to reduce false events and, especially with pinhole collimators, SPECT can reach higher resolutions than PET.[239] However, SPECT is less sensitive than clinical PET due to its ability to acquire coincidences in three dimensions, without the loss of signal associated with the use of collimators or gamma ray technology.[240] Also, PET treats only coincident events along a LOR as true positive signals, thus inherently eliminating much noise (Figure 12). This is in spite of false positives still getting recorded as scattered and as accidental coincidences. Finally, the revival of time-of-flight (ToF) PET has pushed the boundaries further by enabling the determination of the most probable location of origin of each event along the LOR (Figure 12.4).[241, 242]

Once PET images are acquired, they need to be further reconstructed and processed so as to remove noise, motion effects and improve accuracy of the signal visualised and of the quantitative pharmacodynamic data.[243] The regional concentration of the tracer can then be determined by drawing regions of interest (ROI) using computational methods and by co-registration with structural images such as CT or MRI.

In terms of utility, PET surpasses the other functional imaging modalities for sensitivity and ability to inform directly about the metabolic fate of molecules at the receptor level. Conversely, it is an expensive procedure due to the need to prepare the radiotracers with highly trained staff and complex equipment. In the UK, a routine PET/CT scan costs in the range of £635–£1,300,[244] whereas MRI scans do not exceed £900.

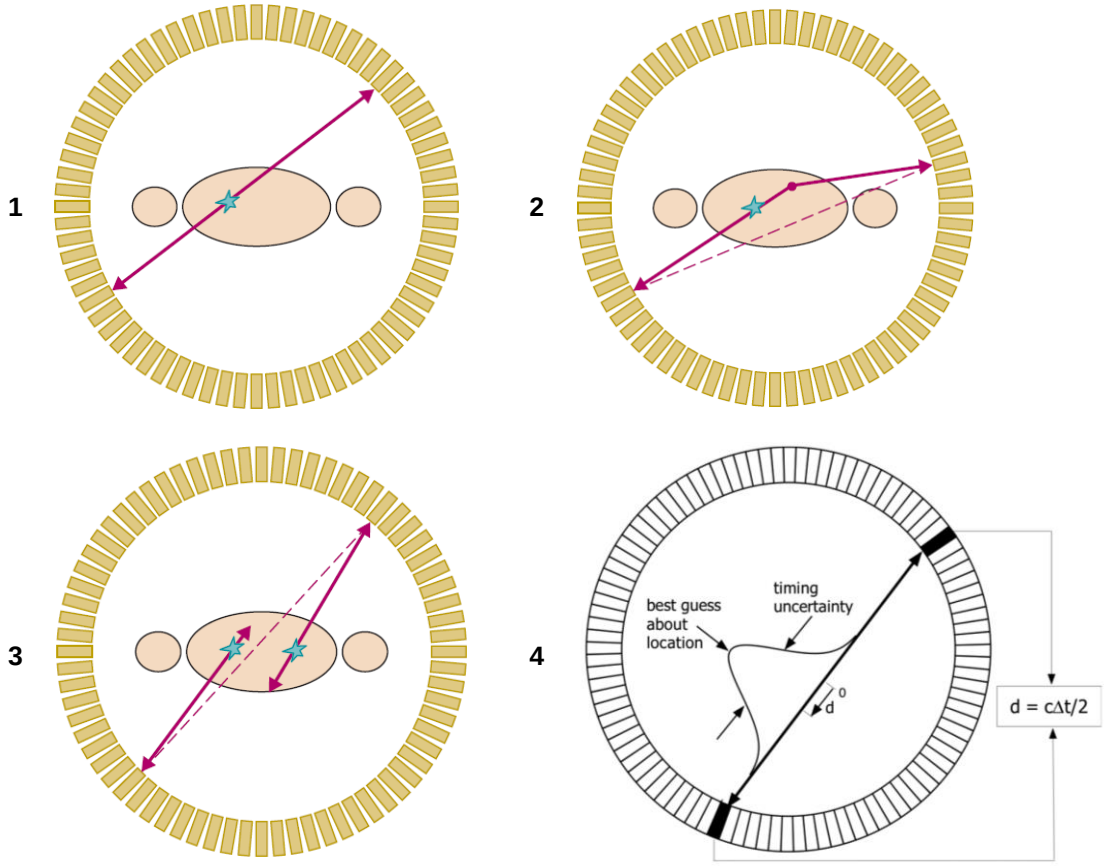

Figure 12 Types of coincident events and time-of-flight (TOF) PET data acquisition

Moreover, the rapid decay of radionuclides requires most radiopharmaceuticals to be produced on site or in proximity of the site of application. Most commonly, PET exploits positrons emitted from decaying ^{11}C ($t_{1/2}$: 20.3 min, positron energy (pE): 960 keV), ^{18}F ($t_{1/2}$: 109.8 min, pE: 640 keV), ^{13}N ($t_{1/2}$: 9.97 min, pE: 1190 keV), or ^{15}O ($t_{1/2}$: 2.1 min, pE: 1700 keV), but also radiometals such as ^{68}Ga ($t_{1/2}$: 68 min, pE: 1890 keV), ^{64}Cu ($t_{1/2}$: 12.7 h, pE: 1350 keV), ^{89}Zr ($t_{1/2}$: 78.41 h, pE: 909 keV) and ^{82}Rb ($t_{1/2}$: 1.27 min, pE: 3150 keV).[245] A relatively long lived radionuclide such as ^{18}F provides a partial solution to this problem, permitting off site production, longer scan times and longitudinal studies to be performed.

The production of positron emitting (β^+) radionuclides starts from the bombardment of stable parent isotopes, typically with high energy protons derived from a charged particle beam. Protons are accelerated by electromagnetic fields which curve the trajectory of the protons and a high alternating voltage between the acceleration chamber electrodes (dees) which induce an outwards spiral motion. The accelerated protons are then made to hit a target in the bombardment chamber, leading to a nuclear reaction and the production of the desired isotope.

In this project, the focus is on the radionuclide ^{18}F. ^{18}F is produced by bombardment of ^{18}O-enriched water, which is found in nature in 0.2% abundance. Upon bombardment, a neutron is recoiled from the target (knockout reaction) resulting in carrier-free aqueous ^{18}F:

$$^{18}O\ (p, n)\ ^{18}F$$

More rarely, fluorine is instead produced from deuteron bombardment of ^{20}Ne and the release of an α particle:

$$^{20}Ne\ (d, \alpha)\ ^{18}F$$

Radionuclides are either utilised directly in the chemical form produced in the cyclotron target (e.g. $[^{15}O]O_2$, $[^{13}N]NH_3$) or, most commonly, they are synthetically bound to molecular fragments (e.g. [^{18}F]fluorodeoxyglucose). ^{18}F can be made to react by either electrophilic or nucleophilic attack. Electrophilic fluorinations rely mostly on the reactive reagent $[^{18}F]F_2$. However, this diatomic reagent is generally unspecific and is commonly produced with the addition of carrier, leading to low specific activities.[246, 247] Nevertheless, other electrophilic fluorination reagents have been developed, most remarkably acetyl hypofluorite[248] and [^{18}F]N-fluorobenzylsulfonimide[249]. Despite the historically prominent role played by electrophilic radiofluorination,[250] it is the nucleophilic approach that is currently most in vogue, thanks to its greater potential to label compounds selectively and with high specific activity, key for receptor imaging, quantitation of the binding and PET micro-dosing studies. Radiolabelling strategies involving nucleophilic radiofluorination will be explored in depth in the radiochemistry chapter of this thesis.

Radiolabelled molecules are made to closely resemble compounds present in an organism without altering their chemical structure. Thus, they can be usefully employed to observe the behaviour of their endogenous analogues, such as glucose metabolism for [^{18}F]FDG. Importantly, PET involves the use of trace amounts of radioactive compounds, usually less than 10 μmol for small molecules, enabling target visualisation without toxicological or pharmacological effects.[251] For this to happen, radiotracers necessitate high specific activities and sufficiently low amounts of carrier compound so as not to interfere with physiological processes. In the following sections a number applications of PET tracers in routine individual

patient management, experimental clinical research and industrial pharmaceutical settings are laid out.

1.3.2 Applications of Positron Emission Tomography

PET for individual patient management in clinical practice

PET imaging plays a pivotal role in clinical practice. [^{18}F]FDG is used routinely to diagnose a variety of conditions that alter cellular metabolism and glucose processing, be them related to cardiovascular, oncological, respiratory or central nervous system disorders. Importantly, it is able to indicate the increased cell metabolism of tumour cells, the occurrence of metastases, an altered cardiac perfusion and the alteration of cognitive function in mental disorders.[252] However, [^{18}F]FDG falls short when it comes to distinguishing fast-growing tumours from healthy fast-growing, glucose-hungry tissues. Similarly, it poorly highlights slow-growing tumours. Moreover, [^{18}F]FDG's relative non-specificity means it struggles to distinguish inflamed or infected tissues from highly metabolic cells, albeit the two sometimes coincide. Finally, it has restricted applications which limit the potential of PET for individualised patient management.[252]

CNS PET is a field of intense research yet only a limited number of tracers are routinely available for individual patient management. [^{11}C]PIB ([^{11}C]Pittsburgh compound B), [^{18}F]florbetapir and [^{18}F]flutemetamol, are employed to image amyloid-β sheet aggregates and can contribute to an Alzheimer's disease diagnosis.[253] [^{18}F]DOPA ([^{18}F]L-3,4-dihydroxyphenylalanine) is used to image amine transport and decarboxylation and inform about the functional state of the nigrostriatal dopaminergic pathway in Parkinson's disease as well as to identify neuroendocrine tumours.[254] A wider variety of PET tracers are used clinically in oncology, where PET is employed to determine the exact functional tumour volume and boundaries prior to surgical intervention, to characterise cancers and to assess the tumour response to a treatment regimen. [^{11}C]Methionine is used as a marker of amino acid transport which relates to protein synthesis and the extent of tumour proliferation. Similarly, [^{18}F]FLT ([^{18}F]fluorothymidine) is a marker of thymidine nucleoside transport and [^{11}C]choline of phospholipid synthesis, both of which can determine the cell proliferation rate by indicating DNA replication and cell membrane formation, respectively.[255, 256] Furthermore, [^{18}F]FMISO ([^{18}F]fluoromisonidazole) visualises the enzymatically active intracellular reductive environment

within viable cells that maintain the capacity to transport substrates, which is typical of fast-growing and radiotherapy and chemotherapy-resistant tumours.[257]

PET in experimental clinical research

PET imaging also plays a crucial role in clinical research. Primarily, tracers with a clinical translation can assist in elucidating the pathophysiology of disease or the role of their target. Focusing on CNS tracers, the use of the cannabinoid type-1 receptor (CB_1R) tracer [^{18}F]MK9470 has been employed to assess the target's involvement in food and addiction disorders, as well as in motor, attention and memory processes.[258] Similarly, [^{18}F]T807 and [^{18}F]THK523 are promising tracers being investigated for the diagnosis of tauopathy, a hallmark of dementia, most likely linked to an exacerbation of the neurodegeneration in dementias.[259] The serotonin 5H2A receptor tracers [^{18}F]setoperone and [^{18}F]altanserin instead, have been employed to study the role of their target in depression and schizophrenia.[260, 261]

Moreover, other tracers are taken to the clinical stage to overcome the deficiencies of the currently available ones. This is the case for the dopamine transporter (DAT) tracer [^{18}F]FE@CIT, which presents an improved specificity of binding to the desired target with respect to other transporter proteins compared to [^{123}I]beta-CIT and [^{123}I]CIT-FP.[262] For imaging the 18 kDa translocator protein (TSPO) receptor correlated with the extent of neuroinflammation, the benchmark tracer [^{11}C]*(R)*-PK11195 comes short in terms of its substrate affinity, non-specific binding, BBB penetration and kinetic profile.[263] Hence, [^{11}C]DAA1106, [^{18}F]DPA714, [^{11}C]PBR28 and [^{11}C]PBR06 among others have been developed to fill the gaps in the TSPO PET imaging market. Nonetheless, [^{11}C]*(R)*-PK11195 has been successfully employed to investigate the extent of inflammation in a wide range of human CNS studies.[264]

PET in drug development

Drug discovery and development is a long and expensive process. Yet, fewer than 10% of the compounds investigated reach clinical trials and up to $400,000 per drug is spent on toxicity studies alone.[265]

PET is increasingly employed in industrial settings to reduce these costs, particularly by allowing early termination of unsuitable compounds.[266] In the early phases of drug discovery, PET can facilitate the understanding of a compound's pharmacodynamics and provide pharmacokinetic and occupancy measures useful to guide dose selection. It can act as a benchmark to validate the pharmacological activity of novel compounds and inform about potential toxicological effects by indicating where the compounds are likely to accumulate.[267] PET is ideally fit for the first phase of translation of compounds into the clinic with limited toxicological concerns. Target occupancy analysis and pharmacodynamic data are then useful to inform phase I and II clinical trials. PET is also ideal to help stratify patients based on the potential for treatment efficacy and to monitor their response to treatment. This is particularly key in neurology, where PET may help to improve the disease classification or exact diagnosis, thereby avoiding the targeting of conditions present only in a subset of the diseased subjects under observation and helping to identify whether a treatment is efficacious beyond the symptomatological effects.[268]

Finally, on a more financial side, PET can help to pharmacologically differentiate a new drug from competitor drugs and it can support the case for EMA/FDA approval. It can also help expand the market size, by anticipating detection of the disease, and monitor the course of treatment.

1.3.3 The current state of nuclear imaging of inflammation

Current routine clinical PET imaging of inflammation far too often relies on detecting inflammatory cells-derived increased glucose metabolism by [^{18}F]FDG.[269] Despite its successes,[270] the scientific community has understood the need for and has taken steps towards more specific biomarkers to image inflammation.[271] Choline imaging already provides some improvements, choline processing in cell membranes being much lower than glucose in certain tissues such as the myocardium and thus enabling a much higher contrast during inflammatory episodes.[272, 273] Moreover, mannose receptor imaging correlates better than [^{18}F]FDG with macrophage activation, especially in relation to arteriosclerotic plaque tracking.[274] Nevertheless, the current focus of most research in PET imaging of inflammation is towards targeting the 18 kDa translocator protein (TSPO).[143]

TSPO is a multifunctional protein located on the outer membrane of the mitochondria of (predominantly) macrophages, mast cells, microglia and astrocytes.[275] Its expression is low in their quiescent state and high during pro-inflammatory cellular activity, as demonstrated by the ability of TSPO blockade to substantially reduce microglial activation and neuronal death in quinolinic acid-injected rat striatum.[276] Among many radiotracers targeting TSPO, the most widespread is certainly [^{11}C]*(R)*-PK-11195, whereas several "second generation" TSPO tracers such as [^{11}C]DAA1106, [^{18}F]DPA714, [^{11}C]PBR28 and [^{11}C]PBR111, acting *via* alternative binding modes are also available.[277] Their applications range from *in vitro* and *in vivo* imaging of CNS inflammation to clinical and post mortem imaging studies.[278-283] Where [^{11}C]*(R)*-PK-11195 lacks a strong blood-brain barrier (BBB) penetration, has moderate target specificity a low signal-to-noise ratio and variable kinetic profile, second generation TSPO tracers demonstrate an improved affinity and bioavailability, which have recently enabled quantitative TSPO PET.[284, 285] The second generation tracers however cannot overcome the hurdle of TSPO displaying polymorphism between subjects. Thus, the categorisation of the population according to TSPO gene polymorphism is essential for true second generation TSPO tracers image interpretation.[286] Further, several TSPO radiotracers lack good binding correlation between human and rodent receptors.[287] Thus, their translation to the clinic is problematic and gives rise to alternative interpretations of the clinical data collected up to the present date depending on what is thought to be the true target of the tracers.[264, 288] Finally, TSPO's link to inflammation, aside from its increased expression, is unclear, which raises further questions as to what TSPO imaging is actually capturing of inflammatory events.[263] An advancement in the field is represented by the discovery of the third generation tracer [^{18}F]GE180. This tracer presents better signal-to-noise ratio, higher binding potential and is more sensitive to TSPO than [^{11}C]PK-11195 in rodents[289, 290] and humans,[291] whereas, similarly to the second generation tracers, it still falters with the receptor polymorphism issue.[292]

In this context, in the last decade a spree of development of new PET tracers targeting inflammation biomarkers has occurred. The list of radiopharmaceuticals for each biomarker outlined in this section is extensive, hence a selection is presented here, while comprehensive reviews on the subject have been published by Wu *et al.*[271] and Dupont *et al.*[293]

One of the targets under investigation is the type 2 cannabinoid receptor (CB_2R) due to its strong links to inflammation. While CB_2R presents minimal expression in resting microglia and macrophages, it is strongly upregulated in concomitance to immune activity.[294] Only a small set of compounds have reached the preclinical stage for CB_2R PET imaging to date, with promising affinity, selectivity and brain uptake data in particular for [^{11}C]NE40 and [^{11}C]A-836339.[295, 296] Also the circulating inhibitory G-protein-coupled somatostatin receptor 2 ($SSTR_2$) is an attractive target due to its involvement in neuroendocrine and inflammatory activity and its high expression on activated macrophages. ^{68}Ga-DOTATATE has demonstrated particular potential as $SSTR_2$ tracer, correlating positively with calcified arteriosclerotic plaques in two studies.[297, 298]

A large amount of effort has gone as well in the development tracers against inflammatory cytokines. Among these is cyclooxygenase-2 (COX-2), an integral membrane glycoprotein responsible for converting arachidonic acid into prostaglandin[299, 300] and a crucial mediator of peripheral and central inflammation.[301] COX-2 imaging is championed by [^{99m}Tc]Celecoxib, which has shown strong binding in cells strongly expressing COX-2, although specific binding has not been demonstrated.[302].

Additionally, some have imaged matrix metalloproteinases (MMPs), responsible for the processing of extracellular proteolysis, a critical step in many inflammatory conditions, particularly of the cardiovascular system.[303, 304] MMPs are found predominantly on microglia, astrocytes and monocytes and their expression is modulated in tune with the release of inflammatory cytokines and prostaglandins, resulting in excitotoxicity, neuronal damage and BBB disruption.[305] Radiopharmaceuticals targeting MMPs include [^{64}Cu]DOTA-CTTHWGFTLC,[306] [^{18}F]CGS27023A,[307] several ^{99m}Tc and ^{123}I SPECT probes employed predominantly in vascular inflammation imaging[308] and radiolabelled C-5-disubstituted pyrimidine 2-4-6-triones, which have recently been modified to feature ^{18}F-triazoles and demonstrate strong potency against MMP-2, MMP-8, MMP-9 and MMP-13.[309]

Furthermore, interleukin-2 (IL-2, a cytokine) PET tracers have enabled indirect imaging of activated T lymphocytes, on the surface of which IL-2 receptors become expressed during inflammatory episodes. The leading tracer in this respect is [^{18}F]FB-IL-2, an [^{18}F]SFB labelled IL-2 construct,[310] whereas ^{123}I and ^{99m}Tc-labelled IL-2 has been extensively employed to image autoimmune,[311] cardiovascular[312] Chron's and other diseases.[313]

Moreover, TNF-α is a cytokine that is abundantly expressed during the acute phase of the immune system activation, as it sustains white blood cell transport to inflammation sites. Conversely, it becomes downregulated in the later stages, where it supports the apoptotic termination of inflammatory cells.[314] [64]Cu-DOTA-etanercept is a PET radiotracer targeting TNF-α which was preclinically validated in tetradecanoyl phorbol acetate (TPA) rodent models of inflammation,[315] and was retained in the CNS only in the initial acute inflammatory phase. Moreover, [^{11}C]tricyclic Nec3 necroptosis inhibitors of structure 3,3a,4,5-tetrahydro-2H-benzindazole are being investigated as potential PET tracers for TNF-α PET imaging and await *in vivo* evaluation.[316]

Another active area of research is the direct labelling of migratory inflammatory cells. Direct leukocyte SPECT imaging via [^{99m}Tc]HMPO labelling is the gold standard in cell labelling, which has largely replaced [^{111}In]oxine leukocyte imaging.[317] However, their complex and hazardous production has prompted the development of techniques to image homing-associated molecules, involved in leukocyte migration.[318] Endothelial adhesion molecules mediate leukocyte tissue infiltration and have been labelled with a range of PET and SPECT radionuclides. E-selectin, whose mAb, mAb fragments and targeting peptides have been labelled with ^{111}In and ^{99m}Tc, participate in the rolling step of the cell-blood vessel adhesion cascade.[319-323] Antibodies and peptides targeting the vascular cell adhesion molecule-1 (VCAM-1) have been labelled with ^{123}I, ^{99m}Tc and ^{18}F to image leukocyte extravasion.[324-326] Moreover, RGD peptides targeting integrin $\alpha_v\beta_3$ have been tagged with ^{68}Ga, ^{64}Cu and ^{18}F, providing an image of endothelial cell migration through the basement membrane during blood vessel formation and can support a diagnosis of angiogenesis.[327-329] Finally, the vascular adhesion protein-1 (VAP-1) imaging has been carried out with ^{123}I and ^{68}Ga-labelled peptides and antibodies and well as with [^{68}Ga]DOTAVAP-P1 and analogues.[330-332] VAP-1 is involved in the early stages of leukocyte recruitment and transmigration and is specifically upregulated during inflammation.

1.4 Project novelty and need

With the development of a novel ^{18}F radiotracer targeting P2X7, this project intends to address the scientific need for:

- A quantitative diagnostic tool for imaging P2X7 *in vivo*.
- An alternative to TSPO tracers to visualise neuroinflammation (see section 1.3.3).
- Assessing the type and degree of involvement of P2X7 receptors in health and disease.
- Tracking clinical trials targeting P2X7, monitoring clinical outcomes and assisting in drug development (see section 1.3.2).
- Differentiating pro-inflammatory and anti-inflammatory phenotypes *in vivo*.

The project intends to innovate the field of neuroinflammation imaging by providing a new BBB-penetrant ^{18}F tracer based on the A-804598 molecular structure (Figure 8).[229]

1.5 Aims

The aim of this project is **to develop a novel radiotracer suitable for imaging P2X7 in vivo**. This is addressed following a sequential approach as described in each of the following chapters.[330-332]

***Chapter 2: Radiotracer design and pharmacokinetic considerations*.** To design a library of structures analogous to the lead radiotracer A-804598 amenable for ^{18}F PET tracer development. The two approaches employed were the computational estimation of a set of physicochemical parameters and the *in silico* molecular docking of a set of structures to achieve a semi-quantitative and visual estimation of the target binding.

***Chapter 3: Synthesis*.** To synthesise, purify and characterise all non-radioactive chemical compounds required for this study.

***Chapter 4: Radiochemistry*.** To develop radiolabelling strategies suitable to produce the tracers in a form useful for *in vitro* and *in vivo* evaluation. Three nucleophilic ^{18}F labelling techniques were employed: fluoroethyl azide fragment labelling followed by a “click” copper catalysed alkyne-azide cyclisation, boronic ester aromatic substitution and quaternary ammonium substitution followed by a reduction and a nucleophilic conjugation.

***Chapter 5: Cell binding assays*.** To assess and quantify the radiotracer uptake in P2X7 cell models using two approaches: a radioligand binding assay and a functional calcium-influx binding assay, aiming to rank the tracers in terms of their target affinity and selectivity.

***Chapter 6: Radioligand tissue binding assays*.** To evaluate the radiotracer binding in a tissue model of neuroinflammation, with the ultimate aim of achieving a semi-quantitative picture of the specificity of tracer binding in a native setting.

Chapter 7* In vivo *evaluation. To assess the best radiotracer in a lipopolysaccharide (LPS) rat model of neuroinflammation, with the goal of measuring the degree of blood-brain barrier penetration and P2X7-rich tissue binding to make a preliminary assessment of whether the tracer has the potential to image P2X7 *in vivo*.

Chapter 2

Receptor-binding radiotracer design and pharmacokinetic considerations

Receptor-binding radiotracer design and pharmacokinetic considerations

1.7 Introduction

The design of a good radiotracer for high-affinity receptor targeting is not a trivial task. This chapter presents the case for the design and selection of a library of radiotracers targeting P2X7. The introductory section in divided in three parts: the first discusses the quantitative measures of ligand pharmacokinetics; the second encompasses further design considerations predominantly of a qualitative nature; the third presents the case for the lead radiotracer scaffold selection.

1.7.1 Quantitative measures of ligand pharmacokinetics

In a biological context, a radiotracer's behaviour at the site of binding can be simplified to the equilibrium between dissociated receptor (R) and ligand (L) and the receptor-ligand complex (RL) (Figure 13).

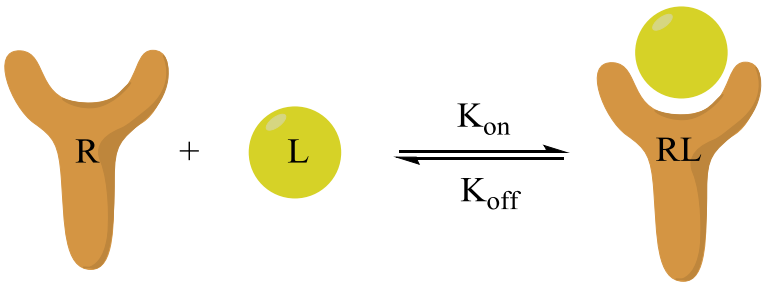

Figure 13 Schematic depicting the receptor-ligand complex equilibrium.

Radiotracers can inform about this equilibrium process *via* dynamic association and dissociation to their target. Qualitatively, *in vivo* PET scanning allows us to appreciate this equilibrium process visually by showing how the tracer accumulates and is cleared from the target sites over time. However, only quantification can provide full insight into the pharmacokinetics of radiotracers. Since pharmacokinetic parameters are key to the lead tracer selection process, a number of concepts need to be defined, which will also be encountered later in the biological evaluation chapters 5-7.

The association and dissociation rates for a molecule binding to a receptor are denoted by the terms K_{on} and K_{off}, respectively (Figure 13). The ratio of the two gives the dissociation constant, K_d, described by the following equation.[333]

$$K_d = \frac{K_{off}}{K_{on}} = \frac{[\mathrm{R}][L]}{[RL]}$$

K_d is an indication of the affinity of a molecule for its target receptor, as is the association constant K_a, the reciprocal of K_d.[334] The receptor-ligand complex concentration is further linked to the dissociation constant by the following expression, derived from the Michaelis-Menten equation, a description of the rate of binding of a substrate to an enzyme.[333]

$$[RL] = \frac{[L]\, B_{MAX}}{[L] + K_d}$$

where B_{MAX} is the total number of binding sites present. At high ligand concentrations, L >> K_d, resulting in B_{MAX} = [RL]. Thus, B_{MAX} also represents the maximal receptor occupancy. At low ligand concentrations (as is often the case for PET tracers) L << K_d, resulting in B_{MAX} / K_d = [RL] / [L], i.e. the amount of complex formed versus the unassociated ligand, known as binding potential (BP). In other words, if [RL] corresponds to the bound radioligand concentration [B] and [L] is the free radioligand concentration [F], the Michaelis-Menten equation becomes

$$[B] = \frac{[F]\, B_{MAX}}{[F] + K_d}$$

and

$$\frac{[B]}{[F]} = \frac{B_{MAX}}{K_D} = BP$$

These parameters can be conveniently quantified *in vitro* by plotting the specific binding versus concentration of tracer (saturation plot) or the bound to free ratio versus the bound fraction (Scatchard plot) as shown in Figure 14.[333] Note that *in vitro* the specific binding curve is the result of the difference between total binding and non-specific binding (NSB) and that the latter increases linearly while specific binding increases hyperbolically up to B_{MAX}. Also, these equations hold only if the assumption that the system is in equilibrium (e.g. the free and bound ligand are constant over the time of measurement). For [F] to be considered “constant”, Hulme and Trevethick[335] recommend an occupancy of <10% for *in vitro* studies. For *in vivo*, others recommend <5%[334] or <3% receptor occupancy.[336]

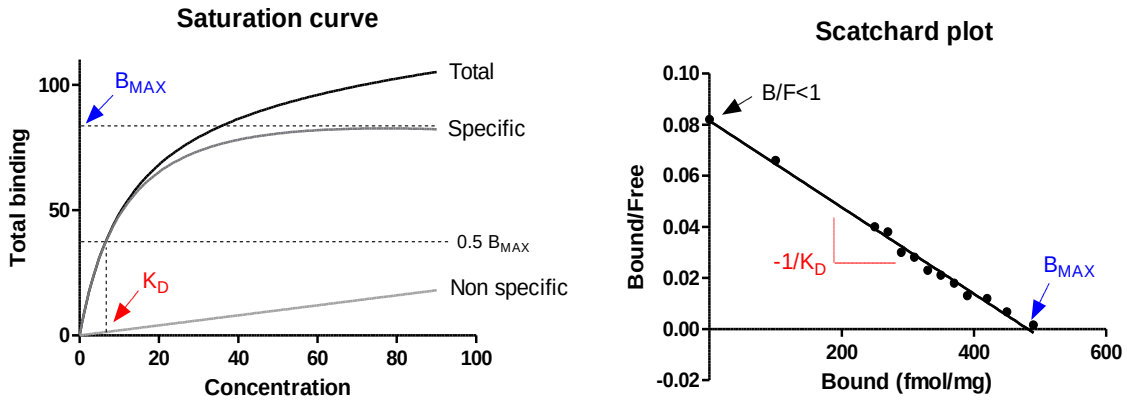

Figure 14 Saturation curve and Scatchard plot

A further measure of receptor-ligand interactions is the IC_{50}, defined as the concentration at which 50% of the binding to the receptor is inhibited.[335] To measure this value, competition assays are employed. Increasing concentrations of non-radioactive ligands are co-incubated with the radiotracer, producing a concentration-dependent response from which IC_{50} values can be extracted (Figure 15). This assay is particularly useful to measure the affinity of compounds relative to other compounds or targets, providing data on the selectivity and modality of binding of a tracer. However, IC_{50} values are relative to the measures of outcome and to the experimental setup, so their interpretation is only valid in relation to similar experimental conditions. This matter will be further expanded upon in chapter 5.

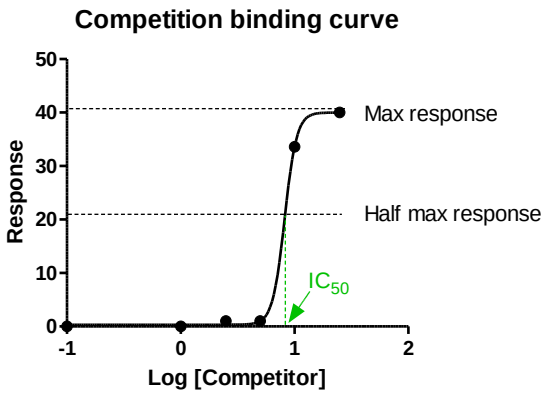

Figure 15 Competition binding curve

One further type of plot is a kinetic binding curve, which displays binding over time at incremental concentrations (association study) or with such a radioligand concentration as to provide high initial receptor occupancy (dissociation study). The ligand will associate and dissociate with hyperbolic or inverse hyperbolic dependence to time, respectively, until a plateau

is reached. When expressing the total binding as a Log function, the dissociation curve becomes a straight line with slope $|K_{on}|$ and $|K_{off}|$.

Saturation, competition and kinetic binding experiments are also useful to assess the modality and type of binding of ligands to their target. Ligands can either be irreversibly or reversibly bound. The former is traditionally seen as less desirable as covalent binding prevents the displacement and washout of the tracer, leading to a lack of true equilibrium. This is however an acceptable modality of binding if the receptor has a high turnover.[337] Reversible binding itself can be comprised of competitive, non-competitive, uncompetitive or mixed reversible binding (Figure 15).

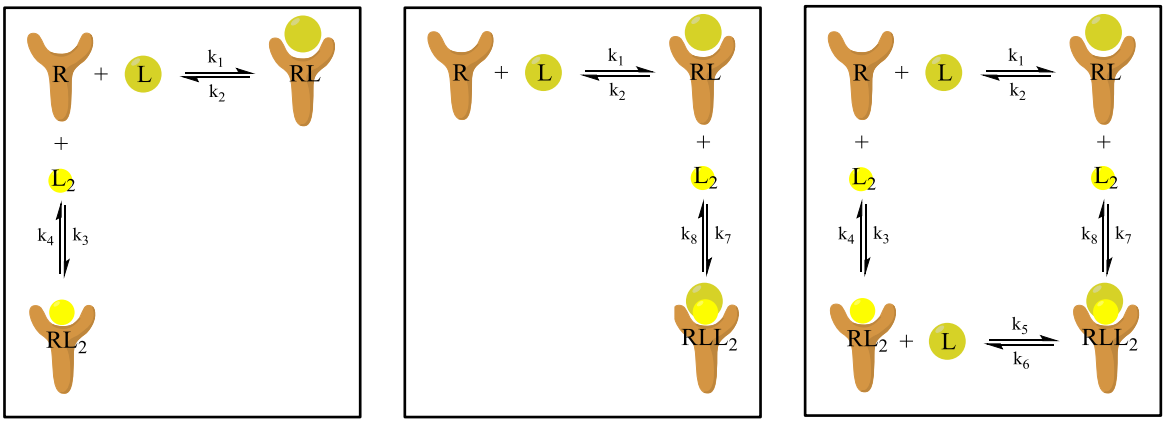

Figure 16 Schematic depicting the receptor-ligand complex equilibrium in the presence of a reversible competitor

Competitive ligands (L and L_2) contend the same binding site. Therefore, complex RL's rate of formation is dependent on the difference between the K_d of both RL and RL_2 complexes and a higher K_d is necessary for RL formation to outcompete RL_2. In contrast, uncompetitive binding does not directly compete against RL's complex formation, actually driving its formation to further bind L_2 to the RL complex, hence decreasing the B_{MAX}. Finally, non-competitive binding solely depends on the concentration of L_2, as while L_2 binds to the same site as L_1, its binding does not prevent RL complex formation and can lead to both L and L_2 to bind to R (RLL_2).

Furthermore, a fourth type of reversible binding exists and is usually referred to as mixed, cooperative or allosteric binding. Similarly to non-competitive binding, both L and L_2 bind concomitantly to the target, but in this instance L_2 affects the binding of L. Most often, this is due to binding to a site other than the orthosteric site, inducing a change in the target's conformation that affects positively, neutrally or negatively the binding of L. Allosteric binding can be assessed with an affinity ratio plot, where the modulated (K_{dapp}) to non-modulated (K_d) rate

constants (defined as the dose ratio), minus 1, is plotted against the concentration of allosteric modulator increased up to the receptor-saturating value. The degree of cooperativity is measured as α, the factor by which K_d is affected. When α>1, there is positive cooperativity, α=1 neutral and α<1 negative cooperativity (Figure 17).[335]

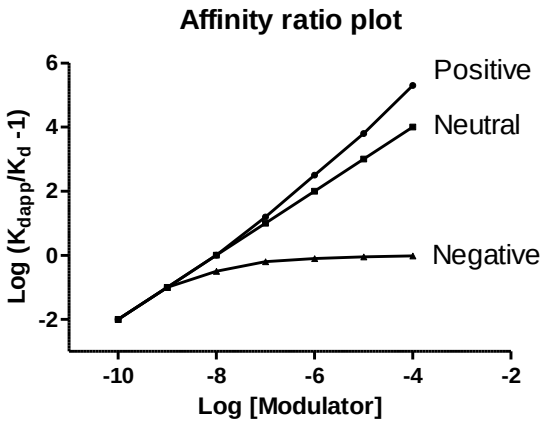

Figure 17 Affinity ratio plot

1.7.2 Design considerations

Similarly to non-radioactive drugs, radiotracer development is an iterative process which is prone to failure. In order to minimise the high attrition rates, PET scientists routinely take into account a number of physicochemical and biological factors which by no means represent a recipe for perfection, but nonetheless enable to streamline the lead radiotracer selection process and its chances to come to human fruition. These considerations start from the choice of the biomedical question and the selection of the biological target. In particular, targets ideally display a strong as possible a density difference between healthy and diseased state to facilitate detection. However, the most fundamental considerations lie in the chemical probe design strategy. The following section is limited to CNS receptor-targeting small molecule radioligands and discusses in particular the importance of: affinity and specificity, bioavailability, metabolism, blood-brain barrier permeability and the necessity for synthetic and radiolabelling accessibility.

Binding affinity and specificity

Binding is strongly governed by the structure-activity relationship (SAR) between the ligand and its target, consisting in the degree of molecular fit that the substrate demonstrates with respect to the binding site. It can be estimated by computational modelling, although true binding affinity can only be determined by experimental means.

Usually, low nanomolar (nM) affinity is desired. However, tracers can in principle succeed with lower potency, particularly if they image a high-density target and as long as the compound is specific and selective for the desired target.[338] Binding selectivity implicates predominant affinity for the desired target. This is different from specificity, which denotes sole binding to the desired target. In this sense, diagnostic radioligands differ from therapeutic drugs, since in the former case aspecific binding may lead to inaccurate images, whereas often for the latter low enough aspecific affinity to avoid adverse effects may be sufficient to reach an appropriate therapeutic window.

In order to determine a compound's affinity and specificity, *in vivo* or *in vitro* screening in cells expressing the target receptor or in native tissue homogenates or slices (autoradiography) is performed. The co-incubation with a homologous compound or knock-out animal model gives data on a compound's specificity of binding, whereas heterologous compound co-incubation informs about the binding selectivity.[339] Specificity of binding is best tested against a set of potentially homotopic targets and against target receptor subtypes. So, for a putative CNS P2X7 tracer, specificity is ideally verified by performing affinity assays against human, rat and mouse P2X7, P2X1-6, P2Y receptors as well as unrelated brain receptors such as adrenoceptors, dopamine, serotonin and histamine receptors.[196, 229, 340]

The initial design of a novel radioligand can take after a known potent ligand. However, this strategy does not guarantee low non-specific binding of the adapted radiotracer, nor optimal washout for quantitative PET imaging.[339] Additionally, if the parent ligand is endogenous, it does not necessarily satisfy the low mass requirements of PET receptor imaging. Sometimes tissue binding studies with analogues labelled with long-lived isotopes such as tritium can be found in the literature, which provide invaluable information on the candidate molecule's binding kinetics.

An alternative design strategy is to synthesise *de novo* libraries of compounds amenable to radiolabelling, possibly offering multiple potential radiolabelling sites. High-throughput screening assays can then support with higher confidence a structure's suitability for PET imaging.[339]

Bioavailability

Upon *in vivo* administration, a chemical interacts with blood and tissue-based species, such as albumin proteins and lipids, which limits its concentration as a free species in the blood. This effect is otherwise known as bioavailability and has profound consequences on the amounts of radiotracers that reach the brain. Therefore, during the radiotracer design phase it is important to take into account a few factors which frequently lead to enhanced binding to such species, although many successful exceptions to these rules of thumb are known.

The most popular way of assessing the suitability of a compound is to follow a modified version of Lipinski's rule of five ():[341]

- Maximum 500 g/mol molecular weight
- Maximum 5 hydrogen bond donors
- Maximum 10 hydrogen bond acceptors
- Lipophilicity of Log P 1.5-3 [342]

Limiting the molecular weight of a molecule enhances its ability to penetrate layers of tissue and reach the target site. However, very small and hydrophilic molecules can have a limiting low plasma circulation time, rendering them too easily excreted for PET detection. The hydrogen donor and acceptor rules of thumb are particularly useful to limit the weak interaction of compounds with the surrounding biomolecules and tissues and facilitate the passive diffusion of the tracer.[343] Finally, the overall lipophilicity should be such as to ensure a degree of aqueous solubility but maintaining some hydrophobic character to enable tissue permeation. High lipophilicity often results in considerable non-selective binding to lipophilic tissues and fatty acid residues on cell membranes, which severely impacts the signal-to-noise in PET acquisitions.

Lipophilicity is commonly expressed as Log P, the partition coefficient, equal to the ratio of concentrations of compound X in a mixture of two immiscible phases (octanol and water) at equilibrium. Another useful measure of lipophilicity is the Log D, which takes into account both ionised and unionised species at a specific pH, usually physiological (pH 7.4). Furthermore, the

polar surface area (PSA), defined as the surface sum over all polar atoms has been shown to be a good descriptor of drug absorption, bioavailability and brain penetration. In particular, values should be smaller than 140 $Å^2$ for optimal cell permeability and smaller than 90 $Å^2$ for maximal BBB permeability.[344] This rule extends to the preference for molecules lacking a formal charge, which considerably increases hydrophilicity and hinders cell penetration and retention.

Metabolism

Blood metabolising enzymes act on compound within minutes from the time of administration, often times derivatising it in such a way as to lose its target affinity. Compounds are often fragmented to more hydrophilic species which can easily be washed out and excluded from BBB entry.[345] However, sometimes lipophilic fragments form which can penetrate through endothelial and epithelial barriers. Both if the fragments are alternatively active metabolites (alternative specific binders) and if they are inactive fragments (non-specific binders), the background noise is increased.[346] This results in a lower signal-to-noise ratio, as PET cannot discern between radioactive signals arising from different molecular species, although to some extent biomathematical modelling can be employed to adjust the output image for radiometabolite formation. Nonetheless, not all metabolism is detrimental. In fact, the enzymatic degradation of compounds impermeable or pumped out from the BBB enables better pharmacological clearing, which in turn sustains tracer washout from the brain and enables simpler biomathematical analysis for quantitative imaging.

Metabolism occurs at varying degrees and increasingly slowly the higher the species complexity is.[345] Thus, small animal testing is not always predictive of the compound behaviour in humans. Nevertheless, it is common practice to analyse metabolites *ex vivo* in small animals or non-human primates, as well as *in vitro* in human serum. Radiometabolites are detected and analysed with the use of radio-high performance liquid chromatography (radio-HPLC), instant thin-layer chromatography (iTLC) and solid-phase extraction (SPE).[346] These techniques are able to quantitatively separate different chemical species and identify them by comparison with non-radioactive analogues or with the use of mass spectrometry.

To assist in a metabolism-safe design of PET probes, some rules of thumb originated from experimental trial-and-error exist. Generally speaking, if the metabolic fate of a scaffold is

known, it is preferable for the radioisotope to sit on the hydrophilic fragment. For ^{11}C tracers, the most common metabolites are originated from demethylation to give [^{11}C]formaldehyde, [^{11}C]formate or [^{11}C]CO_2.[345] Moreover, in ^{11}C tracers hydroxylation,[347] carboxylation,[348] amide hydrolysis[348] and debenzylation[349] can be problematic. For ^{18}F tracers, defluorination[350] is particularly undesirable for CNS probes as it leads to bone and skull [^{18}F]F^- uptake, with consequent signal leach-over into the brain cortex. Defluorination can also occur spontaneously by intramolecular elimination processes, thus moieties susceptible to defluorination such as [^{18}F]fluoromethoxy are best avoided.[351] Moreover, aliphatic fluorine chains such as [^{18}F]2-fluoroethyl are sometimes subject to dealkylation.[352]

The simplest strategy to circumvent unwanted metabolism is to change the label position, possibly without modifying the compound's structure. Moreover, deuteration (especially on aliphatic carbons) can facilitate metabolic retardation;[353, 354] otherwise, if the metabolising enzyme is known, selective blockade can be used to reduce metabolite formation.[355, 356]

Blood-brain barrier permeability

The blood-brain barrier (BBB) is a selectively permeable dynamic interface composed of endothelial cells connected by tight junctions and isolating the brain from the circulation. Radiotracers may penetrate the BBB via either passive diffusion or carrier-mediated transport, depending on their chemical nature. Lipophilic substances have preferential access through the BBB. However, they give rise to the non-specific binding issues described earlier in this section. Aside from the challenges posed by the entry into the brain, it is the retention within the brain which is most crucial to ensure a sufficiently high signal-to-noise ratio for CNS PET imaging. Upon BBB influx, some CNS compounds get metabolised and trapped within the brain, such as [^{18}F]FDG, which undergoes phosphorylation. Instead, other compounds remain unchanged. In either instance, compounds may washout from the brain at various rates, and again either via passive diffusion or via carrier-mediated transport. Therefore, most often, BBB penetration is a balance between the capacity to passive entry and efflux transporter susceptibility, notably to the P-glycoprotein (P-gp) pump, ABC transporters, the multi-drug resistance transporter and organic anion transporters.[357]

For what concerns radiotracer design, BBB influx can be facilitated by the glycosylation of radiotracers with hexose rings (substrates of glucose influx pumps),[358] or by derivatisation with carboxylates (substrates of the monocarboxylate transport system).[359] Additionally, organic anion and cation transporter systems are known to facilitate influx, among many, of cardiac glycosides and monoamine neurotransmitters.[358] Among the efflux pumps, the P-gp is known to interact and transport lipophilic and cationic drugs to the outside of the brain. Hence, aside from the high NSB, excessively high LogP can have the further consequence of limiting the BBB retention. Additionally, strongly aromatic compounds are frequently P-gp substrates.[360] For all BBB transporters, influx and efflux rates vary both according to the brain region,[361] the organism's health state[345] as well as to the species under consideration.[362]

In order to explore BBB-penetration independent of efflux, in animals it is legally accepted in some cases to employ P-gp blockers, such as cyclosporin A or rifampicin.[363] Moreover, experimental models[364-372] and computational predictions[373] of BBB permeability are available which can predict to a certain extent whether a candidate tracer has suitable properties for brain penetration. Finally, transporter-specific *in vitro* assays can inform about the potential binding of a putative radiotracer for individual efflux pumps.[374, 375]

Synthetic and radiosynthetic accessibility

Another important set of considerations during the design phase are the choice of radioisotope, the radiolabelling strategy and the ease of synthesis of the chemical precursors. Radioisotopes differ both in their decay modality, decay energy and their half-life. ^{18}F is a particularly useful isotope since its decay is 97% β^+; its half-life is long relative to ^{11}C, which offers the opportunity of producing the radioisotope off-site, of carrying out multiple imaging scans with one injection, of selecting a later time point to achieve an optimal imaging signal. Finally, ^{18}F's positron energy is lower than that of ^{11}C, which results in a nearly halved positron range in water, which positively affects the image resolution.

Nevertheless, the choice of radioisotope is also dictated by its atomic number: a large majority of pharmaceutically active species contain a carbon and a nitrogen atom; hence ^{11}C and ^{13}N offer the opportunity of radiolabelling most species without any structural modification. Despite this, the choice of radioisotope is also governed by the ease of synthesis or commercial

availability of the precursor needed to perform the radiolabelling and by the structure of the target tracer. The ideal radiolabelling strategy involves less than 2 steps and less than 3 isotope half-lives. Moreover, it needs to be reproducible, ideally automated and capable of producing a radiotracer in high radiochemical yield, radiochemical purity, specific activity and concentration. Some issues frequently encountered in the radiosynthesis stage are the isolation of the radiotracer from the precursor species,[376] isotopic exchange (especially between ^{18}F and ^{19}F)[377] and unwanted addition of carrier tracer (such as $[^{12}C]CO_2$ in syntheses involving $[^{11}C]CO_2$).[378]

Pros and cons on the use of ^{18}F labelling

In this work, the isotope of choice is ^{18}F. Fluorine is present in about 20% of all pharmaceuticals and 30% of all agrochemical compounds as of 2007.[379] Fluorine has not always been seen as a convenient atom in pharmaceutically active compounds, but the huge commercial success of fludrocordisone, an analogue of hydroxycortisone, of 5-fluoroacil, an alternative to natural uracil, as well as that of [^{18}F]FDG, an analogue of glucose, has led this atom to become widely used to explore structural affinity to biological targets.[380] As the most electronegative atom of the periodic table, it is undoubted that fluorine cannot simply be considered an orthologous replacement for hydrogen atoms as it introduces electrostatic and steric variations at the desired site of binding that cannot be overlooked.[381] Most commonly, fluorine is employed in drug analogue designs to constructively improve the molecules' disposition, in terms of its adsorption, distribution, metabolism and excretion (ADME) profile.[382] For instance, the introduction of trifluoromethyl groups can increase the lipophilicity, whereas fluorine-hydrogen substitutions in aromatic rings can both affect the lipophilicity as well as reduce the rate of oxidation by limiting the substrate's interaction with oxidative enzymes.[383] In other cases, metabolic processing can result in the loss of radioactive fluoride or ^{18}F-containing fragments, with consequent positive and negative effects on the clarity of the target-specific signal, as [^{18}F]fluoride is taken up by bones,[384] lipophilic fragments can reach new targets, remain in tissues or get further metabolised, whereas hydrophilic fragments usually get readily cleared from the circulation.[382]

On the target affinity side of the equation, the introduction of fluorine can sometimes be beneficial to better exploit electrostatic interactions and affect selectivity at binding sites. Fluorine can lead to improved H-bonding and introduce new molecular interactions as a

consequence of its effect on the pKa of protonated amines, carboxylic and hydroxyl groups.[385] There are multiple examples in which fluorine has positively impacted the properties of biologically active compounds, such as the metabolic profile in man of [^{18}F]fluoroacetate[386] and [^{18}F]fluoroflumazenil,[387] whereas there are many examples in which it has brought detrimental changes, such as in the dopamine D_2/D_3 receptor antagonist [^{18}F]F-PHNO, where the introduction of a fluorine atom prevented all the specific binding to the targets.[388]

To conclude, the use of fluoride labelling in otherwise fluorine-free compounds cannot be treated as a ubiquitously advantageous choice, yet it should not be discarded a priori as it can bring along positive modifications to bioactive molecules.

1.7.3 Lead radiotracer scaffold selection

Among the many antagonists described in section 1.3.5 (chapter 1), our attention was captured by the cyanoguanidine P2X7 antagonist series, many compounds of which display exceptionally strong pharmacological activity and selectivity for P2X7. First discovered in 2006 in the Abbott Laboratories, they were championed by A-740003[196] and compound **1** (Figure 18).[389] A-740003 showed affinity for the human P2X7 (hP2X7) with an IC_{50} of 40 nM for calcium influx, 156 nM for IL-1β release and of 92 nM for pore formation as observed by Yo-Pro uptake. However, they subsequently found that different substitutions at both sides of the cyanoguanidine could further increase its potency. On the left hand side (LHS) (Figure 18), the addition of a 2-methyl substituent in the quinolinyl group conferred higher microsomal stability in whole blood. Nevertheless, aside from this, the LHS moieties tested did not beat the potency observed with 5-quinolinyl, and included 2-tolyl, indole, benzofurane and pyridine.[389, 390] Further, on the right hand side (RHS) the SAR was explored by insertion of a piperazine with a range of substituents in the region linking the guanidine and the aromatic ring. The variety of piperazine substituents included o-, m- and p-methyl, methoxy and chlorophenyl rings, linked by either alkyl chains, an amide or carbonyl groups, the latter two resulting in the most potent compounds of the series (up to 30 nM in hP2X7).[391, 392] Instead, when a shorter linker was introduced, such as that in A-804598, the IC_{50} rose to 11 nM in hP2X7, 10 nM in rat (rP2X7) and 9 nM in mouse (mP2X7).[229, 393]

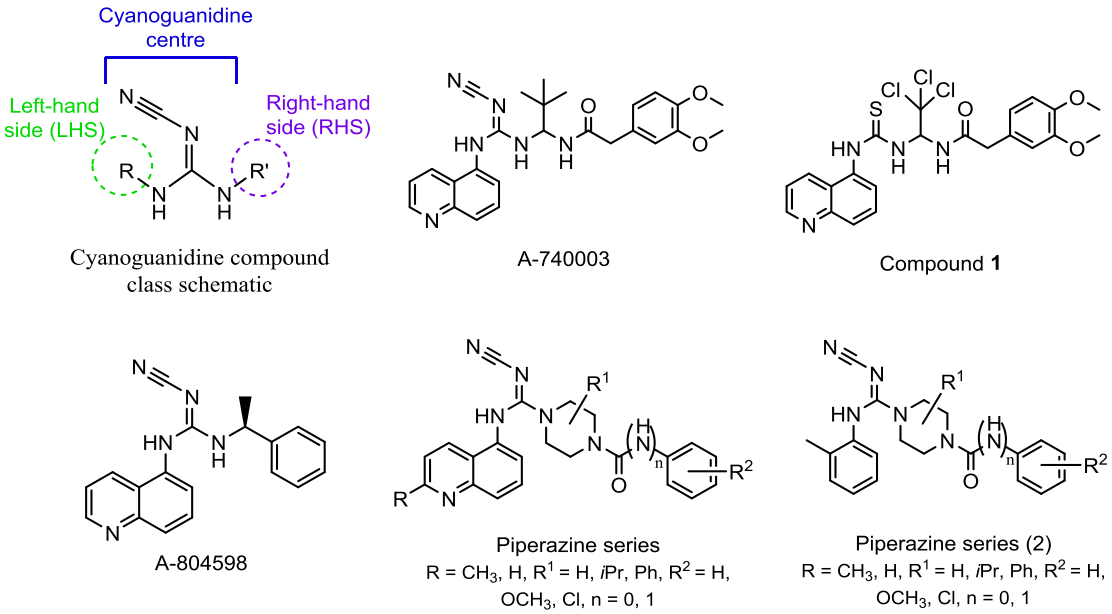

Figure 18 P2X7 cyanoguanidine antagonist series.

Some further insights into the binding modality of P2X7 antagonists with the receptor's ATP-binding pocket were given by a recent *in silico* molecular docking study.[394] Molecular docking is a molecular modelling technique that allows the determination of the predominant binding modes of a ligand with a protein of known three-dimensional structure. The binding modes are determined algorithmically *via* iterative three-dimensional ligand-protein approximations and ranked by a scoring function, a value representative of the overall energetic favourability of the ligand-protein interaction.[395] The three-dimensional conformation of the protein can be derived from X-ray crystallographic structures published in the protein data bank repository (RCSB PDB, www.rcsb.org).[396] Despite the absence of a published P2X7 X-ray crystal structure, the group performed P2X7 homology modelling on the zebrafish P2X4 crystal structure, where the relevant amino acid mutations were accounted for by means of computational simulations. Docking of cyanoguanidine compounds showed that the strongest interactions incurred *via* means of polar H-bond acceptance by the cyanoguanidine moieties. Likewise, triazole and tetrazole antagonists were found to interact with their azole moieties in similarly favourable ways (Figure 19). This matching function suggests that cyanoguanidine might similarly provide rigidity to the molecular scaffold. As for the substituent, the quinoline moiety was confirmed as the best fitting, displaying energetically favourable hydrophobic interactions in the innermost part of the cavity. Instead, the RHS of the compounds showed some hydrophobic behaviour, but given the size of the cavity, larger substituents showed better fitting.

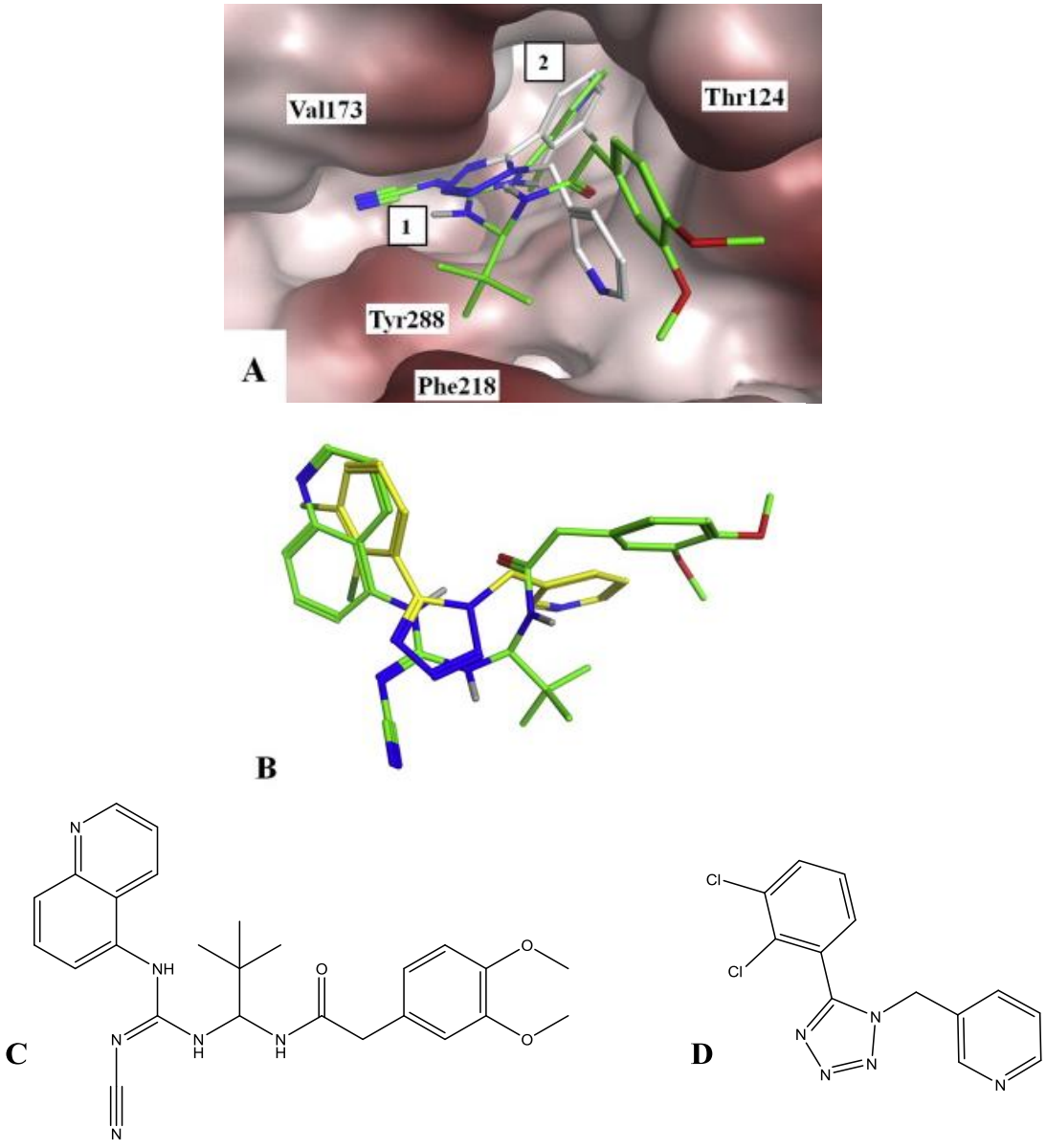

Figure 19 Superimposition of docking conformations of compounds A-740003 and A-438079 at the inactive-state hP2X7 binding site

Antagonist A-740003 displays two methoxy groups at an extreme of the molecule. These appeared to rest externally to the core of the pocket, thus we presume that they bare low impact on the compound's affinity. A-804598, instead, engaged all its cyanoguanidine substituents in hydrophobic interactions at the active site, corroborating the experimentally observed high affinity.[229] Given the stronger potency displayed by A-804598 and its ease of synthesis, we decided to focus our attention on assessing this compound's pharmacokinetic suitability as a radiotracer and amenability for radiolabelling. Most of the data are available from two key studies on this compound by Abbott Laboratories[229] and Pfizer.[67] Selectivity to P2X7 against a wide range of common alternative binding targets has been exhaustively explored. A-804598 is a competitive inhibitor when, under Bz-ATP stimulation, IL-1β uptake was monitored. Also, the

uptake of DNA-binding fluorescent die Yo-Pro (indicative of P2X7 pore activity) was potently blocked in the presence of the candidate antagonist.[229]

Furthermore, A-804598's binding is rapid, stable for up to 3 hours and reversible. The K_d obtained from the ratios of K_{off}/K_{on} (3.38 nM)[67] and from saturation studies is also in the low nM range (3.08 nM,[67] 2.4 nM[229]). The B_{MAX} is of 0.112 pmol/mg in rat brain cortex homogenate[67] and of 0.560 pmol/mg in P2X7-transfected 1321N1 human astrocytoma cells.[229] These values give a B_{MAX} / K_d of ca. 36, which is in the ideal range for PET imaging of B_{MAX} / K_d ≥10.[334] Further, *in vitro* autoradiography studies using [^{3}H]A-804598 showed widespread binding in the wild type Sprague-Dawley rat's CNS. *In vitro* rat cortex homogenate occupancy assays determined a 60% specific binding of the tracer at equilibrium.[67] Collectively, these data are highly desirable for achieving an optimal signal-to-noise ratio upon translation of the ligand for PET imaging.

On the down side, A-804598 does not possess any halogen in its structure. Hence, direct radiofluorination cannot be achieved without structural modifications. Moreover, A-804598's LogP of 3.4-4.8 (Table 3, section 1.9.1) violates Lipinski's modified rule-of-5. This presented us with an opportunity to impart structural modifications that would lower the LogP while providing a site for radionuclide attachment. Understandably, these modifications change the functional binding of the compound which therefore requires re-evaluation in a biological setting (discussed in chapters 5-7).

Nonetheless, as previously discussed, relative tolerance to the nature of the aromatic groups on the LHS and RHS of the cyanoguanidine centre (Figure 18) is apparent from the literature.[397] Thus, we sought to explore structural modifications in the periphery of the molecule *via in silico* molecular docking estimations akin to those employed in Dal Ben *et al.*[394]

1.7.4 Aims

The work outlined in this section aimed at investigating which structural modifications to the lead scaffold A-804598 were most likely to yield a useful PET tracer targeting P2X7.

Firstly, our design strategy involved the analysis of which structural modifications could impart a decrease in LogP coupled with the introduction of a fluorine atom in a position amenable for radiofluorination, whilst keeping in mind the modality of receptor binding of the parent structure. The structures were filtered down to those viable for synthesis and, among those, the compounds for which synthetic precursors were commercially available. Next, *in silico* molecular docking of the remaining scaffolds was performed so as to provide a visual and semi-quantitative estimate of binding.

1.8 Methods

1.8.1 Physicochemical parameter calculations

LogP

The LogP was estimated computationally from the ChemDraw software's Crippen fragmentation-based lipophilicity estimation method.[398] the Viswanadhan's fragmentation method[399] and the MolInspiration miLogP estimation method.[400] Fragmentation methods essentially segment molecules into groups of atoms, each of which is given an individual LogP value based on their steric and electronic contribution to the total molecular LogP. Moreover, the final LogP estimation includes whole-molecule steric and electronic corrections. Furthermore, the miLogP adjusts the LogP estimates to experimentally calculated LogPs for over 12,000 drug-like compounds.

Topological Polar Surface Area

The Topological Polar Surface Area (TPSA) was calculated with the Molinspiration TPSA estimation method. This is based on the summation of surface contributions from all polar fragments, calculated by least squares fitting to a single conformer 3D PSA for over 34,000 drugs from the World Drug Index. TPSAs differ from classical 3D PSAs by the amount of conformers taken into account. Despite some loss in accuracy, the calculations are up to three orders of magnitude faster.[401]

1.8.2 Molecular docking

The experiments were kindly performed by Dr Diego Dal Ben at the University of Camerino, Italy.

Homology modelling

All molecular modelling studies were performed as described in Dal Ben *et al.*[394] on a Core i7 CPU (PIV 2.20 GHZ) PC workstation. Homology modelling and docking studies were carried out using Molecular Operating Environment (MOE by C.C.G., Montreal, CA, version 2012.10) suite. All ligand structures were optimized by semi-empirical RHF/AM1 calculations using the MOPAC[402] package implemented in MOE.

The homology model of the human P2X7 (hP2X7) receptor was built using the inactive and ATP-bound X-ray structures of the zP2X4 receptor as templates (PDB code 4DW0, 2.9 Å resolution and 4DW1, 2.8 Å, respectively). First, alignment of the zP2X4 and hP2X7 receptor primary sequences was performed within MOE. The original zP2X4 receptor boundaries were applied for the corresponding hP2X7 sequence. The missing domains were built by the loop search method implemented in MOE. Once the heavy atoms were modelled, all hydrogen atoms were added and the protein coordinates were then minimized with MOE using the AMBER99 force field[403] until the root mean square (RMS) gradient of the potential energy was less than 0.05 kJ mol^{-1} $Å^{-1}$. Reliability and quality of these models were checked using the Protein Geometry Monitor application within MOE, which provides a variety of stereochemical measurements for inspection of the structural quality in a given protein (backbone bond lengths, angles and dihedrals, Ramachandran φ-ψ dihedral plots, sidechain rotamers and non-bonded contact quality).

Molecular docking

The ligand structures were docked individually into the binding site of the P2X receptor using the AutoDock tool (PyrX interface) by the Scripps Institute.[404, 405]

This method is divided into four stages. 1) A set of unique coordinates for both the receptor and the ligands was generated, maintaining all information about flexible side chains, charges, atoms types and torsional degrees of freedom. 2) The software Autogrid generated a three-

dimensional lattice of regularly spaced points (grid map) described in Cartesian space. Each point represents a “probe” atom to which specific values of energy of interaction with the protein are assigned. AutoGrid affinity grids are calculated for each type of atom in the ligand, typically carbon, oxygen, nitrogen and hydrogen, as well as grids of electrostatic and desolvation potentials. 3) Conformational analysis of the ligands was performed with an Autodock algorithm taking into account various bond rotations and angles and overlaying the structures on the Autogrid-generated grid maps. The free energy was calculated with the AMBER force field. 4) Analysis of conformationally similar complexes and the interaction between ligands and proteins was employed together with the free energy scores to select the final docked complexes. The Binding_Energy parameter was used as an estimate of the variation in free energy (ΔG) arising from the docking.

Post-docking analysis

The docking poses of each ligand-receptor complex were then further subjected to AMBER99 force field energy minimization in MOE until the RMS gradient of the potential energy was less than 0.05 kJ mol^{-1} $Å^{-1}$. Receptor residues within 6 Å distance from the ligand were allowed to move, while the remaining receptor coordinates were kept fixed. AMBER99 receptor partial charges and MOPAC output ligand partial charges were utilized. Upon completion of the compound-binding site energy minimization, receptor coordinates were fixed and a second energy minimization with MMFF94 force field[406, 407] was performed allowing only the ligand atoms to move. For each ligand, the minimized docking poses were then rescored using the dock-pK_i predictor. The latter tool estimates the pK_i for each ligand using the “scoring.svl” script retrievable at the SVL exchange service (Chemical Computing Group, Inc. SVL exchange: http://svl.chemcomp.com). The algorithm is based on an empirical scoring function consisting of a directional hydrogen-bonding term, a directional hydrophobic interaction term, and an entropic term (where rotatable bonds in the ligand are immobilized). The obtained pK_i values must be considered as docking scores and not as prediction of binding affinity. For each compound, the top-score docking poses according to at least two out of three scoring functions were selected for final ligand-target interaction analysis. The use of two different softwares based on different

algorithms and scoring parameters was deliberate and aimed at increasing the degrees of confidence in the output values.

1.9 Results

1.9.1 Physicochemical compound library evaluation

Following initial selection of a range of permutations of A-804598 incorporating ^{18}F, 14 structures were identified as having commercially viable building blocks and reasonably moderate structural modifications from the parent structure A-804598. A set of physicochemical parameters of these structures were computationally derived to assess their degree of compliance with Lipinski's rule-of-5 and the CNS-modified version for heightened BBB permeability (Table 3). The analysis revealed that both the parent molecule A-804598 and its desmethylated version (**1**) have an excessive LogP value. The cyclotriazole series **2-4** and the fluorinated analogues **5-7** of compound **1** demonstrated good adherence to Lipinski's rule-of-5 (LRO5). The amide analogues **8** and **9** showed improved LogP with respect to compound **1**, yet not sufficiently so to comply with the modified LRO5. Understandably, compound **10** had high LogP due to the addition of an aromatic ring. Finally, the pyridinyl compounds **11** and **12** showed an overall acceptable compliance with the modified LRO5, especially upon resizing of the LHS aromatic ring, as in **12**.

Table 3 Physicochemical assessment of a selected group of structures

	A-804598	1: EF1	2: EFA	3: AFA	4: OFA	5: p -EFB	6: m-EFB	7: o-EFB	8: p-EFC	9: EFC2	10: EFD	11: EFE	12: AFE
Crippen LogP*	4.37	4.45	2.61	2.53	2.14	2.21	2.21	2.21	3.65	3.49	5.92	3.13	3.05
± SD	0.47	0.47	0.47	0.47	0.47	0.47	0.47	0.47	0.47	0.47	0.47	0.47	0.47
Viswanadhan LogP*	4.79	4.38	2.59	2.5	2.22	2.52	2.52	2.52	3.96	3.82	6.36	3.59	3.5
± SD	0.49	0.49	0.49	0.49	0.49	0.49	0.49	0.49	0.49	0.49	0.49	0.49	0.49
miLogP*	3.48	2.92	1.37	1.11	0.61	3.08	3.06	3.04	2.72	2.65	4.86	2.44	2.18
Average LogP (target 1.5-3)	4.21	3.92	2.19	2.05	1.66	2.60	2.60	2.59	3.44	3.32	5.71	3.05	2.91
MW (max 500)	315.38	301.35	338.35	287.3	303.3	319.34	319.34	319.34	333.33	315.34	395.44	306.3	255.26
PSA* ($Å^2$)	73.1	73.1	103.82	90.93	111.16	73.1	73.1	73.1	90.17	90.17	73.1	85.99	73.1
Acceptors (max 10)	5	5	8	7	8	5	5	5	6	6	5	6	5
Donors (max 5)	**2**	2	2	2	3	2	2	2	2	2	2	2	2
Violations to LRO5	**0**	0	0	0	0	0	0	0	0	0	0	0	0
Violations to MLRO5	**1**	1	0	0	0	0	0	0	1	1	1	1	0

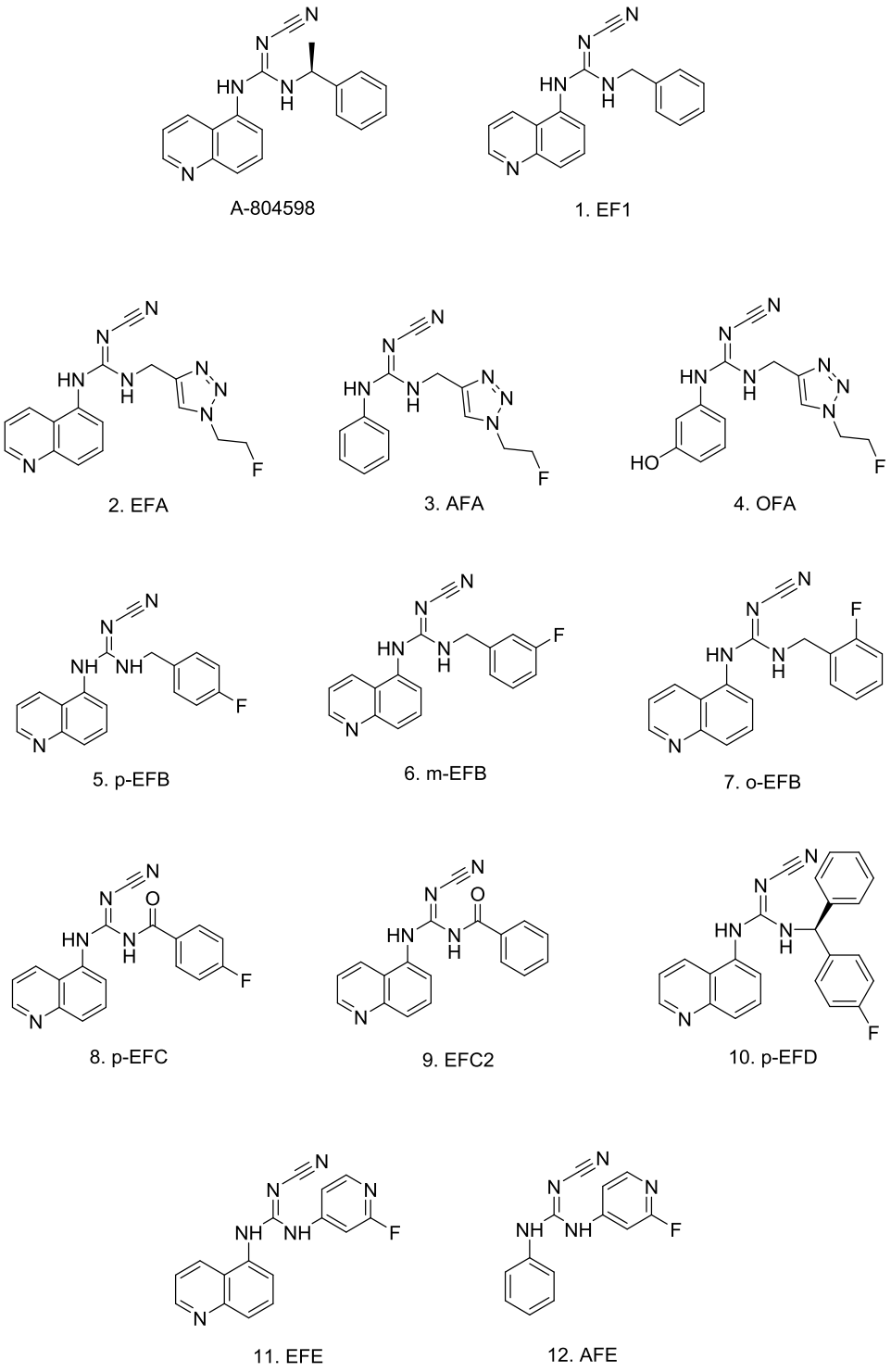

Figure 20 Library of A-804598 analogues examined in this work.

1.9.2 Molecular docking SAR evaluation

The compounds shown in Figure 20 were docked to the hP2X7 receptor by homology modelling to the zP2X4 receptor (Figure 21) in a similar fashion to the work published by Dal Ben *et al.*[394]

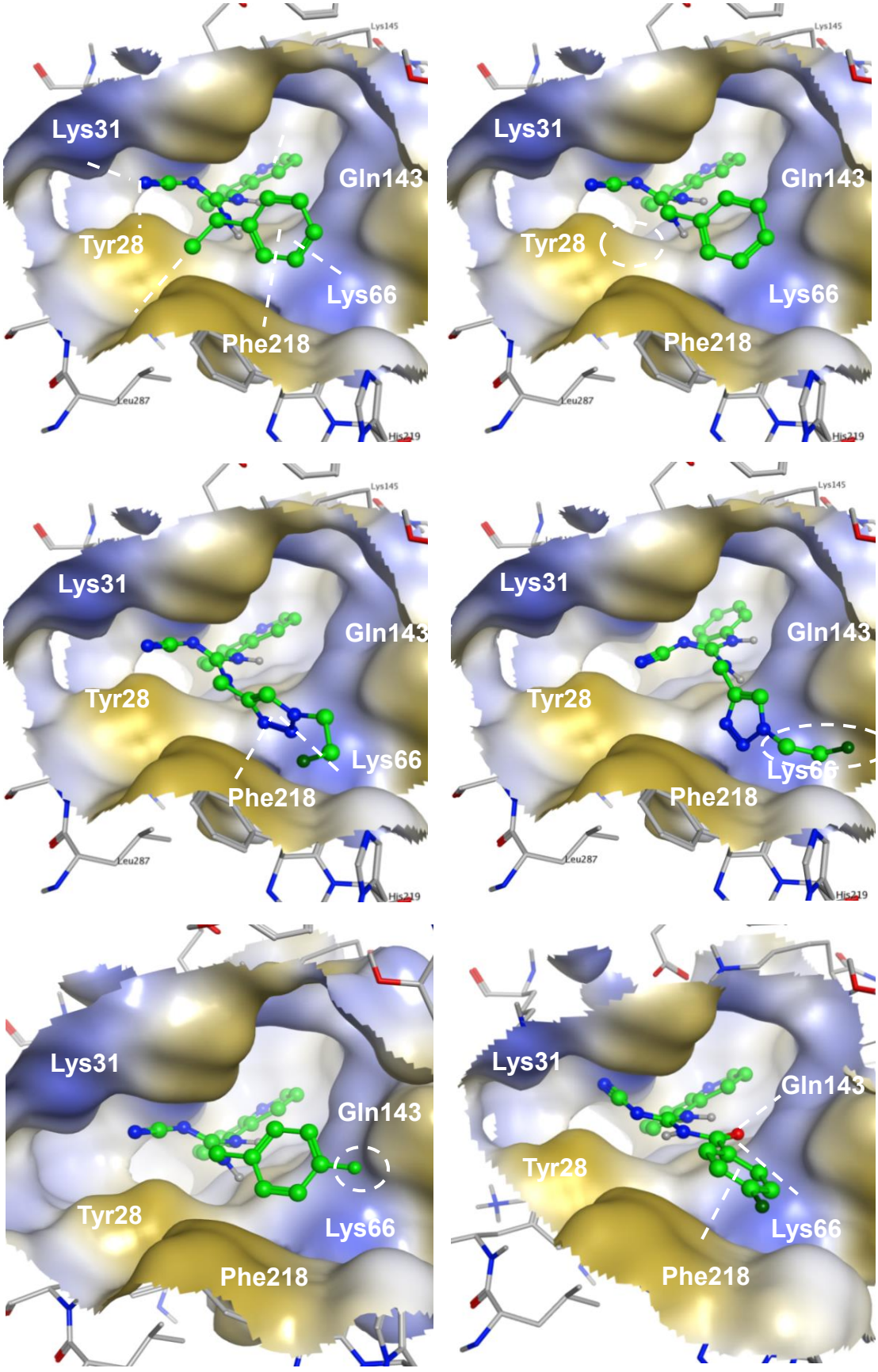

Figure 21 Molecular docking into the hP2X7 receptor ATP-binding pocket of a representative sample of candidate structures

Next, gains in free energy and estimates of affinity were calculated for each compound structure (Table 4).

Table 4 Binding energy and pK_i estimations

Compound	Binding_Energy (kcal/mol)	dock_pK_i
A-804598	-6.31	5.14
1. EF1	-5.92	4.87
2. EFA	-7.01	5.16
3. AFA	-6.02	4.50
4. OFA	-5.65	4.26
5. p-EFB	-5.72	4.90
6. m-EFB	-6.02	4.11
7. o-EFB	-5.57	3.23
8. p-EFC	-6.01	5.54
9. EFC2	-6.04	5.38
10. p-EFD	-7.52	6.31
11. EFE	-5.85	4.49
12. AFE	-5.50	3.47

Taken together, the visual and quantitative estimations of ligand-receptor binding showed the following trends.

1. Removal of the benzyl methyl group did not prevent good ligand-receptor fitting. The methyl group appeared to sit into an area not particularly hydrophobic either, suggesting that if anything it might serve as a structural constraint for the phenyl group to sit in the hydrophobic region between Phe218 and Lys66. However, upon removal of the methyl group an overall estimated ΔG reduction of 0.39 kcal/mol and an estimated pK_i reduction of 0.27 were observed.
2. The triazole ring in compounds **2-4** appeared to sit comfortably in the binding pocket and somewhat interacted with Lys66. Instead, the fluoroethyl chain seemed not to interact with the receptor, preferring rather to sit flexibly in the outer part of the pocket. In the case of compound **2**, the rest of the molecule retained the same 3D conformation and fit to the

pocket, while the molecule overall displayed a greater degree of flexibility. In this instance the binding energy difference was increased by 0.70 kcal/mol compared to the parent structure, while the pK_i remained unvaried. In the case of compounds **3** and **4**, the hydrophobic region at the core of the pocket became less exploited. In both cases, the binding energy and pK_i scores reflected a progressive decrease in affinity for the binding pocket as the LHS aromatic ring is reduced in size and is decorated with a polar group.

3. The fluorine atom on the aromatic ring of compounds **5-7** appeared to fit in the opening of the binding pocket. None of the compounds in this series showed much variation in binding compared to compound **1**. However, the pK_i estimates showed a dramatic drop in affinity for the *ortho* and *meta* positions. Conversely, the *para* position retained its affinity. The binding energy differences instead followed a different trend, showing better fit for the *meta*-fluorinated ring, followed by the *para*- and lastly by the *ortho*-fluorinated compound **1**.
4. The addition of hydrophilic or hydrophobic functionalities at the benzylic position in compounds **8-10** did not alter the 3D conformations within the core of the binding pocket. However, the presence of a polar moiety deformed the conformation in the outer part of the pocket so as to orient the newly introduced carbonyl oxygen towards residues Gln143 and Lys66, thereby stiffening the overall conformation both *via* polar as well as multiple H-bonding interactions. Moreover, the RHS phenyl ring became twisted by 90°, possibly to exploit some π-π stacking interaction with Phe218. The addition of a fluorine atom in compound **8** did not seem to affect the binding, both in terms of ΔG and of pK_i. Conversely, the introduction of a phenyl functionality at the benzylic position (compound **10**) induced a major boost in binding according to both measures, suggesting the filling of a previously untouched hydrophobic pocket.
5. The removal of the methyl spacer between the guanidine and the RHS phenyl ring resulted in an increasingly constrained molecular conformation. For compound **11**, this was only partially detrimental to binding, as observable from the similar binding energy and pK_i estimate to compound **6**, whereas a net loss was observed in comparison to the more flexible compound **2** scaffold. Moreover, the lack of methyl spacer combined with the modification of the LHS aromatic into a phenyl ring severely impacted the affinities, scoring

worse than the related compound **3** and nearly all quinoline guanidine compounds (**1, 2, 5, 6, 8-11**). This is indicative of a deterioration of the ligand fitting within the binding pocket.

1.10 Discussion

The findings outlined in this chapter give an estimate of the physicochemical properties and binding modality of a set of A-804598 analogues to the P2X7 receptor's ATP-binding pocket. The molecular structures were designed according to four parameters:

- Maintenance of the cyanoguanidine moiety and the presence of aromatic substituents on its left and right hand side, key features to the selective binding to P2X7.
- Likelihood to possess LogP and BBB-penetration potential in accordance to Lipinski's modified rule-of-5.
- Amenability for radiofluorination and metabolic stability of the label.
- Synthetic accessibility (ideally < 3 synthetic steps) and synthetic precursor commercial availability.

According to these criteria, a number of potentially interesting scaffolds such as methyl- and 2-ethyl-fluoropyridine guanidines had to be discarded. Initially, it was evaluated whether the removal of the chiral benzylic methyl group would enable a greater synthetic accessibility. This modification did not appear to affect the binding at a visual level, but it did lower considerably the estimated free energy gain and pK_i. Conversely, the LogP was improved, while the other physicochemical parameters under consideration were not affected. Next, the desmethylation was assessed in conjunction with a change in aromatic functionality on the RHS of the scaffold to include a triazole moiety, very widely employed in radiochemistry to conveniently fluorinate substances *via* click chemistry with minimal impact on the overall binding and high radiosynthetic yields.[408, 409] Interestingly, the triazole ring was found to improve the estimated free energy gain of the parent compound as well as maintaining its estimated pK_i. In turn, the lipophilicity was lowered to the target range for BBB permeability. Conversely, the PSA was beyond the target range. Modification of the quinoline moiety to a simpler aromatic system (compound **3**) rendered this molecule fully optimal in terms of physicochemical parameters, but in spite of a loss in affinity with respect to both the parent compound and the quinoline triazole

analogue **2**. Similarly, inclusion of a polar hydroxyl group in the LHS aromatic system (compound **3**) further reduced the target affinity whilst restoring some violations to the rule-of-5, particularly because of excessive hydrophilicity. However, both compound **2** and compound **3** were included in the final library of compounds as a spectrum of hydrophilic, mildly lipophilic and lipophilic triazole-containing structures were deemed useful to test for cellular and BBB permeability in an experimental setting.

Next, a set of RHS aryl-fluorinated A-804598 structures was assessed. This modification did not particularly impact binding for the *para*-fluorinated structure, while losses in binding energy gains only or coupled with decreased estimated pK_i were found for the *meta*- and *ortho*-fluorinated scaffolds, respectively. All three compounds showed good adherence to the rules-of-5. Given this and the lower synthetic accessibility of the *meta*- compared to the *para*-fluorinated structure, only the latter was included in the final compound library.

Additionally, two fluorinated compounds presenting benzyl substituents were considered, one of which polar and small (compound **8**) while the other one non-polar and bulky (compound **10**). Both compounds showed no issues from a conformational point of view and they both demonstrated improved binding both in comparison to the desmethylated parent molecule as well as compared to the parent molecule. Despite the interesting binding insight arising from these structures, both structures had to be excluded from the final compound library because of their excessive lipophilicity and for synthesis-related time-efficiency reasons. Moreover, the strong ligand-receptor binding that they display could actually compromise the reversibility of binding.

Finally, the two fluoropyridinyl compounds **11** and **12** were tested. Both demonstrated reasonable adherence to the rule-of-5, despite a minor Log P violation for compound **11**. However, both compounds showed decreased binding affinities in comparison to their respective triazole derivatives (**2** and **3**), thus they were discarded.

This work stands by the assumption that all compounds only interact with the target's ATP-binding pocket, the only one adequately described to date to enable molecular docking.[394] Despite the latter might not hold true for all cases, as previously suggested by several groups,[227, 228, 235] it facilitates a preliminary structural categorisation of the candidate scaffolds. Future studies will aim at conclusively clarifying the receptor targeting site of the lead molecules.

1.11 Conclusions

In conclusion, a library of cyanoguanidine-containing scaffolds were computationally analysed with respect to their physicochemical properties and SAR to the ATP-binding pocket of P2X7. The former highlighted that alteration of the aromatic structures on the LHS and RHS of the guanidine centre, specifically into heteroaromatics and functionalised aromatics, could positively impact the LogP. Moreover, a more accessible desmethylated version of A-804598, was found by molecular docking to be an acceptable compromise between target affinity, bioavailability and synthetic accessibility, particularly in the presence of the aforementioned structural modifications. However, complete removal of the benzylic carbon position proved detrimental to the conformational flexibility of the molecule. This work resulted in the four candidate structures **2**-**5** (EFA, AFA, OFA and p-EFB, respectively), leaving compounds **6**, **8** and **9** to future investigations.

Chapter 3

Synthesis

Synthesis

1.13 Introduction

This chapter concerns the synthesis of the proposed library of tracers (Figure 22). In particular, the focus is on all non-radioactive compounds, including the radiotracer precursors and cold standards, while the radioactive synthesis is discussed in the following chapter.

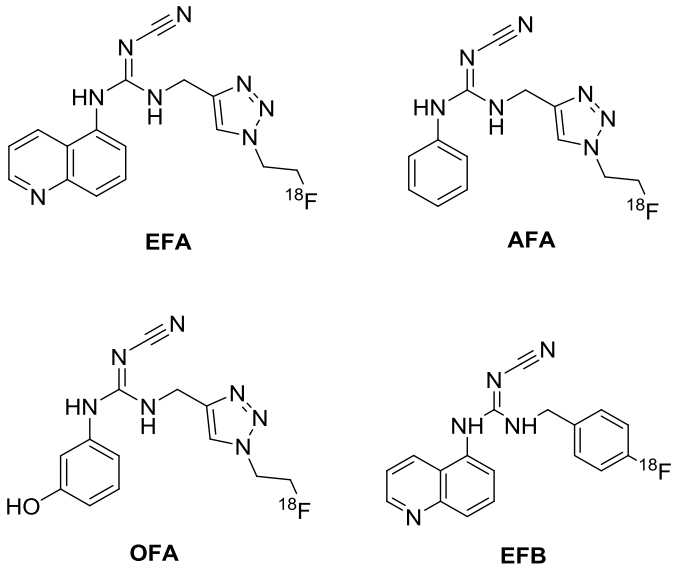

Figure 22 Proposed library of tracers

All intermediate compounds in this synthesis are novel, unless otherwise stated in the experimental section at the end of this chapter. The synthesis of the radiotracer library followed the closely related synthetic procedures adopted by Donnelly-Roberts *et al.*,[229] Glaser and Årstad[410] and Tietz *et al.*[411]

1.13.1 Retrosynthesis and nomenclature

The proposed library of tracers was synthesised *via* the routes represented in Figure 23 *via* a retrosynthetic scheme. The complete IUPAC nomenclature of all compounds can be found in the experimental section of this chapter, whereas abbreviated names were assigned to most structures to facilitate the discussion. The key steps for the formation of the cyclotriazole-functionalised tracers (XFA compounds) are a copper alkyne azide cycloaddition reaction between terminal alkynes (XYL) and a fluoroethyl azide fragment (FEA) and the formation of a trisubstituted guanidine (XYL) *via* a thiourea intermediate (QSMe, ASMe and OSMe). The latter

step is also relevant to the formation of the bisphenyl cyanoguanidine tracer EFB and its boronic ester precursor (QPB). In this chapter, also the synthesis of the XFA indole analogue IMBB from the isothiocyanoindole INCS is described, although this compound has only been indirectly useful for this project.

Other synthetic steps described include the formation of arylthioureas (XSMe) from arylisothiocyanates (XNCS) and the latter from primary arylamines (XNH_2). Instead, fluoroethyl azide (FEA) was synthesised from its tosylate analogue (TsEA), which in turn is derived from 2-fluoroethanol.

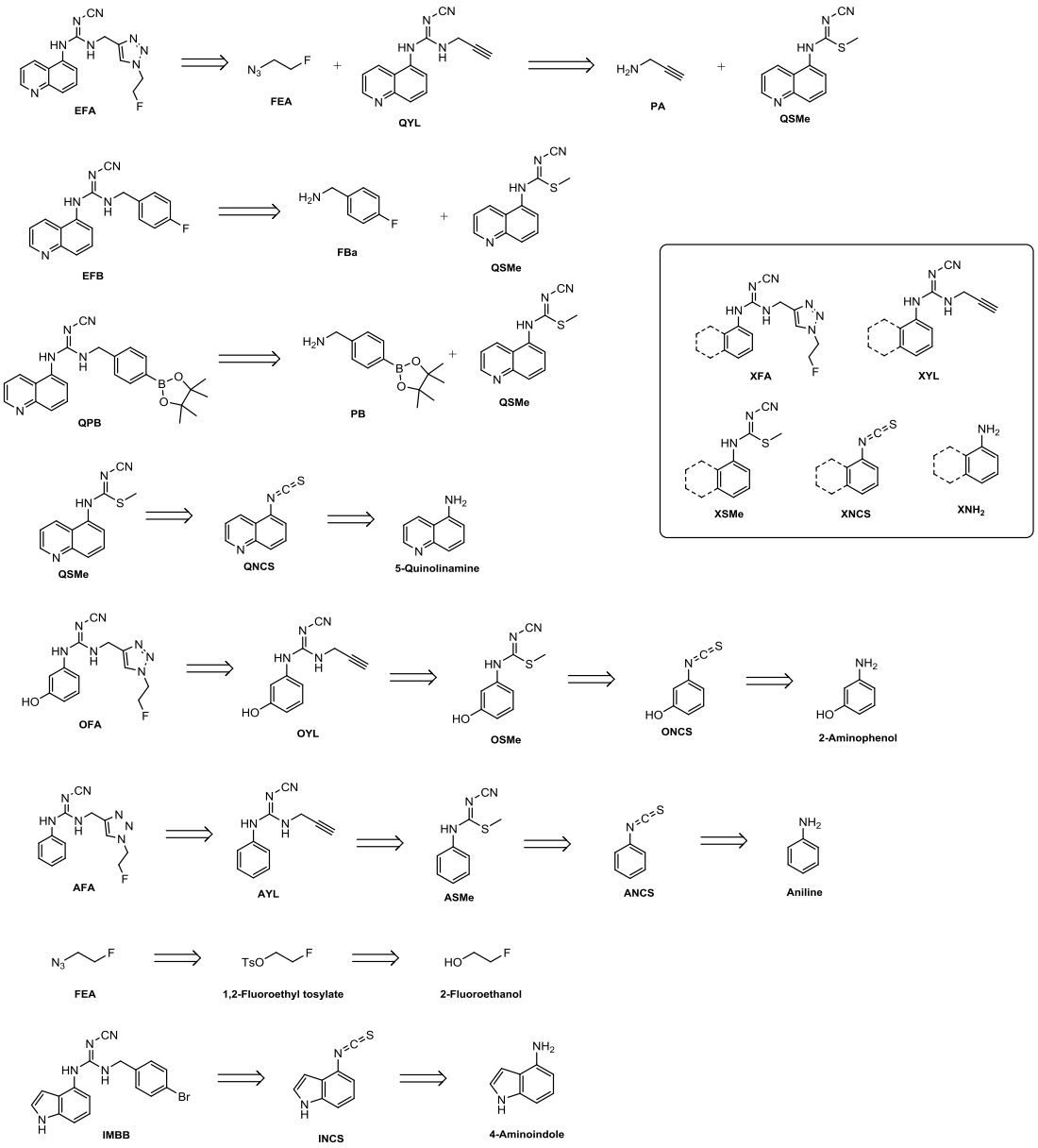

Figure 23 Retrosynthesis and legend of compounds described in this chapter

Trisubstituted guanidine synthesis

The yield-limiting and thus most crucial step of the synthesis of the tracer precursors was the formation of trisubstituted guanidines. The most widely reported procedure involves the acylation of nucleophilic amines with cyanocarbonimidates, where good leaving groups are crucial to the success of the reaction. Most frequently, these are phenol, alkoxy or methanethiol groups.[412-414] The reaction generally proceeds in a variety of solvents and only rarely requires transition metal catalysis. An example is Buschauer's two-step synthesis of an N-alkyl-N'-cyano-N'''-propynylguanidine from diphenyl cyanocarbonimidate for the synthesis of novel histamine H_2-receptor antagonists.[415] In this work, the amine substituents were introduced around the carbon centre one at a time with isolation of the intermediate urea (Figure 24).

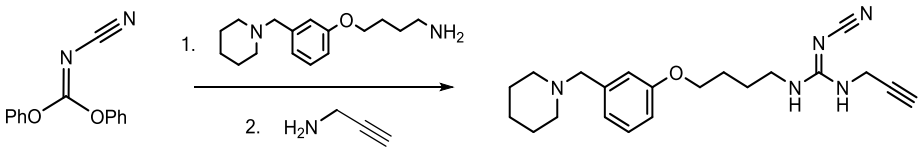

Figure 24 Example of a trisubstituted guanidine synthesis *via* stepwise diphenyl cyanocarbonimidate acylation

Hashimoto *et al.*, alternatively employed thiomethyl leaving groups for the two-step synthesis of H_4-receptor agonist N-alkyl-N'-methyl-N'''-cyanoguanidines with isolation of the intermediate cyanomethylisourea (Figure 25).[416]

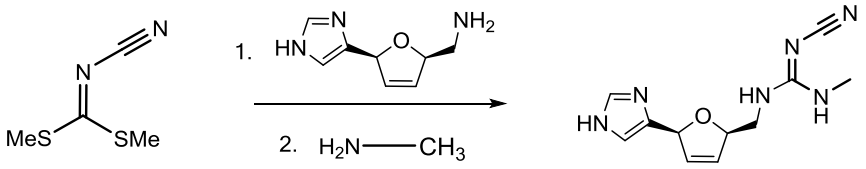

Figure 25 Example of a trisubstituted guanidine synthesis *via* stepwise dimethyl cyanodithioiminocarbonate acylation

Another common strategy is the addition of cyanoamines to ureas or thioureas.[417, 418] This strategy circumvents the need for rare cyanoimidate starting materials (Figure 26), but is not always straightforward, particularly in the presence of propargylamines.

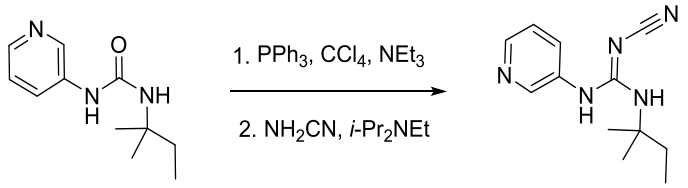

Figure 26 Trisubstituted guanidine synthesis *via* cyanamide addition to a disubstituted urea

Furthermore, many reported guanidine formations by multiple amine additions, particularly from isothiocyanates (Figure 27) or more rarely from dicyanamides (Figure 28).[389, 420, 421] For instance, the synthesis of N-aryl-N'-cyanoguanidines was performed in the presence of sodium dicyanamide and 6 N HCl at room temperature (Figure 28).[421, 422]

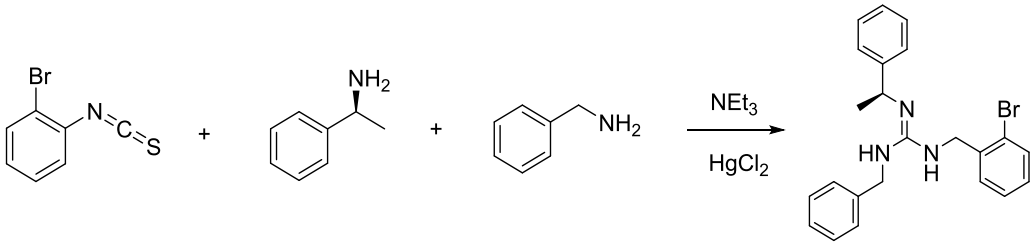

Figure 27 Trisubstituted guanidine synthesis *via* concerted isothiocyanate amination

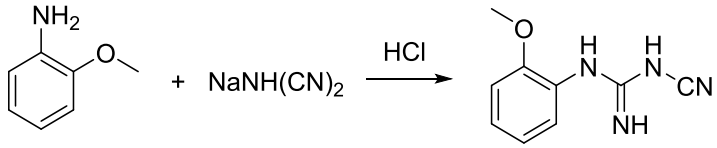

Figure 28 Trisubstituted guanidine synthesis *via* dicyanamide amination

In some cases instead, disubstituted guanidines were exploited as intermediate steps, where the third substitute was added with the aid of benzotriazole leaving groups.[423]

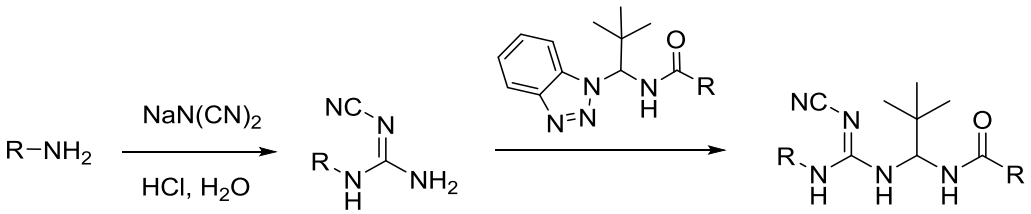

Figure 29 Trisubstituted guanidine synthesis *via* stepwise amine addition to a dicyanamide

Despite the abundance of methods reported in the literature, it is rare to encounter successful additions of propargyl groups and no synthetic strategy to date reports boronic ester-functionalised compounds. Only Donnelly-Roberts and co-workers attempted the preparation of trisubstituted N-cyano-N'-quinolinylguanidines, either *via* mercury-catalysed concerted amine addition to isothiocyanates (Figure 27)[229] or uncatalysed, with the assistance of a benzotriazole leaving group (Figure 29).[389]

1.13.3 Copper catalysed alkyne-azide cycloaddition reactions

Several different reaction mechanisms have been proposed for the copper catalysed alkyne azide cycloaddition click reaction employed in this work for the synthesis of the XFA compound series, suggesting the reaction is much more complex than one would presume.[424]

The first mechanistic insights were given by the inventor of the reaction itself, Barry Sharpless at The Scripps Research Institute (Figure 30). He suggested that following alkyne deprotonation and σ coordination to the in situ sodium ascorbate-reduced metal centre, a cyclic movement of electron density allows the formation of an alkyne-azide bond linked with copper (III) in a six membered metallacycle. This species then undergoes a ring contraction to release the metal centre and resume the catalytic cycle.[425]

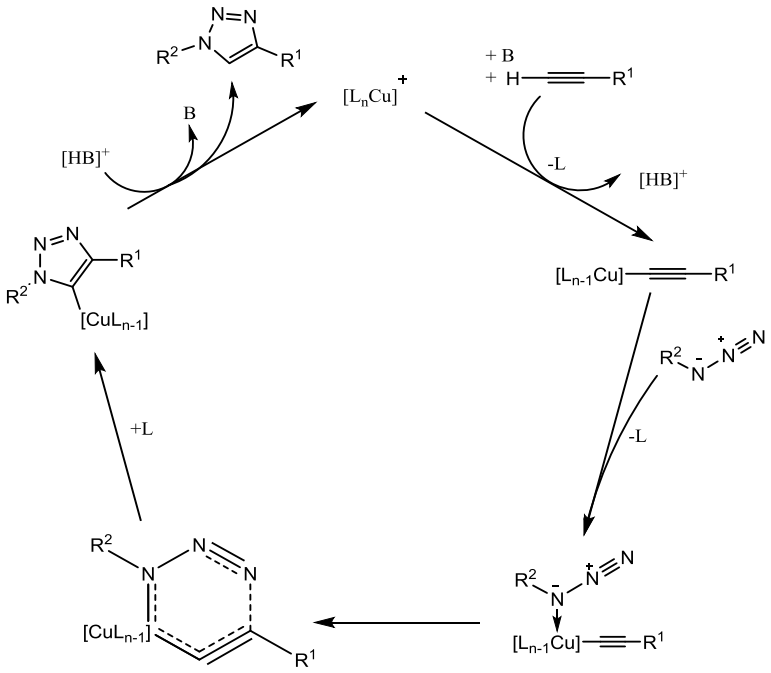

Figure 30 Sharpless mononuclear CuAAC reaction mechanism

This mononuclear mechanism was later refined by Rodionov, Fokin and Finn[426] While testing the effects of BPDS ligand chelation on the reaction mechanism, they identified a second order reactivity with respect to copper, indicative of a dinuclear mechanism. They then showed the same reaction order in ligand-free copper alkyne-azide cycloaddition (CuAAC) chemistry. However, at high copper concentrations the rate order decreased to about 1.3, which suggested a decreased ability of the ligands to bind to the metal centre in the rate-determining step for the reaction (the formation of the C-N triazole bond). Upon finding that commercial copper

acetylides were catalytically inactive, the group demonstrated that double alkyne coordination inactivates the catalyst, whereas single coordination is beneficial (Figure 31). This could be achieved in particular in the presence of highly labile ligands (such as BPDS), which allow easy access to new coordination sites.

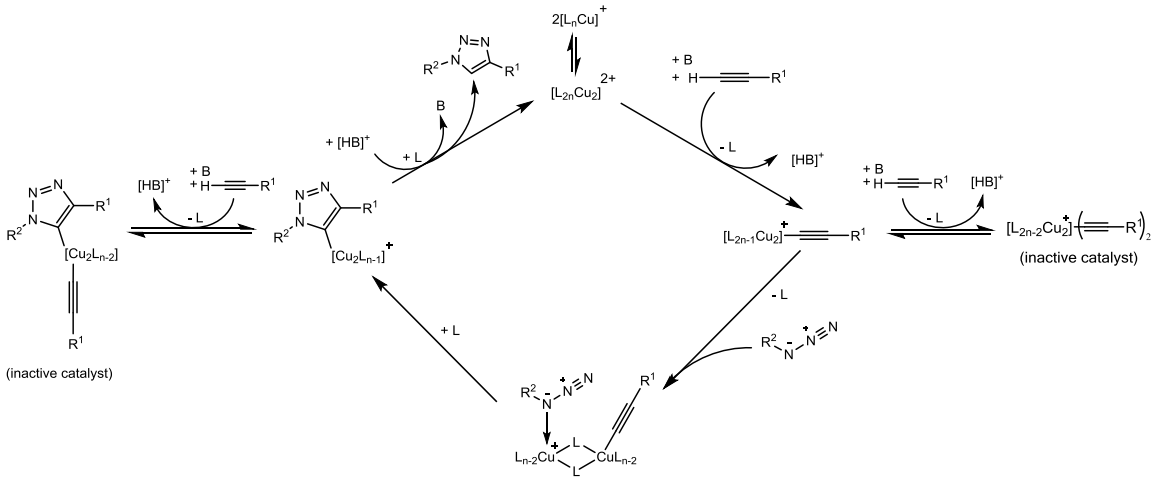

Figure 31 Fokin and Finn dimetallic CuAAC reaction mechanism

Despite the remarkable advances in this field, it is still unclear how the rate determining step can be overcome in the dinuclear catalytic mechanism. Without doubt a range of conditions affect the catalysis, including reagent concentrations, pH, buffering and the presence of ligands.[427] It is also apparent that a number of catalytic mechanisms take place synchronously or sequentially in this reaction, giving little insight into the best parameters to fit each specific CuAAC reaction.

Very recently however, yet another plausible mechanism was suggested by the Bertrand group at the University of California at San Diego upon reporting the isolation of biscopper intermediates from the CuAAC reaction and as well as abundant kinetic experimental data.[428] This study concluded that both mono and biscopper intermediates are involved in the reaction, but that the kinetic profiles of the catalytic reaction of phenyl acetylene with benzyl azide demonstrate the superior catalytic activity of the dinuclear complexes over their mononuclear counterparts (Figure 32). Moreover, protodemetallation is performed by the alkyne, which regenerates the metallated acetylide, whilst excluding the σ-copper acetylide from the biscopper catalytic cycle.

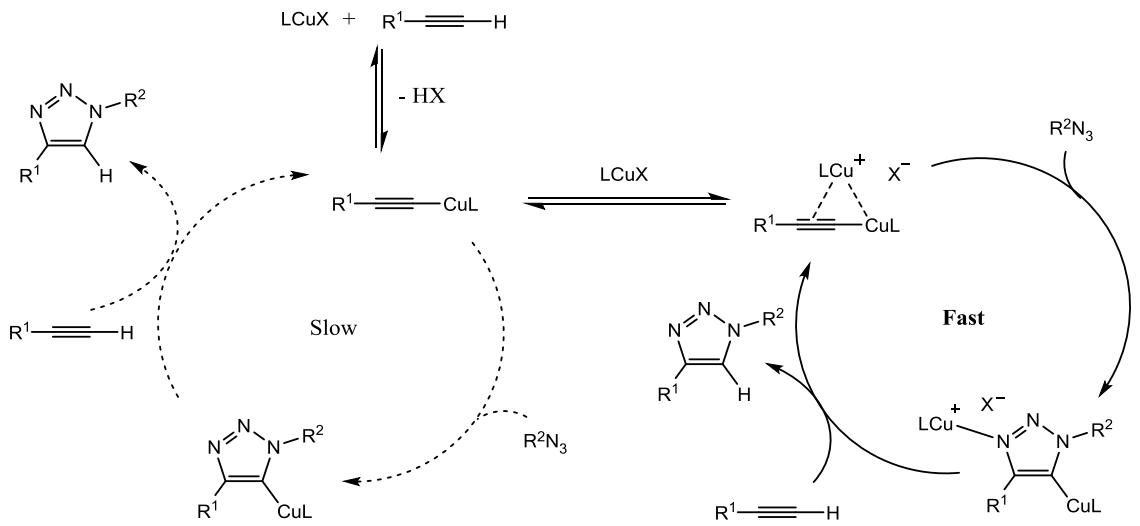

Figure 32 Bertrand group CuAAC reaction mechanism

1.14 Materials and methods

General methods

All reactions, unless otherwise stated, were carried out at room temperature, with magnetic stirring and in a fume hood. Microwave heating was performed with a CEM Discover Analyser. Organic extracts were dried with anhydrous magnesium sulfate and evaporated using an ice cooled rotary evaporator. All synthetic products were dried under vacuum in a desiccator with activated anhydrous calcium carbonate, sealed and stored at 4°C under an inert atmosphere. When specified, samples were dried with an Edwards Modulyo freeze dryer.

Solvents and reagents

Commercial grade reagents and solvents were purchased from Sigma Aldrich, Alfa Aesar, VWR International, Fisher Scientific Ltd., SLS and Santa Cruz Biotechnology and used without further purification, unless otherwise stated.

Chromatography

Flash column chromatography (FCC) was performed on silica gel (Merck Kieselgel 60 F_{254} 230-400 mesh, all solvents are reported as v/v herein). Thin Layer Chromatography (TLC) was performed on aluminium-backed plates pre-coated with silica (0.2 mm, 60 F_{254}) which were developed using UV fluorescence, vanillin, potassium permanganate, iodine or ninhydrin

staining. Chemical and radiochemical analysis and purification was performed manually on an Agilent 1200 series quaternary pump HPLC, coupled to a UV detector (254 nm). Column parameters, mobile and stationary phase are specified in the text. Spectra were recorded and analysed with Laura 4 (LabLogic), GINA Star 5.8 (Raytest) or Chemstation (Agilent Technologies). Chemical mass analysis was performed on an Agilent 1200 HPLC with an Agilent 6520 Accurate Mass QTOF LC/MS with ESI. The instrument was equipped with an autosampler, UV detection (254 nm) and samples were injected directly or through an Agilent Eclipse C18 4.6 mm x 100 mm, 5 µm column or a Phenomenex Kinetex XB-C18 4.6 mm x 150 mm 5 µm column. Spectra were recorded and analysed with MassHunter Workstation 2009 B.02.01 and Analysis 2009 B.03.01, respectively.

Spectroscopy

Infra-red spectra were recorded from solid substances on a Perkin-Elmer Spectrum 100 FT-IR spectrometer. Only selected absorbances (ν_{max}) are reported. ^{1}H NMR and ^{13}C proton decoupled NMR spectra were recorded at 400 MHz in 5 mm tubes on Bruker AV-400 spectrometers. Spectra were analysed with ACD/NMR processor (academic edition), V12.01. Chemical shifts (δ_H and δ_C, respectively) are quoted in parts per million (ppm) and referenced to the appropriate residual solvent peak.[429] Coupling constants (J) are reported to the nearest 0.1 Hz.

1.15 Experimental

1.15.1 5-Isothiocyanato-quinoline (QNCS)

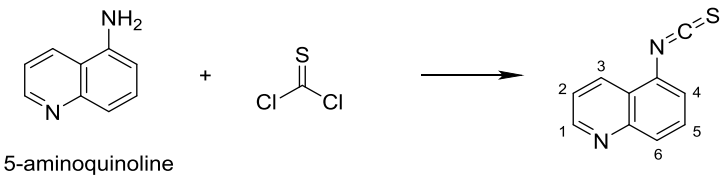

QNCS

$C_{10}H_6N_2S$

Exact Mass: 186.0252

Molecular Weight: 186.2320

This method was adapted from Donnelly-Roberts *et al.*[229] A solution of 5-aminoquinoline (0.72 g, 5.0 mmol) in DCM (15 mL) and saturated aqueous Na_2HCO_3 (1.47 g in 15 mL, 17.25 mmol) at 0°C was added dropwise over 10 min to a solution of thiophosgene (0.38 mL, 5.0 mmol) in

DCM (3 mL). The reaction quickly turned dark red but was stirred at 0°C for further 2 h. TLC monitoring was carried out until completion (9:1 hexane/ethyl acetate, QNCS R_f 0.17). The biphasic mixture was separated with more concentrated Na2HCO3 (10 mL) and DCM backwashes (3 x 10 mL). Then the organic layer was washed with brine (2 x 15 mL), dried with $MgSO_4$ and concentrated under reduced pressure to generate 1.88 g of crude product. Purification was carried out with flash column chromatography (ethyl acetate 25% to 50% gradient in hexane). The pale yellow powder isolated in 62% yield, 0.58g (3.1 mmol) was dried and characterised as 5-isothiocyanato-quinoline. mp 30-40°C; ^{1}H NMR ($CDCl_3$) δ (ppm): 9.00 (dd, 1H, H_1, J = 4.3 Hz, 1.6 Hz), 8.47 (dd, 1H, H_3, J = 8.5 Hz, 1.6 Hz), 8.07 (dd, 1H, H_4, J = 8.6 Hz, 1.0 Hz), 7.68 (dd, 1H, H_5, J = 8.6 Hz, 7.5 Hz), 7.55 (dd, 1H, H_2, J = 8.5 Hz, 4.3 Hz), 7.51 (dd, 1H, H_6, J = 7.5 Hz, 1.0 Hz). ^{13}C NMR ($CDCl_3$) δ: 151.45, 131.24, 129.23, 129.00, 124.74, 123.93, 122.08. HRMS (ESI+): calcd. for $C_{10}H_6N_2S$ (M-H) 187.0325, found 187.0492. IR (v, cm^{-1}) 2129 (N=C=S). Elemental analysis: calc. for $C_{10}H_6N_2S$ C, 64.49; H, 3.25; N, 15.04; S, 17.22; found: C, 64.60 64.63; H, 3.33 3.29; N, 14.92 14.94.

1.15.2 Isothiocyanatobenzene (ANCS)

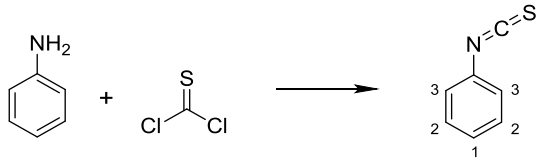

ANCS
C_7H_5NS
Exact Mass: 135.0143
Molecular Weight: 135.1840

This method was adapted from Donnelly-Roberts *et al.*[229] A solution of aniline (0.9 mL, 10 mmol) and saturated aqueous Na_2HCO_3 (70 mmol) at 0°C was added dropwise to a solution of thiophosgene (0.76 mL, 10 mmol) in DCM (15 mL). The reaction quickly turned dark red but was stirred at 0°C for further 2 h. TLC monitoring was carried out until completion (3:1:0.02 hexane/ethyl acetate/triethylamine, ANCS R_f 0.84). The biphasic mixture was separated with more concentrated Na_2HCO_3 (10 mL) and DCM backwashes (3 x 10 mL). Then the organic layer was washed with 10 mL brine, dried with $MgSO_4$ and concentrated under reduced pressure. Purification was carried out with flash column chromatography (1:5-2:1 ethyl acetate/hexane). The pale red powder was isolated in 12.4% yield (0.92 g), dried and

characterised as isothiocyanatobenzene. ^{1}H NMR ($CDCl_3$) δ (ppm): 7.25 (dt, 2H, H_3, J = 7.8 Hz, 2 Hz), 7.18 (tt, 1H, H_1, J = 7.2 Hz, 2 Hz), 7.12 (td, 2H, H_2, J = 7.2 Hz, 7.8 Hz). ^{13}C NMR ($CDCl_3$) δ: 135.19, 131.13, 129.46, 127.23, 125.65. HRMS (ESI^+): calcd. for C_7H_5NS (M+H) 136.0126, found 136.0182. IR (v, cm^{-1}) 2165 (N≡C-S), 2042 (br, N=C=S).

1.15.3 3-Isothiocyanatophenol (ONCS)

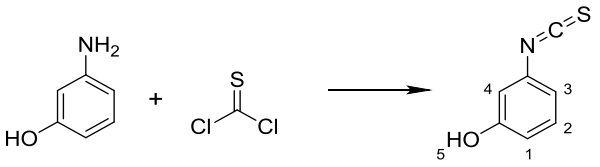

ONCS
C_7H_5NOS
Exact Mass: 151.0092
Molecular Weight: 151.1830

This method was adapted from Donnelly-Roberts *et al.*[229] M-aminophenol (2 g, 18.3 mmol) in ethyl acetate (100mL) and saturated aqueous Na_2HCO_3 (6.15 g, 73.2 mmol) were added dropwise over 10 min to a solution of thiophosgene (1.4mL, 18.3 mmol) in ethyl acetate (140 mL). The mixture was stirred for 2 hours at 0°C until completion as indicated by TLC monitoring (3:2 hexane/ethyl acetate). The product was extracted with further saturated Na_2HCO_3 (50 mL) and ethyl acetate (3 x 20 mL), followed by brine (30 mL), drying with $MgSO_4$ and concentration under reduced pressure. The product was isolated as brown crystals in 83% yield (2.29 g). ^{1}H NMR ($CDCl_3$) δ (ppm): 7.21 (t, 1H, H_4, J = 8.1 Hz), 6.82 (ddd, 1H, H_1, J = 8 Hz, 1.8 Hz, 0.8 Hz), 6.76 (ddd, 1H, H_3, J = 8.2 Hz, 2.4Hz, 0.9 Hz), 6.72 (dd, 1H, H_2, J = 2.1 Hz, 2 Hz), 1.64 (s, 1H, H_5). ^{13}C NMR ($CDCl_3$) δ (ppm): 156.10, 132.14, 130.47, 118.44, 114.74, 112.68. HRMS (ESI^-): calcd. for C_7H_5NOS (M-H) 150.0019, found 150.0118. IR (cm^{-1}) 3268 (ArOH), 2092 (C=N).

1.15.4 4-Isothiocyanato-1H-indole (INCS)

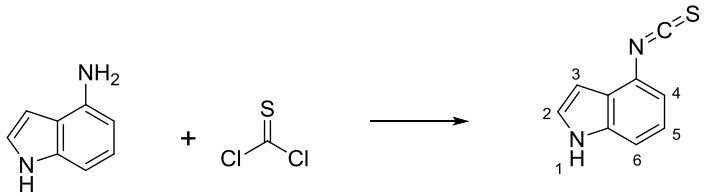

INCS
$C_9H_6N_2S$
Exact Mass: 174.0252
Molecular Weight: 174.2210

To a solution of thiophosgene (0.29 mL, 3.79 mmol) in DCM (3 mL), 4-aminoindole (0.5 g, 3.79 mmol) in DCM (2.5 mL) and saturated aqueous Na_2HCO_3 (2.23 g, 26.5 mmol) were added dropwise. The mixture was stirred for 2 hours at 0°C until completion as indicated by TLC monitoring (3:1:0.002 hexane/ethyl acetate/triethylamine). The product was extracted with further 10 mL saturated Na_2HCO_3 and 3 x 10 mL DCM, followed by 10 mL brine, drying with $MgSO_4$ and concentration under reduced pressure. The product was isolated as green crystals in 86% yield (0.57 g). ^{1}H NMR ($CDCl_3$) δ (ppm): 8.36 (br s, 1H, H_1), 7.34 (d, 1H, J = 8 Hz, H_6), 7.28 (t, 1H, J = 4 Hz, H_3), 7.12 (t, 1H, J = 8 Hz, H_5), 6.99 (d, 1H, J = 8 Hz, H_4), 6.73 (t, 1H, J = 4 Hz, H_2). ^{13}C NMR ($CDCl_3$) δ: 124.30, 124.07, 121.17, 115.61, 109.78, 99.28. IR ($CHCl_3$): 3477 (N-H), 2129 (-N=C=S). HRMS (ESI^+): calcd. for $C_9H_6N_2S$ (M+H) 175.0325, found 175.0324.

1.15.5 N'-cyano-N-(quinolin-5-yl)carbamimidothioate (QSMe)

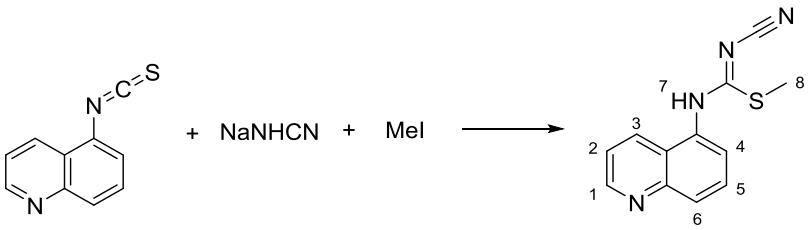

QSMe
$C_{12}H_{10}N_4S$
Exact Mass: 242.0626
Molecular Weight: 242.3000

A mixture of 5-aminoquinoline isothiocyanate (6.38 g, 34.3 mmol) and sodium hydrogencyanamide (2.19 g, 34.3 mmol) in DMF (30 mL) was stirred at room temperature for 1 h. Methyl iodide (2.13 mL, 34.3 mmol) was added at 0°C and the reaction was stirred at room temperature for 2 h. The reaction was poured into water (5 mL) and stirred for further 20 min. The orange precipitate was filtered and washed with water (10 mL). Further purification was performed by flash chromatography on SiO_2 (EtOAc:CH_2Cl_2, 1:1) to obtain methyl N'-cyano-N-(quinolin-5-yl)carbamimidothioate as an orange solid in 70.0% yield (5.77 g). ^{1}H NMR (400 MHz, $CDCl_3$) δ (ppm): 9.02 (dd, 1H, H_1, J = 4.2 Hz, 1.6 Hz), 8.74 (br s, H_7), 8.32 (dd, 1H, H_3, J = 8.5 Hz, 1.6 Hz), 8.22 (dd, 1H, H_6, J = 8.5 Hz, 1.1 Hz), 7.77 (dd, 1H, H_5, J = 8.5 Hz, 7.4 Hz), 7.59 (dd, H_4, J = 7.4 Hz, 1.1 Hz), 7.55 (dd, H_2, J = 8.5 Hz, 4.2 Hz), 2.38 (s, 3H, H_8); ^{13}C NMR (400MHz, $CDCl_3$) δ (ppm): 14.59, 37.37, 122.30, 127.19, 128.80, 130.71, 131.52, 151.36. IR (v, cm^{-1}) 3195 (N-H), 2161 (C≡N), 1509 (N-C=S), 1490 (N-C-N). HRMS (ESI^+): calcd. for $C_{12}H_{10}N_4S$

(M-H) 243.0699, found 243.0695. Elemental Analysis: Calc. For $C_{12}H_{10}N_4S$ C, 59.48; H, 4.16; N, 23.12; S, 13.23; found: C, 59.37, 59.42; H, 4.14 4.22; N, 22.96 23.03.

1.15.6 Methyl N'-cyano-N-phenylcarbamimidothioate (ASMe)

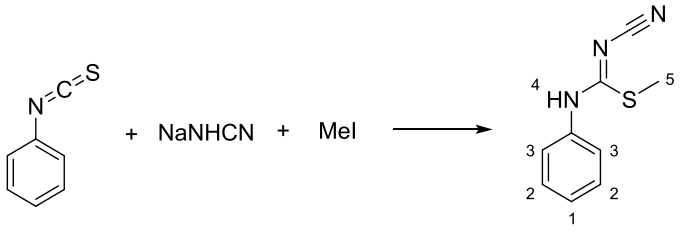

ASMe

$C_9H_9N_3S$

Exact Mass: 191.0517

Molecular Weight: 191.2520

A mixture of isothiocyanatobenzene (0.91 g, 6.78 mmol) and sodium hydrogencyanamide (0.434 g, 6.78 mmol) in DMF (8 mL) was stirred at room temperature for 1 h. Methyl iodide (0.422 mL, 6.78 mmol) was added at 0°C and the reaction was stirred at room temperature for 90 min until completion as assessed by TLC (1:1 DCM/ethyl acetate, ASMe R_f 0.8). The reaction was poured into 25 mL water and stirred for further 20 min. The precipitate was filtered and washed with water (5 mL). Following overnight drying in a vacuum desiccator, the compound was collected without further purification as white granules in 86.9% yield (1.123 g). ^{1}H NMR (d^6-DMSO) δ (ppm) 10.16 (s, 1H, H_4), 7.42 (dt, 2H, H_3, J = 8 Hz, 2 Hz), 7.41 (dt, 2H, H_2, J = 8 Hz, 8 Hz), 7.26 (tt, 1H, H_1, J = 8 Hz, 2 Hz), 2.69 (s, 3H, H_5). ^{13}C NMR (400MHz, d^6-DMSO) δ (ppm): 137.26, 128.90, 126.47, 124.34, 114.88, 14.88. IR (v, cm^{-1}) 3224 (N-H), 2159 (C≡N), 1514 (N-C=S), 1495 (N-C-N). HRMS (ESI$^+$): calcd. for $C_9H_9N_3S$ (M+H) 191.0590, found 192.0581. Elemental Analysis: Calc. for $C_9H_9N_3S$ C, 56.52; H, 4.74; N, 21.97; S, 16.76; found: C, 56.64 56.63; H, 4.28 4.31; N, 21.95, 21.85.

1.15.7 Methyl N'-cyano-N-(3-hydroxyphenyl)carbamimidothioate (OSMe)

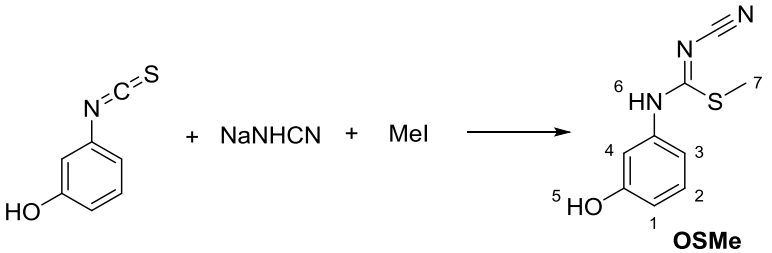

OSMe

$C_9H_9N_3OS$

Exact Mass: 207.0466

Molecular Weight: 207.2510

3-Isothiocyanatophenol (2g, 13.2 mmol) and sodium hydrogencyanamide (849 mg, 13.2 mmol) in dry DMF (60 mL) were stirred overnight at room temperature under an inert atmosphere. When TLC monitoring (7:3 hexane / ethyl acetate) indicated that the staring material had been depleted, methyl iodide (0.82 µL, 13.23 mmol) was added at 0°C and the mixture was stirred room temperature for 2 hours. The mixture was then poured into water (100 mL) and extracted with DCM (5 x 20 mL) and water (3 x 10 mL) to remove DMF. After concentration by rotary evaporation of the combined organic layers, the resulting yellow powder was filtered and dried under a high vacuum overnight. The product was obtained in 43% yield (1.18 g). ^{1}H NMR (DMSO) δ (ppm): 10.05 (br s, 1H, H_6), 9.63 (s, 1H, H_5), 7.17 (dd, 1H, H_2, J = 8.2 Hz), 6.91 (dd, 1H, H_4, J = 2 Hz, 2 Hz), 6.84 (ddd, 1H, H_1, J = 8.2 Hz, 2 Hz, 0.8 Hz), 6.63 (ddd, 1H, H_3, J = 8.2 Hz, 2 Hz, 0.8 Hz), 2.67(s, 3H, H_7). ^{13}C NMR ($CDCl_3$) δ (ppm): 157.54, 138.20, 129.47, 114.77, 114.45, 113.32, 110.84, 14.85. HRMS (ESI^+): calcd. for $C_9H_9N_3OS$ (M+H) 208.0539, found 208.0420. IR (v, cm^{-1}) 3386 (N-H), 3134 (O-H), 2137 (N=C=S, C≡N), 1601, 1492 (C=N).

1.15.8 (*S*)-1-(1-(4-bromophenyl)ethyl)-2-cyano-3-(1H-indol-4-yl)guanidine (IMBB)

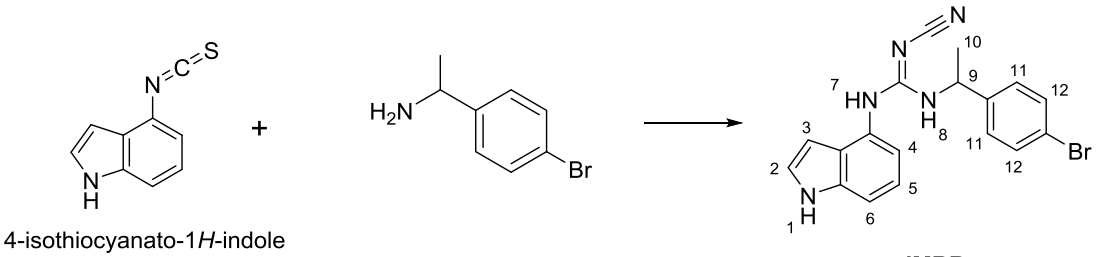

4-isothiocyanato-1*H*-indole

IMBB

$C_{18}H_{16}BrN_5$

Exact Mass: 381.0589

Molecular Weight: 382.2650

1-(4)-Bromophenyl ethylamine (0.17 mL, 1.17 mmol) was added to 4-isothiocyanato-indole (0.205 g, 1.17 mmol) in anhydrous THF (5 mL) and stirred for 1 h at room temperature. Following addition of mercury acetate (0.373 mg, 1.17 mmol) and then sodium hydrogencyanamide (0.225 g, 3.51 mmol), the mixture was stirred for 3 h until a red precipitate was observed. The reaction was quenched with water (15 mL). The sluggish mixture was filtered under reduced pressure through a short pad of celite. The filtrate was concentrated by rotary evaporation and purified by flash chromatography in 7:2:0.9 hexane/ethyl acetate/methanol. The product was isolated as a dark orange powder in 28% yield (124 mg). ^{1}H NMR (DMSO) δ (ppm): ^{1}H NMR ($CDCl_3$) δ (ppm): 8.54 (s, 1H, H_7), 7.44 (d, 2H, J = 8.6 Hz, H_{12}), 7.43 (d, 2H, J = 8.6 Hz, H_{11}), 7.30 (dd, 1H, J = 5.0 Hz, H_5), 7.23 (t, 1H, J = 8.0 Hz, H_2), 7.18 (d, 1H, J = 5.0 Hz, H_6), 7.07 (d, 1H, J = 8.0 Hz, H_3), 6.97 (d, 1H, J = 5.0 Hz, H_4), 6.44 (br s, 1H, H_1), 5.05 (m, 1H, H_9), 1.61 (br s, 1H, H_8), 1.37 (d, 3H, J = 6.6 Hz, H_{10}). ^{13}C NMR 157.43, 137.12, 131.13, 128.87, 128.52, 125.20, 121.28, 99.13, 22.11. IR ($CHCl_3$) cm^{-1}: 3361 (N-H), 2253 (C≡N), 2173 (-S-C≡N). HRMS (ESI^+): calcd. for $C_{18}H_{16}BrN_5$ (M+Na+2H) 406.0627, found 406.0638.

1.15.9 2-Cyano-1-(quinolin-5-yl)-3-(4-(4,4,5,5-tetramethyl-1,3,2-dioxaborolan-2-yl)benzyl)guanidine (QPB)

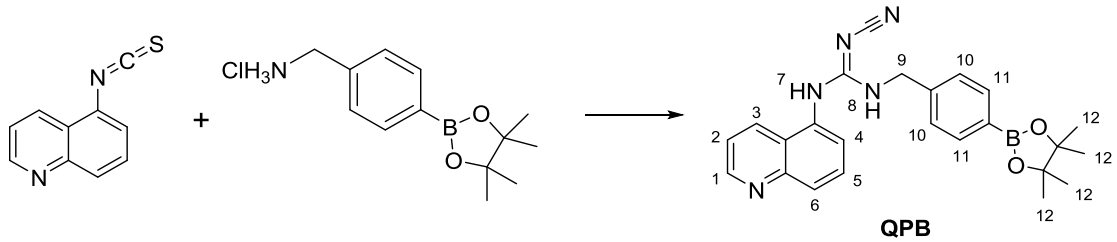

QPB

$C_{24}H_{26}BN_5O_2$

Exact Mass: 427.2180

Molecular Weight: 427.3150

A mixture of 4-(aminomethyl)phenylboronic acid pinacol ester hydrochloride (0.5 g, 1.86 mmol) and 0.391 mL triethylamine (2.78 mmol) was added to 5-isothiocyanato-quinoline (0.346 g, 1.86 mmol) in anhydrous THF (15 mL) and stirred for 1 h at room temperature until it appeared cream white. Following addition of mercury acetate (0.592 mg, 1.86 mmol) and then sodium hydrogencyanamide (5.55 mmol), the mixture was stirred for 4 days until dark black. The reaction was quenched with water (15 mL). The sluggish mixture was filtered under reduced

pressure through a short pad of celite and was washed with ethyl acetate (30 mL). The filtrate was concentrated by rotary evaporation and purified by flash chromatography with a gradient of 1-10% methanol in ethyl acetate. The product was isolated as a white solid in 18.4% yield (147 mg). ^{1}H NMR (DMSO) δ (ppm): 9.45 (br s, 1H, H_7), 8.94 (dd, 1H, H_1, J = 4 Hz, 1.6 Hz), 8.18 (m, 1H, H_4), 8.02 (d, 1H, H_3, J = 8.2 Hz), 7.79 (dd, 1H, H_5, J = 8.6 Hz, 7.6 Hz), 7.64 (d, 2H, H_{11}, J = 7.6 Hz), 7.59 (dd, 1H, H_2, J = 8.2 Hz, 4 Hz), 7.51 (d, 1H, H_6, J = 7.6 Hz), 7.24 (d, 2H, H_{10}, J = 7.6 Hz), 4.35 (s, 2H, H_9), 1.30 (s, 12H, H_{12}). ^{13}C NMR (DMSO) δ (ppm): 159.34, 150.71, 148.43, 134.42, 131.31, 129.31, 128.55, 126.38, 125.89, 125.47, 121.66, 117.18, 83.56, 44.47, 24.64. HRMS (ESI^+): calcd. for $C_{24}H_{26}BN_5O_2$ (M+H) 428.2253, found 428.2256. IR (v, cm^{-1}) 2170 (C≡N), 1515 (B-aryl), 1363 (B-O).

1.15.10 Mixture of Mono-N-Boc-QPB and Mono-N'-Boc-QPB

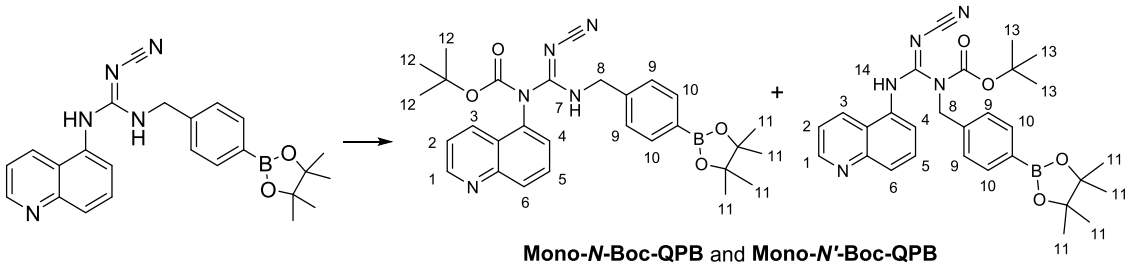

Mono-*N*-Boc-QPB and **Mono-*N'*-Boc-QPB**
Chemical Formula: $C_{29}H_{34}BN_5O_4$
Exact Mass: 527.27
Molecular Weight: 527.43

A mixture of QBP (80 mg, 0.187 mmol) and $(Boc)_2O$ (367 mg, 1.68 mmol) was dissolved under magnetic stirring into an excess of DIPEA (ca. 1 mL). Following addition of DMAP (69 mg, 0.562 mmol), the reaction was warmed to 60°C and monitored by LC/MS. After 6 hours, the reaction was diluted with DCM and concentrated by rotavaporation. Then, a flash chromatography column was run in a 30% to 60% gradient of ethyl acetate in hexane. This synthesis was only sufficient to afford a mixture of Mono-N-Boc-QPB and Mono-N'-Boc-QPB as a yellow paste in 6.9% yield (6.7 mg). ^{1}H NMR ($CDCl_3$) δ (ppm): 9.34 (dd, 1H, H_1, J= 8.4 Hz, 1.6 Hz), 9.02 (dd, 1H, H_3, J = 4.6 Hz, 1.6 Hz), 8.95 (m, 1H, H_4), 7.90 (d, 1H, H_5, J= 9.2 Hz), 7.71 (d, 1H, H_6, J = 9.2 Hz), 7.56 (dd, 1H, H_2, J = 8.4 Hz, 4.6 Hz), 7.43 (d, 2H, H_{10}, J = 8 Hz), 7.09 (d, 2H, H_9, J = 8 Hz), 5.57 (br s, 1H, H_7-H_{14}), 5.27 (s, 2H, H_8), 1.54 (s, 12H, H_{11}), 1.46 (s, 9H, H_{12}-H_{13}). ^{13}C NMR ($CDCl_3$) δ (ppm): 159.64, 157.66, 154.01, 152.14, 151.88, 150.35, 149.78, 137.10, 133.58,

127.96, 125.87, 121.74, 120.88, 108.16, 83.34, 81.09, 52.73, 28.90, 28.18, 27.71. MS (ESI^+): found 518.27 (unknown fragmentation).

1.15.11 2-Cyano-1-(prop-2-yn-1-yl)-3-(quinolin-5-yl)guanidine (QYL)

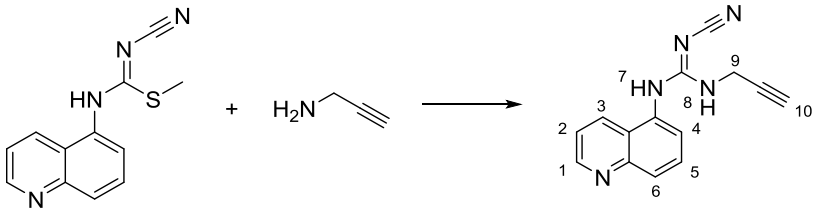

QYL
$C_{14}H_{11}N_5$
Exact Mass: 249.1014
Molecular Weight: 249.2770

To a mixture of triethylamine (110 µL, 820 umol) and propargylamine (1 mL), 410 umol of N'-cyano-N-(quinolin-5-yl)carbamimidothioate (QSMe) were added and stirred until fully dissolved. The solution was then stirred for 60 min in a microwave reactor at 50°C, 300 W. The reaction was left to cool slowly and the precipitate was collected by removal of the supernatant and overnight evaporation in a fume hood of the residual propargylamine. The precipitate was then purified by vacuum-assisted hot EtOH filtration to obtain QYL as a white powder in 89% yield (91 mg). ^{1}H NMR (400 MHz, DMSO) δ (ppm): 9.53 (br s, 1H, H_7), 8.94 (dd, 1H, H_1, J = 4.2 Hz, 1.6 Hz), 8.25 (dd, 1H, H_3, J = 8.2 Hz, 1.6 Hz), 8.01 (dd, 1H, H_4, J = 8.6 Hz, 0.9 Hz), 7.78 (dd, 1H, H_5, J = 8.6 Hz, 7.3 Hz), 7.60 (dd, 1H, H_2, J = 8.2 Hz, 4.2 Hz), 7.47 (dd, 1H, H_6, J = 7.3 Hz, 0.9 Hz), 7.35 (br s, 1H, H_8), 3.91 (br s, 2H, H_9), 3.20 (s, 1H, H_{10}).^{13}C NMR (DMSO) δ: 156.78, 150.53, 131.12, 129.08, 128.34, 125.52, 121.51, 30.66. HRMS (ESI^+): calcd. for $C_{14}H_{11}N_5$ (M+H) 250.1087, found 250.1101. Elemental Analysis: Calc. for $C_{14}H_{11}N_5$ C, 67.46; H, 4.45; N, 28.10; found: C, 67.32; H, 4.60; N, 28.15. IR (v, cm^{-1}): 3260, 3194 (N-H), 2167 (C≡N), 1579 (guanidine C=N), 1371 (wagging alkyne C-H).

1.15.12 2-Cyano-1-phenyl-3-(prop-2-yn-1-yl)guanidine (AYL)

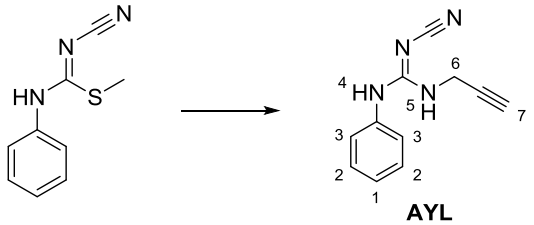

AYL

$C_{11}H_{10}N_4$

Exact Mass: 198.0905

Molecular Weight: 198.2290

To a mixture of triethylamine (366 µL, 2.63 mmol) and propargylamine (2 mL), methyl N'-cyano-N-phenylcarbamimidothioate (ASMe, 1.31 mmol) was added and stirred until fully dissolved. The solution was then stirred for 60 min in a microwave reactor at 50°C, 300 W, and the reaction progress was monitored by analytical HPLC on a 4.6 mm x 150 mm, 5 um pore C_{18} Zorbax column with a 5-95% MeOH gradient in 0.1% TFA water over 12 min. The reaction was left to cool slowly and the precipitate was collected by removal of the supernatant and overnight evaporation in a fume hood of the residual propargylamine. The precipitate was then recrystallized from ethanol/water and the product was isolated as red crystals in 76% yield (198 mg). ^{1}H NMR (MeOD) δ (ppm): 7.41 (dt, 2H, H_3, J = 7.8 Hz, 3.6 Hz), 7.28 (m, 2H, H_2), 7.25 (m, 1H, H_1), 4.03 (d, 2H, H_6, J = 2.5 Hz), 2.63 (t, 1H, J = 2.5 Hz, H_7). ^{13}C NMR (MeOD) δ (ppm): 180.29, 137.94, 130.75, 127.90, 126.56, 118.78, 80.57, 72.66, 32.09. HRMS (ESI^+): calcd. for $C_{11}H_{10}N_4$ (M+H) 199.0978, found 199.0982. IR (v, cm^{-1}): 3285 (alkyne C-H), 2175 (C≡N/C≡C), 1595 (guanidine C=N), 1345 (wagging alkyne C-H).

1.15.13 2-Cyano-1-(3-hydroxyphenyl)-3-(prop-2-yn-1-yl)guanidine (OYL)

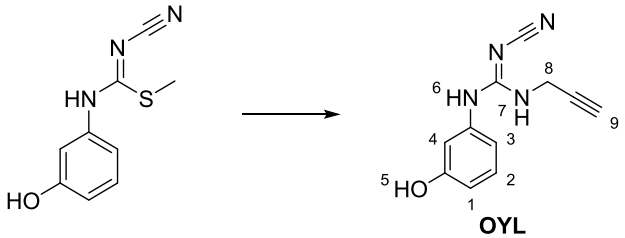

OYL

$C_{11}H_{10}N_4O$

Exact Mass: 214.0855

Molecular Weight: 214.2280

3-Isothiocyanatophenol (200 mg, 0.97 mmol) and 2 mL propargylamine (31.22 mmol) were added under inert atmosphere to triethylamine (267 µL, 1.9 mmol),. The mixture was stirred until

it had become a homogeneous solution, and stirred at 50°C for 60 min in a microwave reactor, 300 W. The red crude product was then concentrated under reduced pressure to afford red crystals of 2-cyano-1-(3-hydroxyphenyl)-3-(prop-2-yn-1-yl)guanidine in 56% yield (116 mg). ^{1}H NMR (DMSO) δ (ppm): 7.13 (t, 1H, H_2, J = 8.1 Hz), 6.66 (t, 1H, H_4, J = 1.6 Hz, 2.2 Hz), 6.63 (ddd, 1H, H_1, J = 8.1 Hz, 1.6 Hz, 0.8 Hz), 6.57 (ddd, 1H, H_3, 8.1 Hz, J = 2.2 Hz, 0.8 Hz), 3.95 (s, 2H, H_8), 2.08 (s, 1H, H_9). HRMS (ESI$^+$): calcd. for $C_{11}H_{10}N_4O$ (M+H) 215.0928, found 215.0923.

1.15.14 2-Azidoethanol

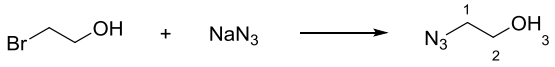

2-azidoethanol
$C_2H_5N_3O$
Exact Mass: 87.0433
Molecular Weight: 87.0820

This procedure was previously reported by Demko and Sharpless.[430] Bromoethanol (5.7 mL, 80 mmol) in 25 mL water and sodium azide (13.65 g, 210 mmol) were stirred at reflux for 16 h before cooling, saturation with magnesium sulfate and extraction with DCM (3 x 15 mL). The combined organic layers were dried over magnesium sulfate and transferred to a new round bottomed flask under inert atmosphere for the subsequent reaction. ^{1}H NMR ($CDCl_3$) δ (ppm): 3.74 (t, 2H, H_2, J = 6 Hz), 3.40 (t, 2H, H_1, J = 6 Hz), 3.04 (br s, H_3).

1.15.15 2-Azidoethyl-4-methylbenzenesulfonate (TsEA)

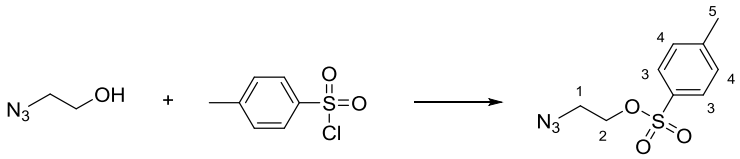

TsEA
$C_9H_{11}N_3O_3S$
Exact Mass: 241.0521
Molecular Weight: 241.2650

The previously synthesised 2-azidoethanol (80 mmol) in DCM (30 mL) was protected from light and mixed with triethylamine (15.61 mL, 112 mmol) and methylbenzenesulfonyl chloride (18.30 g, 96 mmol). After four hours the solution had turned brown. Glycine (1.20 g, 16 mmol) was added and the solution was stirred for two further hours. The organic layer was then washed with 1N NaOH (2 x 80 mL), dried over $MgSO_4$ and the crude was purified by flash

chromatography with a 5:1 to 2:1 hexane/diethyl ether gradient. The product was isolated as a clear yellow oil in 18% yield, 3.4 g and remained stable at room temperature for up to a year before turning dark yellow. ^{1}H NMR ($CDCl_3$) δ (ppm): 7.80 (dd, 2H, H_3, J = 8.6 Hz, 0.8 Hz), 7.36 (dd, 2H, H_4, J = 8.6 Hz, 0.8 Hz), 4.13 (t, 2H, H_1, J = 4 Hz), 3.46 (t, 2H, H_2, J = 4 Hz), 2.43 (s, 3H, H_5). ^{13}C NMR ($CDCl_3$) δ (ppm): 145.09, 132.24, 129.78, 127.65, 68.06, 49.31, 21.34. HRMS (ESI^+): calcd. for $C_9H_{11}N_3O_3S$ (M+H) 242.0594, found 242.2246.

1.15.16 2-Fluoroethyl-4-methylbenzenesulfonate

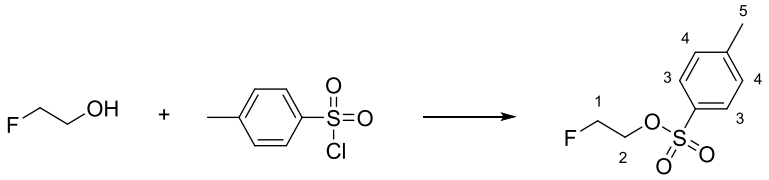

2-Fluoroethyl-4-toluenesulfonate
$C_9H_{11}FO_3S$
Exact Mass: 218.0413
Molecular Weight: 218.2424

This method was adapted from Glaser and Årstad.[410] 2-Fluoroethanol (2 g, 31.22 mmol) and pyridine (5.1 mL, 62.44 mmol) were added successively under inert atmosphere to p-toluenesulfonyl chloride (8.9g, 46.8mmol) in dry DCM (8mL). The mixture was then stirred overnight at room temperature until reaction completion as indicated by TLC. Then HCl (12 mL, 1.2 mmol) and DCM were added in succession, and the two layers were separated. The aqueous layer was further extracted with DCM (3 x 5 mL) and the combined organic layers were washed with potassium carbonate (3 x 4 mL), dried over $MgSO_4$, filtered and concentrated under reduced pressure. The crude product was purified by flash chromatography on silica gel (6:4 hexane/ethyl acetate), giving 2-fluoroethyl-4-methylbenzenesulfonate in 22% yield, 1.47 g. HRMS (ESI^+): calcd. for $C_9H_{11}FO_3S$ (M+H) 218.0486, found 219.0491.

1.15.17 2-Fluoroethylazide (FEA)

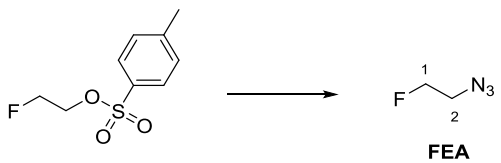

FEA
$C_2H_4FN_3$
Exact Mass: 89.0389
Molecular Weight: 89.0734

This method was previously reported in Glaser and Årstad.[410] To a solution of 2-fluoroethyl-4-methylbenzenesulfonate (1.47 g, 6.7 mmol) in dry DMF (12 mL) sodium azide (482 mg, 7.41 mmol) was added. The mixture was left to react for 24 h at room temperature, filtered and the filtrate used as a stock solution in subsequent reactions without further purification or concentration. (Attempts to isolate neat 2-fluoroethylazide may result in an explosion).[410] HRMS (ESI^+): calcd. for $C_2H_4FN_3$ (M+H) 90.0462, found 90.0378 .

1.15.18 General procedure for the cycloaddition of 2-fluoroethyl azide with alkyne-functionalised cyanoguanidines (XFA)

An alkyne-functionalised cyanoguanidine (1 eq.) and a mixture of copper sulfate pentahydrate (0.05 eq.) and sodium ascorbate (0.1 eq.) in 0.3 mL water were added under argon in a microwave vial to a solution of 2-fluoroethyl azide (FEA, 1.2 eq.) in DMF. The reaction was heated in a microwave reactor until all starting material was depleted. The product was then diluted with DCM and extracted with water (4 x 5 mL) and DCM (4 x 5 mL) washes. The residue was purified by flash chromatography on silica.

1.15.19 2-Cyano-1-((1-(2-fluoroethyl)-1H-1,2,3-triazol-4-yl)methyl)-3-(quinolin-5-yl)guanidine (RefEFA)

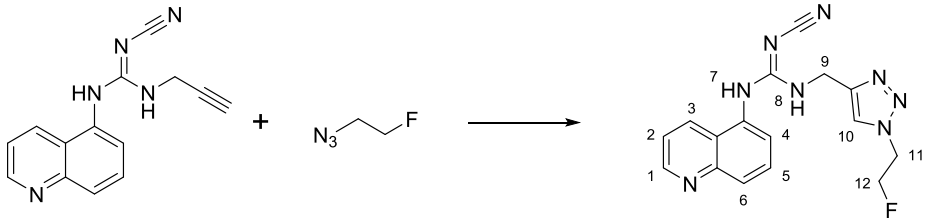

RefEFA
$C_{16}H_{15}FN_8$
Exact Mass: 338.1404
Molecular Weight: 338.3504

2-Cyano-1-(prop-2-yn-1-yl)-3-(quinolin-5-yl)guanidine (QYL, 200umol, 50 mg) and a mixture of copper sulfate pentahydrate (10 µmol, 2.5 mg) and sodium ascorbate (20 µmol, 4 mg) in 0.3 mL water were added under argon in a microwave vial to a solution of 2-fluoroethyl azide (FEA, 0.17M) in DMF. The reaction was heated in a microwave reactor to 80°C for 40 min until all starting material was depleted as assessed by TLC (1:2:10 methanol/hexane/ethyl acetate, R_f 0.27). The mixture was then diluted with DCM (10 mL) and washed with DCM (5 x 8 mL) and

water (5 x 6 mL) to remove DMF. The organic phase then underwent flash column chromatography with a 3-6% methanol gradient in a 10:1 mixture of DCM and ethyl acetate (R_f 0.08) and the product was isolated as an off white powder in 14% yield (27 µmol). ^{1}H NMR (DMSO) δ (ppm): 9.43 (s, 1H, H_7), 8.94 (d, 1H, H_1, J = 4.1 Hz), 8.16 (s, 1H, H_8), 8.01 (d, 1H, H_3, J = 8.4 Hz), 7.79 (t, 1H, H_4, J = 8 Hz), 7.63 (d, 1H, H_5, J = 8 Hz), 7.59 (dd, 1H, H_2, J = 8.4 Hz, J = 4.1 Hz), 7.50 (d, 1H, H_6, J = 8 Hz), 7.24 (d, 1H, H_{10}, J = 7.4 Hz), 4.34 (s, 2H, H_9), 1.29 (s, 4H, H_{11}-H_{12}). ^{13}C NMR (DMSO) δ (ppm): 159.35, 150.71, 148.43, 142.42, 134.42, 131.31, 129.31, 128.55, 126.38, 125.89, 125.46, 121.65, 117.18, 83.57, 44.47, 24.64. HRMS (ESI^{+}): calcd. for $C_{16}H_{15}FN_8$ (M+H) 339.1477, found 339.1501; calcd. for (M+Na) 361.1296, found 361.1297. IR (v, cm^{-1}) 2167 (C≡N), 1592 (Guanidine C=N), 1569 (conjugated C=N), 1025, 801 (C-F). Purity was confirmed by UV-HPLC using method B (Table 8, Section 1.19.1), as shown in Figure 33.

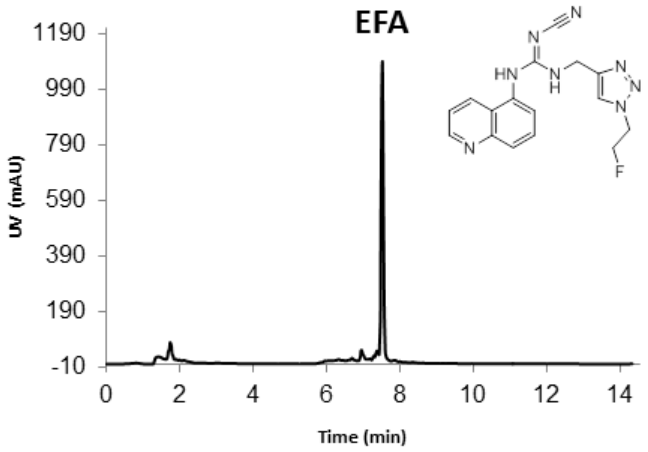

Figure 33 RefEFA purity

1.15.20 2-Cyano-1-((1-(2-fluoroethyl)-1H-1,2,3-triazol-4-yl)methyl)-3-phenylguanidine (RefAFA)

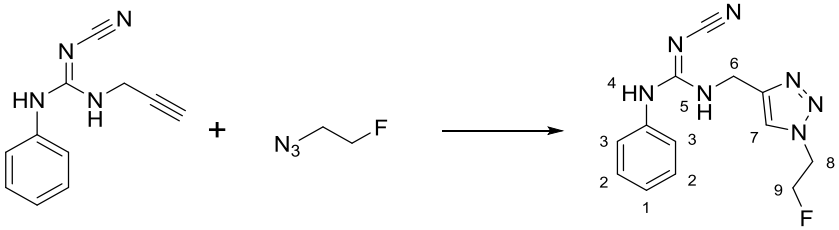

RefAFA
$C_{13}H_{14}FN_7$
Exact Mass: 287.1295
Molecular Weight: 287.3024

2-Cyano-1-phenyl-3-(prop-2-yn-1-yl)guanidine (AYL, 200 µmol) and a mixture of copper sulfate pentahydrate (25 mg, 10 µmol) and sodium ascorbate (5.6 mg, 28 µmol) in water (2 mL) were

added under argon in a microwave vial to 2-fluoroethyl azide (FEA, 240 µmol, 0.05M) in DMF. The reaction was heated in a microwave reactor for 20 min at 80°C and 300 W. The mixture was then diluted with DCM (4 mL) and extracted with washed with DCM (3 x 5 mL) and water (3 x 5 mL) to remove DMF. The residue was purified by flash chromatography with a gradient from 5:1 hexane/ethyl acetate to 100% ethyl acetate. The product was isolated as a white powder in 38% yield (22 mg). ^{1}H NMR (MeOD) δ (ppm): 7.95 (s, 1H, H_7), 7.41 (dt, 2H, H_3, J = 2 Hz, 8 Hz), 7.27 (dt, 2H, H_2, J = 2 Hz, 8 Hz), 7.26 (dd, 1H, H_1, J = 2 Hz, 8 Hz), 4.75 (dd, 2H, H_9, J = 4 Hz, 7 Hz), 4.69 (m, 2H, H_8), 4.52 (s, 2H, H_6). ^{13}C NMR (MeOD) δ (ppm): 130.80, 127.88, 126.58, 125.15, 83.81, 82.11, 52.07, 51.88, 37.94. HRMS (ESI$^+$): calcd. for $C_{13}H_{14}FN_7$ (M+H) 288.1368, found 288.1408 $(M+H)^+$; calcd. for (M+Na) 310.1187, found 310.1182. IR (v, cm^{-1}) 3219, 3141 (N-H), 2166 (C≡N), 1546 (Guanidine C=N), 1518 (conjugated C=N), 1025, 694 (C-F). Purity was confirmed by UV-HPLC using method D (Table 8, Section 1.19.1), as shown in Figure 33.

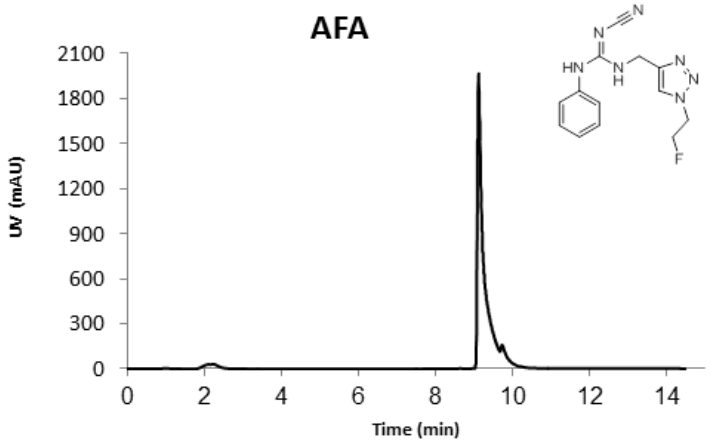

Figure 34 RefAFA purity

1.15.21 2-Cyano-1-((1-(2-fluoroethyl)-1H-1,2,3-triazol-4-yl)methyl)-3-(3-hydroxyphenyl)guanidine (RefOFA)

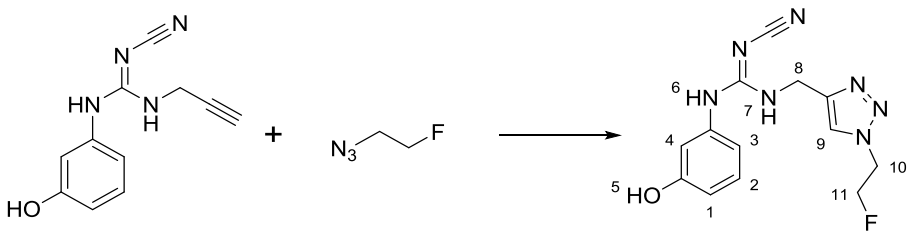

RefOFA
$C_{13}H_{14}FN_7O$
Exact Mass: 303.1244
Molecular Weight: 303.3014

2-Cyano-1-(3-hydroxyphenyl)-3-(prop-2-yn-1-yl)guanidine (OYL, 930 µmol) and a mixture of copper sulfate pentahydrate (11.5 mg, 46 µmol) and sodium ascorbate (18.4 mg, 93 µmol) in water (0.5 mL) were added under inert atmosphere to 2-fluoroethyl azide (FEA, 1.12 mmol, 0.05M) in DMF. The reaction was stirred at room temperature for 30 h. The mixture was then poured into water (5 mL), and extractions with DCM (3 x 5 mL), saturated Na_2HCO_3 (3 x 5 mL) and brine (1 x 5 mL) followed. The residue was then dried over anhydrous sodium sulfate, filtered and concentrated under reduced pressure. The crude was then purified with flash chromatography on silica with 19:1 ethyl acetate/methanol. Further purification was carried out on an HPLC C_{18} Zorbax 9.4 x 250 mm, 5 µm pore column, with a 5-95% gradient of acetonitrile in water. The product was isolated as 28 mg of white powder (10% yield). ^{1}H NMR (D_2O) δ (ppm): 7.92 (s, 1H, H_9), 7.23 (t, 1H, H_2, J = 8 Hz), 6.75 (dd, 1H, H_3, J = 8 Hz, 2.3 Hz), 6.75 (d, 1H, H_1, J = 8 Hz), 6.68 (t, 1H, H_4, J = 2.3 Hz), 4.64 (m, 2H, H_{11}), 4.45 (m, 2H, H_{10}), 3.26 (s, 2H, H_8); ^{13}C NMR (D_2O) δ (ppm): 158.17, 154.43, 140.05, 137.48, 129.90, 125.41, 118.5, 108.81, 103.72, 82.26, 49.27, 40.67. HRMS (ESI^+): calcd. for $C_{13}H_{14}FN_7O$ (M+H) 304.1317, found 304.1323. IR (v, cm-1) 3307 (O-H), 3201, 3178 (N-H), 2244 (C≡N), 1498 (C=N), 1011, 670 (C-F). Purity was confirmed by UV-HPLC using method E (Table 8, Section 1.19.1), as shown in Figure 33.

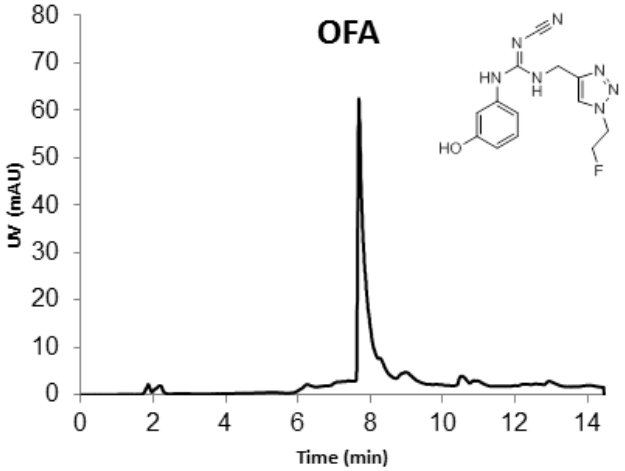

Figure 35 RefOFA purity

1.15.22 2-Cyano-1-(4-fluorobenzyl)-3-(quinolin-5-yl)guanidine (RefEFB)

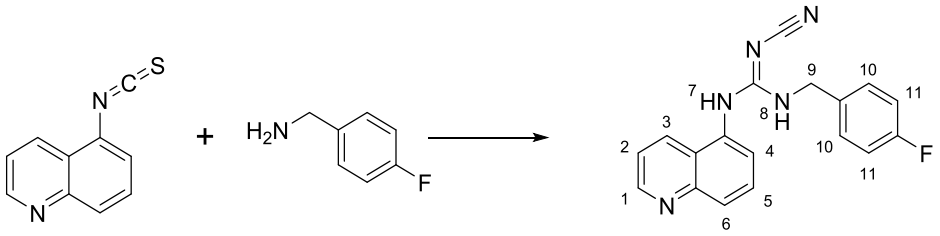

RefEFB
$C_{18}H_{14}FN_5$
Exact Mass: 319.1233
Molecular Weight: 319.3434

A mixture of 0.62 mL 4-fluorobenzyl amine (5.36 mmol) and 1.12 mL triethylamine (8.04 mmol) was added to 5-isothiocyanato-quinoline (1g, 5.36 mmol) in anhydrous THF (25 mL) and stirred for 1 h at room temperature. Following addition of mercury acetate (5.36 mmol) and then sodium hydrogencyanamide (16.08 mmol), the mixture was stirred for 24 h until dark black. The sluggish mixture was filtered under reduced pressure through a short pad of celite and was washed with acetone (30 mL). The filtrate was concentrated by rotary evaporation and purified by flash chromatography with a gradient of 0.8:10:0 – 1:10:0 – 1:7.5:2.5 methanol/diethyl ether/ethyl acetate. The product was then dried by rotary evaporation and recrystallized from acetone. 2-cyano-1-(4-fluorobenzyl)-3-(quinolin-5-yl)guanidine was isolated as a white powder in 8% yield (140 mg). ^{1}H NMR (MeOD) δ (ppm): 8.94 (dd, 1H, H_1, J = 4 Hz, 1.6 Hz), 8.29 (dd, 1H, H_3, J = 8 Hz, 1.6 Hz), 8.17 (d, 1H, H_4, J = 8.6 Hz), 7.88 (dd, 1H, H_5, J = 8 Hz, 8.6 Hz), 7.67 (d, 1H, H_6, J = 8 Hz), 7.64 (dd, 1H, H_2, J = 8 Hz, 4 Hz), 7.37 (dd, 2H, H_{11}, J = 5.4 Hz, 7.7 Hz), 7.07 (dd, 2H, H_{10}, J = 5.4 Hz, 7.7 Hz), 6.96 (s, 1H, H_8), 4.47 (s, 2H, H_9). HRMS (ESI$^+$): calcd. for $C_{16}H_{15}FN_8$ (M+H) 339.1477, found 339.1501; calcd. for (M+Na) 320.1306, found 320.1307. IR (v, cm^{-1}): 2181 (C≡N), 1706 (guanidine C=N), 1509 (N-CN), 1025 (C-F). Purity was confirmed by UV-HPLC using method J(Table 8, Section 1.19.1), as shown in Figure 33.

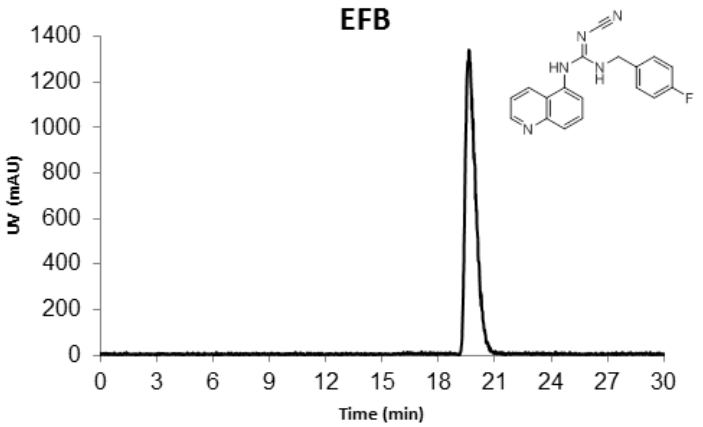

Figure 36 RefEFB purity

1.15.23 4-Cyano-N,N,N-trimethylanilinium tri-fluoromethanesulfonate (4-TBACN)

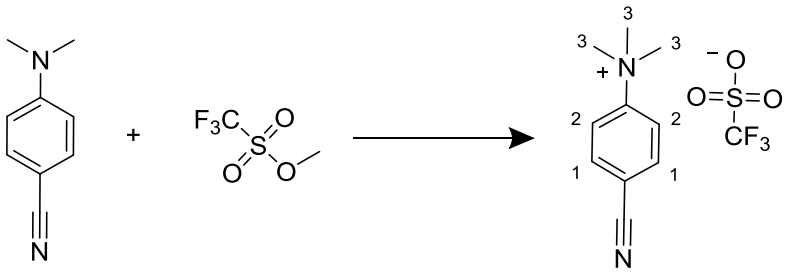

4-TBACN
$C_{11}H_{13}F_3N_2O_3S$
Exact Mass: 310.06
Molecular Weight: 310.29

This method was previously reported in Haka *et al.*[431] 4-(dimethylamino)-benzonitrile (2.43g, 16.6 mmol) and methyl trifluoromethanesulfonate (2.1 mL, 18.3 mmol) were dissolved in DCM (30 mL) under an inert atmosphere. Upon overnight stirring under argon at room temperature the solution turned cloudy. The precipitate was collected by vacuum filtration, washed with ethyl acetate and recrystallized in MeOH/EtOAc to give the product as pale yellow crystals in 10% yield (0.562 g). ^{1}H NMR (400 MHz, D_2O): 8.01 (s, 4H, H_1-H_2), 3.65 (s, 9H, H_3). ^{13}C NMR (400 MHz, D_2O): 134.67, 121.17, 56.84. IR (v, cm^{-1}): 2242 (C≡N), 1500 ($^{+}$N-R_4), 1260, 1161 (SO_2-O), 1025 (C-F).

1.16 Discussion

In this work, the synthesis of trisubstituted cyanoguanidines is inspired by Donnelly-Roberts *et al.*[229] This protocol consists of a one-pot mercury-assisted substitution at the carbon centre of an isothiocyanate of both *(S)*-(-)-1-(4-bromophenyl)ethylamine and sodium cyanamide in anhydrous THF. The reaction is described to proceed under mild conditions and a short reaction time. In our hands, the reaction was repeated under the same conditions with the indole isothiocyanate analogue INCS as starting material, successfully producing in 28% yield the trisubstituted cyanoguanidine indole product IMBB (see experimental and Figure 23 for structures).

1.16.1 Synthesis of QPB and EFB

The same protocol was employed for the synthesis of the *para*-benzyl boronic ester substituted guanidine analogue QPB and the *para*-benzyl fluoride analogue EFB (Figure 37).

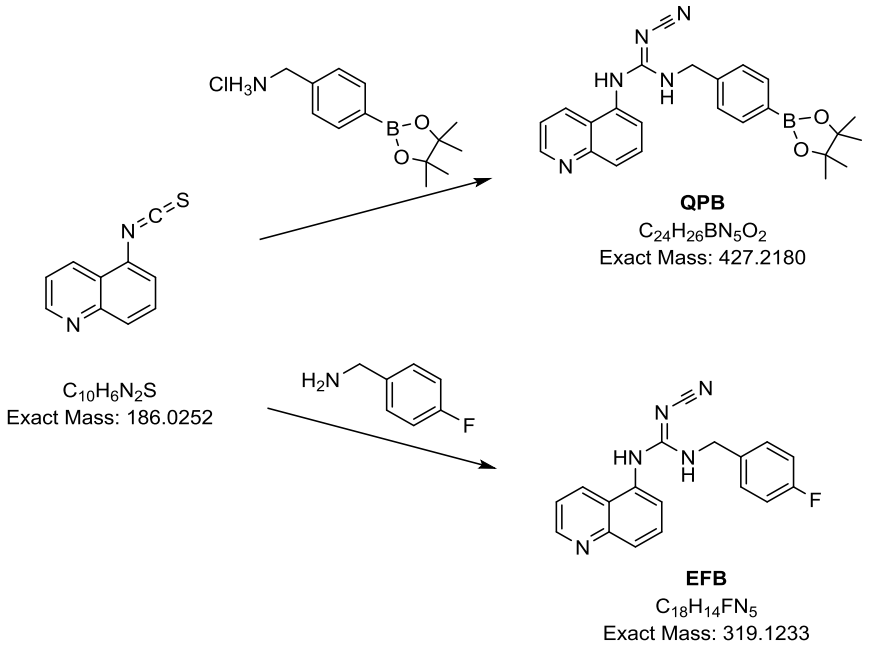

Figure 37 QPB and EFB synthetic scheme.

In both cases, the reagents showed quantitative conversion by TLC (20:4:1 ethyl acetate/hexane/triethylamine) and LC/MS, indicating good tolerance of mercury catalysis by the benzyl boronic ester moiety. However, while the HPLC purification method described in Donnelly-Roberts *et al.*[229] failed to yield more than 1% product, flash chromatography afforded higher yields. This could be further improved by recrystallization of impure fractions in acetone.

1.16.2 Introduction to QYL synthesis

Only few successful syntheses of terminal alkyne-substituted cyanoguanidines have been reported to date.[432-435] All these reactions share a similar mechanism involving cyanocarbon imidate formation in alcoholic solvents, which are problematic in terms of solubility for the scaffolds in question. Additionally, all present remarkably differently functionalised R groups on the LHS N-terminus compared to the aromatic groups of the structures under scrutiny. Therefore, the Donnelly-Roberts protocol[229] appeared more closely related despite the lack of alkyne substituents. Despite the success in synthesising the previously described trisubstituted cyanoguanidines *via* this method, significant refinements proved to be necessary to prepare the propargyl quinoline-substituted analogue QYL, the aniline-substituted analogue AYL and the phenol-substituted analogue OYL (see Figure 23 for structures). A number of chemical differences between these species and the benzyl guanidine species should be noted. Firstly, propargyl groups are more susceptible to deprotonation by a base than benzyl groups. In particular, cyanoguanidines can act as bases (Figure 38), possibly with the assistance of metal coordination to the triple C–C bond.

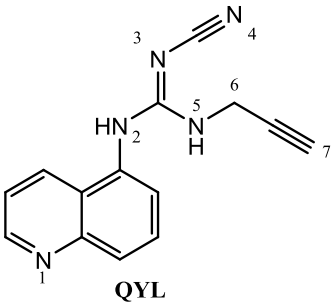

QYL

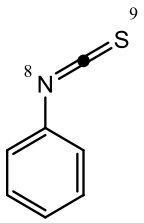

ANCS

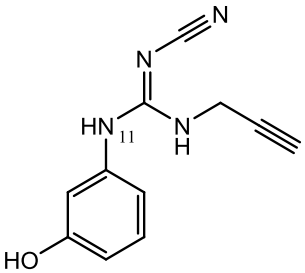

OYL

Atom	N1	N2	N3	N4	N5	C6	C7	N8	S9	O10	N11
pKa	**4.4**	**23.9**	**-8.3**	**N/A**	**1.8**	**24.5**	**24.6**	**23.9**	**-8.3**	**8.8**	**24.3**

Figure 38 pKa estimates for reagent and product hydrogen-accepting or donating atoms.

[1] Estimates based on University of Kentucky's ChemAxon software. Acidity and basicity values were calculated with the ACE modification of the JChem formula.

Secondly, the product QYL could cyclise given the proximity between the nitrile, the imine and the alkyne unsaturations. Thirdly, propagylamines mix well with all other reagents, whereas acetylenic cyanoguanidines are not soluble in most solvents, except for high boiling polar aprotics. Finally, the stability of the intermediates may vary, as π-π interactions might favour benzyl-aryl to alkyne-aryl proximity.

This chapter outlines all approaches explored, as shown in Figure 39, and speculates as to why several attempts resulted unsuccessful. Table 5 is also provided as a guide to the large body of work that went into the optimisation of this reaction.

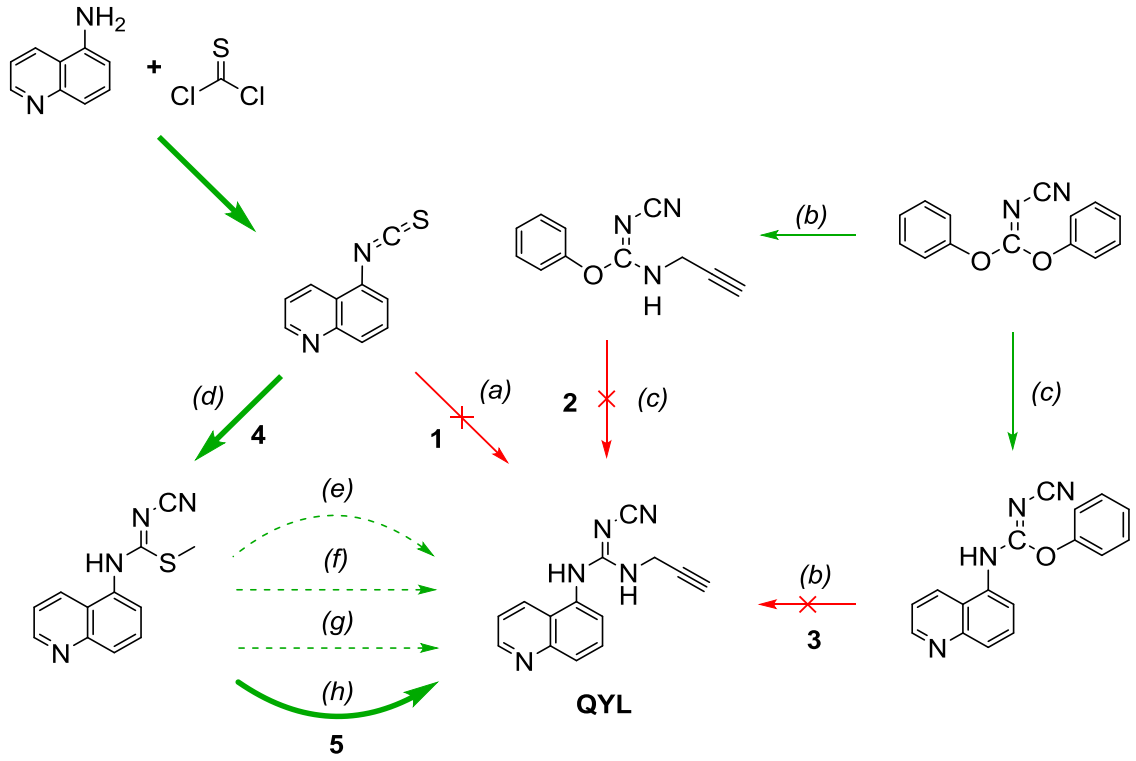

Figure 39 Scheme describing all routes attempted to synthesise precursor QYL

Table 5 Summary of reactions leading to the production of trisubstituted guanidines.

Starting material	Product	Conditions	Yield	Notes
INCS	IMBB	Stoichiometric $Hg(OAc)_2$	28%	
QNCS	QPB	Stoichiometric $Hg(OAc)_2$	18%	FCC purification
QNCS	EFB	Stoichiometric $Hg(OAc)_2$	8%	FCC purification
QNCS	QYL (direct route)	Stoichiometric $Hg(OAc)_2$	0%	
QNCS	N,N',N''-cyanopropargyl- 2-bromo-4-pyridinyl guanidine	Stoichiometric $Hg(OAc)_2$	0%	
QNCS	QYL	rt or reflux, with NEt_3 and $Hg(OAc)_2$	0%	FCC purification
DPCI	QYL	with/without MW and PPh_3	0%	Intermediate disubstituted guanidine formation observed with both PA and 5-aminoquinoline
DPCI	QN_3	With/without MW	0%	As above
QNCS	QSMe	rt, then MeI trapping	70%	FCC purification
QSMe	QYL	Stoichiometric $Hg(OAc)_2$, THF	4.2%	Double FCC purification
QSMe	QYL	Stoichiometric $Hg(OAc)_2$, DCM	Traces	Double FCC purification
QSMe	QYL	Stoichiometric $Hg(OAc)_2$, Et_2O	6.5%	Double FCC purification
QSMe	QYL	Stoichiometric $Hg(OAc)_2$, neat with NEt_3	0%, violent reaction	
QSMe	QYL	Neat with NEt_3 with/without $Hg(OAc)_2$ or $ZnCl_2$, 25-80°C and 0-150 min.	See HPLC conversion analysis below	Non isolated
QSMe	QYL	Neat with NEt_3, no catalyst, MW, 50°C, 1h	35%	Evaporation, then FCC purification
QSMe	QYL	Neat with NEt_3, no catalyst, MW, 50°C, 1h	89%	Hot filtration
ANCS	AYL (*via* ASMe)	Neat with NEt_3, no catalyst, MW, 50°C, 1h	>99%	Hot filtration
ONCS	OYL (*via* OSMe)	Neat with NEt_3, no catalyst, MW, 50°C, 1h	>99%	No purification required

1.16.3 Attempted 1-step mercury-assisted QYL synthesis

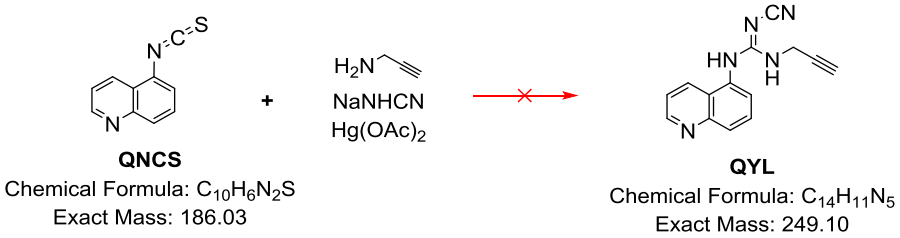

QNCS
Chemical Formula: $C_{10}H_6N_2S$
Exact Mass: 186.03

QYL
Chemical Formula: $C_{14}H_{11}N_5$
Exact Mass: 249.10

Figure 40 Scheme describing the mercury-assisted route to synthesise QYL.

The Donnelly-Roberts reaction protocol was applied to the propargyl analogue QYL but LC/MS inspection of the crude indicated a failure in obtaining the correct product even after heating the mixture at reflux overnight. A large extent of degradation was visible by TLC (1:4:5 methanol/hexane/ethyl acetate) and was not found to be due to silica sensitivity, as assessed by 2D TLC. All products were isolated by FCC for further analysis but none of the masses corresponding to each TLC spot could be matched with a plausible side reaction. It is possible that extensive degradation had been occurring over time and that any or a combination of guanidine substituent migration, formation of three membered ring structures and expulsion of nitrogens had been taken place.[436].

The reaction was repeated with pure and fresh starting materials. The mixture was kept in an inert atmosphere, shielded from light and kept at <30°C. 1 eq. triethylamine was also added to the mixture to ensure full deprotonation of the propargylamine and act as secondary catalyst.[437] However, no product was formed as determined by LC/MS of the crude, although TLC (1:2 ethyl acetate/hexane) indicated exhaustion of the starting 5-isothiocyanato quinoline and a lower extent of product degradation. Following addition of $Hg(OAc)_2$ and NaNHCN, a new spot at R_f 0.47 was isolated by flash chromatography and analysed by LC/MS. Frustratingly, the masses obtained could again not be associated to any plausible side reaction. The most likely culprit was postulated to be the alkyne functional group characteristic of this reaction, or its combination with mercury and other functionalities present in the compound. However, given the lack of plausible explanations for the observed reactivity, a different route to yield the product was sought.

1.16.4 Further attempts to QYL synthesis

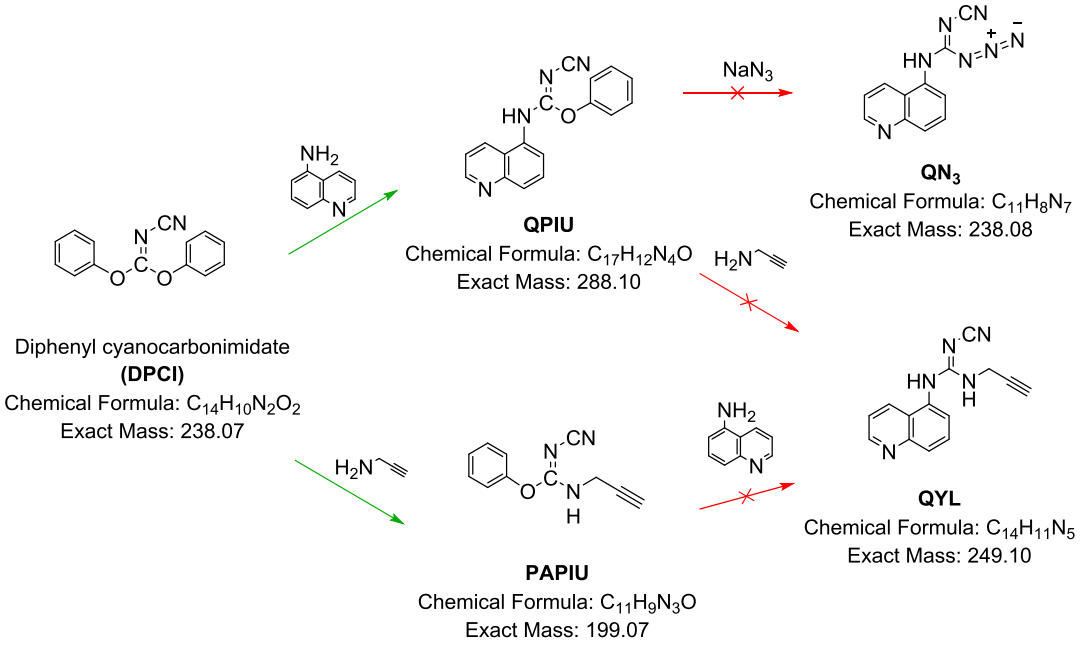

Figure 41 Scheme describing further routes to synthesise QYL.

In order to circumvent the issues caused by the synthesis of the cyanoguanidine fragment, the stepwise amine addition to a cyanocarbon imidate as described for compounds 12a and 31 in Buschauer *et al.* was investigated.[415] In this publication, a variety of different electron rich and electron poor amines are tested, affording yields >50%. The procedure involves the initial formation of a urea intermediate after 2 h room temperature mixing in acetonitrile before continuing to full guanidine formation in methanol or ethanol. In our hands, initial quinoline addition to form the intermediate QPIU was inspected by TLC (1:1 ethyl acetate/hexane, R_f DPCI: 0.82, R_f 5-aminoquinoline: 0.25, R_f propargylamine with NEt_3: 0.49; R_f QPIU: 0.91) and LC/MS (QPIU MS (ESI^+) m/z 289.1094 $(M+H)^+$) indicating successful product formation. However, addition of the second amine did not yield QYL as desired following overnight room temperature stirring or heating to reflux. This could be explained by the possible high steric and electronic hindrance prohibiting propargylamine access to the diaryl urea carbon in the intermediate. In line with this argument, no reports of aryl amine addition in good yields were found in the literature. Additionally, alkyl-aryl π- π interactions might have prevented the propargylamine approaching the urea. Nonetheless, attempts to functionalise with an azide the RHS guanidine substituent with 1 eq. sodium azide resulted in no reactivity after overnight stirring at room temperature and heating for a further hour.

Additionally, in an attempt to corroborate the steric hindrance hypothesis, the effect of stepwise addition of propargylamine prior to aminoquinoline was investigated. The intermediate akyl-urea PAPIU could be observed by TLC (1:1 ethyl acetate/hexane, R_f PAPIU: 0.64) and LC/MS (PAPIU MS (ESI^+) m/z 200.0834 $(M+H)^+$). However, subsequent addition of 1 eq. 5-aminoquinoline under argon did not yield the desired product overnight at room temperature nor after 1 h reflux (reaction monitoring: TLC, LC/MS).

At this point, it appeared that steric hindrance was unlikely the key impediment to the desired reactivity. Rather, it appeared that the removal of the second phenol could be improved by the use of a stronger driving force, such as the formation of a P=O bond in presence of 1 eq. triphenylphosphine.[419] Nevertheless, after 2 h reflux or 1 h microwave heating at 120°C, 300W in DMF, no reactivity was observed by LC/MS or TLC.

1.16.5 QYL synthesis *via* the QSMe intermediate

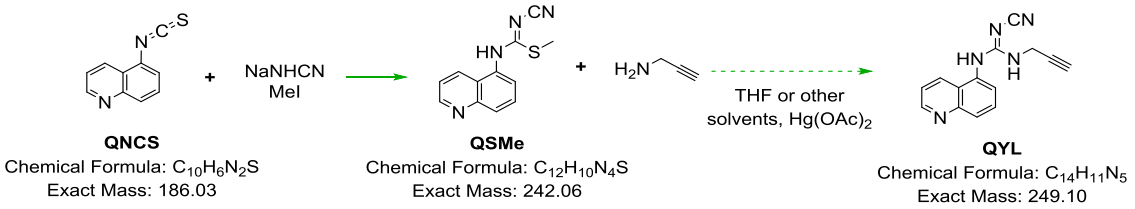

Figure 42 Scheme describing the QSMe route for the synthesis of QYL.

Given the difficulty in driving the substitution of the second phenol group, the leaving group was substituted with a methyl thiol. This functional group was shown to be easily removable by precipitation as a mercury salt.[421] This approach required the synthesis of the intermediate thiourea QSMe, by a protocol also described within the patent. In this reaction, the primary amine attacks the isothiocyanate at the δ+ carbon. Rather than proceeding with a second conjugate substitution as in the previous synthetic strategy, the sodium salt is trapped with methyl iodide in high yield (Figure 43).

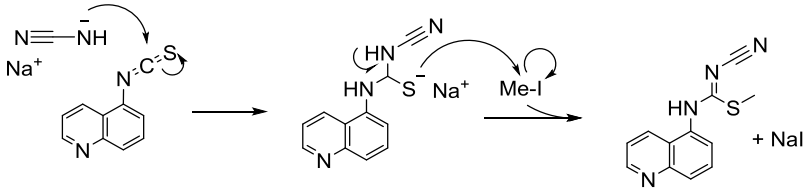

Figure 43 QSMe reaction mechanism.

The synthesis of QYL then proceeded with the attack of the thiourea carbon and the release of methyl thiol. An examination of the literature suggested to employ either mercury acetate or triethylamine catalysis,[421] although Betschmann *et al.* reported on several occasions the use of zinc chloride catalysis or no catalysis at all [391, 392, 438]. In our hands, the reaction was initially performed in a 100 mg scale in the presence of mercury acetate, as the reaction appeared mechanistically simpler. After stirring as a suspension at 40°C for 48 h in anhydrous THF, TLC analysis (1:1 ethyl acetate/ DCM, QSMe R_f 0.31, QYL R_f 0.18) showed depletion of the starting material and LC/MS detected the product QYL (found: $(M+H)^+$ 250.1098, $(M+Na)^+$ 272.09). Double flash chromatography (1-5% methanol in DCM, then 4:1-2:1 ethyl acetate/ DCM) was necessary to isolate the product obtaining just trace amounts. Scaling up the production also did not yield more than 44 mg (4.2% from 1 g starting material) of pure product. Finally, in order to increase the dissolution of the reagents the reaction was attempted first in DCM, then in diethyl ether. The latter improved the yield to 6.5% starting from a 150 mg scale. A neat reaction in solvating propargylamine was also attempted, although violent mercury acetate reactivity with the latter was observed.

TLC analysis showed that extensive byproduct formation was present in the crude product both when performed with silica, alumina and neutral silica as stationary phases, suggesting a lack of involvement of the analytical procedure in the decomposition process. Consequently, low yields were imputed to two reasons: the reaction was producing extensive unknown byproduct alongside the desired product (hence the need of extensive isolation steps) and the purification procedure was suboptimal and prone to product loss. In order to tackle the first issue, a way to monitor more closely than by TLC spot formation or LC/MS mass appearance the formation of the desired product had be introduced. Having isolated a small amount of product, an HPLC method suitable for the identification of the starting materials propargylamine and QSMe, the product QYL, and the formation of byproducts could be designed (HPLC method: 150 x 4.6 mm 150 x 4.6 mm Agilent Zorbax C18 column; 1 mL/min flow; A: water with 0.1% TFA; B: methanol with 0.1% TFA; gradient: 5% B for 3 min, then ramp to 95% B over 7 min and 2 min at 95%. Inverse ramp to 5% in 1 min and then 5% for 3 min. Injection as 50:50 methanol/water filtered solution. QSMe Rt: 13.56 min; QYL Rt: 13.92 min). Although the separation achieved was sub-

optimal and the propargylamine was not eluted as a single peak, the compounds could be distinguished when monitoring the reaction under different conditions and when assessing the effect of different workups. The section that follows lists the data collected from the HPLC analysis, which led to improved reaction and workup conditions.

1.16.6 QYL synthesis: optimisation of reaction conditions by HPLC monitoring

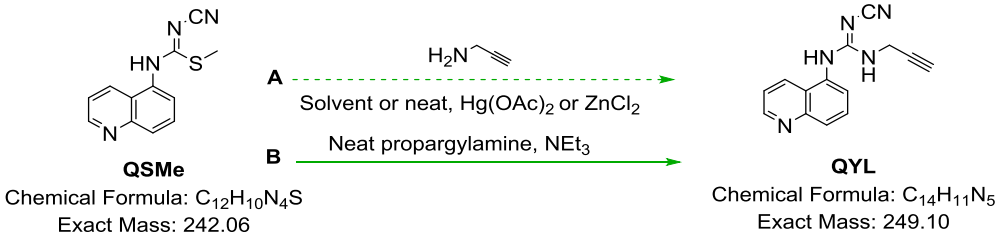

Figure 44 Scheme describing the two routes employed to optimise the synthesis of QYL.

The aim of this optimisation work was to maximise the amount of QYL (product) by identifying which conditions would lead to maximum conversion of the reagents, regardless of the extent of byproduct formation. Previous attempts at this reaction had in fact shown that the reaction proceeded slowly and already after a short time presented byproducts detectable by TLC. The variation of reagent HPLC peaks was monitored to analyse the composition of the crude reaction mixtures.

All reactions were performed in a microwave reactor at 300 W, as the same extent of byproduct formation had been observed, but with much shorter reaction times than in the case of conventional heating. Secondly, all reactions were performed with 2 eq. triethylamine and in neat propargylamine, aside from the mercury catalysed reaction which was performed in diethyl ether due to near propargylamine-mercury acetate incompatibility. Four different HPLC peaks were analysed: the starting material, QSMe, eluting at 13.5 min; the product, QYL, eluting at 12.6 min; and two byproducts eluting at 12.3 min and 14 min. Reaction time, temperature and the effect of catalysis were investigated. As can be seen from the graphs (Figure 45), the conversion varied considerably over time, reaching its peak at 60 min and 20 min for the catalyst-free and mercury catalysed reactions, respectively, whereas at later time points decomposition outweighed product formation. Instead, the zinc catalysed reaction displayed a continuous increment in yield, yet reaching about half the maximum yield of the neat reaction

after 90 min. Analysis of the product yield at 60 min and 40°C showed that the absence of transition metal catalysis could provide enhanced conversion rates compared to the mercury catalysed case. Zinc catalysis instead, resulted in intermediate conversions (Table 6).

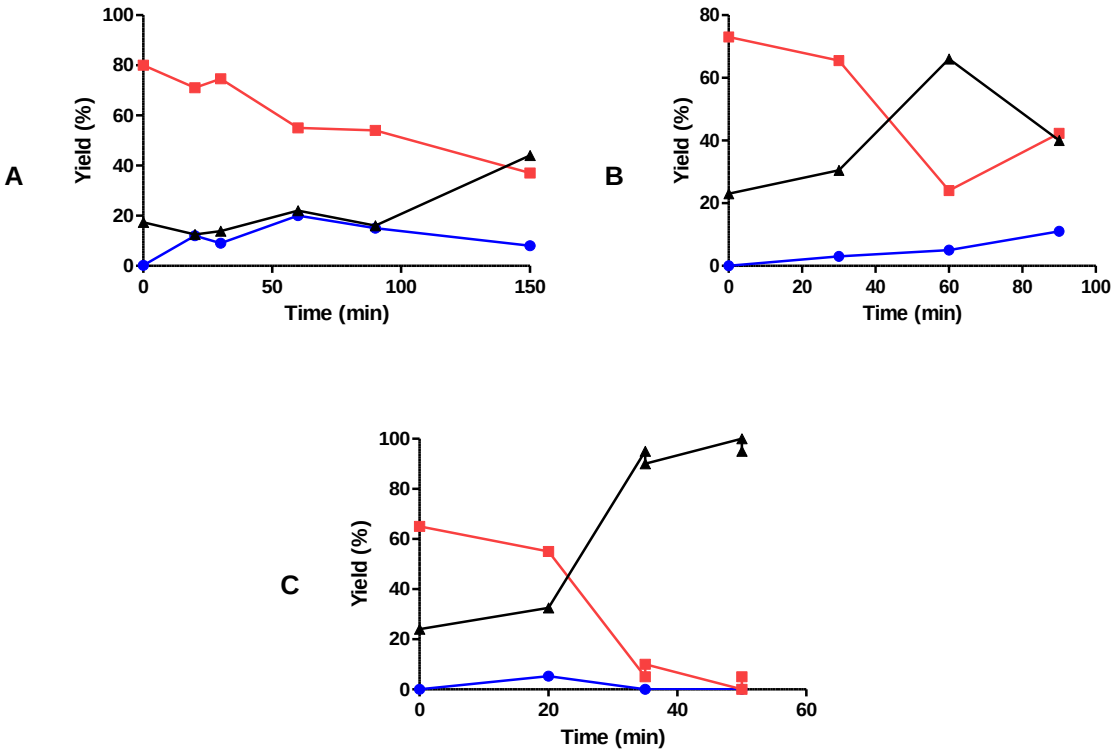

Figure 45 Effect of time and catalysis on the conversion rate of QSMe to QYL

Table 6 Effect of catalysis on the QYL conversion rates

Reaction conditions at 40°C and 60 min microwave	Reaction yield (QYL %)	Leftover starting material (QSME %)	Other products (%)
Neat in triethylamine	20	55	25
Zinc chloride catalysis, in THF	5	24	71
Mercury acetate catalysis, in THF	0	5	95

The observed effect is probably due to a detrimental side reaction between mercury and the alkyne moiety (Figure 46). Compared to mercury, zinc is a harder metal, hence less attracted to soft alkynes. Nonetheless, its double positive charge is still capable of desulfurisation.[439] Triethylamine could instead catalyse the reaction by both assisting in propargylamine deprotonation and methyl sulfide protonation (Figure 47). Moreover, while zinc and mercury act as stoichiometric byproduct precipitation agents, triethylamine would be regenerated at each desulfurisation cycle, and would therefore be acting as an actual catalyst.

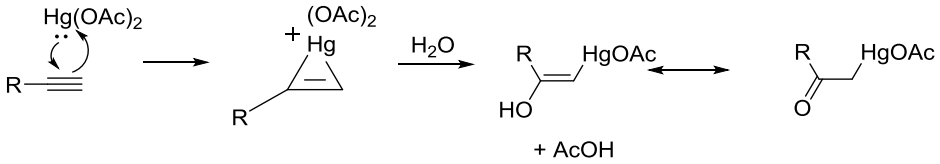

Figure 46 Possible side reaction

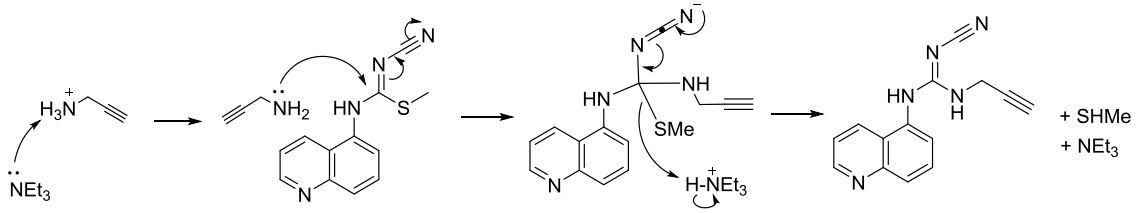

Figure 47 Proposed triethylamine catalysed conjugate substitution mechanism

The effect of temperature variation on the conversion rates was then analysed. Upon heating the reaction mixture in a microwave reactor at 300 W for 60 min between 40°C and 80°C, product formation peaked at 50°C. The product then was degraded or decomposed linearly, giving rise to higher byproduct formation.

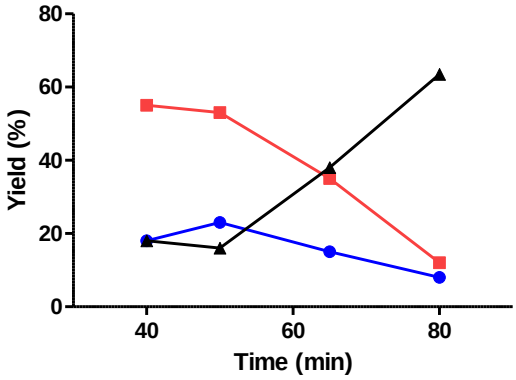

Figure 48 Effect of temperature on the conversion rate of QSMe to QYL

In conclusion, despite the identification of the byproducts was unsuccessful, ideal conditions to maximise product formation were devised by HPLC analysis of the crude mixtures. Thus, it was found that without metal catalysis at 50°C, microwave heating at 300 W for 60 min could afford maximal product formation.

1.16.7 QYL synthesis: optimisation of the purification procedure

In the previous attempts, the isolation of the desired product was performed by flash chromatography, with considerable product losses and poor overall yields. QYL suffers from poor solubility in most solvents other than partially in a combination of DCM and methanol and fully only in DMSO or DMF. Hence, purification by flash chromatography was unsuitable. HPLC also was not ideal. A 10 mg scale fraction of the celite-filtered crude could be dissolved in MeOH, diluting in water to a 30:70 methanol/water 9 mL solution and then filtering the precipitates. This method remained applicable only to such small scale purifications. Starting from the analytical method, the HPLC method was scaled up proportionally to a 150 x 21 mm, 5 µm, C18 Hypersil silica Thermo Scientific column, achieving optimal separation with a 5-30% 0.1% TFA methanol gradient in 0.1% TFA over 20 min at 20 mL/min. However, predictably, the freeze-dried collected fractions resulted only in sub-milligram amounts of product, rendering this procedure inefficient and time-consuming.

Interestingly, it was observed that precipitation occurred in the crude metal catalyst-free neat reaction mixture after cooling the reaction mixture in a long and narrow microwave tube. It was therefore deduced that the poor solubility of the product could be exploited as a means of purification. The precipitate was only mildly insoluble in the crude supernatant, as a thick suspension was forming upon shaking. Both precipitate and supernatant were analysed by TLC and HPLC. The precipitate was found to contain >90% of the desired product, but also several impurities. After allowing the residual propargylamine to evaporate overnight, the precipitate was purified by flash chromatography, obtaining the pure product in 35% yield. However, the poor solubility of the precipitate greatly reduced the yield.

As an alternative method, recrystallisation was attempted by exploiting the product's mild solubility in alcoholic solvents. Addition of nearly boiling ethanol to the precipitate lead to a yellow ethanolic solution and to a white precipitate. This was possibly due to the decreased solvent-solute interaction. Upon isolation of the white precipitate, nearly boiling water was added to the hot ethanolic supernatant. This induced further precipitation, which upon cooling lead to the combined isolation of the pure product in up to 89% yield. The protocol was later simplified to the version described in the experimental section.

1.16.8 Synthesis of AYL and OYL

The extensive work carried out on the quinoline compound of the XYL series proved fruitful also for the synthesis of its analogues. AYL was synthesised in solventless conditions with excess propargylamine and with triethylamine in a microwave reactor under the same conditions as QYL. This afforded quantitative conversion. Following removal by evaporation of propargylamine, the compound could then be isolated in high yields by recrystallization in ethanol and water. It is interesting to note this compound's higher solubility in ethanol, probably an effect of the altered polarity induced by the reduction in aromaticity and the decrease in molecular size. Finally, OYL was synthesised in the same conditions as above, but afforded a clean product which did not require further purification.

1.16.9 Synthesis of EFA, AFA and OFA (collectively XFA)

The precursor was not found to be soluble in any solvent other than DMF and DMSO. This ruled out the widespread literature use of ^{t}BuOH.[441, 442] Instead, the closer related Glaser protocol was adopted.[410] Monitoring of the reaction progression was executed by LC/MS and TLC (10:1:1 DCM/ethyl acetate/methanol). Among the variety of methods reported for copper alkyne azide cycloaddition chemistry,[410, 441, 443, 444] maximum conversion rates were achieved by heating at 80°C for 40 min in a microwave reactor and by washing with DCM/weakly alkaline water to remove the DMF prior to flash chromatography. However, product loss was high both in the DMF extraction procedure and in the flash column chromatography, due to partial solubility of the product in water and the low solubility in the organic solvent. This resulted in an imperfect protocol, yet sufficient to isolate and identify the product required. A similar procedure was employed for the rest of the XFA compound series with similarly moderate yields. This reaction can certainly be improved with additional work, particularly by iteratively exploring a range of temperatures and times of reaction and by exploring other purification methods.

1.17 Conclusions

In this chapter the synthesis and purification of all the novel materials that constitute this work was presented. Extensive part of the discussion concerned compound QYL, the synthesis and optimisation of which is complex. While a detailed study would be necessary to further elucidate

why many of the attempted synthetic routes to QYL failed, it is apparent that mercury is incompatible with propargylamine. Solubility issues with both the thiourea starting material as well as the trisubstituted guanidines in most solvents often times lead to poor conversions. Neat reactant mixtures were finally adopted, employing an excess of the liquid propargylamine both ensuring good catalysis and solvation. However, the product was not afforded in good yields until hot filtration was identified as a most convenient purification methodology affording >80% product. This novel synthetic strategy is much more robust than the original method and was able to afford in a straightforward manner the related compounds AYL and OYL.

Finally, the synthesis of all cold reference standards was presented. Despite the modest yields which call for further work particularly in the purification stages, sufficient amounts of products could be isolated for the characterisation and biological evaluation of the tracers.

Chapter 4

Radiochemistry

Radiochemistry

This chapter concerns the radiochemical manipulations necessary to synthesise the target radioactive molecules and the context in which these radiosynthetic techniques lie within.

1.18 Introduction to the radiochemistry of [^{18}F]fluoride

Radiofluorination chemistry dates back to 1948 when Cady and co-workers devised ways to catalytically radiolabel hypofluorite compounds such as trifluoromethylhypofluorite and explored the radiosynthesis of xenon hexafluorite.[445] Since then, interest in radiofluorination has maintained a steady pace. To date, the most widely utilised PET radiotracer is the ^{18}F-labelled glucose analogue [^{18}F]FDG, used to image cell metabolism. Yet, many other fluorinated radiotracers are employed in the clinic. To name a few, [^{18}F]FLT is used to track cell proliferation in oncology; [^{18}F]FMISO is used to image tissue hypoxia; [^{18}F]fallypride is a high affinity dopamine receptor antagonist while [^{18}F]haloperidol is the labelled version of a drug targeting a range of neurotransmitter receptors to control psychosis.

^{18}F can be produced in the form of electrophilic fluorine [^{18}F]F_2 from either ^{20}Ne(d, α)^{18}F or ^{18}O(p, n)^{18}F.[446] The reactivity of this synthon is very strong, which results in low radiofluorination selectivity. Moreover, the production of [^{18}F]F_2 usually involves the addition of carrier fluoride, resulting in much lower specific activities than for nucleophilic fluoride. Despite the advent of post-target production of F_2[447] and the development of milder and more regioselective electrophilic fluorinating reagents[249, 448, 449] have substantially advanced this field, nucleophilic fluorination is to date a more widespread and versatile technique to incorporate radioactive fluorine into chemical structures and it is the radiolabelling methodology of choice throughout this work. Nucleophilic [18F]fluoride is produced in a cyclotron by irradiation of [^{18}O]H_2O with high energy particles. The resulting aqueous radiofluoride produced is highly solvated by water molecules, which renders it a poor nucleophile. Trapping on cation exchange cartridges and elution with alkali metal cations complexed to a phase transfer catalyst, such as the cryptand Kryptofix-222 (K222) leads to much higher nucleophilicity of this radionuclide, making it suitable to carry out radiofluorinations. Alternatively, elution with tetrabutylammonium hydrogen carbonate gives [^{18}F]TBAF, also a strong nucleophile.[450]

1.18.1 Nucleophilic aromatic radiofluorinations

This and the following section focus on describing the current landscape of nucleophilic fluorinations, which are at the heart of this project (Figure 49). Nucleophilic fluorinations can be further divided in direct and indirect fluorinations, the latter which indicate the labelling of a fragment with ensuing incorporation into a more complex scaffold. We will start by exploring direct nucleophilic fluorinations at aromatic rings, then to move to aliphatic structures.

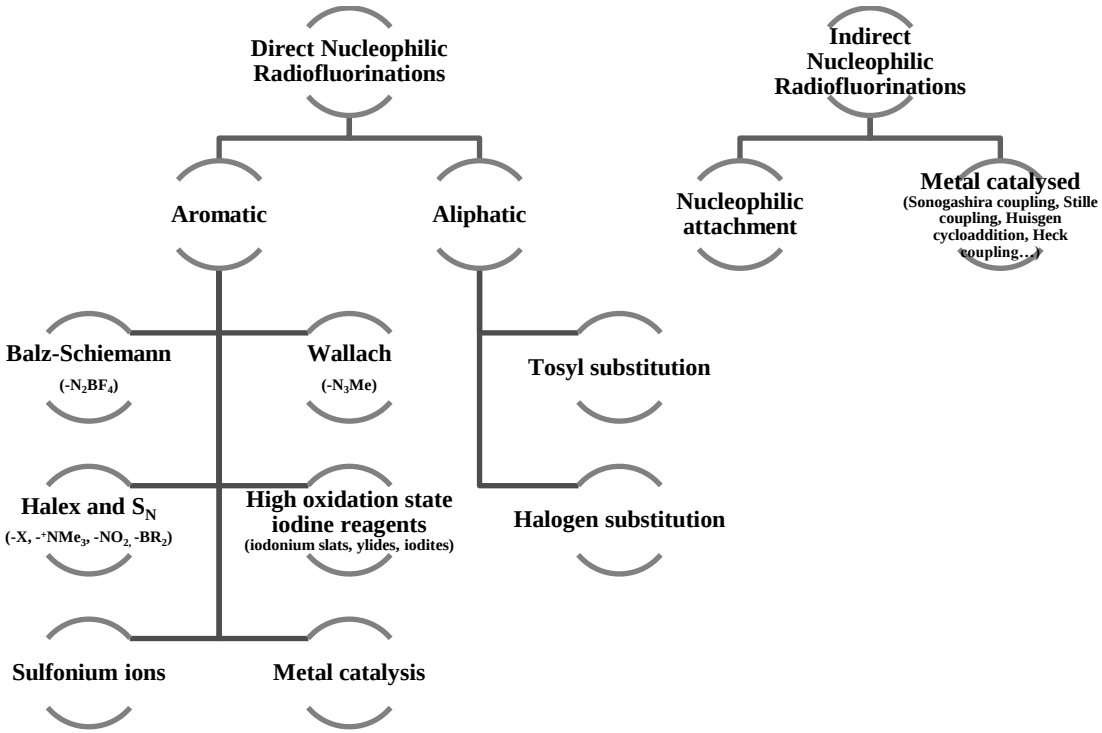

Figure 49 Types of nucleophilic fluorinations discussed in this chapter

Nucleophilic aromatic fluorinations traditionally involve the use of good leaving groups. Initial attempts at performing radiofluorinations in the 80s involved the use of the Balz-Schiemann reaction and the Wallach reaction (Figure 50). Both leveraged the strong leaving group ability of diazide-containing groups.[451] However, both produced low radiochemical yields (RCYs) or specific activities due to presence of carrier fluoride in the reactant.

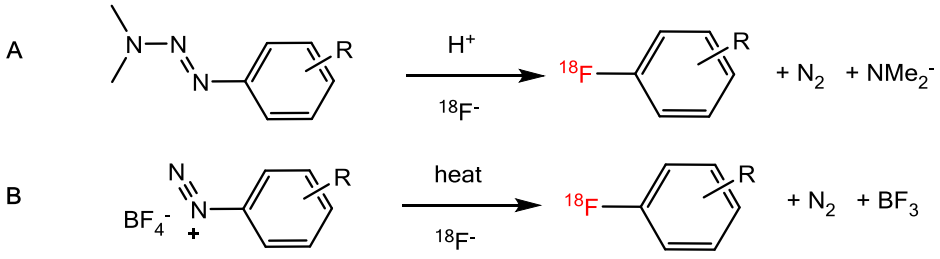

Figure 50 Wallach and Balz-Schiemann reaction

These reactions were soon outperformed by more efficient nucleophilic substitutions: an electronic pull by electron withdrawing substituents in the *ortho* or *para* positions is capable of promoting substitution of the leaving group by resonance stabilisation of the anionic intermediate (Figure 51). Electron withdrawing substituents are not always desirable, but they can be either removed or transformed to chemically useful functional groups to introduce molecular complexity in the scaffolds. The most widely used leaving groups for such purpose are the trimethylammonium,[452-455] nitro[456-458] and halogen.[459-462]

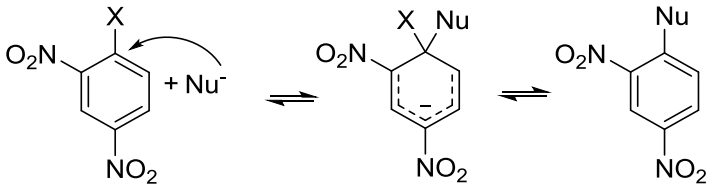

Figure 51 The nucleophilic substitution mechanism

Each of these methods has its own advantages and limitations. Trimethylammonium salts are high yielding, and the product is easily separated from the leaving triethylamine group. However, this and all other methods in this series require high temperatures and can be unsuitable for delicate substrates.[463] Fluorination of aromatic rings with *meta* leaving groups require even harsher conditions or proceed only with the use of microwave irradiation.[464] More commonly, synthons and prosthetic groups are employed to circumvent degradation issues or byproducts of the precursor (Figure 52).[465]

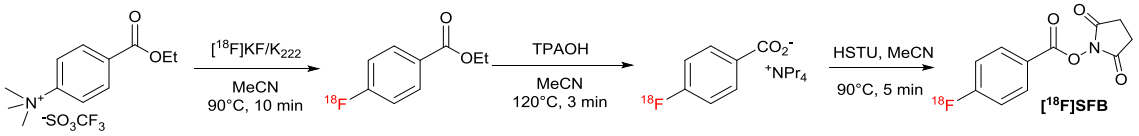

Figure 52 Example of synthon strategy: synthesis of [^{18}F]SFB *via* an [^{18}F]fluorobenzoate synthon

The most widely used aromatic synthons are the trimethylammonium- and nitro-benzonitrile and benzaldehyde groups, although also ketones and halides are commonly exploited for indirect synthesis.[466] The chemical simplicity inherent to these groups enables straightforward labelling. Nevertheless, many further chemical modifications of the resulting radiolabelled molecules are possible, including reductions, oxidations, halogenations and functionalisations with entirely new substituents, making the synthesis of an extensive array of radioaryl compounds possible. Among these, indirect palladium-mediated aromatic radiofluorinations are common. For

example, *para*-fluoroiodobenzene can undergo a Sonogashira coupling with terminal alkynes,[467] a Stille coupling with organotin compounds[468-471] and a Suzuki coupling with boronic acid-functionalised rings.[472]

Moreover, there is extensive research on the use of iodonium salts for radiofluorinations. Attractive from the point of view of the amenability of radiolabelling of electron neutral and electron-rich aryls, iodonium salt radiofluorinations can yield radioactive fluoroarenes in high specific activity (Figure 53a).[473] However, the precursors' stability wanes when functional substitutions are introduced to the aryl rings. So far, this represents the major limitation to their use.[474] Extensive research into synthetic routes to aryliodonium salts has found that electron rich arenes such as anisoles, thiophenes, arylstannenes and arylborates lead to high fluorinating regioselectivity, especially when combined with specific diaryliodonium counterions,[475] while the use of inorganic hypervalent iodonium salt reactants can facilitate their synthesis. The often poor stability of the latter has driven the field in the direction of one-pot precursor syntheses, as detailed in a recent review by Merritt and Olofsson.[476]

Further oxidation of the iodine to iodonium ylides further expanded the application of the hypervalent iodine radiofluorinations.[477] These species demonstrate moderate-to-high RCYs and good stability (Figure 53b).[478] The spirocyclic ylides (Figure 53c) developed in the Vasdev group at the Massachusetts General Hospital at Harvard University also appear relatively straightforward to synthesise, virtually removing all barriers to this electron-rich aromatic radiofluorination route,[479] the exception being primary amine-functionalised rings. Similarly, a recent patent on the radiofluorination of iodyl benzene derivatives (iodites) reported higher yields with a range of electron-donating and electron-withdrawing groups and excellent specific activities.[480] This route has also the advantage of appearing more straightforward than other iodine routes. Harsh radiofluorination conditions are necessary, however, despite this, applications have started to crop up in the literature (Figure 53d), though again, this labelling strategy is not viable for hydrogen-donating (primary or secondary) amines.[411]

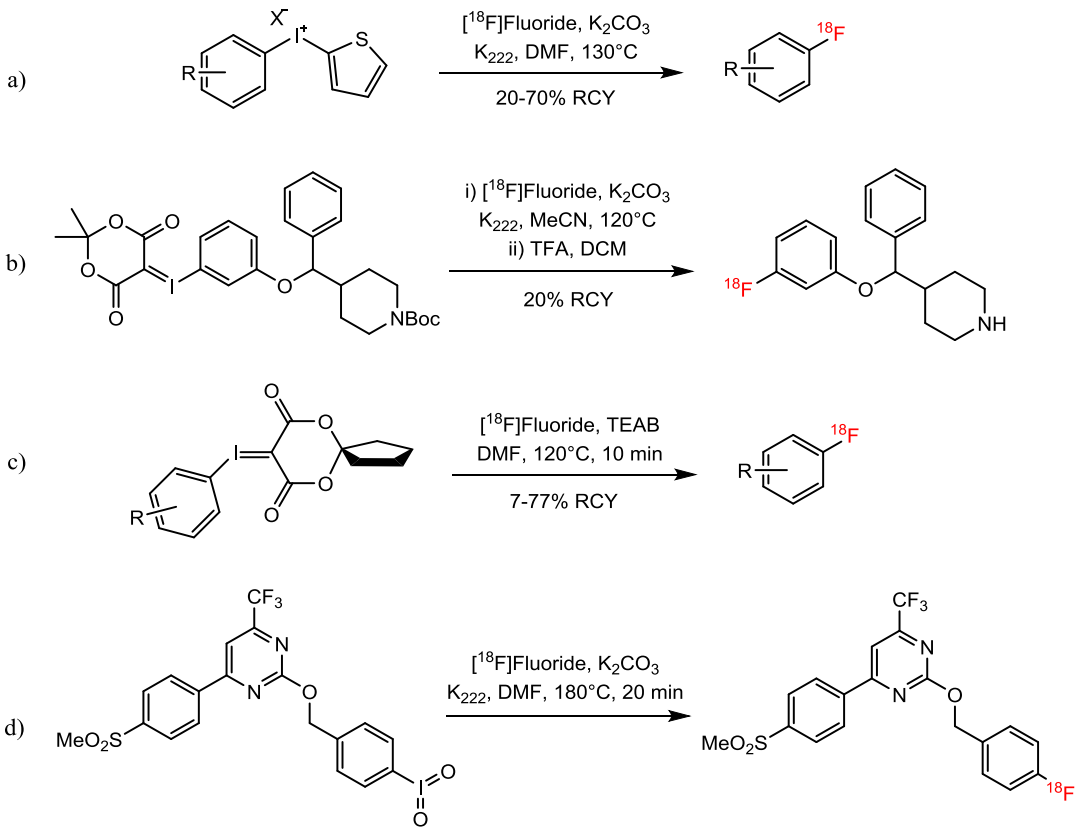

Figure 53 Reactions of aryl iodonium salts and iodonium ylides with ^{18}F

Despite the apparent large variety of methods available, problems still arise in the presence of electron rich aromatic rings, such as phenols and anilines. For this reason the generation of novel radiofluorination methods continues, including a spree of recent developments. Only a few notable and relevant examples will be described hereafter, while a detailed analysis of the current aromatic radiofluorinations landscape can be gathered from several recent reviews.[474, 481-483]

The Gouverneur group at the University of Oxford published a study in 2014 showing that [^{18}F]aryl fluorides can be formed under conditions that tolerate a vast array of functional groups.[484] Starting from boronic esters, the copper complex [Cu(py)$_4$]OTf$_2$ is used to catalyse the desired radiofluorination within 20 minutes in DMF at 110°C. This reaction is particularly interesting as a wide selection of boronic esters is available commercially; the reaction is compatible to air and oxygen, and gives high specific activity products. However, its main limitation is the necessity of using conspicuous amounts of precursor. Moreover, once more primary amines and alcohols pose a problem to the radiochemical substitution, with yields dropping to 5-7% and recovering only when protecting groups are in place.

Another valuable contribution is the work done by the Årstad group at University College London on radiofluorination of sulfonium ions (Figure 54).[485] Previous studies on sulfonium ions highlighted its potential as a precursor, without significantly managing to increase the appeal of the reaction due to feasibility issues.[486-488] In this route, amines are tolerated, although the nucleophilicity of the ^{18}F fluoride is susceptible to the presence of H-donors, leaving primary and secondary amine-functionalised aryls once more out of reach. The synthesis of the precursor requires an intermediate, poorly stable iodinium salt, which needs to be consumed rapidly for the formation of the much more stable sulfonium ion.

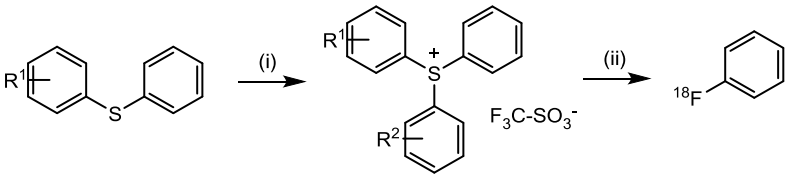

Structure	R	Temp (°C)	N.i. RCY (%)	DC RCY (%)
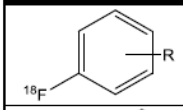	2-COOCH3	110	80±5	65±1
	H	150	40±4	13±2
	H	150	40±5	17±2
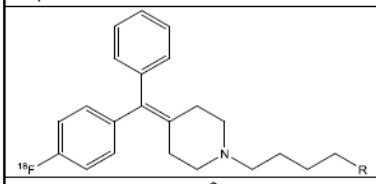	OCOOCH3	110	29	n/a
	OH		n/a	9±3
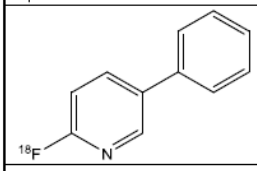	-	110	84±8	54±9
	-	50	80±8	51±2
	-	25	68±8	41±1
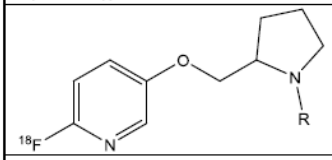	Boc	110	77	n/a
	H		67±5	51±5
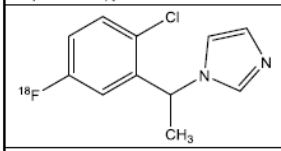	-	110	31±2	20±2
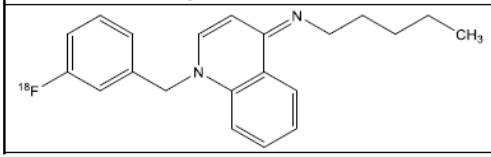	-	120	47±6	30±6

Figure 54 Sulfonium ion fluorinations

RCYs are moderate to high for a range of functional groups, and remarkably so for electron-rich aromatic rings.

Finally, a method to fluorinate aromatic rings relying on the use of nucleophilic fluoride coupled with metal catalysis has been developed. The latter offers enhanced rates of radiolabelling, as well as reactivity, selectivity and substrate diversity. The method is a palladium-catalysed aromatic fluorination developed by Hooker and Ritter (Figure 55A).[489] This is effective in a variety of aromatic substrates, including electron rich rings. However, the catalyst requires an involved synthesis and it is air sensitive and unstable over time, thus requiring fresh preparation before each use. Additionally, difficulties in the translation of this method have been reported by the developers. These have prompted them to investigate a water-tolerant arylnickel complex as an alternative catalyst, which – in the presence of an oxidant and under mild conditions – is able to yield. C-^{18}F bonds in short reaction times (Figure 55B).[490]

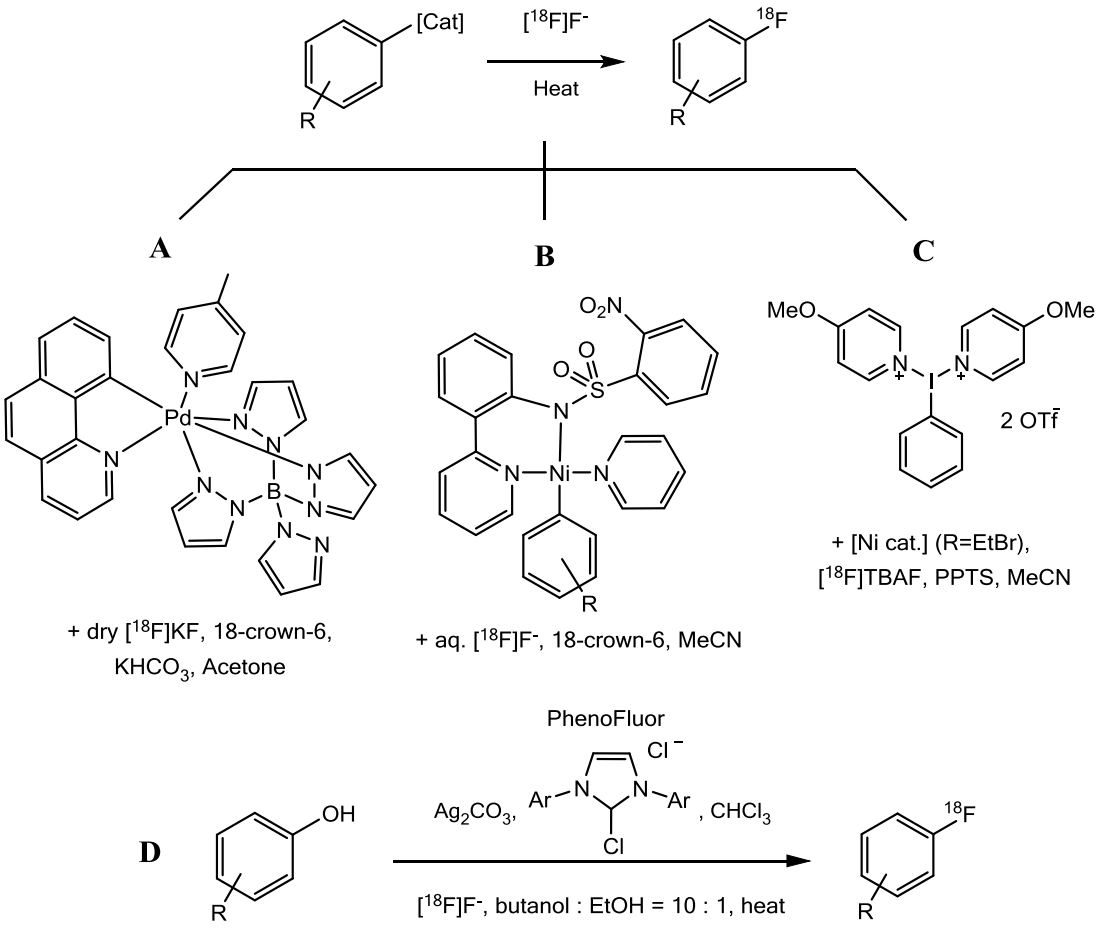

Figure 55 Metal-catalysed aromatic fluorination In particular, the use of the oxidant-compatible reagents [^{18}F]TBAF and pyrodonium *p*-toluenesulfonate (PPTS) has opened up this method to large scale radiosyntheses and has demonstrated translational potential (Figure 55C).[491, 492] The future also awaits the advent of synthetically simpler catalysts, such as Ag_2NO_3, which has been

very recently shown to be effective in deoxyradiofluorinations of phenols in the presence of the reagent PhenoFluor (Figure 55D).[493]

1.18.2 Nucleophilic aliphatic radiofluorinations

Unlike aromatic substitutions, for aliphatic radiofluorinations and indirect aliphatic labelling, activating groups are not usually required, provided a good leaving group is present. Consequently, where multiple good leaving groups are present in a molecule, each may be susceptible to nucleophilic fluoride attack, thus requiring protection to direct the labelling. A classic example of aliphatic fluorination is [^{18}F]FDG: the radioactive atom is introduced by substitution to the triflate activated 2-hydroxyl group. In order to drive selectivity, acyl protection and deprotection of the other hydroxyl groups is employed.[494]

Short aliphatic structures however are particularly attractive from a radiosynthetic viewpoint as they allow the introduction of ^{18}F into more complex molecules *via* indirect labelling. A common use is the labelling of a ditosyl, dibromo or diiodo aliphatic chain, where the first leaving group serves as an ^{18}F attachment point, whereas the second provides a site of attachment to the nucleophilic part of a more complex structure.[495] Of a similar nature is the use of monotosyl, bromo or iodo chains, functionalised with an azide group at the opposite end. These fragments are ideal for indirect ^{18}F Huisgen 1,3-dipolar cycloaddition or “click” radiofluorination, a reaction widely exploited in this work. The radiochemical version of this reaction first appeared in the literature in 2006, as a quick and efficient method to tag peptides with fluorine radiolabels.[496] This work relied on the use of CuI catalysis, a base and a reducing agent (sodium ascorbate) to link [^{18}F]fluoroalkynes (produced in 36-81% RCYs) to peptides. The final labelled peptides were obtained in 54-99% yields and high radiochemical purity (RCP) in 30 min.

Since then, click radiochemistry became a very popular field, mostly for peptide and protein radiolabelling with either CuI, in situ reduced $CuSO_4$ or Cu powder as source of copper for catalysis.[497, 498] Moreover, strained cycloalkynes and norbonenes have been shown to have sufficient energetic affinity for tetrazines to undergo intermolecular cycloadditions without the need for copper catalysis.[499-501] Worthy of special mention to exemplify the versatility of click reactions in radiochemistry are a set of high specific activity radiolabelled RGD peptides which target tumour integrin $\alpha_v\beta_3$ synthesised in 52% N.D.C. RCY with copper alkyne-azide

cycloadditions (CuAACs). In 2007, a robust method for the synthesis and cycloaddition of the fragment [^{18}F]fluoroethyl azide to a range of small alkyne-functionalised molecules and a model peptide was devised.[410] This was widely employed in the following years to radiolabel a wide variety of candidate PET tracers.[502-504] Moreover, strain-promoted copper-free click chemistry was used to prepare a number of tumour targeting radiofluorinated bombesin probes.[505] This demonstrated not only the ease with which click chemistry can be applied to radiochemistry, but also that it enables the facile introduction of a wide array of functional groups and to fine tune a compound's hydrophilicity, both which need to be explored to ensure optimal target binding. Similarly, click chemistry can be applied to radiometal labelling *via* the introduction of a metal chelate and a linker. This technique was widely employed to label peptides with ^{64}Cu, ^{111}In, ^{99m}Tc, ^{68}Ga, ^{89}Zr and other metals,[506-509] including aluminium, which in turn can bind an ^{18}F ion.[510] Finally, click chemistry has been shown to work directly on target (*in vivo* bioconjugation), whereby an azide tagged antibody can be engineered to reach a specific biological species and then be labelled selectively by its radiolabel-bearing biorthogonal conjugate.[511, 512]

In recent years, several other reactions have been explored that enable the indirect aliphatic fluorination of a variety of organic molecules *via* the use of metal catalysts, ranging from the simple to the complex. Several interesting radiosynthetic advancements have been made in the area of metal-catalysed allylic fluorination reactions. An iridium[513, 514] and a palladium catalytic system[515] have both been shown to label linear, branched, aromatic, aliphatic and functionalised allyls with RCYs around 50%. Recently, a new method has become available to introduce chiral labels into aliphatic moieties. The Doyle group at Princeton University reacted racemic epoxides with chiral cobalt [^{18}F]fluoride catalysts under mild conditions, achieving >85% ee with moderate-to-high RCY.[516] Previously, enantiomeric labelling relied on the isolation of the desired enantiomer prior to the radiolabelling and radiolabelling from the corresponding cyclic sulfonates[517] or by selective displacement of differentially protected diols.[518]

Finally, the Groves lab at Harvard University recently introduced a manganese-catalysed method to introduce an ^{18}F label upon disruption of a C-H bond.[519] This method is air stable and

due to the relative chemical similarity between fluorine and hydrogen (with all the caveats discussed in chapter 2, section 1.7.2), it is a very promising method for high throughput productions of radiopharmaceuticals from cold pharmaceutical screening hits. The major issues with this method lie in the separation of the final product from the hydrogen-containing starting material and in the susceptibility of alkyl fluorides to *in vivo* dehydrogenation.[345]

1.18.3 Radiosynthesis in this work

The radiosynthetic reactions performed in this work are outlined in Figure 56. Please refer to this figure also as a legend for abbreviated compound names, whereas the complete IUPAC nomenclature of all compounds can be found in the experimental section of this chapter.

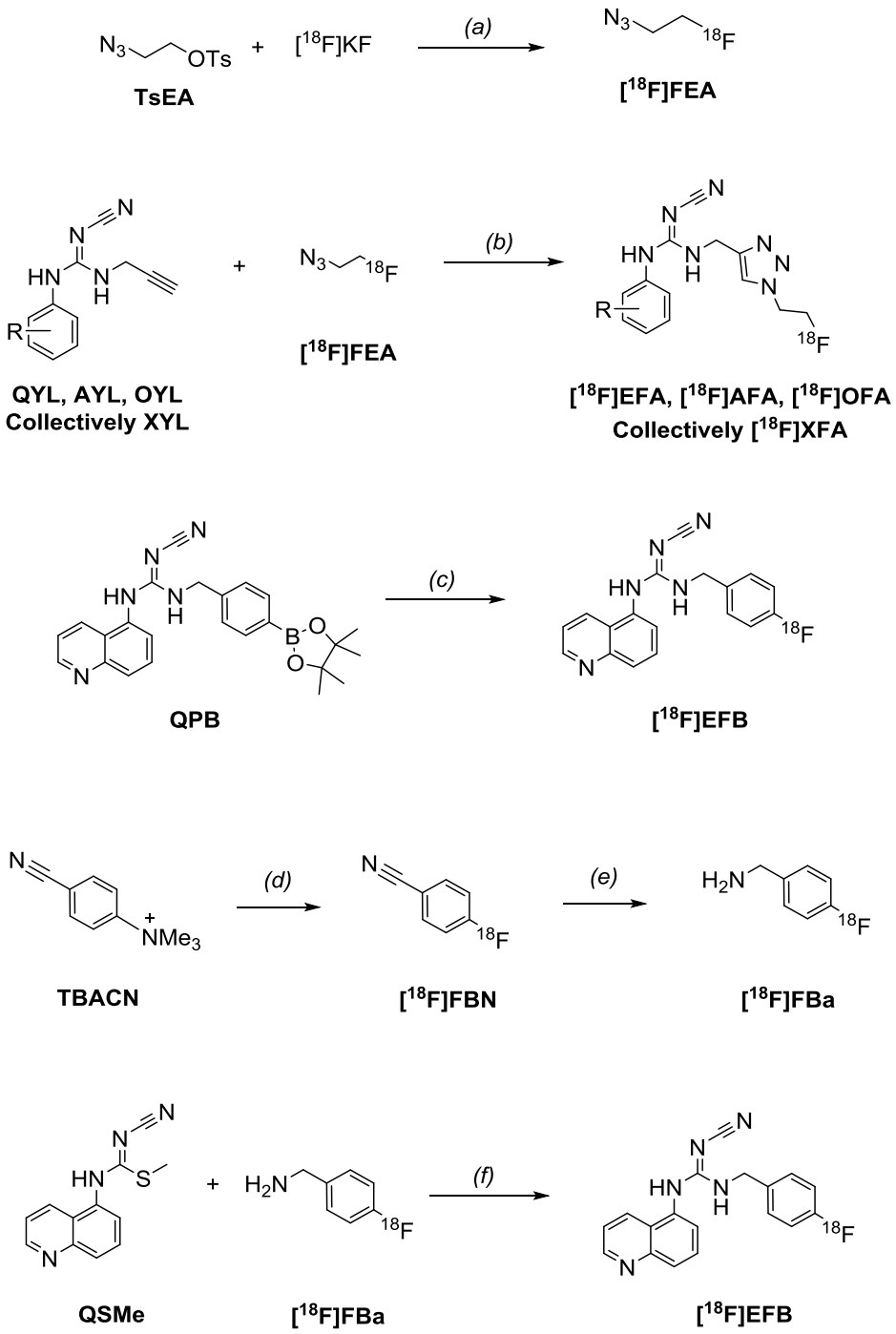

Figure 56 Radiosynthesis in this work

1.18.4 Radiochemical nomenclature

Often times, confusion arises as to the exact meaning of certain radiochemical terms due to the variety of terms employed by the scientific community for each parameter. To prevent such misunderstandings, Table 7 summarises the intended meaning of a set of sometimes ambiguous terms.

Table 7 Radiochemical nomenclature and concepts employed within this chapter.

Abbreviation	Full term	Description
Hot	Radioactive	Radioactive compound.
Cold	Non-radioactive	Non-radioactive compound.
AUC	Area under the curve	Integration of the area delimited by a peak in an HPLC chromatogram, after background subtraction.
N.D.C. RCY	Non decay-corrected radiochemical yield	Percentage of radioactive product versus total radioactive starting material from start of synthesis, irrespective of its radioactive decay.
D.C. RCY	Decay-corrected radiochemical yield	Percentage of radioactive product versus total radioactive starting material from start of synthesis, corrected for its radioactive decay.
n.i. RCY	Non-isolated radiochemical yield	Analytical HPLC-derived percentage of the areas under the curve of the crude radioactive product versus the radioactive starting material indicated in each context. Sometimes it is referred to as “conversion” in the text.
RCP	Radiochemical purity	Analytical HPLC-derived percentage of radioactive product area under the curve versus total area under the curve.
QC run	Quality control run	Analytical HPLC of the product aimed at determining the final chemical and radiochemical purity of the radiotracer, its identity and its specific activity.
SA	Specific activity	Tracer radioactivity per mole of compound as defined by the area under the curve of the carrier product in the UV chromatogram of a QC run. The area under the curve is converted in mass units by the use of a compound-specific calibration curve.
EOB	End of bombardment	Time at which the cyclotron target bombardment is concluded and the resulting radioactivity is dispensed to a hot cell.
SOS	Start of synthesis	Time at which the first radiochemical manipulation is performed.
EOS	End of synthesis	Time at which the last radiochemical manipulation is performed.
Synthesis time	Synthesis time	Time from SOS to EOS.

Table 7 (continued)

Abbreviation	Full term	Description
Cold standard co-injection	Cold standard co-injection	Radiotracer HPLC injection mixed with cold tracer standard.
Carrier-added reaction	Carrier-added reaction	Radiochemical reaction competing with an analogous cold reaction due to the presence of an added cold radiosynthon-equivalent substance (in this context $K^{19}F$ instead of $K^{18}F$). This practice enables the characterisation of products and byproducts by LC/MS.

1.19 Materials and methods

All materials and methods are described in chapter 3, with the following modifications.

The HPLC and LC/MS apparatuses were equipped with a FC-3200 NaI/photomultiplier tube (PMT) LabLogic detector. Column parameters, mobile and stationary phase are specified in the text. Radioactive TLCs (ITLCs) were developed with the methods specified in the text and analysed on a Bioscan Flow-Count ITLC scanner equipped with a FC-3600 Plastic Scintillator/PMT LabLogic detection probe. Spectra were recorded and analysed with Laura 4 (LabLogic). HPLC column specifications: Kinetex Phenomenex XB-C18 with guard, 4.6 x 150 mm, 5 µm, 100 Å; Agilent Eclipse XDB C18, 9.4 x 250 mm, 5 µm, 100 Å. Solid phase extraction (SPE) cartridge specifications: Sep-Pak light lC18 Short SPE, 130 mg, 55-105 µm (cat. no. WAT023501, Waters), Sep-Pak tC18 Plus Long SPE Cartridge, 900 mg, 37-55 µm (cat. no. WAT036800, Waters), Sep-Pak Accell Plus QMA SPE Cartridge, 130 mg, 37-55 µm (cat. no. WAT023525, Waters), Strata-X-CW, 200 mg/3 mL, 33 µm (cat. no. 8B-S035-FBJ, Phenomenex), Oasis HLB Plus Short SPE Cartridge, 225 mg, 60 µm (cat. no. 186000132, Waters).

All reactions were performed in 3 mL or 5 mL Wheaton V-vials, except for the microwave reactions, performed in microwaveable tubes and reactions >110°C were 16 x 125 mm borosilicate tubes with PTFE/silicone-lined screw caps (Sigma Aldrich).

1.19.1 Chromatographic methods

Throughout the project much time was devoted to the development of HPLC methods. A typical method development workflow is showed in Figure 57. On a given column, initial gradient scouting for organic molecules is performed with a programmed increase in organic solvent

content (%B) in water or buffer. If the peak(s) elute away from the solvent front, an isocratic method is run at the observed %B at which elution occurs. For peak(s) that elute with the solvent front, the initial %B is lowered while maintaining the chosen ramp, then the ramp steepness is decreased until the peak(s) are separated from each other/the solvent front. Peaks are then further resolved by, in order, lowering the %B, modifying the temperature, switching organic solvent or altering the flow rate. Moreover, for unresolved peak(s) or peak(s) with variable retention times, the isoelectric point is sought and the compound is buffered accordingly. In all instances, the pressure is maintained constant during injections.

In this work, the use of acetonitrile was preferred to methanol due to the better solubility of the compound series in the former solvent and due to the possibility of evaporating it together with water by azeotropic distillation. Moreover, where applicable, SPE cartridge elution in methanol was found to be less effective than in acetonitrile. All HPLC methods developed are shown in Table 8 and reflect the progressive improvements in the analysis and purification of each compound.

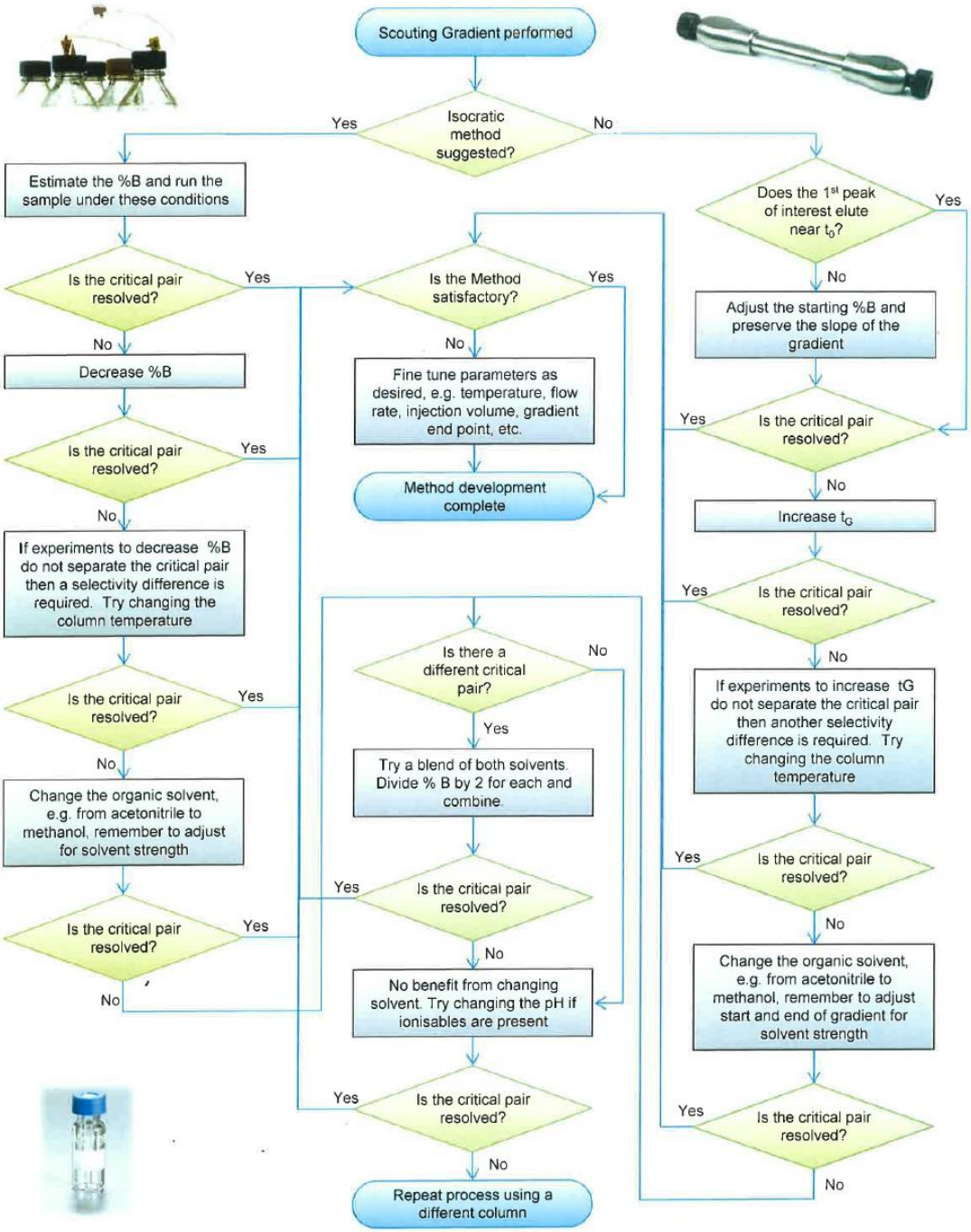

Figure 57 HPLC method development strategy flow chart

Method	Compound	Analytical HPLC				Semi-preparative HPLC			
		Solvents	Mobile phase gradient	Flow rate and column	R_t	Solvents	Mobile phase gradient	Flow rate and column	R_t
A	**[^{18}F]FEA**	A: H_2O B: MeCN	3 min 5% B; 7 min ramp 5-95% B; 2 min 95% B; 1 min ramp 95-5% B; 1.5 min 5% B.	1 mL/min, Kinetex or 5 mL/min, Semiprep Eclipse if column switch was impractical	7:00 min with both methods	A: H_2O B: MeCN	20%-50% B over 22 min; 50-20% B over 3 min.	3 mL/min, Semiprep Eclipse 9.4 x 250mm	9:30 min
B	**[^{18}F]EFA**	A: H_2O B: MeCN (both with 0.1% FA for LC/MS)	3 min 5% B; 7 min ramp 5-95% B; 2 min 95% B; 1 min ramp 95-5% B; 1.5 min 5% B.	1 mL/min, Kinetex	8:30 min	A: 25mM NaH_2PO_4 B: MeCN	5-20% B over 2 min; 20-50% B over 16 min; 50% B for 1 min; 50-5% in 1 min.	4 mL/min, Semiprep Eclipse 9.4 x 250mm	8:20 min
C	**[^{18}F]EFA**	A: H_2O B: MeCN	Isocratic 15% B for 20 min; 15-80% B for 5 min; 80% B for 5 min; 80-15% for 2 min.	0.4 mL/min, Kinetex	14:30 min	A: 25mM NaH_2PO_4 B: MeCN	Isocratic 15% B for 18 min; 15-30% B for 7 min; 30% for 5 min.	4 mL/min, Semiprep Eclipse 9.4 x 250mm	11:10 min
D	**[^{18}F]AFA**	A: H_2O B: MeCN	3 min 5% B; 7 min ramp 5-95% B; 2 min 95% B; 1 min ramp 95-5% B; 1.5 min 5% B.	1 mL/min, Kinetex	8:10 min	A: 25mM NaH_2PO_4 B: MeCN	Isocratic 30% B for 1 min; 30-50% B for 9 min; 50-30% B for 2 min; 30% B for 1 min.	5 mL/min, Semiprep Eclipse 9.4 x 250mm	3:40 min
E	**[^{18}F]OFA**	A: H_2O B: MeCN	3 min 5% B; 7 min ramp 5-95% B; 2 min 95% B; 1 min ramp 95-5% B; 1.5 min 5% B.	1 mL/min, Kinetex	7:50 min	A: 25mM NaH_2PO_4 B: MeCN	25% B for 1 min; 25-55% B for 14 min; 55% for 0.5 min; 55-25% for 1.5 min; 25% for 1 min.	5 mL/min; Semiprep Eclipse 9.4 x 250mm	3:50 min
F	**[^{18}F]OFA**					A: 25mM NaH_2PO_4 B: MeCN	Isocratic 15% B for 12 min; 15-80% B for 8 min; 80% for 10 min; 80-95% for 1 min; 95% in 4 min; 95-15% in 5 min.	4 mL/min; Semiprep Eclipse 9.4 x 250mm	11:30 min

Table 8 RadioHPLC methods

Table 8 (continued)

Method	Compound	Analytical HPLC					Semi-preparative HPLC			
		Solvents		Mobile phase gradient	Flow rate and column	R_t	Solvents	Mobile phase gradient	Flow rate and column	R_t
G	[^{18}F]EFB	A: 0.1% TFA H_2O	B: MeCN	1 min 5% B; 9 min 5-95% B; 2 min 95% B; 2 min 95-5% B; 1.30 min 5% B.	1 min/mL, Kinetex	8:10 min				
H	[^{18}F]EFB	A: pH 6.2 phosphate	B: MeCN	14 min 10-90% B ramp; 1 min 90% B; 90 sec 90%-10% ramp.	1 mL/min, Kinetex	8:50 min	A: H_2O	B: MeCN	15% for 5 min; 15%-35% ramp for 1 h; 35% for 2 min; 35%-20% for 2 min; 20% for 1 min.	3 mL/min, Semiprep Eclipse 9.4 x 250mm	51:10 min
J	[^{18}F]EFB	A: H_2O	B: MeCN	30 sec at 20% B ; 23.5 min 20%-33.5% ramp ; 3 min 33.5%-70% ramp ; 2min 70% ; 1 min 70%-20% ramp.	1 mL/min, Kinetex	19:10 min	A: H_2O	B: MeCN			

1.19.2 Radiotracer calibration curves

Specific activities were determined via the use of compound-specific calibration curves. Defined concentrations of pure non-radioactive compounds were prepared and serially diluted. A minimum of 3 concentrations were analysed in duplicate by analytical HPLC methods B (EFA), D (AFA), E (OFA) and J (EFB). The best linear fit was then found with MS Office Excel resulting in the calibration curves and respective equations shown in Figure 58. The latter were then utilised to derive the specific activity of each experimental run, given a specific injected volume in the HPLC. During the calibration curve data acquisition it was particular important to ensure that prior to each run the internal HPLC pressure was stable, that the columns were thoroughly clean and that the injected samples were thoroughly dissolved and at the correct dilution. Finally, it is useful to note that the UV activity of the carrier EFB in most experimental [^{18}F]EFB runs was below the detection limit of 300 GBq/µmol.

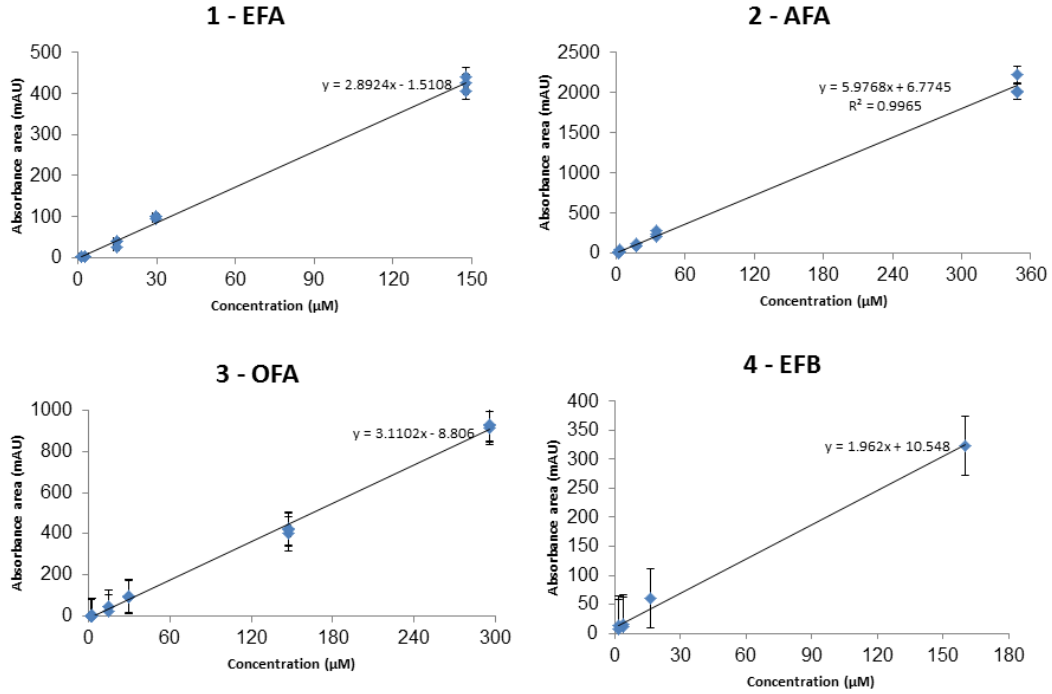

Figure 58 Compounds EFA AFA OFA and EFB HPLC UV calibration curves.

1.20 Experimental

1.20.1 General radiosynthesis of [^{18}F]XFA compounds

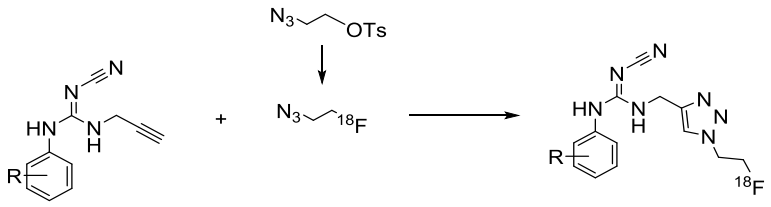

[^{18}F]XFA

[^{18}F]Fluoride was produced at the St Thomas' Hospital PET Centre by the $^{18}O(p,n)^{18}F$ reaction through cyclotron-accelerated proton irradiation of enriched (95%) [^{18}O]H_2O. 150 MBq of aqueous [^{18}F]fluoride were trapped in a Sep-Pak QMA cartridge pre-activated with NaOH (5 mL 1N), water (10 mL) and K_2CO_3 (5 mL 1N) followed by water (10 mL). The fluoride was released with Kryptofix 222 / potassium carbonate (30 mM:15 mM, 0.65 mL) dissolved in 85:15 acetonitrile / water. The solution was dried three times at 90°C for 5 min in a Wheaton V-vial and under a flow of nitrogen. Tosylethyl azide (4.1 mg, 17 µmol) in acetonitrile (0.4 mL) was added to the dried fluoride and heated at 80°C for 15 min. Upon cooling of the reaction mixture to room temperature, propargyl precursor (20 µmol) in DMSO (0.3 mL), sodium ascorbate (19.8 mg) in water (0.2 mL) and copper sulfate (7.5 mg) in PBS (0.2 mL, 0.1 M) were added in this order under a nitrogen atmosphere. Following heating for 20 min at 100-110°C (vide infra), the mixture was passed through a Whatman Spartan 13 mm 0.2 µm RC Minitip filter and injected onto a an HPLC apparatus for purification by semi-preparative methods B, D or E (Table 8). The acetonitrile/water product fraction was then dried for about 1 hour at 90-110°C under a stream of nitrogen, reformulated in the desired volume of PBS and sampled for QC analysis (analytical methods B, D or E).

1.20.2 2-Cyano-1-((1-(2-fluoroethyl)-1H-1,2,3-triazol-4-yl)methyl)-3-(quinolin-5-yl)guanidine ([^{18}F]EFA)

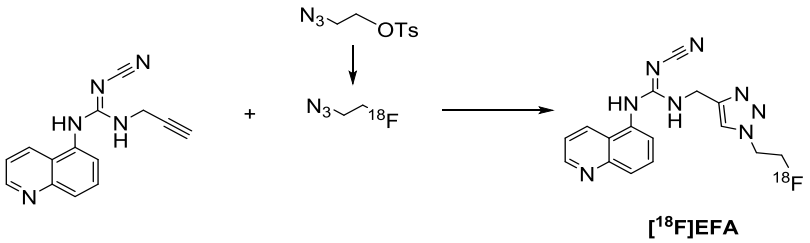

[^{18}F]EFA

To [^{18}F]FEA, 5 mg QYL were added to the click reagents described in the general method and heated at 110°C for 20 min. The product was isolated in 160 min in >99% RCP, 4-26% D.C. RCY, and ~4 GBq/μmol specific activity.

1.20.3 2-Cyano-1-((1-(2-fluoroethyl)-1H-1,2,3-triazol-4-yl)methyl)-3-phenylguanidine ([^{18}F]AFA)

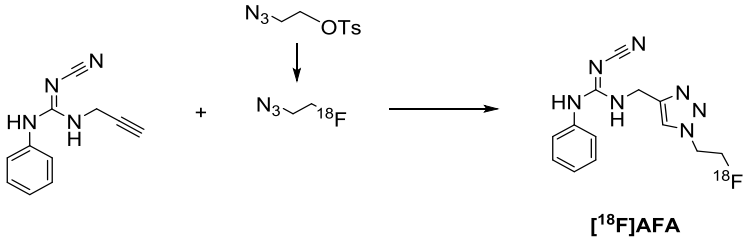

[^{18}F]AFA

To [^{18}F]FEA, 4 mg AYL were added to the click reagents described in the general method and heated at 100°C for 20 min. The product was isolated in 210 min in >99% RCP, 10-42% D.C. RCY and ~6 GBq/μmol specific activity.

1.20.4 2-Cyano-1-((1-(2-fluoroethyl)-1H-1,2,3-triazol-4-yl)methyl)-3-(3-hydroxyphenyl)guanidine ([^{18}F]OFA)

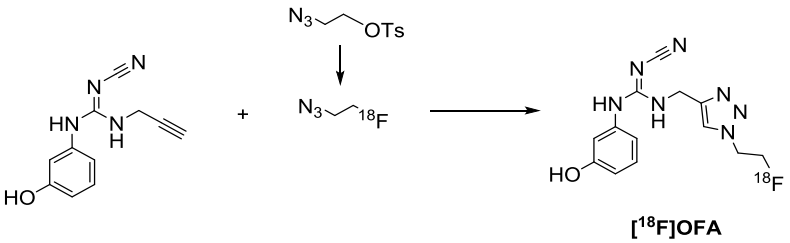

[^{18}F]OFA

To [^{18}F]FEA, 4 mg OYL in 0.3 mL DMF were added to the click reagents described in the general method and heated at 100°C for 20 min. The product was isolated in 260 min in >99% RCP, 5-9% D.C. RCY and ~1 GBq/μmol specific activity.

1.20.5 Optimised radiosynthesis of EFA (HPLC route)

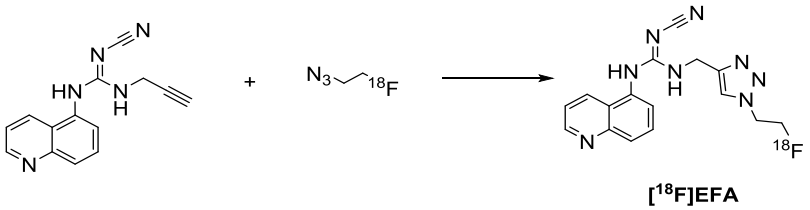

[^{18}F]EFA

[^{18}F]Fluoride was produced, trapped, eluted and dried as per the general method described in section 1.20.1. Tosylethyl azide (2.1 mg, 8.5 μmol) in 0.4 mL acetonitrile was added to the dried fluoride and heated at 80°C for 15 min. The solution was then diluted in water to 1 mL and purified by semi-preparative HPLC method A. The fragment [^{18}F]FEA was isolated in 30% acetonitrile in water (ca. 4 mL). The propargyl precursor QYL (4 μmol) in DMSO (0.3 mL) and a mixture of copper sulfate (4 μmol) in PBS (0.1 mL, 0.1 M), BPDS (2 μmol) in water (0.1 mL) and sodium ascorbate (15.2 μmol) in water (0.2 mL) were added under a nitrogen atmosphere. Following heating for 20 min at 100°C, the mixture was concentrated on a tC18 Sep-Pak cartridge and eluted in EtOH (300 μL). Dilution with water to 5 mL was followed by injection onto an HPLC apparatus for purification with semi-preparative HPLC method C (Table 8). The acetonitrile/water product fraction was then concentrated on a new tC18 Sep-Pak cartridge, eluted in EtOH and diluted in PBS or water prior to sampling for QC analysis (analytical methods B and C) resulting in >10 GBq/μmol specific activity.

1.20.6 Optimised radiosynthesis of EFA (Oasis HLB route)

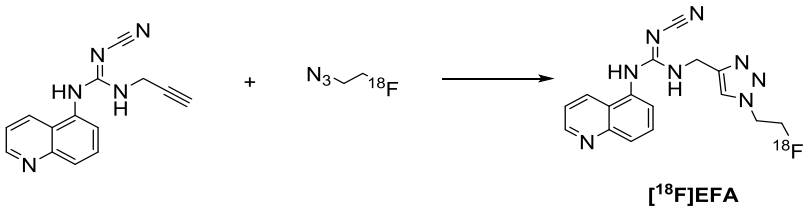

[^{18}F]EFA

[^{18}F]Fluoride was produced, trapped, eluted and dried as per the general method described in section 1.20.1. Tosylethyl azide (2.1 mg, 8.5 μmol) in acetonitrile (0.4 mL) was added to the dried fluoride and heated at 80°C for 15 min. The solution was then diluted in 10 mL water and passed sequentially through a light C18 Sep-Pak and an Oasis HLB cartridge. The cartridges were washed with water (20 mL) prior to elution of [^{18}F]FEA by acetonitrile (0.9 mL) in a second

V-vial. To this were added the propargyl precursor QYL (4 µmol) in DMSO (0.3 mL) and a mixture of copper sulfate (30 µmol) in 0.1 M PBS (0.1 mL), BPDS (2 µmol) in water (0.1 mL) and sodium ascorbate (100 µmol) in water (0.2 mL) were added under a nitrogen atmosphere. Following heating for 20 min at 100°C, the mixture was diluted to 5 mL in water, passed through a Whatman Spartan 13 mm 0.2 µm RC Minitip filter and injected onto an HPLC apparatus for purification with semi-preparative method C (Table 8). The isolated product was concentrated on a tC18 Sep-Pak cartridge, eluted in EtOH and diluted in PBS or water prior to sampling for QC analysis (analytical methods B and C) resulting in >10 GBq/µmol specific activity.

1.20.7 2-Cyano-1-(4-fluorobenzyl)-3-(quinolin-5-yl)guanidine ([^{18}F]EFB) (boronic ester route)

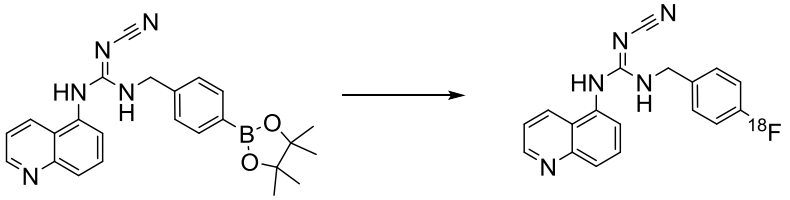

QPB **[^{18}F]EFB**

This method was adapted from Tredwell *et al.*[484] [^{18}F]Fluoride was produced, trapped, eluted and dried as per the general method described in section 1.20.1. Upon cooling to 25-50°C it was aerated with >10 vial volumes of compressed air for 5-10 min. To the [^{18}F]fluoride QPB (5-40 µmol), Cu $(OTf)_2(py)_4$ (5-50 µmol) and pyridine (0-100 µmol) were added and dissolved in DMSO (0.3 mL) or DMF (0.3 mL). Heating at 110°C for 5-20 min was followed by quenching with water (0.2 mL) and analysis by analytical HPLC method G. The product was not isolated but reached n.i. RCY of 7.7% in 85 min from SOS to end of radiolabelling.

1.20.8 4-Fluorobenzonitrile ([^{18}F]FBN)

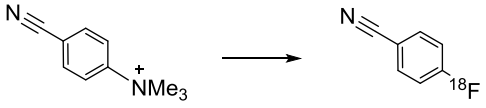

TBACN **[^{18}F]FBN**

This method was previously described by Koslowsky *et al.*[521] To dried [^{18}F]fluoride (1-1.5 GBq), 4-cyano-N,N,N-trimethylanilinium trifluoromethansulfonate (2 mg) in DMSO (0.3 mL) was added and reacted for 15 min at 110°C. Once the reaction was completed, the mixture was diluted with

water (30 mL) and passed through a Sep-Pak Plus C18 Waters SPE cartridge. The cartridge was washed with additional water (5 mL) before elution in THF (2 mL) in 40-60% D.C. RCY and >95% RCP. Radio-TLC (SiO_2, petroleum ether/ethyl acetate (1:1), Rf 0.7).

1.20.9 4-Fluorobenzyl amine ([^{18}F]FBa)

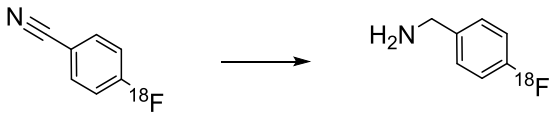

[^{18}F]FBN **[^{18}F]FBa**

2mL [^{18}F]FBN in THF was transferred without further purification into a reaction vial containing $NaBH_4$ (10 mg), $Co(OAc)_2$ (5 mg). To this, water (1 mL) was added and the mixture was mixed and allowed to react at rt for 3 min. Next, the mixture was diluted in 40 mL pH 6.2 phosphate buffer (6.7:1 NaH_2PO_4:Na_2HPO_4) so as to limit the organic solvent to 5%. The mixture was filtered (0.2 µm pore Whatman Spartan filters) and loaded on a Phenomenex Strata-X-CW SPE cartridge. Following an acetonitrile (5 mL) wash, a purple band formed in the cartridge and could be entirely eluted in the second of three aliquots of 5% TFA acetonitrile (0.6-0.7 mL each) in 45-55% D.C. RCY (22-34% overall D.C. RCY) and >93% RCP. Radio-TLC (SiO_2, nBuOH/HOAc–H_2O (4:1:1), Rf = 0.4).

1.20.10 2-Cyano-1-(4-fluorobenzyl)-3-(quinolin-5-yl)guanidine ([^{18}F]EFB) (fluorobenzyl amine route)

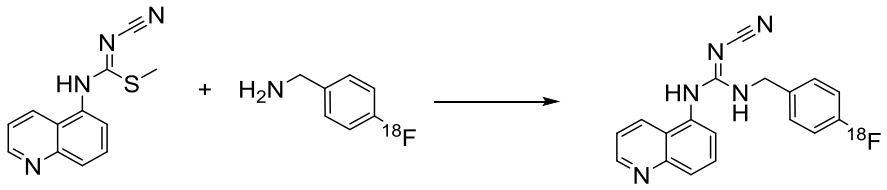

QSMe **[^{18}F]FBa** **[^{18}F]EFB**

0.4-0.7 mL of [^{18}F]FBa in 5% TFA acetonitrile were neutralised with triethylamine (2 eq., 110-112 µL) and added to of QSMe (11 µmol, 3.6 mg) in a sealed vessel. The reaction vessel was heated at 160°C for 15 min, cooled to 50°C and the solvent was concentrated at 50°C under a stream of nitrogen for 7-10 min. Next, the crude mixture was diluted in water (2 mL) ensuring <15% acetonitrile was present and injected in an HPLC semi-prep C18 column with method H

to provide isolation of the pure product in >99% purity and >300 GBq/μmol specific activity. The product was diluted to 30-50 mL in water and passed through a light C18 Sep-Pak cartridge for concentration in ethanol (200-500 μL). The resulting product was obtained in high purity and 4.0% overall D.C. RCY in 3 h and 30 min from SOS. QC testing was performed with HPLC methods H and J (Table 8).

1.21 Results and discussion

1.21.1 Tosylethyl azide radiolabelling

Initially following Galante's procedure,[522] 2-tosylethyl azide in 0.4 mL acetonitrile was added to dried K222.K^{18}F in a V-vial. Cooling the dried fluoride with an inert gas before exposing it to a tosylethyl azide/acetonitrile solution was found to be crucial to incorporate H^{18}F. V-vials are particularly suitable for radiofluorinations as their shape maximises the recovery of the product. In this context, mixing is not particularly important as reagent convection governs the reactivity. A standard 5-95% acetonitrile analytical ramp was employed to analyse the reaction outcome (Figure 59 and analytical HPLC method A, Table 8), separating unreacted [^{18}F]fluoride (solvent front, R_t = 2.5 min) from the product [^{18}F]fluoroethyl azide (R_t = 7 min) and from an unknown byproduct, possibly bromoethyl fluoride (R_t = 9.4 min). The unreacted tosylethyl azide was then visible in the UV trace (about R_t = 10.2 min).

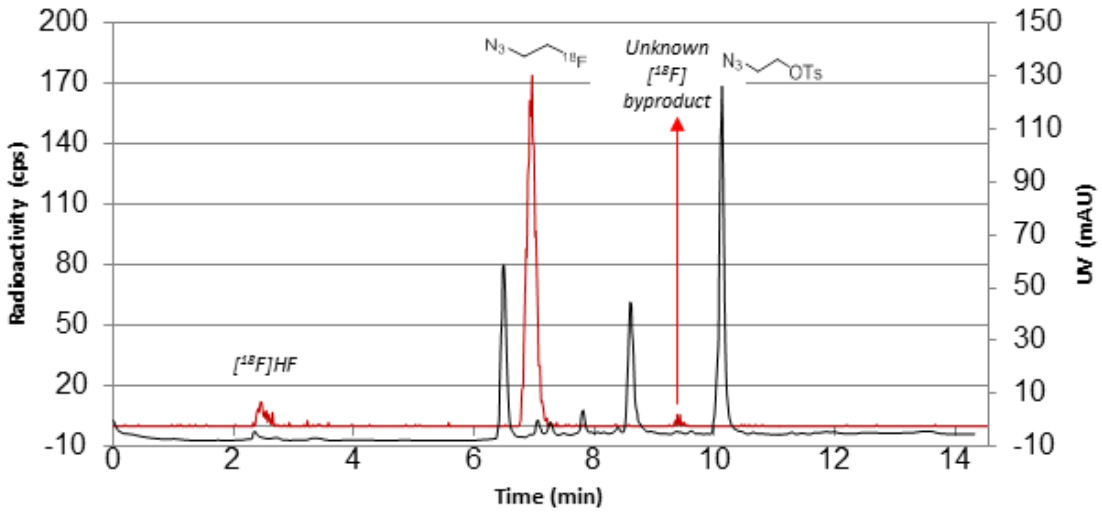

Figure 59 Crude fluoroethyl azide (FEA) HPLC run with analytical method A

Much effort was devoted to minimising the presence of cold byproducts in the final solution. While carrier fluoroethyl azide could not be readily detected due to absence of a UV

chromophore, the other cold impurities were hampering product formation and specific activity. This matter will be discussed in detail in section 1.21.3.

1.21.2 Click radiolabelling: optimisation of the reaction conditions

Reaction monitoring was performed with the methods described above. In order to quantify the yield improvements upon modification of the reaction conditions, the n.i. RCY of the intermediate [^{18}F]fluoroethyl azide to [^{18}F]XFA rather than that of [^{18}F]fluoride to the product was considered. This allowed us to more closely analyse the effect of parameter optimisation on the product formation, regardless of the outcome of the first step of the radiolabelling.

During the radiochemical optimisation phase, a typical analytical chromatogram of the crude resembled the curve displayed in Figure 60, where each [^{18}F]XFA tracer displayed a slightly different retention time (R_t) between 8.30 min and 11 min.

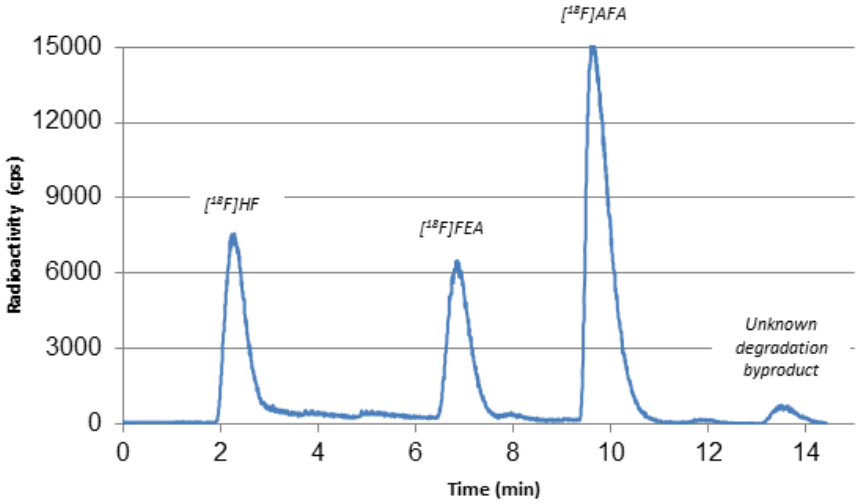

Figure 60 Analytical chromatogram of a crude [^{18}F]XFA reaction

The non-isolated radiochemical yields (n.i. RCYs, reported in Table 9, Table 10 and Table 11) were expressed as percentage of area under the curve (AUC) of product with respect to total AUC ([^{18}F]XFA + [^{18}F]fluoroethyl azide).

Several parameters were found to have little influence on the n.i. RCYs despite minor variations in the literature, i.e. it was equally suitable to employ copper sulfate in 0.008 mmol or 0.015 mmol and sodium ascorbate in 4 or 5 eq. with respect to copper, without variations in yield. Instead, the proportion and volume of solvents affected the yields, as described by Zhou *et al.*[523] In this study it was found that increasing volumes of water or acetonitrile lowered the yields; however, the presence of excess DMF, reduced the detrimental effect of water. Generally

speaking, yields were more strongly correlated to the volume of the reaction or the concentration of the reagents than to the proportion of solvents (as long as MeCN<H2O<<DMF/DMSO). This can be explained by the second order kinetics with respect to the alkyne precursor and the availability of the copper catalyst in its +1 oxidation state in the reaction mixture. Consequently, in this work quantities of solvents were minimised, whilst ensuring appropriate solvation of the catalytic mixture and its interaction with the precursor.

On the other hand, it is known that the copper-chelating bathophenanthroline disulfonic acid disodium (BPDS) ligand strongly enhances the rate of click reactions (Figure 61).[522] BPDS poses some additional challenges with respect to the purification of the final product, particularly when the latter is hydrophobic, as BPDS can clutter HPLC spectra.[523]

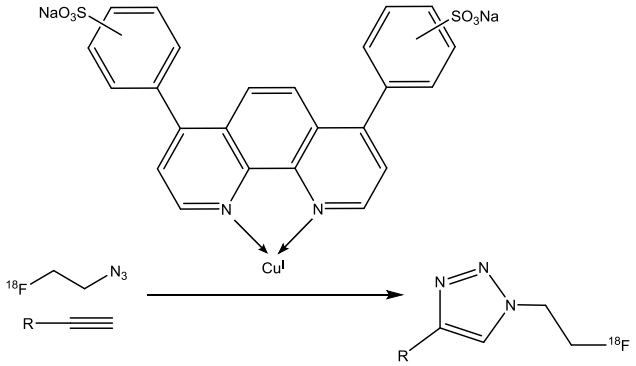

Figure 61 The bathophenanthroline disulfonic acid disodium salt ligand

Furthermore, the order of addition of the reagents was significant: copper and the BPDS ligand were always pre-mixed in 0.05-0.1 M PBS before addition to the reaction pot.[522] In the literature,[522] around 1 eq. BPDS with respect to copper have been reported to increase click n.i. RCYs and reduce the time and temperature requirements. However, in our hands it was found that there were transfer and mixing issues in connection to BPDS due to formation of solid precipitate when mixed with copper, leading to loss of catalyst, difficulties in sampling the crude and overall apparent or actual decreases in conversion rates. In hindsight, BPDS in water could have been added directly to the reaction pot without prior mixing with copper, possibly improving the ease of transfer and mixing. Nonetheless, it was found that without BPDS, modifying other parameters such as outlined in Table 9 could lead to excellent conversion rates and improve the final product's chemical purity.

Moreover, optimisation work involved modifications in the modality of sampling the reaction product. Where the crude product was a heterogeneous mixture with precipitates and its injection as such in an HPLC would have been problematic, several solutions were explored. Firstly, simple filtration; then filtration followed by dilution of 50 µL crude in 200 µL 50:50 methanol/water; finally, dilution (which decreases organic solvent percentage and consequent lack of column retention) with no filtration followed by a short centrifugation to precipitate any suspended solid with sampling of 50uL of the supernatant. All methods were acceptable, but gave somewhat different n.i. RCY ratios for the same product. For consistency, all data presented exploited the last sampling method.

Table 9 and Figure 62 summarise the results that lead to the optimisation of the conversion from [^{18}F]FEA to [^{18}F]EFA. Initially a protocol by Galante *et al.* was employed.[522] This was demonstrated for 6-halopurine fluoroethyl-triazoles, but was described as being easily adaptable to the labelling of other triazole compounds. Nevertheless, despite mixing for 20 min in acetonitrile or 45 min in DMF (a better precursor solvent) no conversion was observed. Upon mixing in a microwave reactor at 300 W for 10 min at room temperature as suggested by several previous studies,[524-526] some product was detected. It appeared clear that harsher conditions were necessary. Glaser[410] and De Jesus[527] reported employing heating at 80°C and variable amounts of starting materials. However, initially microwave heating was retained, as it had appeared beneficial in the previous iterations (Table 9, entry 3). When the reaction was performed with 10 µmol, 20 µmol or 30 µmol of alkyne starting material, a much higher conversion was observed. This was similar in all cases, but with an approximatively linear increase together with starting material concentration. An intermediate amount was adopted during further optimisations, seeking to balance the consumption of starting material and increased conversion. Next, the precursor solvent was changed to improve the solvation and boost the reactivity. Indeed, a slightly increased n.i. RCY (Table 9, entries 6-7) was observed. The reaction was then modified to exclude BPDS, which was found to cause mixing issues, as described above. This resulted in increased conversions, albeit very dependent on the fluoride batch. Furthermore, increasing the temperature to 110°C lead to more than doubling of the conversion rate, whereas a reaction temperature of 150°C had a detrimental effect. This effect was possibly due to the reaching of the boiling point of [^{18}F]FEA (130°C). At this stage, the main

source of activity loss was found to be in the transfer from the V-vial used for fluoride drying to the microwave vial, suggesting as a possible optimisation avenue the modification of the microwave-assisted step. The abolition of microwave heating was found to affect positively the n.i. RCYs (cf. entry 7 and 11). The conversion rate was further improved by removal of BPDS and by adjustment of the heating to 100°C (entry 13).

Table 9 [^{18}F]EFA from the intermediate [^{18}F]FEA under different conditions.

Entry	Scale (SM µmol)	Time (min)	Temperature (°C)	MW?	Organic solvent	Catalysis	n.i. RCY ± SD
Lit 1[522]	10	1	rt	N	MeCN	Cu/BPDS/Na	n/a
1	10	20	rt	N	MeCN	Cu/BPDS/Na	0%
2	20	45	rt	N	DMF	Cu/BPDS/Na	0%
3	20	10	rt	Y	DMF	Cu/BPDS/Na	6.40%
Lit 2 [410]	15	15	80	N	DMF	Cu/Na	n/a
Lit 3 [527]	7.5	15	80	N	DMF	Cu/Na	n/a
4	10	20	80	Y	DMF	Cu/BPDS/Na	20.8%
5	20	20	80	Y	DMF	Cu/BPDS/Na	22.1%
6	30	20	80	Y	DMF	Cu/BPDS/Na	25.0%
7	20	20	80	Y	DMSO	Cu/BPDS/Na	23.6%
8	20	20	80	Y	DMSO	Cu/Na	37.0% ± 14.6%
9	20	20	110	Y	DMSO	Cu/Na	81.7% ± 26.0%
10	20	20	150	Y	DMSO	Cu/Na	15.8% ± 5.5%
11	20	20	80	N	DMSO	Cu/BPDS/Na	74.3%
12	20	20	80	N	DMSO	Cu/Na	77.7% ± 14.8%
13	20	20	110	N	DMSO	Cu/Na	91.8% ± 14.3%
14	20	20	100	N	DMSO	Cu/Na	99.5% ± 1.4%

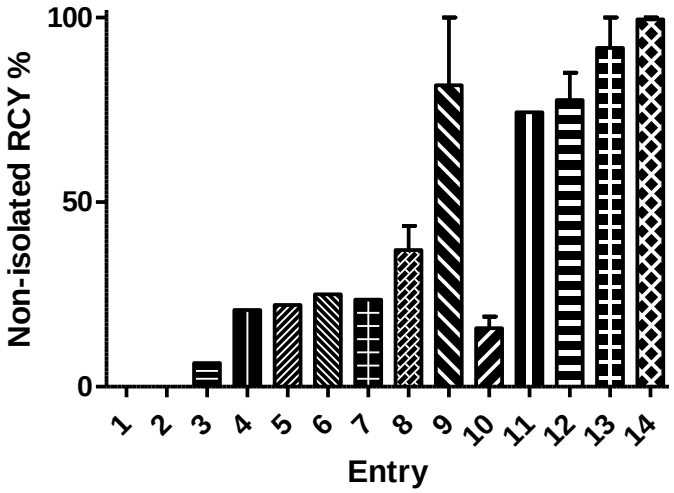

Figure 62 [^{18}F]FEA - [^{18}F]EFA conversion n.i. RCY summary extract from Table 9

A similar line of approach was also employed for all other radiotracers, with the benefit of the conclusions drawn in the analogous case of [^{18}F]EFA. The reaction to synthesise [^{18}F]AFA was attempted in the same conditions as entry 7 for [^{18}F]EFA, achieving good n.i. RCY (Table 10). Similarly to [^{18}F]EFA, the removal of BPDS increased the yields; instead, heating to 110°C proved detrimental. Finally, heating without microwaves at 100°C gave quantitative n.i. RCYs (Figure 63).

Table 10 [^{18}F]AFA from the intermediate [^{18}F]FEA under different conditions

Entry	Scale (SM µmol)	Time (min)	Temperature (°C)	MW?	Organic solvent	Catalysis	n.i. RCY ± SD
1	20	20	80	Y	DMSO	Cu/BPDS/Na	61.0%
2	20	20	80	Y	DMSO	Cu/Na	79.6 ± 11.5%
3	20	20	110	Y	DMSO	Cu/Na	56.9 ± 12.6%
4	20	20	100	N	DMSO	Cu/Na	99.6 ± 1.3%

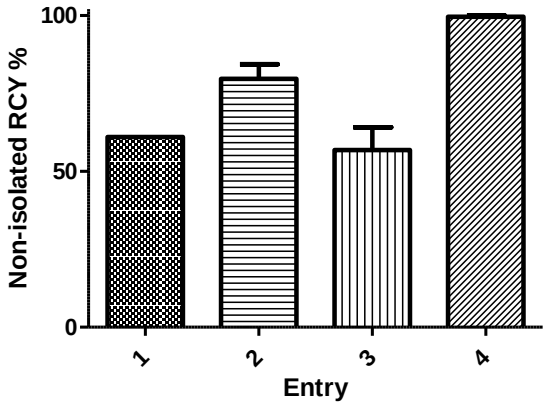

Figure 63 [^{18}F]FEA - [^{18}F]AFA conversion n.i. RCY summary extract from Table 10

The radiosynthesis of [^{18}F]OFA started with a 65% n.i. RCY with microwave irradiation. Reaction optimisation was attempted by microwave-assisted heating (Table 11, entries 1-3), resulting in an initial increase in conversion, followed by a drop at 140°C, consistent with the previous tracer optimisation observations. Microwave irradiation was then abolished, resulting in quantitative n.i. RCYs at 90-110°C (Figure 64).

Table 11 [^{18}F]OFA conversion from the intermediate ^{18}FEA under different conditions

Entry	Scale (SM µmol)	Time (min)	Temperature (°C)	MW?	Organic solvent	Catalysis	n.i. RCY ± SD
1	25	20	80	Y	DMF	Cu/Na	65.0% ± 31.9%
2	25	20	110	Y	DMF	Cu/Na	79.3% ± 22.8%
3	25	20	140	Y	DMF	Cu/Na	38.25%
4	25	20	80	N	DMF	Cu/Na	61.4% ± 13.1%
5	25	20	90	N	DMF	Cu/Na	100%
6	20	20	110	N	DMF	Cu/Na	100% ± 0%

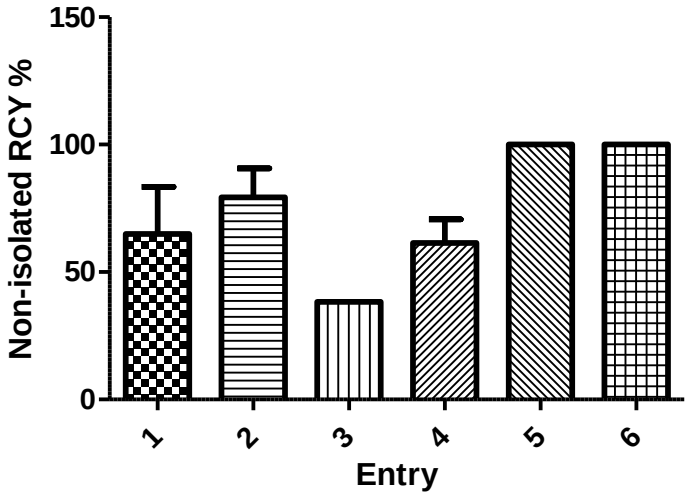

Figure 64 [^{18}F]FEA - [^{18}F]OFA conversion n.i. RCY summary extract from Table 11

The identity of each radiotracer was confirmed by co-injection with the cold standard and/or addition of carrier (as defined in section 1.18.4).

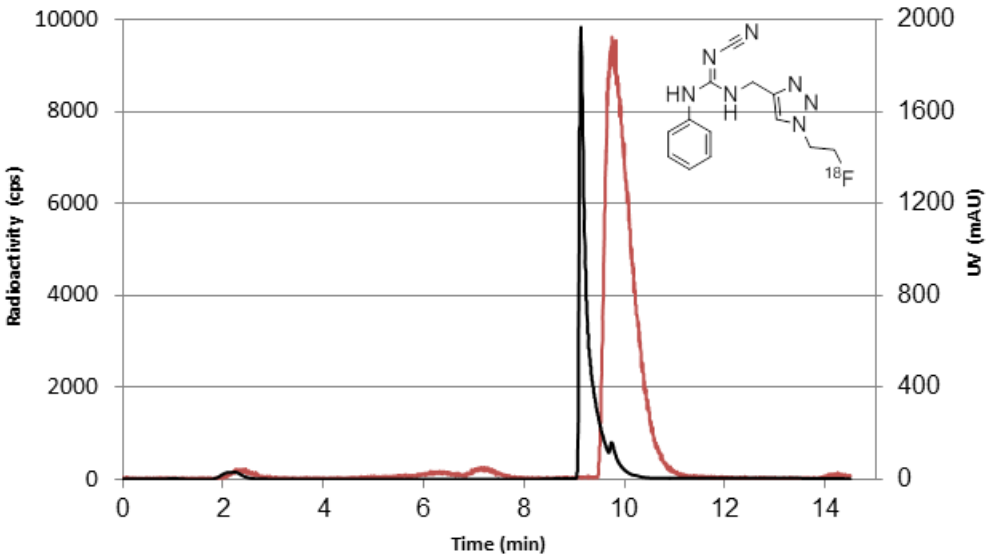

Figure 65 [^{18}F]AFA co-injection with cold AFA, analytical HPLC method D

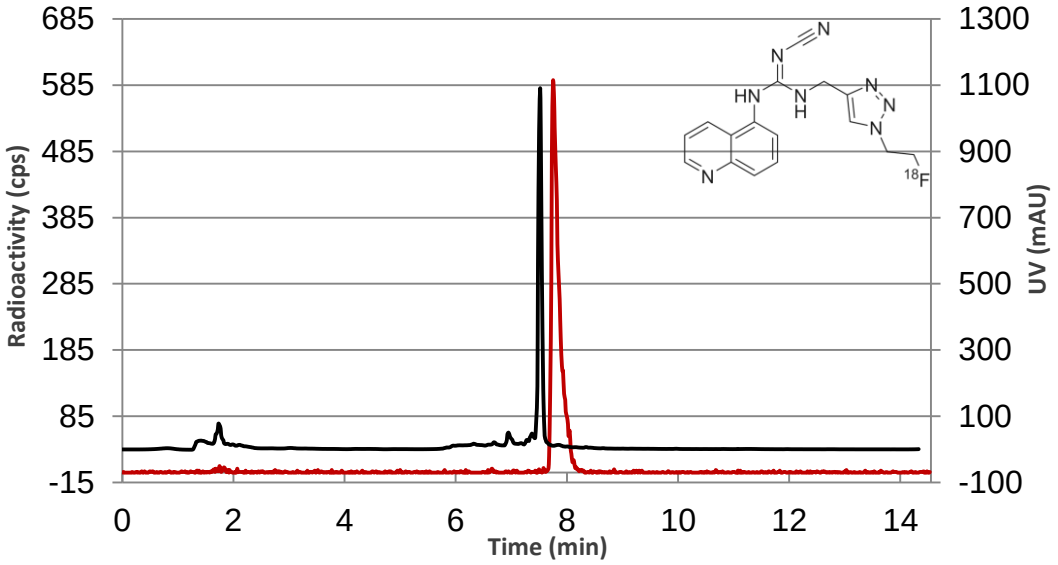

Figure 66 [^{18}F]EFA co-injection with cold EFA, analytical HPLC method B

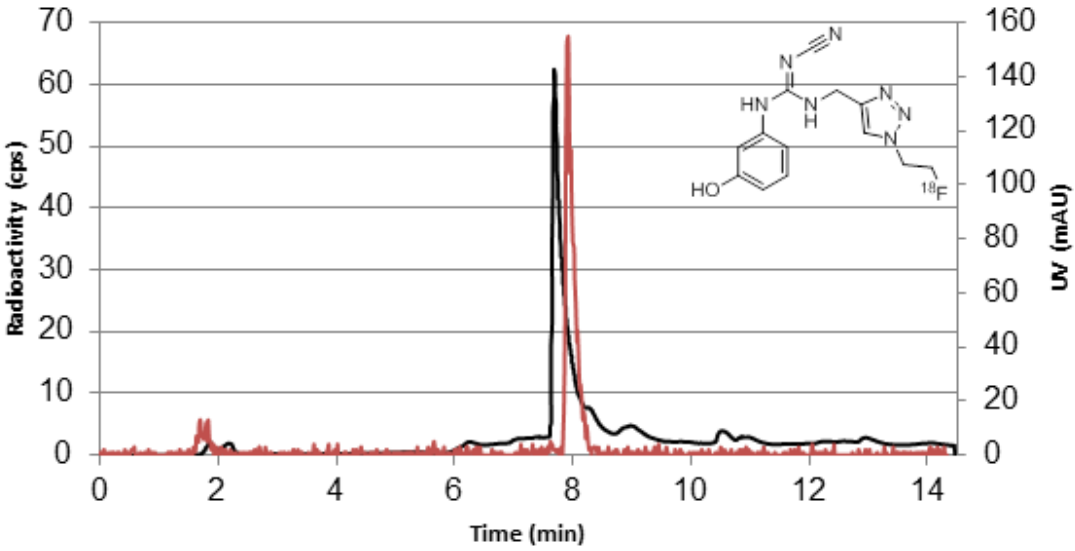

Figure 67 [^{18}F]OFA co-injection with cold OFA, analytical HPLC method E

1.21.3 Click radiolabelling: optimisation of the purification procedure

Following successful conversion of the precursors to the desired products, the specific activity required optimisation. The specific activity (SA) is by definition:

SA (GBq/μmol) = activity (GBq) / mass (μmol)

Thus, given the unfeasibility of increasing the activity beyond the low GBq level in a research environment, the focus was shifted to carrier mass reduction. The strategy was threefold: reduction of the mass of precursor employed, optimisation of the reaction conditions so as to minimise carrier formation and elimination of all unwanted substances during isolation. While

efforts to comply with the first 2 points of this strategy were described above, this section details the optimisation of the product isolation and the analysis of the purified radiotracers.

For the most part, tracer isolation was performed by semi-preparative HPLC. Iterative HPLC method modifications and testing, resulted in the optimal methods described in Table 8. We then focused on improving the isolated radiochemical yield through the iterations described in section 1.21.2 and consistently reaching an overall 10-42% D.C. RCY for [^{18}F]AFA, 4-26% D.C. RCY for [^{18}F]EFA, 5-9% D.C. RCY for [^{18}F]OFA and >99% RCP for all tracers. For the determination of the final RCP and SAs, HPLC-isolated tracers were dried by azeotropic evaporation under a flow of nitrogen and re-dissolved in the desired volume of PBS. A 50 µL aliquot was then sampled by analytical HPLC, allowing the determination of the desired parameters upon comparison with a standard mass-curve. The specific activities obtained ranged between 0.5-61 GBq/µmol for [^{18}F]AFA, 0.1-14 GBq/µmol for [^{18}F]EFA and 0.3-2 GBq/µmol for [^{18}F]OFA. This was due mostly to the insufficiently clear UV baseline and some variability in retention times, leading to difficulties in unmistakenly identifying the carrier peak in all instances.

To further improve the specific activity, two issues were acted upon: the poor chemical purity of the intermediate radiolabelled fragment [^{18}F]FEA and the suboptimal isolation of the final product [^{18}F]XFA. Concerning the former, it has been established that tosylethyl azide, azidoethanol and the elimination byproduct vinyl azide are all present at completion of the tosylethyl azide labelling, reacting with the substrate to form cold byproducts.[351, 410, 528] Three methods have been established for the fast purification of [^{18}F]FEA: flow-trap distillation,[529, 530] vacuum distillation[523] and solid phase extraction.[528] The first is effective at isolating [^{18}F]FEA in 50% D.C. RCY and medium specific activities by distillation with MeCN at 130°C. The second method works at a temperature of 90°C, which is lower than the boiling point of vinyl azide and thus prevents its co-distillation giving >80% yields and high specific activities. The authors also claim that it resolves the issue of backflow of distilled product which can often lead to lower yields or extra distillation time. In this context, the procedure was attempted albeit resulting in extensive backflow of the product and overall poor yields. Instead, unpublished research in our department showed that optimal separations could be obtained by HPLC method D (Table 8)

with less development work required (Figure 68). However, the radiolabelled fragment was isolated in about 4 mL 30% acetonitrile, leading to different requirements for the click reaction.

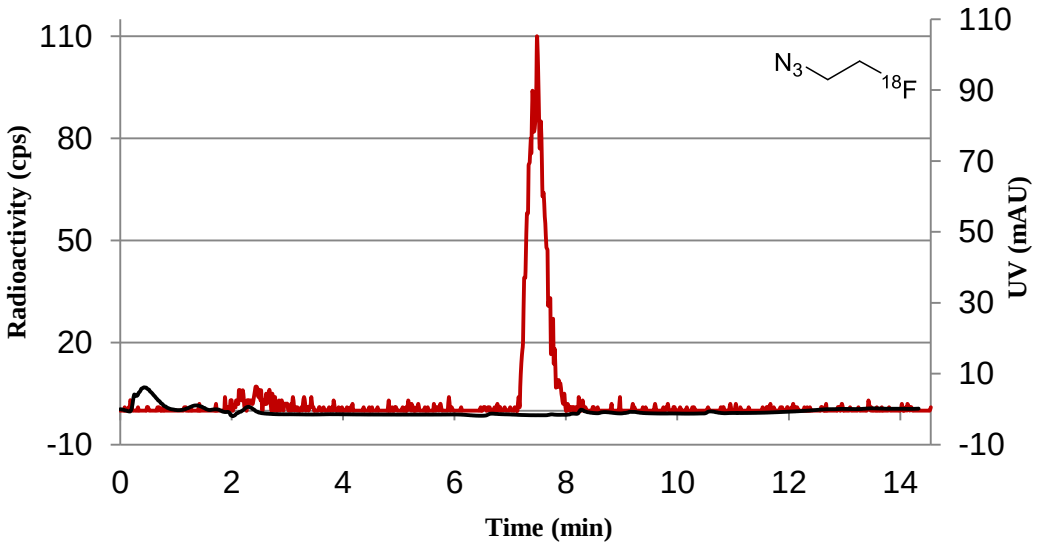

Figure 68 Pure [^{18}F]FEA after purification by semi-preparative HPLC method A

This was utilised as an opportunity to further improve the reaction conditions. 2 µmol (0.5 eq.) of diluted BPDS could be reintroduced without making the - now diluted - mixture as dense as previously observed, thus decreasing the reaction times to 5 min and removing the need for heating. Also, lower reagent masses were employed, reducing the precursor to 4 µmol (1 eq.), 1 eq. copper sulfate, 3.8 eq. sodium ascorbate and 2.1 eq. tosylethyl azide. In order to further remove UV-active contaminants, the product was trapped on a tC18 cartridge and eluted in 300 µL EtOH, then readjusted for HPLC injection to a suitable percentage in water. Taken together, this improved considerably the analytical HPLC UV baseline, giving carrier signal under our detection limit (calculated as approximately 5 nmol for EFA). Despite a significant byproduct could be observed, it could be successfully separated from the desired product by isocratic elution.

A further attractive alternative from the point of view of radiosynthetic automation and reduction of the overall time of tracer production was found in Zhou's cartridge-based click radiochemistry purification method developed at Washington University.[528] This improved procedure involved trapping of the unreacted precursor and impurities in the solvent front in a light C18 Sep-Pak cartridge, followed by trapping of the [^{18}F]fluoroethyl azide fragment in an Oasis HLB cartridge with removal of waste reagents such as the K222 cryptand and carbonate. Following elution in 0.9 mL MeCN from the Oasis HLB cartridge, the clean [^{18}F]FEA (Figure 69) could be reacted in

a new vial with the click reagents and the radiotracer precursor QYL with heating. Following HPLC purification, the mixture could then be diluted in water and concentrated on a tC18 Sep-Pak cartridge. Quality control was performed by HPLC method C (Table 8) yielding >99.9% pure [^{18}F]EFA in 1.2 mL ethanol and a very clear UV baseline indicative of a high specific activity final product (>10 GBq/μmol) (Figure 70).

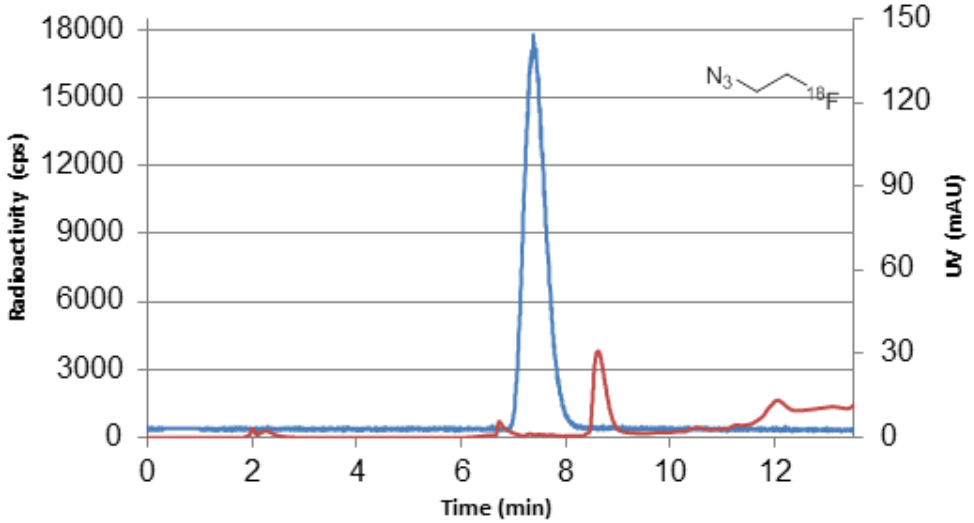

Figure 69 Pure [^{18}F]FEA after sequential C18-SPE and HLB-SPE purification

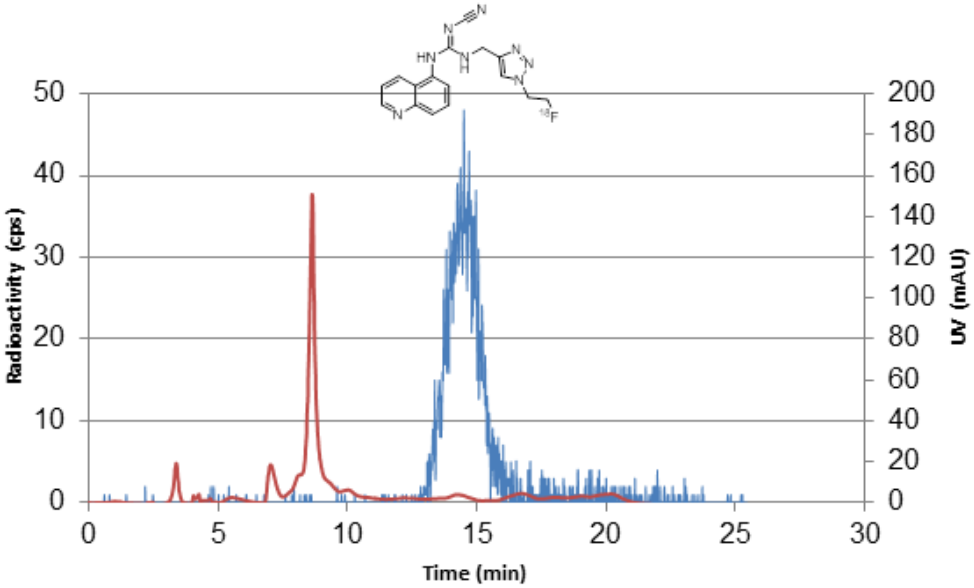

Figure 70 [^{18}F]EFA QC at end of synthesis with analytical HPLC method C

1.21.4 Attempted radiosynthesis of [^{18}F]EFB *via* a boronic ester radiofluorination

The boronic ester nucleophilic substitution reaction was explored as an attempt to directly radiofluorinate compound QPB (Figure 56 for structure). The resulting product [^{18}F]EFB presents a fluorine atom *para* to a methylguanidine group. The aromatic ring in this compound is electron rich, which is a known challenge in nucleophilic radiofluorinations. The boronic ester

fluorination attempted is that reported by Tredwell and co-workers.[484] Whilst realising this method was unlikely to produce high RCYs, it was decided to explore this radiosynthetic strategy with some slight modifications aimed at reducing the basicity of the guanidine amine and facilitating the fluoride attack, as suggested by work carried out by the Aigbirhio group at the University of Cambridge.[531, 532].

Table 12 below shows the various conditions attempted. Initially, the strength of the protocol was tested by replicating the bisphenyl boronic ester labelling described in the literature.[484] In our hands, this was found to be lower yielding despite multiple iterations, possibly due to differences in n.i. RCY calculation methods. Moreover, the yield was found to strongly vary depending on the concentration of precursor. This represents a major drawback of the published method, as it demands copious amounts of precursor. The method was then applied to the boronic ester precursor QPB at various precursor and catalyst concentrations, as well as in the presence or absence of air or the use of caesium as counter ion. Although some trace amounts of product could be detected (Figure 71), no remarkable yield improvement was observed.

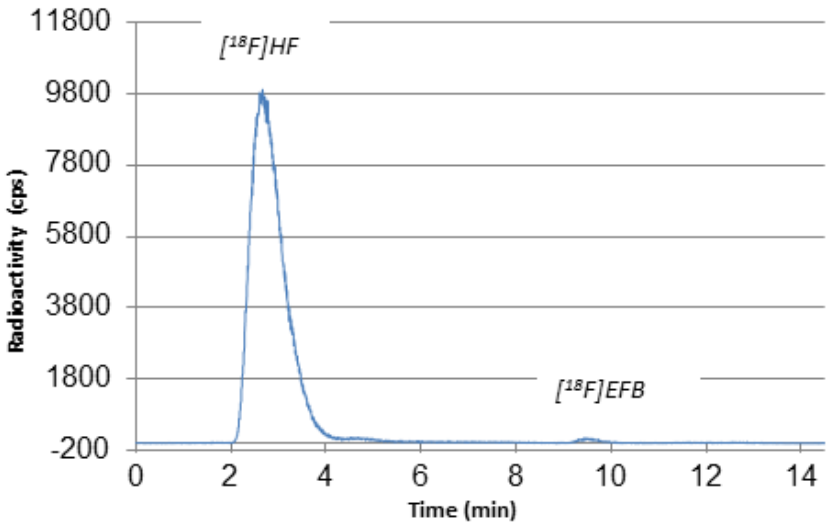

Figure 71 [^{18}F]EFB crude radioactivity trace with analytical HPLC method G

Table 12 [^{18}F]EFB boronic ester fluorination attempts under different conditions

Entry	Scale (SM µmol)	Cu catalyst µmol	Temperature (°C)	Time (min)	Air	Solvent (0.3 mL)	0.01 mmol base	n.i. RCY %
Bisphenyl Lit.[484]	60	5.3	110	20	Y	DMF	K_2CO_3	74
Bisphenyl replicate 1	60	5	110	20	Y	DMF	K_2CO_3	20

Bisphenyl replicate 2	10	5	110	20	Y	DMF	K_2CO_3	0
1	10	5	110	20	Y	DMSO	K_2CO_3	2.0
2	10	5	110	20	**N**	DMSO	K_2CO_3	2.9
3	10	**20**	110	20	Y	DMSO	K_2CO_3	2.3
4	10	20	110	20	**N**	DMSO	K_2CO_3	7.3
5	**40**	**5**	110	20	Y	DMSO	K_2CO_3	2.8
6	**30**	5	110	20	**N**	DMSO	K_2CO_3	5.3
7	**30**	**20**	110	20	**N**	DMSO	K_2CO_3	7.7
8	10	10	110	20	Y	**DMF**	K_2CO_3	0[(a)]
9	10	7	110	20	Y	DMSO	**Cs_2CO_3**	0
10	10	5	110	5-20	Y	DMSO	**3 x K_2CO_3**	0
11	10	50	110	5-20	Y	DMSO	K_2CO_3	0
12	10	50	110	5-20	Y	DMSO	**3 x K_2CO_3**	1.4
13	**20**	50	110	5-20	Y	DMSO	3 x K_2CO_3	0.9
14	10	50 **+ 100 pyridine**	110	5-20	Y	DMSO	3 x K_2CO_3	2.3
15	10	50	110	5-20	Y	DMSO	**3 x Cs_2CO_3**	1.4

Further iterations were inspired by the work of Scott and co-workers at the University of Michigan in relation to their work on GSK3 radiotracer development.[532] They observed some higher degree of radiolabelling upon addition of excess amounts of scavenging base. In their rationale, higher equivalents of copper catalysis should have sufficed to drive fluoride substitution. However, the presence of an N-carbamothioylimidamide had to be counteracted by a competing excess of free base, such as dimethylaminopyridine (DMAP) or pyridine. Thus, a number of reactions in line with this rationale were attempted, while also altering the nucleophilicity of the fluoride. However, no yield increases were observed (Figure 72).

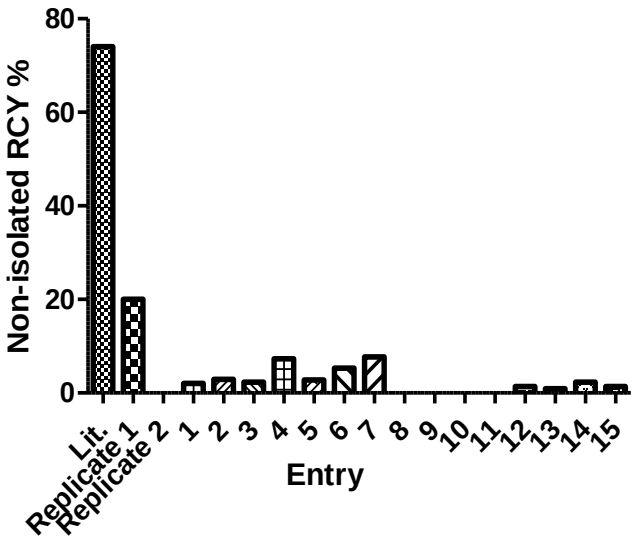

Figure 72 QPB - [^{18}F]EFB conversion n.i. RCY summary extract from Table 12

Next, we attempted the preparation of a Boc-protected version of the precursor QPB to obviate the electron donating complications posed by the unprotected guanidine. Consequently, the labelling procedure would now necessitate a second acidic deprotection step. Unfortunately, the preparation of this compound was not immediately straightforward and could only afford a mixture of mono-Boc protected QPB (see chapter 3), leading us to set aside this labelling method altogether to concentrate on the more promising approach described in the following section. The difficulty in Boc-acylating this class of compounds is not new and it is known that, among other byproducts, a dimerised cyclic version of the starting material can form.[533]

1.21.5 [^{18}F]EFB radiosynthesis *via* [^{18}F]Fluorobenzyl amine

This procedure relied on the synthetic route described by the Wuest group at the University of Alberta in three separate instances (Figure 73).[411, 521, 534]

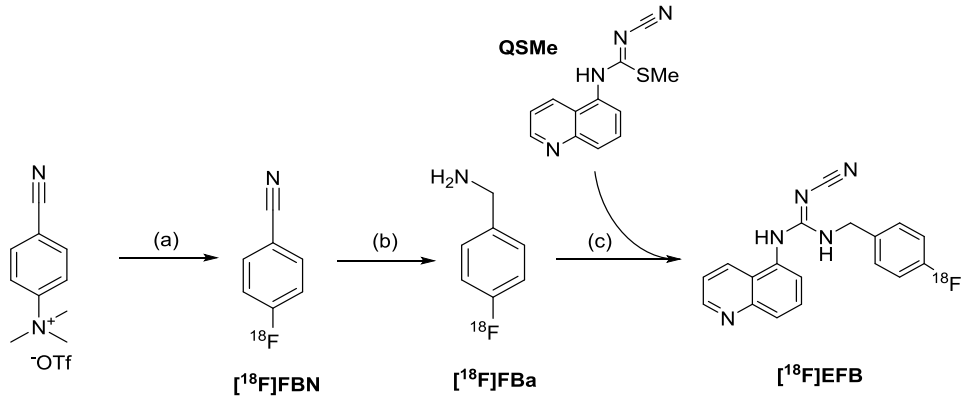

Figure 73 Scheme of synthesis of [^{18}F]EFB *via* [^{18}F]FBN and [^{18}F]FBa

The procedure for the manual synthesis of [^{18}F]FBa was applied with only minor alterations to the literature method.[521] Radiofluorination of the quaternary ammonium salts to [^{18}F]FBN was attempted under different conditions with the aim of improving the average n.i. RCYs to 80-85% as described by Turkman *et al.* (Table 13).[535] In order to ensure an efficient radiolabelling (Figure 74, entry 5), it was of paramount importance to produce the trimethylammonium triflate salt in the highest possible purity *via* double recrystallization in methanol.

Table 13 [^{18}F]FBN synthetic attempts

Entry	Scale (SM µmol)	Time (min)	Temperature (°C)	n.i. RCY (%)
1	3.2	15	95	63.0 (n=8)
2	3.2	20-25	95	65.2 (n=3)
3	3.2	15	110	42.9 (n=2)
4	6.4	15	95	68.0 (n=2)
5	6.4	15	110	75.9 (n=4)
6	6.4	20	110	66.9 (n=2)

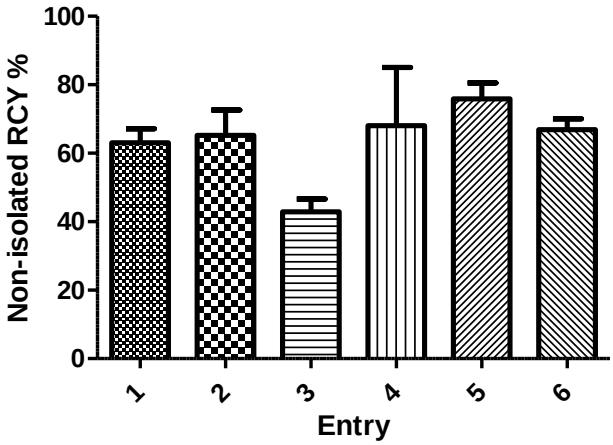

Figure 74 TBACN - [^{18}F]FBN conversion n.i. RCY summary extract from Table 13

The isolation of the radiolabelled compound from the unreacted fluoride and precursor compound was carried out in a tC18 Sep-Pak cartridge. Being the radiolabelled [^{18}F]FBN the only non-ionic radioactive product, this easily resulted in near-quantitative retention in the cartridge and elution in 2 mL THF. The highest recovery rates of about 80% were in particular achieved when loading the crude mix as a <2% DMSO solution in water.

Next, the nitro reduction by cobalt-assisted sodium borohydride hydrogenation could be performed quantitatively. Curiously, the reaction was shown to produce higher yields in the presence of water.[521] The authors reason that the limited yields in organic solvents could be due to a detrimental accumulation of cobalt borite on the vial walls, leading to unavailability of the metal centre for catalysis coupled with absorption and sequestration of significant amounts of product. In the presence of water instead, this byproduct precipitates without the tendency to stick. These observations appear to be further supported by the mechanistic observations made in the 80s by Osby and co-workers at Cornell University.[536] Through observing that the reaction proceeds in the presence of $CoCl_2$ but not Co_2B alone, that the reaction proceeds independent of precursor concentration and is first order borohydride-dependant, they concluded that the nitrile precursor must first undergo activation by the cobalt boride *via* nitrogen-boride coordination, followed by rate-determining borohydride addition from undissolved, uncoordinated $NaBH_4$ (Figure 75).

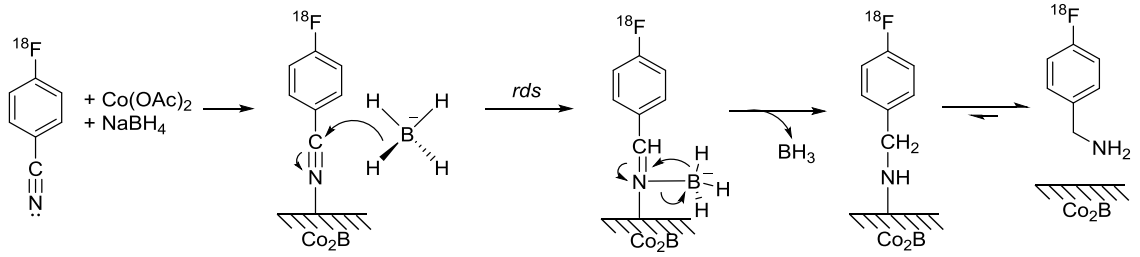

Figure 75 Possible mechanism of nitrile reduction

In our hands, the nitrile reduction proceeded on average at 67.1% n.i. RCY after 1.5 min (n=3), 90.1% after 3 min (n=7) and 82.5% after 5 min (n=14) at room temperature as assessed by ITLC. Purification of the resulting crude mixture was carried out in three distinct ways. In our hands, the literature-suggested Waters C18 plus Sep-Pak solid phase extraction in basic media resulted in unreliable <50% product recoveries. Replacement with a polymeric yet still hydrophobic Phenomenex Strata-X SPE cartridge led to slightly improved 50-60% product recoveries. However, the purity of the resulting [^{18}F]FBa was a matter of concern, as this method failed to remove unreduced fluorobenzonitrile and only part of the [^{18}F]FBa could be retained. Thus, further optimisation was carried out by introducing a Phenomenex Strata-X-CW weak cation exchange cartridge purification step. After preconditioning the cartridge with phosphate buffer at pH 6.2, the crude product was loaded in 5:95 THF / pH 6.2 phosphate buffer (as suggested by the FBa titration curve shown in Figure 76) was loaded and trapped on the cartridge by cation exchange. Acetonitrile washes removed the unreacted, non-cationic unreacted starting material, allowing for the recovery of 50-60% of a highly pure, distinctively violet band of [^{18}F]FBa in <750 µL acidic acetonitrile. Admittedly, this method is still suboptimal due to the substantial loss of product in the loading and elution steps and could possibly be further improved by tweaking the buffering strategy or the solid phase.

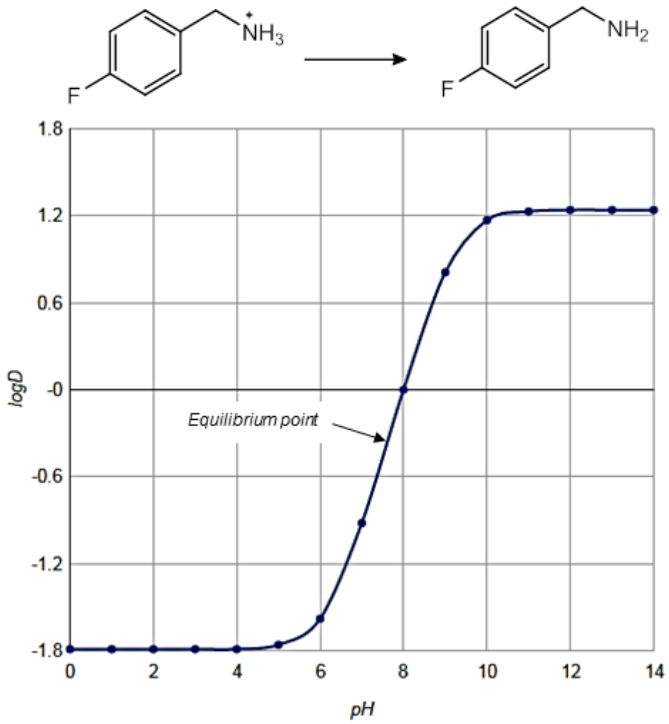

Figure 76 Titration curve for fluorobenzyl amine

The resulting [^{18}F]FBa was obtained in high purity as indicated by ITLC (R_f 0.4, lit.[521] 0.4) and HPLC (Figure 77).

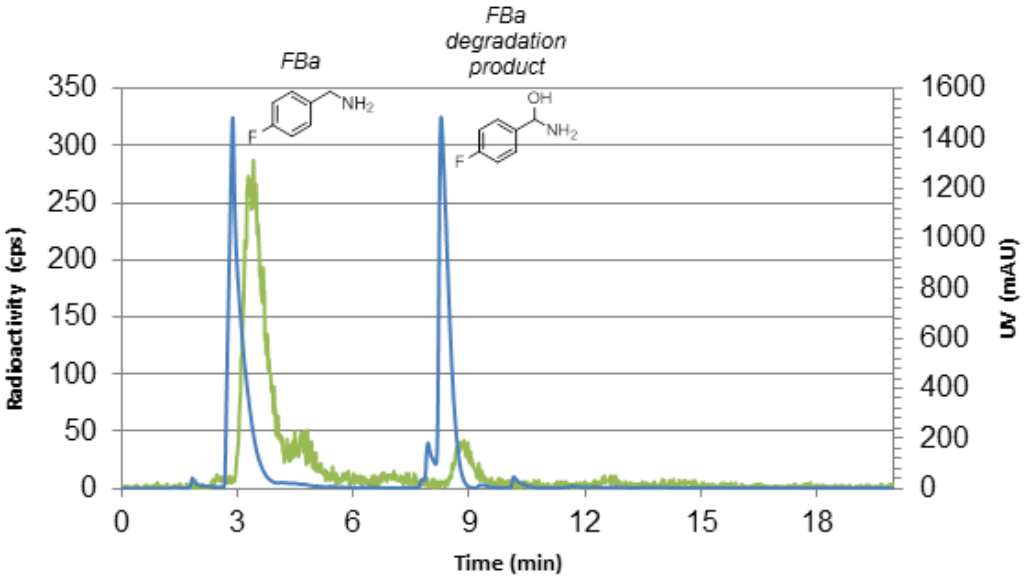

Figure 77 Co-injection of [^{18}F]FBa with cold FBa standard with analytical HPLC method H

Next, we neutralised the 10-40 µL TFA present in the [^{18}F]FBa acetonitrile solution with two to four times as many equivalents of triethylamine, as indicated in Table 14 and Figure 78. When required for mass spectrometric identification of the product, the mixture was mixed at this point with 1-2 eq. cold fluorobenzyl amine carrier before mixing with QSMe and heating (refer to Figure 73 above for the reaction scheme).

Table 14 Radiosynthetic attempts for the synthesis of [^{18}F]EFB

Entry	Scale (µmol QSMe)	TEA (eq. to TFA in solvent)	Solvent	Initial Volume (mL)	Adjusted Volume (mL)	Temperature (°C)	Time (min)	n.i. RCY (%)
1	11	**2**	MeCN + 5% TFA	0.5-2	1-2	**25**	**5**	3.4 (n=1)
2	11	2	MeCN + 5% TFA	0.5-2	1-2	**140**	**15**	77.1 (n=3)
3	11	2	MeCN + 5% TFA	0.5-2	1-2	140	**30**	60.9 (n=2)
4	11	2	MeCN + 5% TFA	0.5-2	1-2	140	**45**	75.3 (n=2)
5	11	**4**	MeCN + 5% TFA	0.7	1	**25**	**5**	9.2 (n=2)
6	11	4	MeCN + 5% TFA	0.7	1	**140**	**15**	46.0 (n=2)
7	11	4	MeCN + 5% TFA	0.7	1	140	**35**	53.0 (n=2)

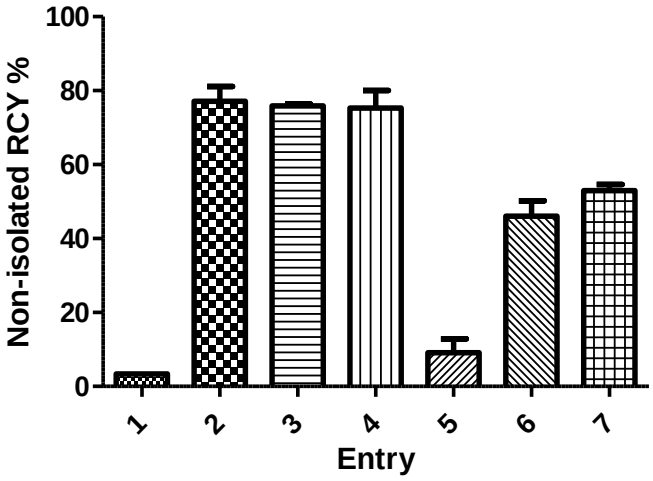

Figure 78 [^{18}F]FBA - [^{18}F]EFB conversion n.i. RCY summary extract from Table 14

The conversion to the product was calculated based on integration of the area under the peak with analytical HPLC method H. However, in a successive optimisation step it was found that this method was not suitable for the separation of the desired substance from an unwanted byproduct (Figure 79). Therefore further reaction optimisations were performed using analytical HPLC method J. Table 15 and Figure 80 show the further optimisations which could be carried out with the latter method.

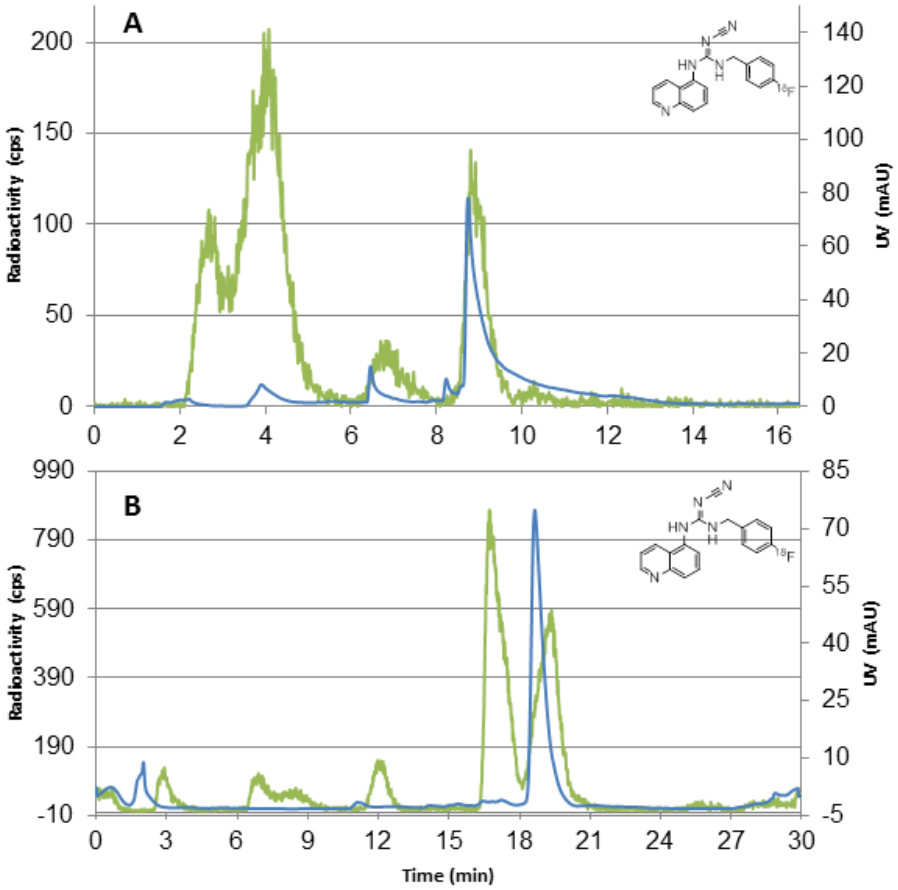

Figure 79 Analytical HPLC elutions of crude EFB with method H and method J

Table 15 Further radiosynthetic attempts for the synthesis of [^{18}F]EFB

Entry	Scale (umol QSMe)	TEA (eq. to TFA)	Solvent	Initial Volume (mL)	Adj. Vol. (mL)	Temp (°C)	Time (min)	EFB n.i. RCY (%)	Unreacted FBa n.i. RCY (%)	Previously undetected byproduct n.i. RCY (%)
1	11	2	MeCN + 5% TFA	0.5-0.7	1	**120**	15	41.4 (n=2)	7.0 (n=2)	13.7 (n=2)
2	11	2	MeCN + 5% TFA	0.5-0.7	1	**125**	15	39.0 (n=2)	15.3 (n=2)	19.6 (n=2)
3	11	2	MeCN + 5% TFA	0.5-0.7	1	**130**	15	43.5 (n=2)	10.1 (n=2)	41.4 (n=2)
4	11	2	MeCN + 5% TFA	0.5-0.7	1	**140**	15	35.9 (n=2)	6.2 (n=2)	47.6 (n=2)
5	11	**3**	MeCN + 5% TFA	0.5-0.7	1	140	15	32.7 (n=1)	3.7 (n=1)	37.5 (n=1)
6	11	2	MeCN + 5% TFA	0.5-0.7	1	**150**	15	41.1 (n=3)	7.7 (n=3)	38.4 (n=3)
7	11	2	MeCN + 5% TFA	0.5-0.7	1	**160**	15	43.8 (n=2)	3.5 (n=2)	38.6 (n=2)

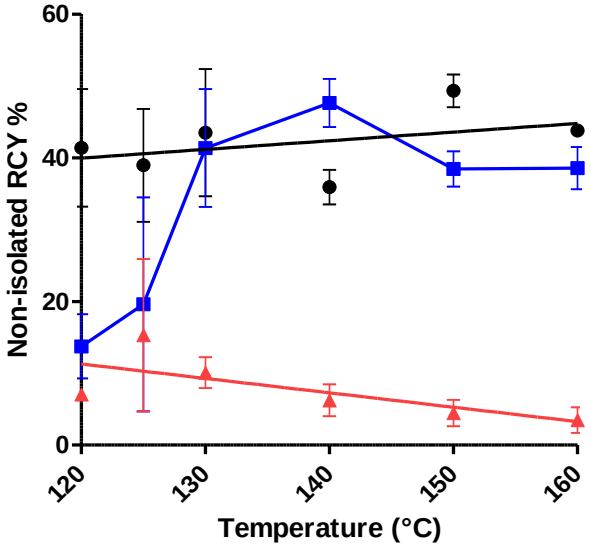

Figure 80 [^{18}F]FBa - [^{18}F]EFB conversion n.i. RCY summary extract from Table 15

Next, the product was isolated by semi-preparative HPLC with method H and concentrated on a C18 light Sep-Pak cartridge in <360 µL ethanol. The purity, identification and specific activity of the product could be calculated from the final QC performed with analytical HPLC method J. Purity was consistently >99% (Figure 81) and the product co-eluted with its cold counterpart upon co-injection (Figure 82c), although a second UV peak representative on an impurity could be observed.

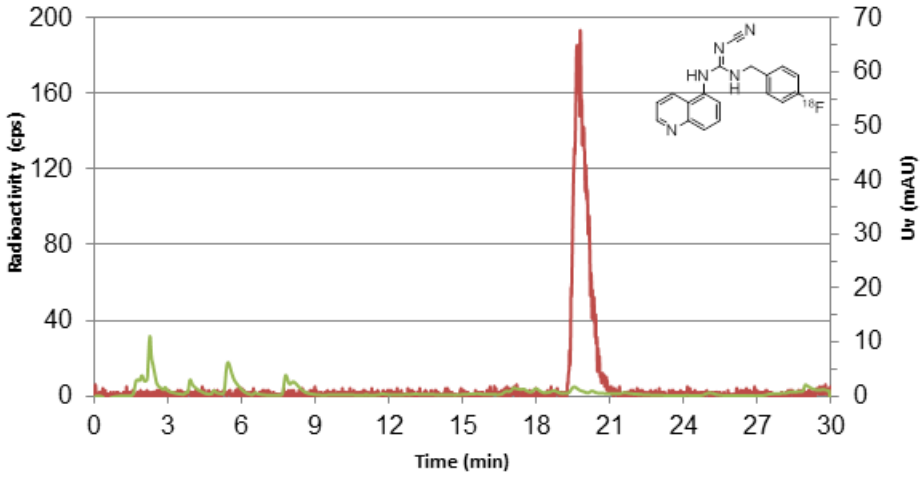

Figure 81 QC run with analytical HPLC method J

In order to further confirm the identity of the radioactive peak, the cold standard co-injected tracer UV chromatogram was compared to that of the final radiotracer alone (Figure 82a).

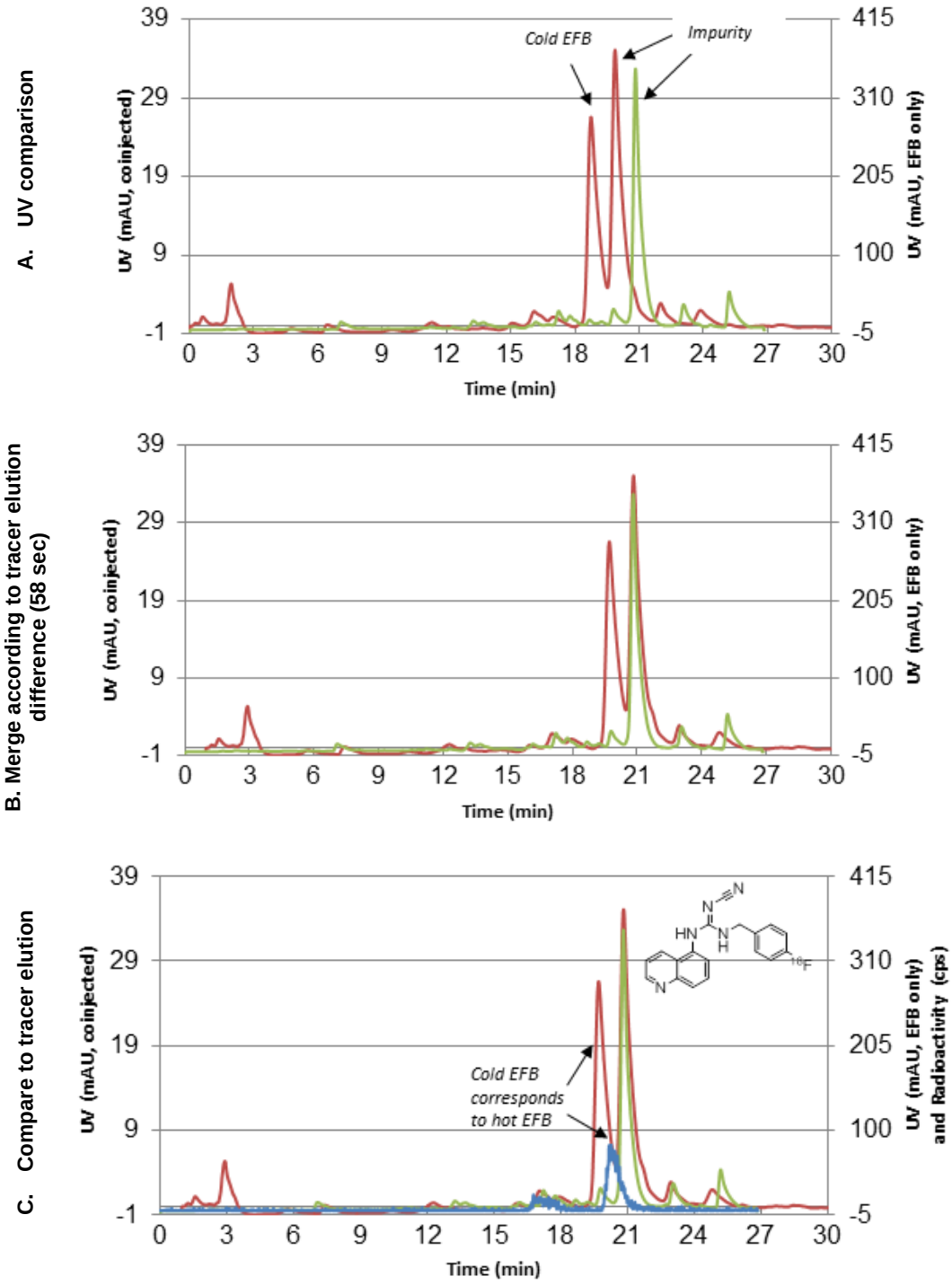

Figure 82 Identification of product with and without cold product co-injection with analytical HPLC method J

The 58 sec elution difference between runs could be accounted for by the variations in retention inherent to the instrumentation setup. Upon merging the two UV traces (Figure 82b) proportionally to the radioactive tracer retention difference (chromatogram not shown), the cold radiotracer eluted at 20 min, before the radioactive peak at 20.8 min (Figure 82.2), as expected from the order and distance between the UV and the radioactivity detectors in our HPLC setup. Mass analysis found that the peak at 21 min represented an impurity of ionised mass of 216

m/u, which could not be further identified. Instead, the fraction corresponding to the hot peak and before the impurity at 21 min, resulted in an ionised mass $(M+H)^+$ of 320 m/u, as desired. Finally, the product was isolated by semi-preparative method H, which enabled the separation of two further peaks, both seemingly corresponding to the desired product by mass detection but likely to be two different, non-interchangeable conformations (Figure 83). Nevertheless, the major peak at 51 min was fully isolable and separable from both the minor peak at 53 min and the strong UV impurity at 54 min, resulting in >300 GBq/µmol specific activity.

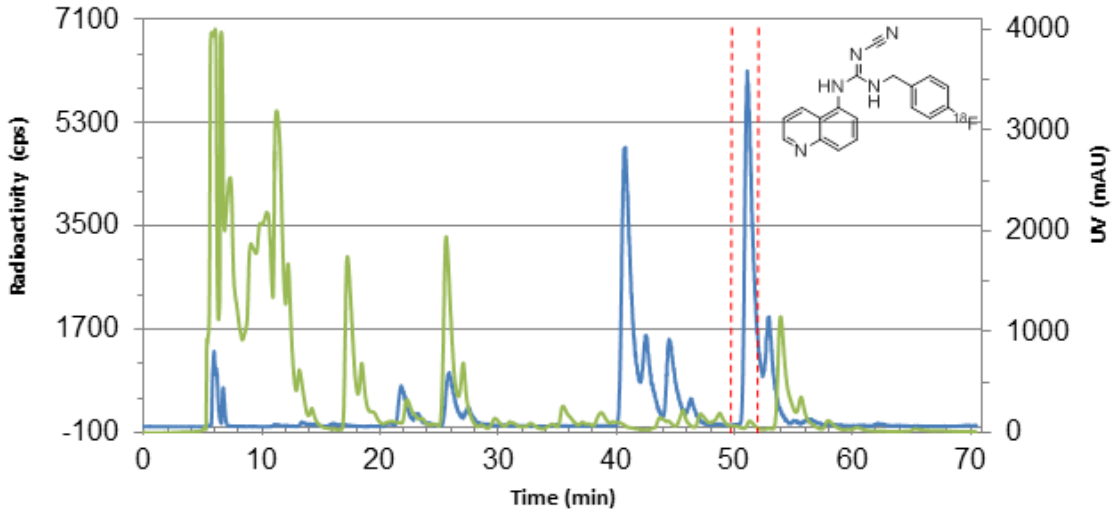

Figure 83 Semi-preparative purification of the product EFB with semi-preparative HPLC method H

1.22 Conclusions

The work presented in this chapter describes the radiosynthesis and purification of four novel ^{18}F tracers. Three of them (the [^{18}F]XFA series) were developed *via* indirect copper alkyne azide cycloaddition radiolabelling. Extensive optimisation was performed to maximise reaction yields and reduce the carrier mass. The product conversion optimisation concentrated on the alteration of the reaction parameters, on the introduction of the rate-accelerating ligand BPDS and on the use of microwave heating. The latter optimisation focused on improving upon the analytical and semi-preparative HPLC methods and on the superior purification of the synthon [^{18}F]fluoroethyl azide. This work resulted in the production of [^{18}F]EFA in 4-26% RCY, >99% RCP and >10 GBq/µmol, of [^{18}F]AFA in 10-42% RCY, >99% RCP and 0.5-61 GBq/µmol and of [^{18}F]OFA in 5-9% RCY, >99% RCP and 0.3-2 GBq/µmol.

Radiosynthesis of [^{18}F]EFB was initially attempted *via* boronic ester radiofluorination. Despite multiple optimisations, this resulted in overall unsatisfactory radiochemical yields. Therefore, an attractive alternative was found in a 3-step indirect radiofluorination strategy incorporating the synthon [^{18}F]fluorobenzyl amine. Upon several optimisation steps, including alteration of the reaction conditions and elaboration of a new solid-phase-extraction-assisted purification strategy, the reaction could afford the desired product in >99% RCP, >300 GBq/μmol and with a modest (3-5%) yet sufficient RCY to perform biological evaluation studies.

Chapter 5

Cell binding assays

Cell binding assays

1.23 Introduction

The affinity and selectivity of the radioligands for P2X7 was established with the use of two different assays. Radioligand binding assays evaluated the tracers' affinity in a cell line where P2X7 expression can be altered upon pre-treatment with different substances and competition assays were employed to indicate the degree of target selectivity. Secondly, non-radioactive calcium influx assays were used to quantify the functional effect of P2X7 antagonists on the ion transporter role of the receptor. The latter assay was used to indicate the affinity of the tracers in the context of this experimental setup for easy comparison with antagonists described elsewhere in the literature.

1.23.1 BV-2 microglia as cell model for the radioligand binding assays

The BV-2 immortalised microglia mouse cell line commonly employed in our division and elsewhere in the context of neuroinflammation studies[537, 538] was chosen as a model for the radioligand binding assays. An important feature of microglia is their innate ability to differentiate their response to external and environmental stimuli. Typically, these brain immune cells reside in a surveiling state, known as M0, where they present ramifications used for surveillance for pathogens and injury. When certain stimuli are sensed, microglia can change their phenotype (a.k.a. polarise) to a pro- or anti-inflammatory amoeboid-looking activated state,[539] known respectively as M1 and M2 (Figure 84).[540] This change involves the expression of inflammatory receptors and the release of a range of cytokines, inflammatory mediators and growth factors.[541]. Of particular interest for this project are the LPS and IL-4 stimuli, treatments of choice to induce the alteration of the P2X7 receptor expression and of the microglial phenotype towards M1 and M2, respectively.

Despite the widespread historical distinction between M1 and M2 microglia, it is important to note that this classification comes with its limitations in that microglia are better known to exhibit a wide spectrum of markers uniquely expressed depending on the exact environmental and pathophysiological conditions.[542] This is particularly true *in vivo*.[543] However, the M1-M2 categorisation remains useful for a preliminary tracer screening and characterisation.

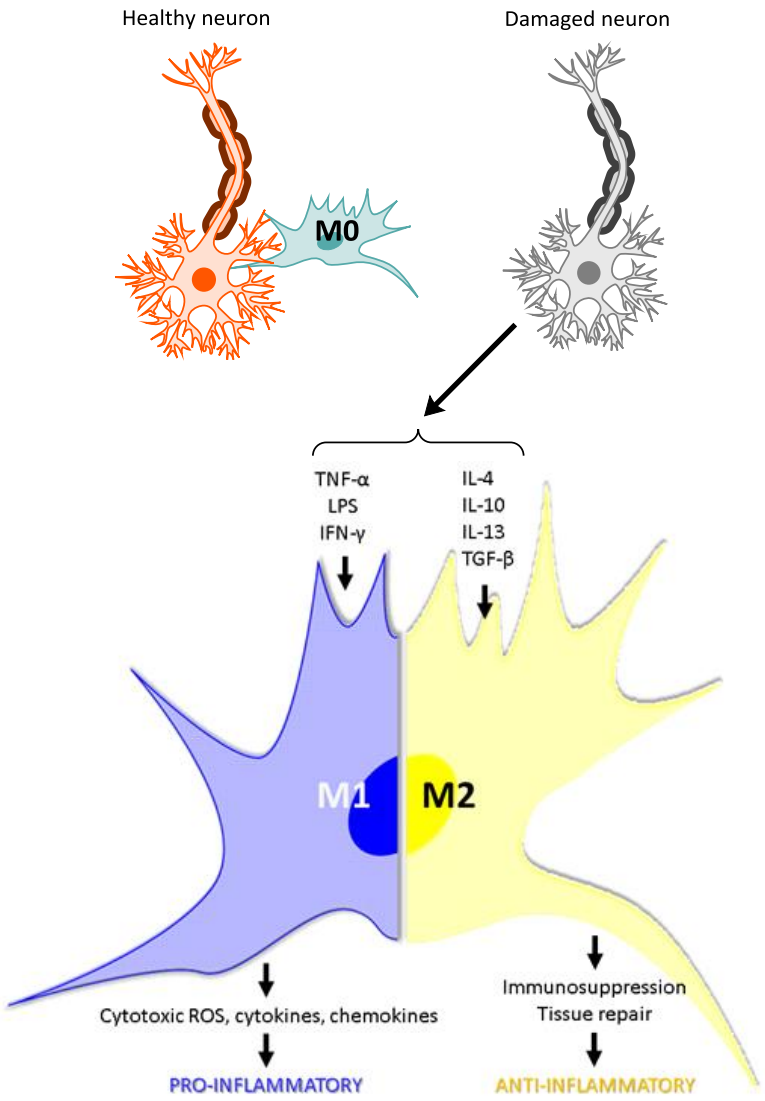

Figure 84 Functional differentiation of microglia in response to neuronal injury

1.23.2 Transfected P2X7 cells for calcium influx functional assays

Calcium influx functional assays rely on the intracellular detection of calcium by a fluorescent dye pre-incubated with an agonist responsible for the ionic flux. The cell membrane-permeable dye needs to be primed by esterase enzymes to its active, negatively charged form before being trapped intracellularly. Upon receptor-mediated intracytoplasmic flux, the calcium is detected by the active dye, which fluoresces (Figure 85).[544] Practically speaking, the value of interest is the difference between the baseline calcium flow in the presence of an agonist (ATP or BzATP) and that with co-incubation of a blocking agent.

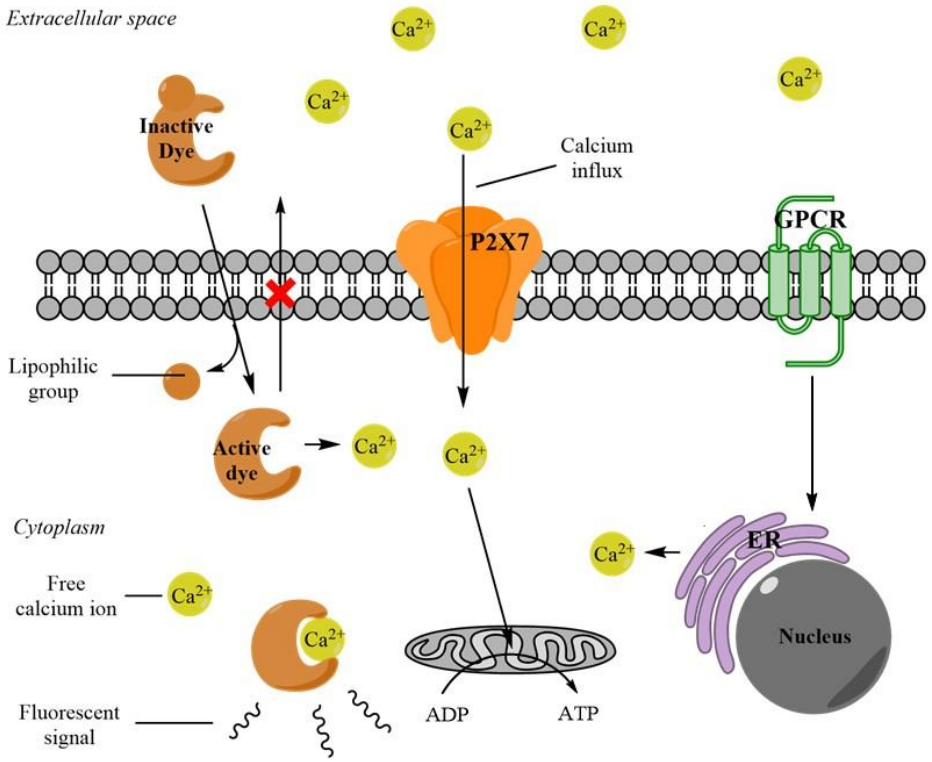

Figure 85 Fluorescence-mediated calcium detection

The typical ATP-mediated Ca^{2+} flow response is a sharp peak followed by a sustained plateau phase (Figure 86).[545] Omission or sequestration of extracellular Ca^{2+} has been shown to uniquely affect the plateau signal. Thus, the latter represents calcium response through membrane receptors, while the peak is characteristic of intracellular Ca^{2+} ($[Ca^{2+}]_i$) release (endoplasmic reticulum and mitochondrial Ca^{2+} stores).[545] The latter, in turn, are regulated by complex pathways beyond the scope of this thesis.[546-548]

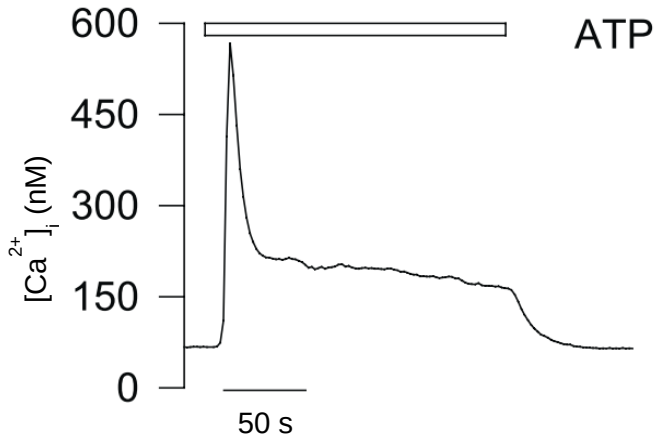

Figure 86 Typical ATP-mediated $[Ca^{2+}]_i$ response in rat cortical astroglial cells

The P2X7-selective antagonist oxATP irreversibly reduces the plateau phase, suggesting a dominant role of P2X7 in calcium influxes.[545] This is further supported by the fact that BzATP, a potent P2X7 agonist, evokes a much higher signal than aspecific P2 agonist ATP.[214] In this work, pEC_{50} values for BzATP in adherent HEK293 cells were taken from Hibell *et al.*[549] and calculated with respect to the Yo-Pro dye uptake response (Table 16). The values remain unvaried with increasing lengths of agonist exposure times.[550]

Table 16 BzATP agonist pEC50 values for a range of P2X7 receptor isoforms[549]

Agonist	hP2X7	rP2X7	mP2X7
100 µM BzATP	6.8±0.14	6.3±0.13	-
200 µM BzATP	-	-	4.7±0.07

1.24 Materials

The materials used in this work were purchased as indicated hereafter. Buffers: Dulbecco's phosphate buffered saline (DPBS, Sigma), heat inactivated foetal bovine serum (FBS, Sigma), RPMI 1640 (Gibco), DMEM-F12 (Sigma-Aldrich), PBS tablets pH 7.4 (Applichem Lifescience). Antibiotics: Gentamicin (Sigma), Penicillin (Invitrogen, Italy), Streptomicin (Invitrogen, Italy). Cell harvesting: Trypsin-EDTA solution (Sigma), RIPA lysis buffer system (Santa Cruz biotechnology). Transfection reagents: pcDNA3 plasmid (Invitrogen), G418 sulfate (Geneticin). Cell viability: MTT (3-(4,5-Dimethylthiazol-2-yl-)-2,5-diphenyl-2H-tetrazolium bromide, Sigma), trypan blue (Sigma). Cell treatments: recombinant Mouse Interleukin-4 (IL-4, Source BioScience), lipopolysaccharide from E.coli (L2880 LPS, Sigma). RT-PCR: RNeasy mini kit (Qiagen, Courtaboeuf, France), iScript™ cDNA synthesis kit (Bio-Rad, Marnes-la-Coquette, France), SYBR Green Supermix (Bio-Rad). Pre-staining treatments: protease free BSA (Acros Organics), Triton X-100 (Yorlab), paraformaldehyde (PFA, Sigma), fluorescein isothiocyanate (FITC) anti-mouse CD16/CD32 2.4G2 Fc receptor block (Insight biotechnology). Antibodies: extracellular domain-targeting P2X7 antibody (Dr Gary Buell, Ares-Serono, Geneva, Switzerland), APR-004 P2X7 rabbit polyclonal antibody (targeting the C-terminal intracellular 576-595 epitope of P2X7, Alomone labs, Jerusalem, Israel), AHP2024 C-terminal AIF-1 goat polyclonal antibody (Abd Serotec now Bio-Rad, UK), DAPI (Prolong Gold antifade reagent by Life technologies, USA and DAKO DAPI), Alexa Fluor 488 and Alexa Fluor 594 conjugated goat

anti-rabbit secondary antibodies (Invitrogen or Insight biotechnology). Assays: Fura-2/AM (Molecular Probes, Inc., Eugene, OR, USA), 2′(3′)-O-(4-Benzoylbenzoyl)adenosine 5′-triphosphate triethylammonium salt (BzATP, Sigma), Brilliant blue G (BBG, Acros Organics).

1.24.1 Buffers

Table 17 Buffers used in this work.

Application	Buffer
Radiotracer solutions for in vitro	DPBS
Radioligand assay washes	DPBS
Cell harvesting in radioligand assays	RIPA
BV-2 cell cultures	RPMI, 10% FBS, 25 mg/mL gentamycin
BV-2 plating for experiments	RPMI, 5% FBS, 25 mg/mL gentamycin
HEK293 and B16 cell cultures	DMEM-F12, 10% FBS, 100 U/mL penicillin, 100 mg/mL streptomycin
Transfected HEK293 and B16 cell cultures	DMEM-F12, 10% FBS, 100 U/mL penicillin, 100 mg/mL streptomycin, 0.2 mg/mL G418 sulfate
Calcium assays	Ca^{2+}-containing (1 mM) saline solution (150 mM NaCl, 5 mM KCl, 1 mM MgCl, 5.5. mM glucose, 20 mM Hepes, pH 7.4)

1.25 Methodology

1.25.1 Radioligand cell binding assays

BV-2 microglia cell culture

Immortalised BV-2 microglia were donated by Professor R. Donato (University of Perugia, Perugia, Italy); they were generated by infecting primary mouse microglia cultures with a v-raf/v-myc oncogene-carrying retrovirus (J2).[551] BV-2 were cultured in RPMI media containing 25 mg/mL gentamycin, supplemented with 10% foetal bovine serum (FBS) for expansion, and 5% FBS when plated for experiments. Pilot experiments to determine the correct cell density to prevent overcrowding and standardise treatments across plate types had previously been performed. All cells were from between passage number 39 and 45. On experiment days, the microglia were polarised by treatment with PBS (1µl/mL), LPS at 1µg/mL or IL-4 at 20ng/mL for 6 hours prior to use for gene expression analysis, immunostaining or radiotracer incubations.

Cell viability: mitochondrial activity MTT assay and trypan blue assay

The viability of microglia was quantified using MTT or trypan blue assays. In the former, the tetrazolium dye MTT is bio-reduced in the mitochondria of viable cells to purple formazan, detectable by spectrophotometry. Following PBS, LPS or IL-4 treatment, cells were exposed to a final concentration of 250 µg/mL MTT for 30 min. Formazan, which is insoluble in cell culture medium was then dissolved in 0.1% DMSO and the absorbance was measured at 490 nm with a spectrophotometer.

The second assay relies on the ability of the trypan blue dye to stain only necrotic and apoptotic cells, as it is otherwise unable to cross cell membranes and bind to intracellular proteins. Upon staining, the cells were manually counted and their viability was recorded as a percentage.

Protein assay

Alongside ensuring consistent cell viability, uniform cell numbers for tracer screening were guaranteed by quantifying the protein content in the final radioligand binding assay step. The samples were analysed by spectrophotometry and protein content was automatically calculated with reference to the absorption at 280 nm.

RT-PCR

Total RNA from microglial cell cultures was extracted with the RNeasy mini kit according to the manufacturer's instructions. RNA quality and concentration were assessed by spectrophotometry with the Nanodrop™ apparatus (Thermoscientific, Wilmington, DE, USA). Total RNA (1-2 µg) was subjected to reverse transcription using the iScript™ cDNA synthesis kit. RT-PCR was performed in duplicate for each sample using SYBR Green Supermix for 40 cycles with a 2-step program (5 seconds of denaturation at 96°C and 10 seconds of annealing at 60°C). Amplification specificity was assessed with a melting curve analysis. Primers were designed using Primer3. The relative expression of *P2RX7*, the gene of interest (GOI), was determined relative to the reference gene of the glyceraldehyde 3-phosphate dehydrogenase (GAPDH). Analyses were performed with Biorad CFX manager 2.1.

Radioligand binding assay protocol

Radiotracers were synthesised and purified as outlined in chapter 4. Radiotracer solutions were formulated in PBS with and without the presence of BBG block and self-block. BV-2 cells plated in the cluster plates listed in Table 18 and treated as outlined previously (top of section 1.25.1) were washed once with PBS and incubated with the radiotracer solutions in triplicate or sextuplicate. Cells were then cooled to 4°C for 1 h, similarly to the tissue incubations described in chapter 6. Thereafter, unbound radiotracer fractions were collected together with 2 x PBS washes. Cells were treated with RIPA for 5 min, scraped and collected together with 2 x PBS washes. From the combined bound fractions, 20 µL of re-suspended cells were collected for protein assays. The bound and unbound fractions from the cell-containing wells and the control empty wells were then analysed by gamma counting with 120 s counting time, background correction, ^{18}F half-life correction, and ensuring that dead time and counting error were <10%. The bound and unbound fraction values for each sample were then summed and normalised to the mean radioactive dose. Results were expressed as normalised bound fractions over the total radioactive dose.

Table 18 Tracer cell binding assay values

Cluster plate	Approx. cell number (x 10^3)	Incubation volumes (mL)	Wash volumes (mL)	RIPA volumes (mL)
24-wells	50-100	0.1	0.4	0.2
12-wells	100-200	0.4-0.5	0.8	0.4
6-wells	1,000	1	1	0.5

1.25.2 Immunostaining

Immunocytochemical (ICC) staining

Cells were plated in chamber slides and grown to confluency in 200 µL gentamicin-RPMI with 5% FBS. After rinsing with 1 x 250 µL PBS, cells were exposed to 4% PFA for 10 min at room temperature. After rinsing with 3 x 250 µL PBS, blocking and permeabilisation was performed with 2% BSA, 5% FBS and 0.1% Triton X for 60 min at room temperature. The block mixture was then tipped off and primary antibodies diluted to the correct concentration (as detailed in Table 19) were applied overnight at 4°C. Following rinsing with 3 x 250 µL PBS, the secondary antibodies were applied for 2 h at room temperature in darkness. After rinsing with 3 x 250 µL

PBS, the chambers were removed and DAPI mounting medium was applied. Visualisation of the immunostaining was performed after 30 min with an EVOS digital fluorescence microscope. Control wells containing PBS instead of primary and/or secondary antibody solutions were implemented.

Table 19 Antibody concentrations for immunocytochemistry and immuno-flow cytometry

Antigen	Concentration of primary antibody/PBS	Concentration of secondary antibody/PBS
AIF1	1:1000	1:250
$P2X_7$	1:400	1:250

Immuno-flow cytometry (IFC)

6 M cells from each treatment type were plated and grown to confluency in gentamicin-RPMI with 5% FBS. Each well was then washed with PBS, trypsinised and diluted with gentamicin-RPMI and 5% FBS in 15 mL Falcon tubes. Triplicate fractions of each sample were centrifuged for pelleting at 423 g for 6 min after each stage of the protocol. After washing with 2 mL PBS, the cells were blocked with FITC Fc receptor blocking solution for 30 min on ice. Without prior washes, the cells were then incubated for 1 h at 37°C on an Innova40 incubator shaker (New Brunswick Scientific) at 100 rpm with 1 mL primary P2X7 APR-004 antibodies at the concentrations indicated in Table 19 with or without control antigens at 1:1 w/w with respect to the antibody. After washing with 2 mL PBS, the cells were incubated in darkness with 1 mL secondary antibodies at the concentration indicated in Table 19 for 1 h at 37°C with 100 rpm shaking. After a 2 mL PBS wash, the cells were pelleted, resuspended in 100 µL PBS and analysed by flow cytometry with a BD FACSCalibur with the settings indicated in Table 20 and the CellQuant and Flowing softwares.

Table 20 Flow cytometry parameters

Parameter	Amplification voltage	Amplification Gain	Amplification modality
FSC	E00	1.50	Lin
SSC	380	1.00	Lin
FL1	405	1.00	Log

1.25.3 Functional assays

The materials and methods employed in this section are described in Cabrini *et al.*[30] The assays were kindly performed by Dr. Simonetta Falzoni in the Di Virgilio laboratory, University of Ferrara, Italy.

Cell cultures and transfections

HEK293 and B16 cells were cultured in DMEM-F12. The media was complemented with 10% heat-inactivated foetal bovine serum (FBS), 100 U/ml penicillin, and 100 mg/ml streptomycin. HEK293 cells were transfected with the calcium phosphate method as described in Rizzuto *et al.*[552] and Morelli *et al.*[553] All cDNAs were in pcDNA3 plasmid. Stably P2X7 transfected, single cell-derived clones were obtained by limiting dilutions. Transfected cells were then kept under selection in the presence of 0.2mg/ml G418 sulfate. Instead, B16 cells natively expressed the mouse P2X7 receptor. Surface expression of P2X7 was performed by indirect immunofluorescence and flow cytometry with a P2X7 mouse monoclonal antibody directed against the extracellular domain of the human P2X7 receptor.

Measurement of cytosolic Ca^{2+}

Experiments were performed in a Ca^{2+}-containing (1 mM) saline solution (150 mM NaCl, 5 mM KCl, 1 mM MgCl, 5.5 mM glucose, 20 mM Hepes, pH 7.4) at 37°C. Cytosolic free Ca^{2+} measurements were performed in a thermostat-controlled and magnetically stirred PerkinElmer fluorimeter with the fluorescent indicator Fura-2/AM, as described previously (Section 1.23.2).[554] Briefly, cells were loaded with 1 μM Fura-2/AM for 30 min in the presence of 250 μM sulfinpyrazone to reduce excretion of intracellular Fura-2. Cells were then rinsed and re-suspended in saline solution at a final concentration of 500,000/ml.[59] Excitation ratio and emission wavelengths were 340/380 and 505 nm, respectively. The calcium ionophore ionomycin (1 μM) was added at the end of each time course as an internal assay control. Inhibitory activity was measured as intracellular Ca^{2+} ($[Ca^{2+}]_i$) flux variation from baseline while in the presence of 100% activating BzATP (100 μM for hP2X7 and rP2X7, 200 μM for mP2X7). Inhibition was measured on both peak and plateau phases. The final value was chosen as the most accurate of the two measurements, or alternatively from the plateau.

1.25.4 Statistical analysis

Data are expressed as means ± SEM from three independent replicates unless otherwise indicated. Statistical analysis was performed with GraphPad Prism 5.0 (San Diego, USA) as a one-way ANOVA with a multiple comparisons Bonferroni post-test unless otherwise specified in the figure captions. Protein assays were analysed with a one-sample t-test against the mean as hypothetical value. Different symbols were used to indicate significant difference towards different controls (* towards empty well, $ towards PBS-treated cells, £ towards LPS-treated cells, unless otherwise indicated). In all cases, one symbol indicates $P<0.01$; two symbols indicate $P<0.005$; three symbols indicate $P<0.001$. Where unspecified, no significance was found.

1.26 Results

1.26.1 PCR primer validation

The suitability of polarised BV-2 cells for P2X7 antagonist evaluation was initially established by RT-PCR. Two primers unique to the P2X7 sequence were tested. Melting curve analysis showed that exons 2-3 and exon 11 both gave suitable amplification at several dilutions (1:10 – 1:6250 with 5 x increments in-between) after 40 cycles in contrast to an unselective primer. Instead, the amplification with lowest dilution (1:2) stalled and was thus avoided. The amplification elicited per cycle was visualised as the difference between the bound fluorescent SYBR Green dye value and the background value (ΔR_n), normalised to the signal of the passive reference dye.

1.26.2 BV-2 treatments elicit alternative P2X7 mRNA expression

Semi-quantitative P2X7 mRNA expression in treated against untreated BV-2 microglia at various time points and concentrations was found with exons-2-3-initiated RT-PCR. PBS, LPS and IL-4 treatments, known to induce M0, M1 and M2 microglial profiles, respectively,[541] resulted in the expression relative to the reference gene GAPDH shown in Figure 87.

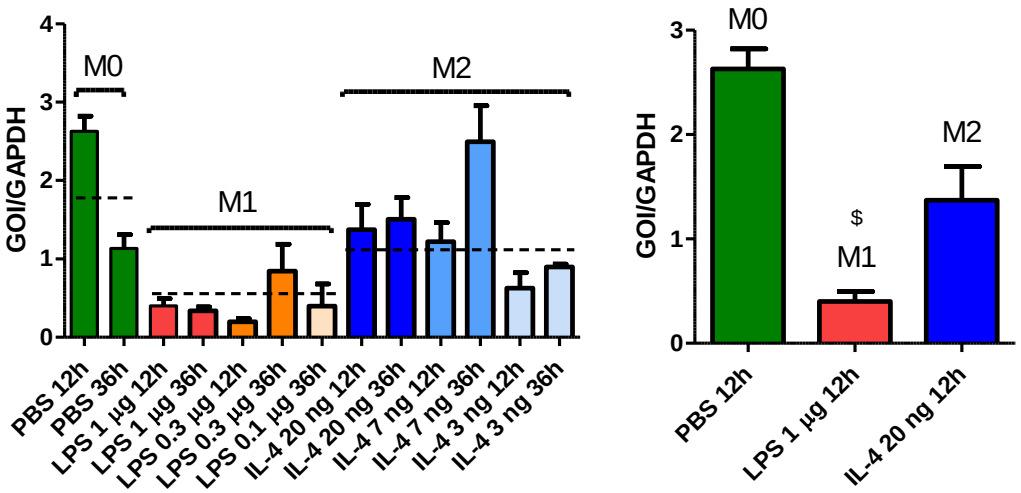

Figure 87 P2X7 mRNA expression in M0, M1 and M2a BV-2 cells as assessed by RT-PCR analysis

The P2X7 receptor resulted significantly downregulated with increasing concentrations of LPS already at 12 h, while it was only mildly downregulated with IL-4. Moreover, the expression difference between 1 µg LPS and 20 ng IL-4 increased proportionally with concentration already at 12 h. These treatments were thus employed throughout this work together with 12 h PBS in equal volumes to the other treatments (significance of $P<0.01$ with respect to LPS, but non-significant with respect to IL-4).

1.26.3 BV-2 P2X7 receptor expression

Receptor surface expression was evaluated visually with immunostaining. Visual inspection revealed P2X7 expression specific to the outer cell membranes and processes in PBS, IL-4 and LPS-treated cells. Low non-specific binding of the receptor was observed. Figure 88 also shows that P2X7 co-localised with human Iba-1 (a.k.a. AIF-1), a marker of microglial activation, in IL-4-treated cells.

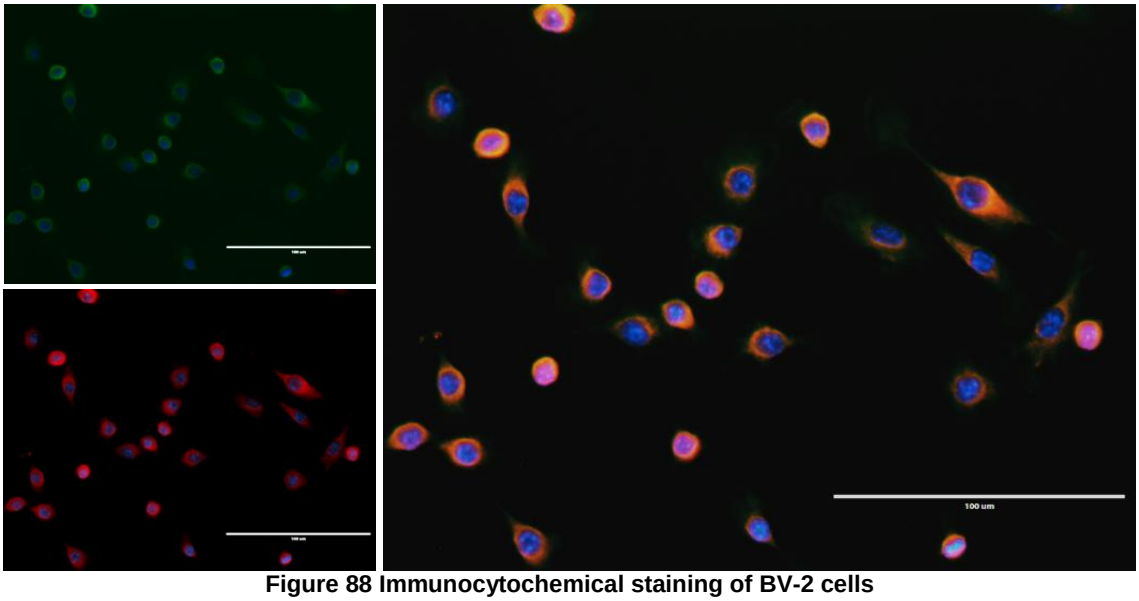

Figure 88 Immunocytochemical staining of BV-2 cells

1.26.4 Radiotracer binding correlation to P2X7 genetic expression in BV-2 cells

[^{18}F]AFA (0.65 nM at 1.17 GBq/μmol), [^{18}F]EFA (3.3 nM at 0.1 GBq/μmol), [^{18}F]OFA (7.55 nM of at 0.08 GBq/μmol) and [^{18}F]EFB (11 nM at >300 GBq/μmol) were incubated for 1 h at 4°C in alternatively polarised microglia and in empty wells (Figure 89). The binding of [^{18}F]AFA and [^{18}F]EFA reflected the P2X7 mRNA expression with respect to the three BV-2 treatments. With [^{18}F]AFA, LPS showed a statistically significant 96% decrease in binding with respect to PBS, and a significant 97% decrease with respect to IL-4. No significance was reached in the 143% increase in binding in IL-4 with respect to PBS. Instead, LPS decreased [^{18}F]EFA binding by 69% with respect to PBS.

However, all tracers' cell binding did not result significantly higher than that by the empty wells. In all experiments, no significant change in MTT output from control (PBS) conditions was found and trypan blue assays indicated >99% cell viability. Consistent protein concentrations in each well were found by MTT and protein assays.

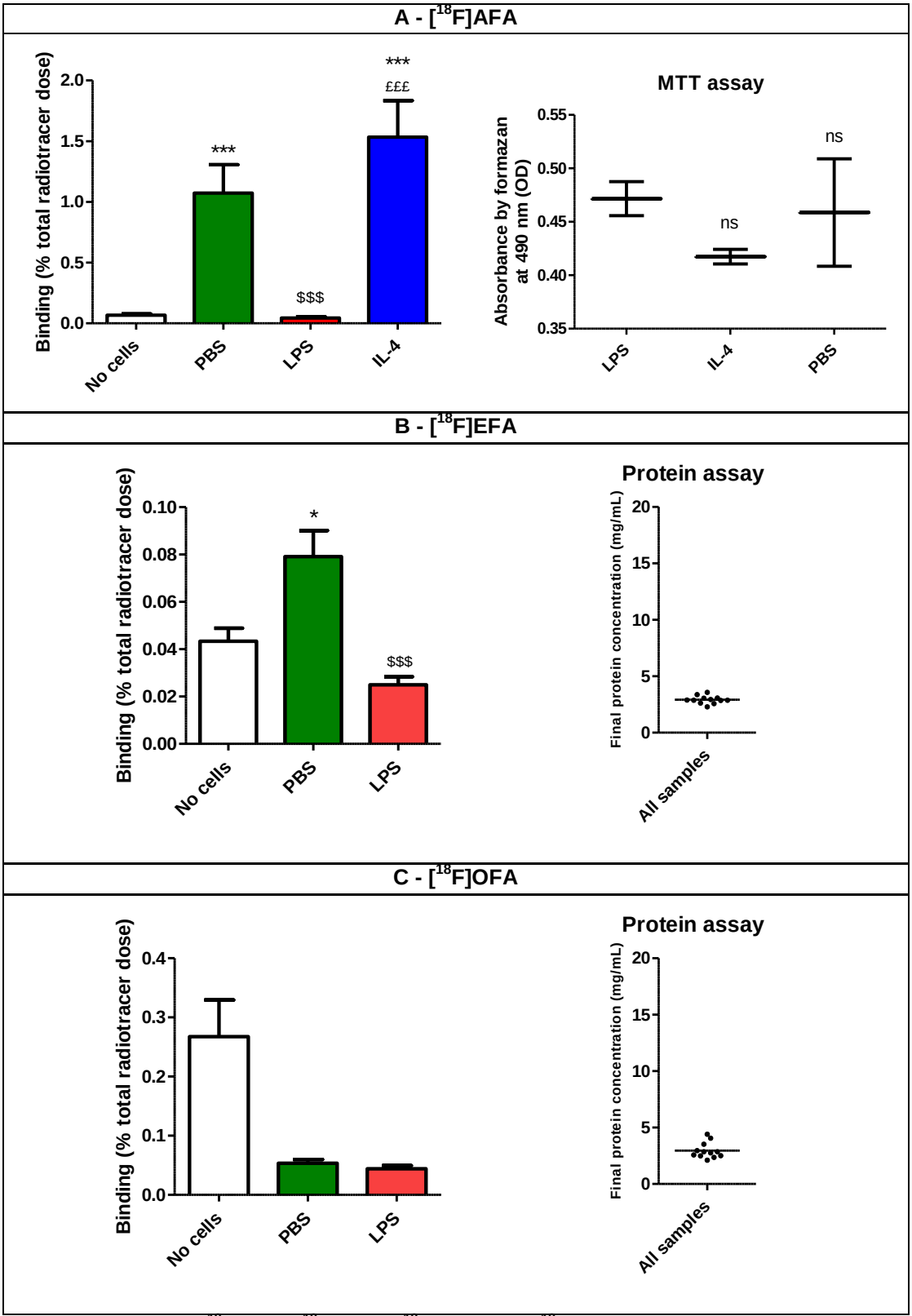

Figure 89 Binding of [^{18}F]AFA , [^{18}F]EFA , [^{18}F]OFA and [^{18}F]EFB in differentially polarised BV-2 cells and in empty wells

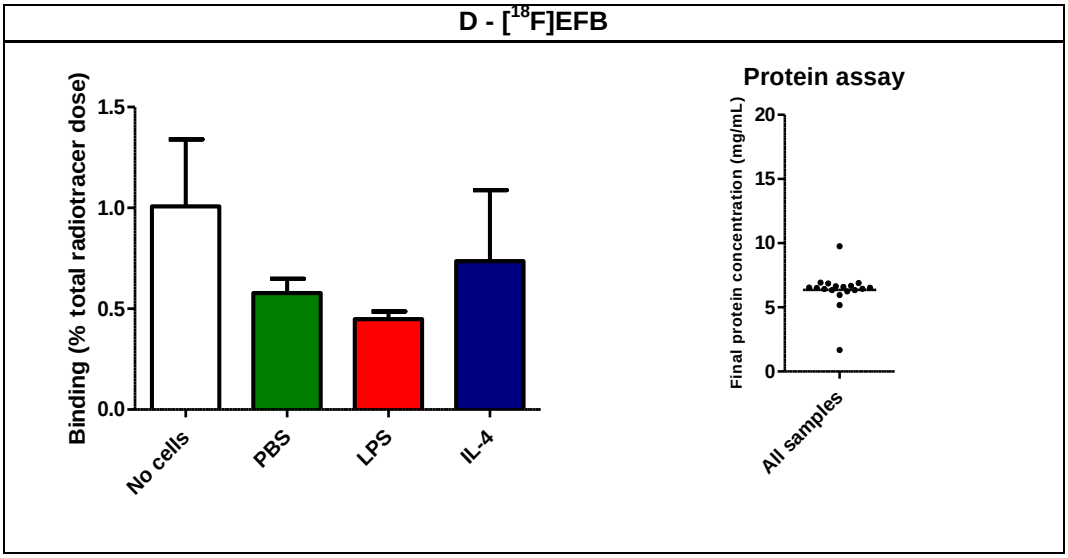

Figure 89 (continued)

1.26.5 Exploration of the causes of high well binding

The steady state conditions of the assays were challenged by varying the concentration (75 pM - 7.5nM) and time of incubation (1 h – 4 h) of [^{18}F]AFA (1.1 GBq/µmol) (Figure 90). The temperature was left unvaried so as to maintain a state of relative cells stasis with minimal receptor expression alterations.[555]

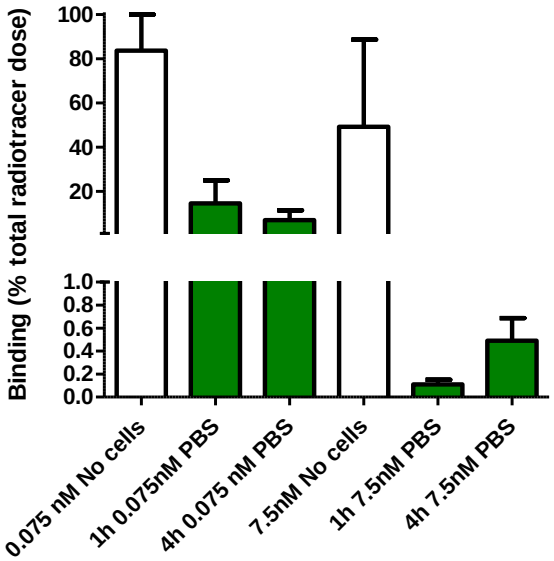

Figure 90 [^{18}F]AFA kinetic binding in BV-2 cells and related protein assay (

The tracer cell binding did not significantly change between 1 h and 4 h of incubation and decreased with increasing concentrations. Also, significantly higher binding was observed in unseeded wells, suggesting a lack of involvement of kinetic and saturation binding in the observed effect. Moreover, at low [^{18}F]AFA concentrations the cells appear to be significantly

inhibiting the binding to the well. Protein assays showed consistent cells numbers in each fraction.

Secondly, the ability of the well material to bind the tracers was investigated. The experiment was conducted with [^{18}F]AFA (13 nM, 60 MBq/µmol) and unfunctionalised aqueous [^{18}F]HF in plastic and glass wells (Figure 91). No significant variation was observed between well types or the radiochemical species. Also, the binding was generally very low compared to the total dose applied (Figure 91). This experiment indicated no special affinity of our radiotracer for the plastic wells used in previous experiments.

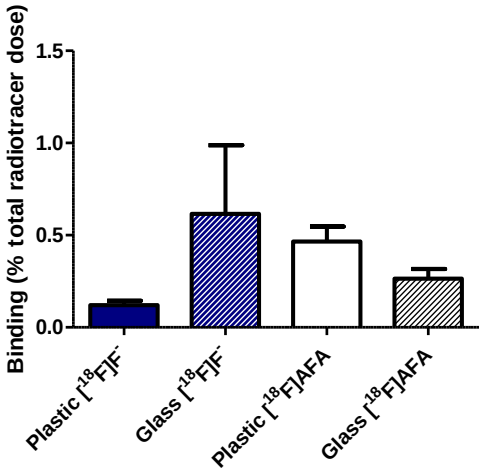

Figure 91 [^{18}F]AFA and aqueous [^{18}F]F$^-$ binding in plastic and glass wells (

Next, direct receptor blockade was attempted with the use of P2X7-selective antagonist Brilliant Blue G (BBG) and the cold standard of AFA (self-block, SB) at a range of concentrations.

[^{18}F]AFA (0.2 nM, 1.13 GBq/µmol for BBG and 0.9 nM at 0.55 GBq/µmol for SB) was incubated with 0 M to 1 mM BBG in 10^3 increments and with 0 M to 100 µM SB with 3 x increments. Both in the presence of either SB or BBG (Figure 92) no significant variation in binding was observed. These results corroborated the hypothesis that the binding observed was either unspecific to P2X7 or that the receptor expression levels were too low to yield sufficient bound radiotracer detection.

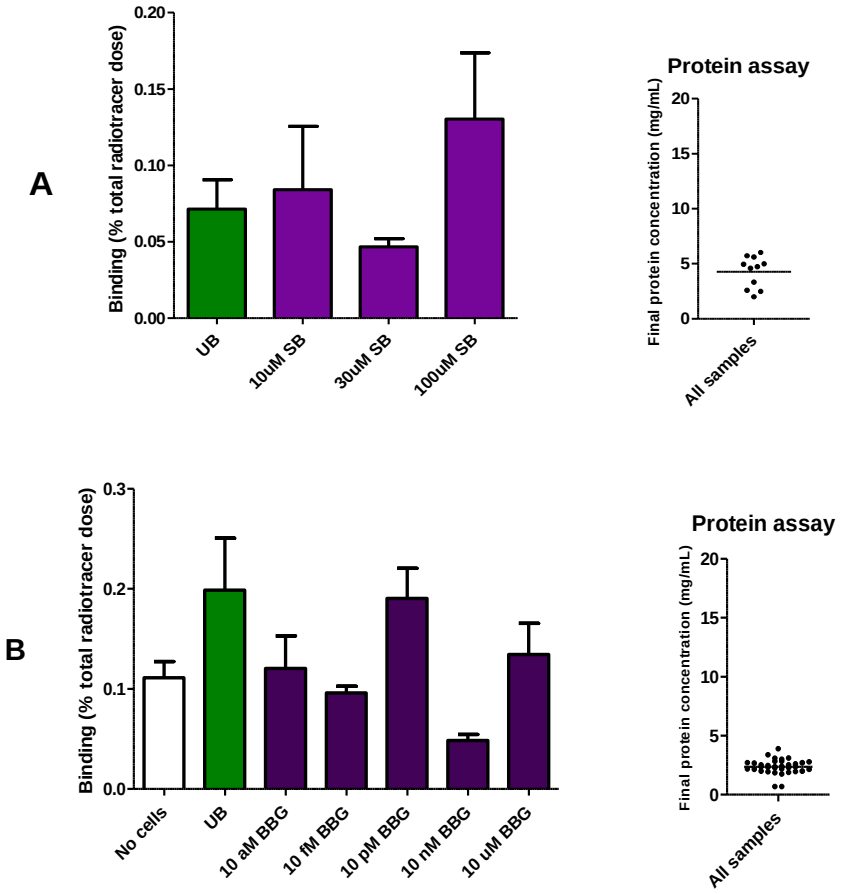

Figure 92 [^{18}F]AFA binding with and without block in BV-2 cells

1.26.6 Quantitative BV-2 P2X7 receptor expression

In order to elucidate whether the receptor expression levels were sufficiently high for radiotracer detection, flow cytometric analysis of P2X7 in polarised BV-2 cells was performed. This showed low significance between the fluorescence signal in treated cells and that arising because of non-specific binding (secondary antibody only and control peptide co-incubated cells), while antibody-free cells displayed a significantly lower signal (Figure 93). Given the narrow difference between specific and non-specific fluorescence signal (Figure 94), the low receptor expression could explain the lack of ability to discriminate between selective and unselective P2X7 radiotracers.

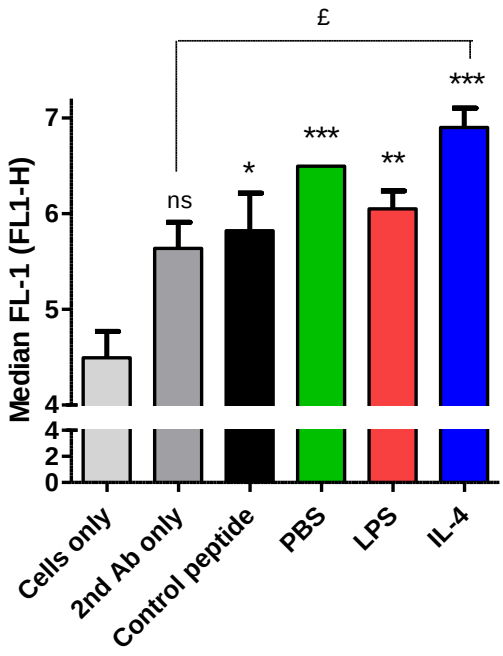

Figure 93 Variation in fluorescence intensity in alternatively treated cells and controls

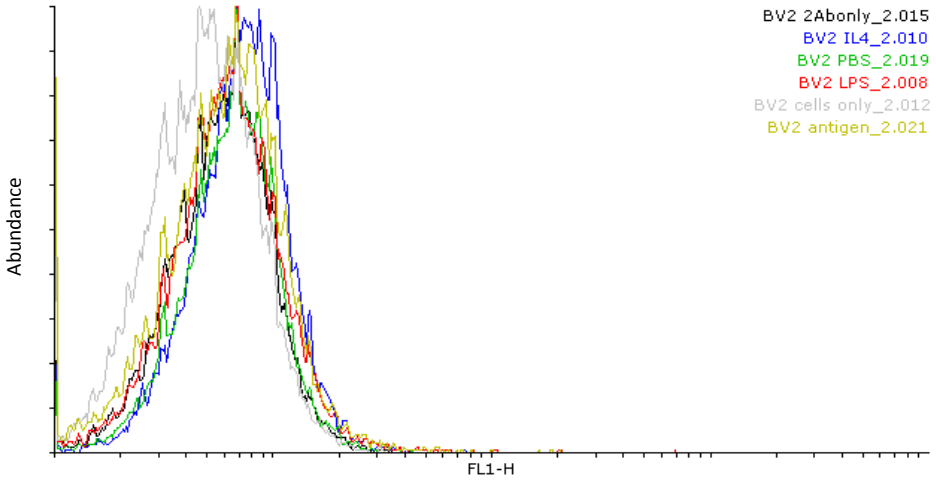

Figure 94 Overlay histogram of all cell populations as analysed by flow cytometry

1.26.7 Calcium influx functional assays

Dose-inhibition curves for the 4 tracers were measured against the established P2X7 blockers A-740003 and BBG, both with nM affinity for the radiotracer.[214]

All compounds were evaluated over a range of concentrations between 0.01-25 μM. Data were plotted as the variation from the baseline $[Ca^{2+}]_i$ flux. The data were then logarythmically transformed and fitted to a four parameters variable slope before IC_{50} values were extracted and converted to K_i measures *via* the Cheng-Prusoff equation. Figure 95 and Table 21 show, respectively, the data with fitted slopes and the extracted binding data.

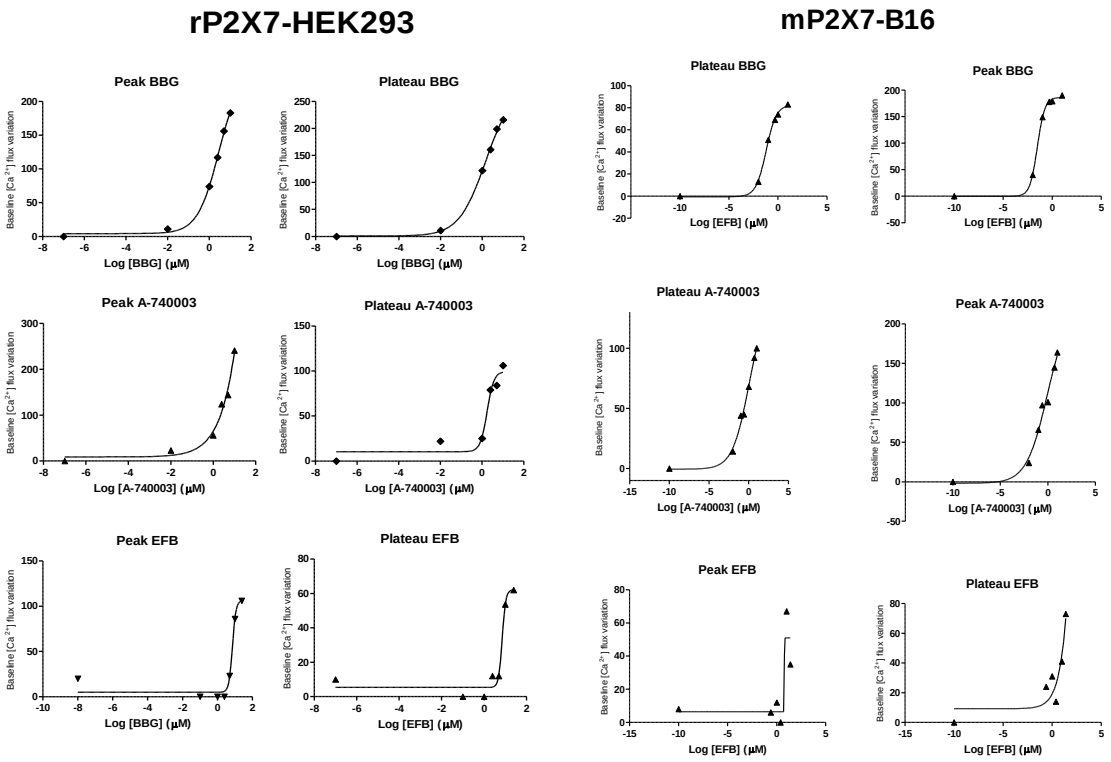

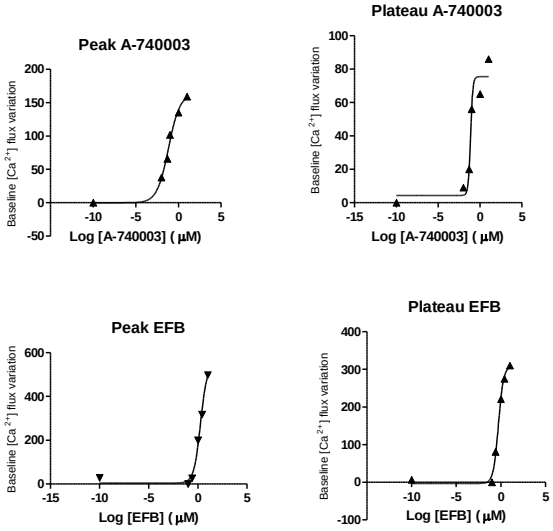

Figure 95 Calcium influx assays in the presence of P2X7 selective control blocks A-740003 and BBG Table 21 Calcium influx binding data for selected antagonists and P2X7 receptor subtypes

Antagonist	P2X7 isoform	[BzATP] (mM)	Peak IC_{50} (nM) (R^2)	Plateau IC_{50} (nM) (R^2)	IC_{50} (nM)	pIC_{50} (M)	Literature pIC_{50} (M)	K_i (nM)	pK_i (M)
EFB	Human	0.100	1791 (0.99)	**534.0** (0.99)	534.0	6.27	-	0.850	9.07

EFB	Rat	0.100	**7213** (0.97)	7233 (0.97)	7213	5.14	-	36.1	7.44
EFB	Mouse	0.200	**6005** (0.82)	$7.309x10^{9}$ (0.84)	6005	5.22	-	547	6.26
AFA	Human, rat, mouse	h,r 0.100 m 0.200	**-**	-	-	<4	-	-	<4
OFA			**-**	-	-	<4	-	-	<4
EFA			**-**	-	-	<4	-	-	<4
A-740003	Human	0.100	**66.07** (0.99)	74.02 (0.96)	66.07	7.18	7.36±0.04;[556] 7.36±0.01; [214]	0.100	9.98
A-740003	Rat	0.100	$1.101x10^{9}$ (0.98)	**1738** (0.95)	1738	5.76	7.75±0.03;[556] 7.74±0.02;[214] 7.14 [67]	8.67	8.06
A-740003	Mouse	0.200	845.2 (0.98)	**1082** (0.99)	1082	5.97	6.57±0.04 (BALB/C);[214] 6.17 ± 0.05 (C57BL/6)[214]	97.2	7.01
BBG	Human	0.100	-	-	-	<4	<4;[556] 6.57±0.23 [215]	-	<4
BBG	Rat	0.100	2885 (1.00)	**1441** (1.00)	1441	5.84	5.08±0.07;[556] 5.09± 0.06;[214] 6.90±0.97 [215]	7.21	8.14
BBG	Mouse	0.200	31.01 (1.00)	**61.66** (1.00)	61.66	7.21	<4 [214]	5.59	8.25

No data are presented for AFA, EFA and OFA as the compounds did not induce functional inhibiton in this model. Also, no data were collected for BBG in hP2X7-H293 cells as the compound is poorly selective towards the human strain of the receptor. EFB exhibited a low nM affinity for the human P2X7 receptor, while a more moderate affinity was seen in rodent receptors.

1.27 Discussion

The work presented in this chapter aimed at exploring the degree of affinity and selectivity of the compound series developed. These results come with limitations which prevent us from fully establishing the extent of P2X7 targeting. This section intends to explore the latter and present ideas for future research into the validation of the library of tracers.

1.27.1 P2X7 expression in polarised microglia

P2X7 expression in BV-2 cells subject to alternative treatments was evaluated by mRNA RT-PCR with reference to GAPDH, a universally abundant, stably and constitutively expressed housekeeping gene involved in eukaryotic cell glycolysis.[557] The choice of GAPDH as the reference gene does not come without limitations. In particular, the gene can on occasion undergo upregulation by LPS, making it problematic as a control.[558] Despite this, there are no reports of its upregulation in BV-2 cells, where it is widely employed as a housekeeping gene.[541] The RT-PCR revealed a statistically significant downregulation of the receptor mRNA after LPS treatment with respect to PBS treatment; whereas lower (albeit not statistically significant) expression was observed in 1 µg LPS compared to 20 ng IL-4 treatment at 12 h (Figure 87). Instead, the expression levels did not significantly differ between treatments and from the background signal, suggesting that protein expression is generally low in this cell model. Internalisation can be excluded as a cause of low surface receptor presentation as immunocytochemistry localised the receptor uniquely on cell membranes. On the other hand, ligand binding, especially in an agonist capacity, was not ICC-tested. This might have induced receptor internalisation, as sometimes observed for P2X7 in the presence of ATP.[559]

The mRNA expression levels suggest that P2X7 is characteristic of a resting (M0) and neuroprotective (M2) microglial phenotype. This matches previous observations in dynamically-activated mouse peritoneal macrophage P2X7 mRNA.[560] Conversely, in human peripheral blood mononuclear cells and monocytes P2X7 mRNA was shown to become mildly upregulated in the presence of IL-4 (x1.2), whereas a stronger increase in expression was seen after LPS treatment (x2.0).[561] This was not the case in BV-2 and N9 LPS-treated microglia[562, 563] as well as in a further study on alternatively polarised mouse macrophages, where no P2X7 mRNA variations were found.[564] Furthermore, western blot analysis of BV-2 and N9 microglia P2X7 receptor expression demonstrated that P2X7 protein expression was downregulated upon stimulation by M1-inducing LPS.[563] This was in contrast with the finding of this work that the latter is unaffected by polarising treatments at a protein expression level (Figure 93, section 1.26.6). Taken together, these results suggest that P2X7 regulation differs between cell types and depends strongly on the experimental conditions.

On a different note, *in vivo* P2X7 expression was not explored in this work, hence defining whether P2X7 is more characteristic of an M1 or and M2 phenotype *in vivo* is not possible. However, an overall tendency towards upregulation in response to any (pro or anti-inflammatory) stimulus seems to dominate the literature, while its expression in M0 polarised microglia appears generally low.[164, 565, 566]

1.27.2 Radioligand binding assays

The radioligand binding assays in alternatively treated BV-2 cells resulted in a surprisingly high binding in the empty wells, which was unexpected particularly since immunocytochemical staining clearly indicated P2X7 expression on the outer cell membranes (Figure 88). This binding pattern did not appear to be caused by oversaturation of the target, as demonstrated by the persistence of this effect even at picomolar concentrations of [^{18}F]AFA (Figure 90), albeit future studies will need to explore the binding at further concentrations and with the remaining radiotracers. Moreover, empty well binding was not imputable to the well material, nor it differed from that of unfunctionalised [^{18}F]fluoride, as demonstrated by the constant binding observed in different well materials and with different radioactive molecules (Figure 91). Additionally, independent from the empty well binding, after 1 h of incubation steady state appeared to have been reached, as demonstrated by the lack of significant binding variation after 4 h (Figure 90). Yet, receptor blockade indicated a lack of P2X7-selective binding for [^{18}F]AFA (Figure 92), while alternative microglial polarisation correlated to the binding of [^{18}F]AFA and [^{18}F]EFA but not [^{18}F]OFA or [^{18}F]EFB (Figure 89). These trends remained poorly significant in light of the high well binding, which suggested either lack of specific binding to P2X7, high non-specific binding or too low receptor expression for radiotracer binding detection, calling for further investigations. The latter should involve the use of a benchmark P2X7 tracer such as [^{3}H]A-804598[67] so as to fully elucidate the extent of P2X7 cell expression. Also, the use of P2X7-transfected cells such as P2X7-HEK293 would maximise receptor expression and ensuing detection of putative tracer binding.

1.27.3 Calcium influx assays

Receptor-transfected cells are ideal to maximise calcium fluxes and facilitate their detection.[567] In this work, human (hP2X7) and rat (rP2X7) P2X7 HEK293 cells were employed, while for the mouse receptor (mP2X7), natively high P2X7-expressing B16 cells were more readily available. Cell transfection has the effect of rendering the signal from all other calcium pathways negligible. Thus, IC_{50} values arising from plateau or peak readings (as discussed in section 1.23.2) were substantially indistinguishable. Further complications however arose from the use of different cell lines and transfected receptors. The assay was performed in both human and rodent cells lines. The human and rat receptor cavities present similar topologies and physicochemical properties, where the most significant difference is a phenylalanine residue (Phe288) in the rat receptor in place of a tyrosine (Tyr288) in the human isoform.[394] Despite functional behaviour similarities to the rat receptor, the human recombinant P2X7 displays a distinct pharmacological profile with respect to agonist and antagonist sensitivity.[568] In fact, in order to induce maximal calcium influx, hP2X7-HEK293 cells require lower agonist concentrations than mP2X7-B16 cells. Additionally, the chosen P2X7 agonist BzATP is much more potent than the endogenous ligand ATP.[214]

Furthermore, IC_{50} values are not fully comparable between different cell lines as they measure the effectiveness of an inhibitor towards the blockade of a specific biological function in a precise cellular environment. Also, they can considerably be affected by the composition of the buffer, the temperature of the assay and the concentration of the agonist. Ideally, the experiments should have been designed in such a way as to explore the effect of these variables on the inhibition effect.[549] Nevertheless, it is possible *via* the Cheng-Prusoff equation to derive the inhibition constant (K_i), an absolute measure of inhibitor affinity to the receptor.[569] It must be noted that also this measure can fluctuate to some extent according to the binding components in the incubation system, the substrate specificity and any substrate or inhibitor depletion.[570]

The Cheng-Prusoff equation is:

$$Ki = \frac{IC50}{\frac{[A]}{[EC50]} + 1}$$

where [EC_{50}] represents the concentration of agonist required for the receptor to be 50% effective, and [A] is the concentration of agonist employed in the IC_{50} measurement. The equation can only be applied in this form to competitive antagonists,[571] such as A-804598, the parent scaffold to this work's radiotracer library.[229] Besides, A-804598 might also be interacting with an allosteric pocket, as on one occasion even the application of a high mM concentration of BzATP was unable to fully reverse its inhibitory activity.[67] Additionally, the fact that the structural modifications introduced upon the parent scaffold do not modify the ligand binding modality is an assumption, the breach of which renders the use of this equation inappropriate.

In our hands, the calcium assays showed no specificity of the three XFA compounds for the target. Instead, EFB showed 0.850 nM, 36.1 nM and 547 nM K_i in human, rat and mouse P2X7 receptors, respectively, when considering the peak or plateau dataset displaying the best fit to a four parameters variable slope. As indicated by the R^2 values in Table 21, these were not optimal for all datasets, showing the need for further replicates and for higher antagonist concentrations. Additionally, control P2X7 antagonists A-740003 and BBG failed to match literature affinities. For instance, according to Able *et al.*[67], the compound A-740003 would have an rP2X7 pK_i of 7.57±0.04 M, while in our hands it resulted in 8.06 M affinity. This warrants further work into this assay, with the primary aim of revalidating the protocol with the known inhibitors and a secondary aim of repeating the work on all the novel molecules.

1.28 Conclusions

In this chapter, two *in vitro* assays for the determination of the tracer library target affinity were reported. A radioligand binding assay was based on alternatively polarised BV-2 microglia. However, the results were corrupted by the low signal-to-noise level as indicated by the high well binding across the entire tracer library. Still, RT-PCR indicated that P2X7 is genetically under-regulated in LPS-treated M1 microglia and upregulated in IL-4-treated (M2) when compared to PBS-treated (M0) cells, whereas ICC staining indicated unique expression on outer cell membranes and processes. However, IFC indicated a lack of distinction between expression levels resulting from alternative BV-2 polarisation, suggesting post-translational receptor regulation or surface expression variations induced by ligand-binding.

Furthermore, a preliminary calcium influx functional assay was performed on hP2X7-HEK293, rP2X7-HEK293 and mP2X7-B16 cells. Here, compound EFB resulted potent against P2X7, with K_i affinities of 0.850 nM, 36.1 nM and 547 nM for human, rat and mouse P2X7 receptors, while no XFA receptor reached <0.1 mM selectivity for P2X7. Nevertheless, this assay did not display optimal curve fitting in all cases, which demands further replicates and the use of higher antagonist concentrations. Additionally, control P2X7 antagonists failed to match literature affinities, indicating a need for further validation of the assay protocol. Despite the lack of conclusive quantitative data, given that EFB showed some extent of functional affinity for P2X7, it was selected as a candidate for *in vivo* evaluation, whereas the binding of the [^{18}F]XFA ligands was assessed in rodent tissue models, as discussed in the following chapters.

Chapter 6

Tissue binding assays

Tissue binding assays

1.29 Introduction

Tissue autoradiography relies on the phenomenon of luminescence, as displayed by phosphors applied on a screen. Exposure to radioactivity excites individual electrons within the phosphor, which then slowly relax down to their ground state upon photon emission. The latter is captured with high precision by a Phosphorimager, enabling resolutions up to 10^{-4} m (thus higher than in PET) and proving an excellent technique to understand in detail which regions a tracer binds to.[572] The results can be quantified by calculating the digital light units (DLU) emitted within user-defined regions of interest (ROIs). This value can be directly correlated to the concentration of tracer present in each ROI *via* a radiotracer-concentration-to-DLU standard curve.[573]

Tissue autoradiography can be performed in two contexts: *ex vivo* and *in vitro*. *Ex vivo* involves culling the animal after it has been injected with the radiotracer and following an amount of time necessary for the radiotracer to distribute to the target organs. This can be useful to understand and quantify precisely the whole-body distribution and tissue accumulation of tracers. For CNS-targeting compounds, it is often employed to assess the extent of blood-brain barrier (BBB) permeability. *In vitro* autoradiography is performed entirely on culled animals. It is still useful to assess the specificity and kinetics of binding of a compound, in particular regardless of its biodistribution and metabolic profile but still in a native setting. Moreover, it can be employed to evaluate tissue receptor expression. In this work, to provide a rough evaluation of the brain distribution and target selectivity of the [^{18}F]XFA radiotracers, regardless of their ability to penetrate the BBB, *in vitro* autoradiography was the technique of choice.

1.29.1 Introduction to brain injury models and polarised microglia

Immature hypoxic ischemic (HI) mice were employed as a model for assessing the tracer uptake in an inflamed tissue. This model is characterised by an ischemic event induced by unilateral carotid artery cauterisation. This in itself does not induce injury, as perfusion is maintained through collateral circulation. However, on subsequent exposure to hypoxia, a hemispheric ischemia occurs as blood flow preferentially decreases in the ligated hemisphere.[574]

This is an acute model of neuroinflammation. Within minutes from the generation of the infarct, oxygen/glucose deprivation causes neuronal death and an immediate microglial response (Figure 96).[575] Then, after a period of latency in which microglia and macrophages infiltrate the ischemic areas to combat the expanding encelopathy, a delayed secondary neuronal death phase occurs. In the core of the infarct, pan-necrosis ensues. Necrotic tissue is characterised by the presence of amoeboid-like microglia, whereas in the proximity of living neurons, active yet ramified glia have been observed.[576] These gradually become predominantly and ubiquitously activated and acquire a round morphology. Microglia initially respond to the insult by assuming an M2, neuroprotective phenotype. However, ischemic neurons then prime microglial polarisation towards an M1, neurotoxic phenotype. In the cortical zones around the ischemic infarct (penumbra), an early recruitment of activated microglia and infiltrated macrophages was found to rescue brain tissue from the expanding neuronal necrosis.[577] In the external perimeter of the lesion, microglia display a phagocytotic behaviour and this was also corroborated in temporarily macrophage-depleted rodents.[578, 579] Moreover, a stronger neuroinflammatory response to HI is present in postnatal day 9 compared to postnatal day 30, suggesting a higher suitability of the more immature model for the purposes of this study.[580] Further details on the role of microglia in ischemic brain injuries can be found in these reviews.[581-583]

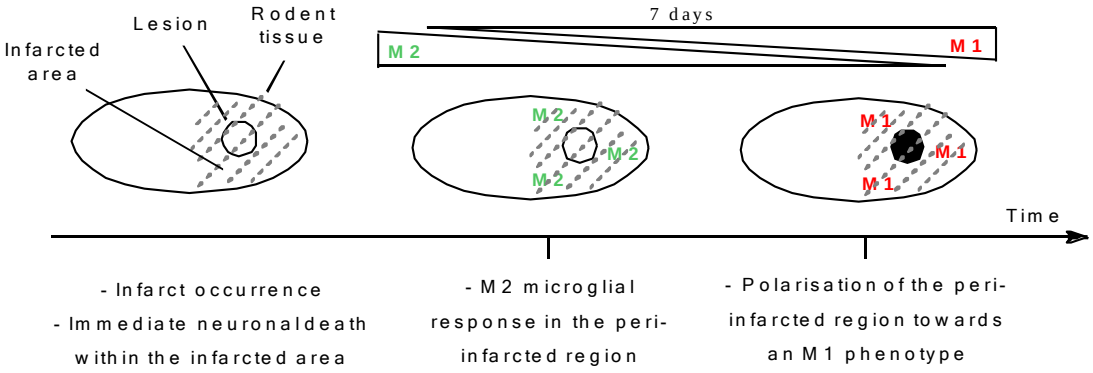

Figure 96 Representative schematic of the microglial response to a hypoxic ischemic infarct over time in rodent tissues

In the unfolding of these events, P2X7 expression is temporarily upregulated in the periphery of the insult. This is particularly characteristic to microglia until day 4 post-ischemia, closely resembling the M2 microglial expression pattern. Thereafter, the expression returns to basal levels in microglia, then to increase on neurons and astrocytes and in the peri-necrotic region.[186]

These patterns are observed selectively in the ipsilateral region (Figure 97).[584] However, on one occasion widespread P2X7 and activated microglia tissue distribution, including the contralateral side, was shown at 24 h post-ischemia by IHC.[565] Also, on other cell types, such as on oligodendrocyte precursor cells and on radial glial cone cells, a decrease in P2X7 expression in the cortical, subcortical white matter and hippocampal regions was reported.[585, 586]

1.29.2 Aims

The work presented in this chapter aimed at:

- Developing an *in vitro* autoradiography assay with wild type rat brain tissue slices.
- Exploring the tracer binding in the native inflamed tissue setting of the hypoxic ischemic mouse, resulting in a preliminary assessment of the tracer binding profiles.

To this aim, the regions of interests for the analysis of the radiotracer binding in HI tissues were:

- A hotspot region focused on the binding in the subcortical, infarcted lesion.
- A penumbra region in the cortical, peri-infarct region.
- A whole-hemisphere region for full comparison between the damaged and the control, intact brain.

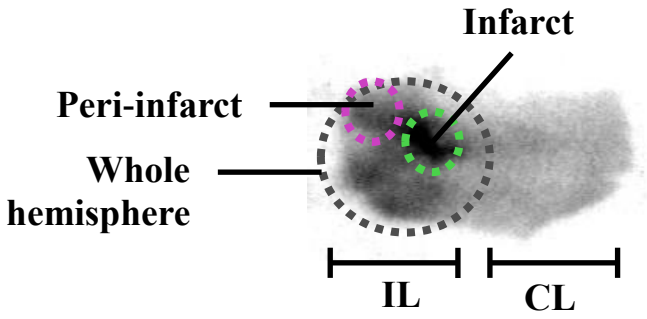

Figure 97 Hypoxic ischemic mouse tissue regions of interest of radiotracer binding

1.30 Methodology

1.30.1 Animal provenance and tissue preparation

BALB/C mice pups were raised in-house at St Thomas' Hospital after mating between wild-type Harlan UK Ltd. BALB/C mice. Isoflurane-anesthetised postnatal day 7 mice were subject to a

left carotid artery cauterisation. The animals were then awaken and placed in a hypoxic chamber (8% oxygen) for 3.5 hours.[587] One day later, the mice were sacrificed by an authorised Schedule 1 procedure. The brains were removed, submerged in a 20% sucrose solution for 20 min and snap-frozen in liquid nitrogen before storage at -80°C. The frozen cortical (hypoxic ischaemic mouse) 20 µm brain sections were then cut with a Maskold 5030 microtome using an optimal cutting temperature (OCT) embedding medium to mount the tissue on the sample holder. The slices were then thaw-mounted onto microscope slides which were then stored at -20°C until the time of assay. Instead, wild-type male Sprague-Dawley rats weighing 300 g were bought from Charles River Laboratories International, Inc. and were directly culled without prior procedures. Following dissection, their brains were cut into sagittal slices. The animals were housed under pathogen-free conditions in a temperature- and humidity-controlled environment and given access to food and water ad libitum. All experimental procedures were performed after over a week of acclimatisation in the new environment and in accordance with the Animals (Scientific Procedures) Act 1986, Amendment Regulations 2012 and approved by the local ethics committee. Project licence: Licence holder – Prof Reza Razavi, PPL 70/8230 and Dr Diana Cash, PPL 70/8480. Personal Licence: Licence holder: Enrico Fantoni, PIL 70/3001. All experiments were carried out in the Rayne Institute, St. Thomas' Hospital, King's College London between 2015 and 2016.

1.30.2 Tracer tissue binding assays and autoradiography

Radiotracers were synthesised and purified as outlined in the experimental section. Radiotracer solutions at 0.1-5 nM were formulated in PBS with and without the presence of 10 µM Brilliant Blue B (BBG), 10 µM ATP or 10 µM self-block. Tissue slides were allowed to slowly thaw to room temperature prior to washing in cold PBS. The slides were then completely submerged in 15 mL of buffered radiotracer (20 mM PBS/0.1% BSA, pH 7.4 at 4°C) and incubated for 1 h at 4°C as determined from time course and saturation experiments. The slides were then submerged for 2 x 1 min in cold 20 mM PBS and 1 x 1 min in cold distilled water. Following drying in a cool airstream, the slides were exposed overnight at room temperature together with 3 standards of different concentrations to ^{18}F-sensitive phosphor screens (Amersham, UK) in X-ray cassettes. Phosphor screens were then imaged using a GE Healthcare Typhoon or a

Version 5.0 Perkin Elmer OptiQuant. Regions of interest were defined with Image J (Version 1.48, open source software).

1.30.3 Statistical analysis

All data were background corrected and expressed as mean ± SEM from three independent replicates unless otherwise indicated. Statistical analysis was performed with GraphPad Prism 5.0 (San Diego, USA) as a two-way ANOVA with Bonferroni post-test unless otherwise specified in the figure captions. *: P<0.01; **: P<0.005; ***: P<0.001 with respect to the contralateral (CL) unblocked (UB) tissue slices. $^{\#}$: P<0.01; $^{\#\#}$: P<0.005; $^{\#\#\#}$: P<0.001 with respect to the ipsilateral (IL) unblocked (UB) tissue slices. Where unspecified, no significance was found.

1.31 Results

1.31.1 Method development in wild type rat brain

All incubated tracers were >95% pure with variable specific activity and concentration, both because of the inherent variability of the tracer production at this stage of the project.

Incubation of 0.1 nM of 60 GBq/µmol [^{18}F]AFA with sagittal wild type rat cortical brain slices (Figure 98) was performed according to a literature procedure.[67]

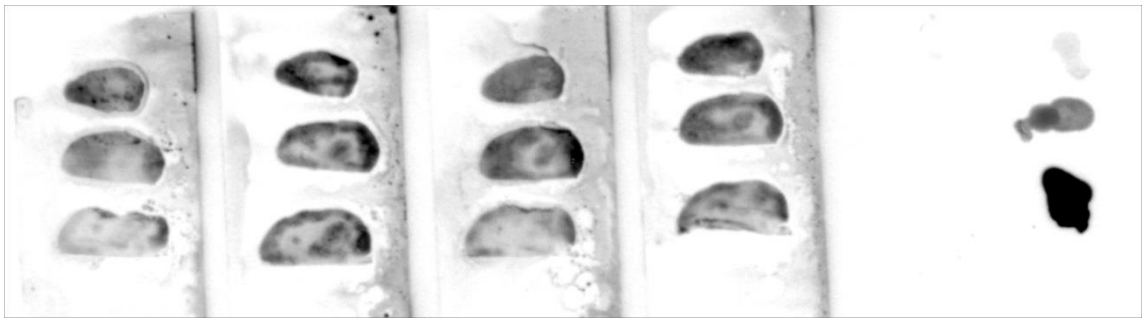

Figure 98 Preliminary [^{18}F]AFA incubations

The method was further explored with wash lengthening to 2 min, giving widespread non-specific binding, while Trizma or PBS buffering did not impact the tracer binding. The study was repeated in rat mid-brain slices and 10.6 GBq/µmol [^{18}F]AFA at 0.2 nM, in the presence and absence of 1 mM P2X7-selective block BBG over 2 - 180 min. After 1 h, 2 h or 3 h incubation, similarly heterogeneous binding was observed in the unblocked slices. Instead, receptor

blockade resulted in increased binding in selected brain regions identified by comparison with the Paxinos rat brain atlas (Figure 99).[588]

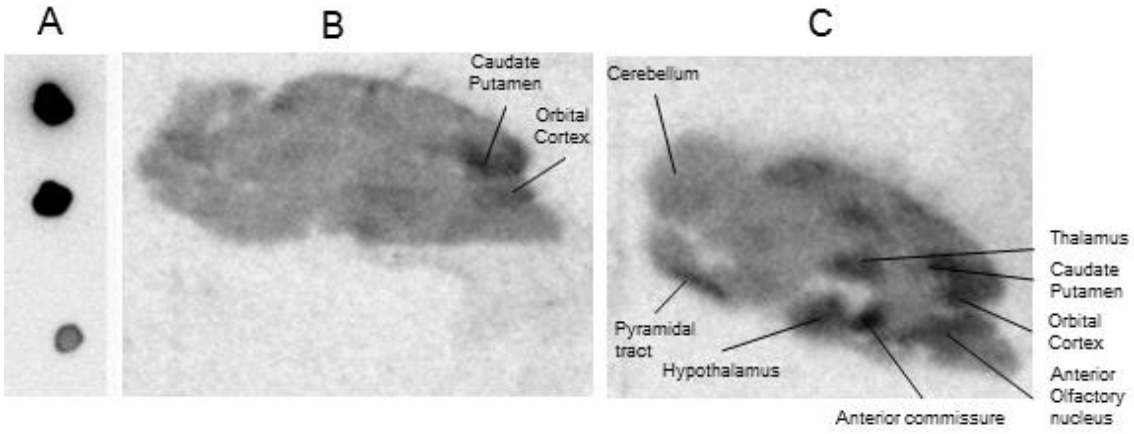

Figure 99 Rat mid-brain slices from the incubation of 0.2 nM, 10.6 GBq/μmol [^{18}F]AFA

1.31.2 Hypoxic ischemic mouse tissue binding of [^{18}F]XFA tracers

The conditions employed in wild type rat brains were integrally translated to immature hypoxic ischemic (HI) mouse brains for the study of [^{18}F]AFA, [^{18}F]EFA and [^{18}F]OFA binding.

Incubation of 11.7 GBq/μmol [^{18}F]AFA at 0.2 nM resulted in a marked increase in binding in all regions compared to the respective control regions in the non-ischemic hemisphere. Conversely, the lesion site displayed uneven binding across replicates, resulting in a lack of significance with respect to the control hemisphere (Figure 100). Binding in the hypoxic hemisphere did not decrease significantly with BBG blockade in any of the ROIs, whereas an increased binding was observable in the infarct region. Instead, significant inhibition of binding was observable in the presence of self-blockade. In line with the previous findings, no decrease in binding was found in the infarct region.

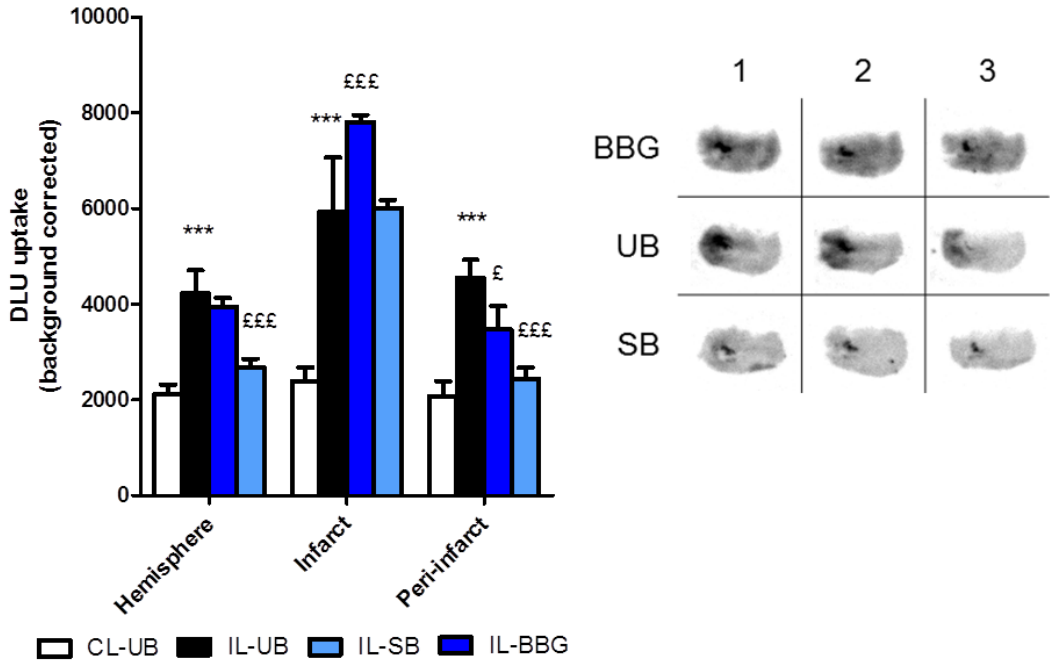

Figure 100 Tissue binding in 3 ROIs in HI mouse brain slices incubated with unblocked or blocked [^{18}F]AFA

Next, incubation of 5.4 GBq/μmol [^{18}F]EFA at 0.2 nM showed increased, but not significant binding in the damaged whole hemisphere and peri-infarct regions compared to the contralateral side, and significant decrease in binding with BBG blockade.

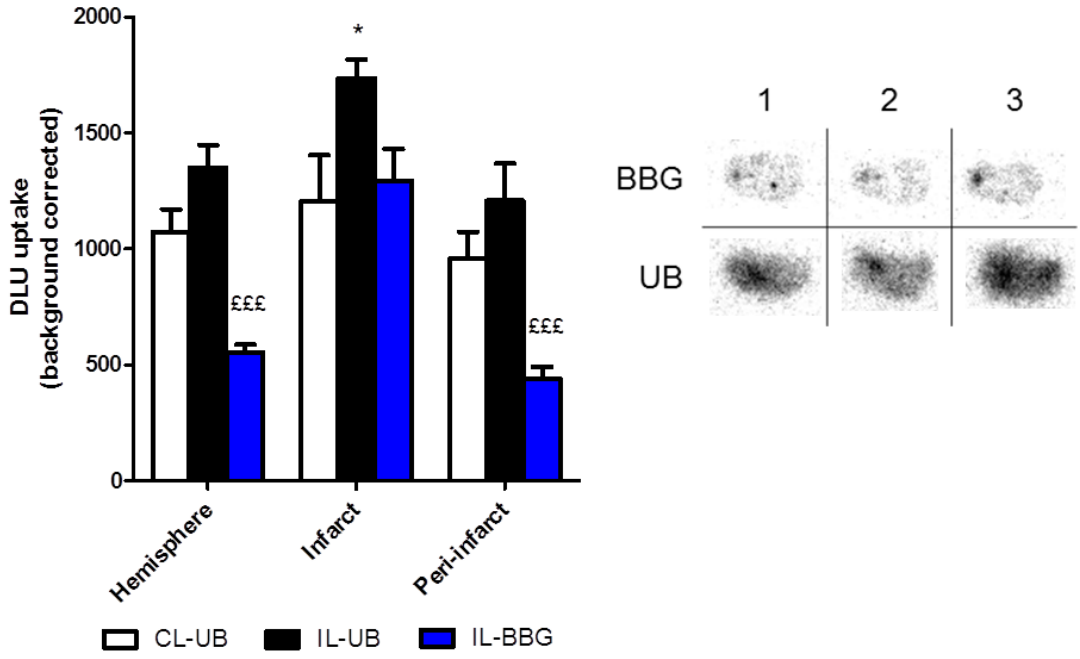

Figure 101 **Tissue binding in 3 ROIs in HI mouse brain slices incubated with unblocked or blocked [^{18}F]EFA**

Instead, in the infarct region no variation of binding as found with BBG blockade. Unfortunately, the images were not as clear as in the other incubation studies, resulting in a lower incidence of statistically significant binding compared to [^{18}F]AFA.

Finally, incubation of 0.73 GBq/μmol [^{18}F]OFA at 0.2 nM gave a marked binding increase in the damaged hemisphere, particularly in the lesion site. However, statistically significant increase in binding was observed upon blocking in the infarct and whole hemisphere regions, indicative of extensive non-specific binding.

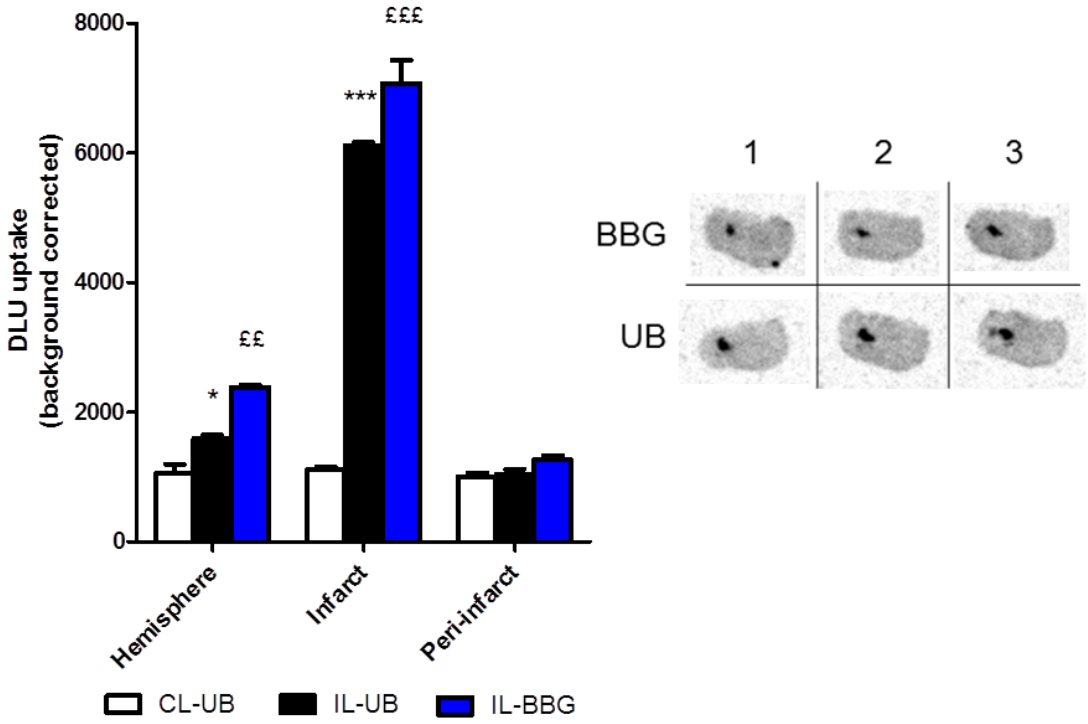

Figure 102 Tissue binding in 3 ROIs in HI mouse brain slices incubated with unblocked or blocked [^{18}F]OFA

1.32 Discussion

1.32.1 Wild type rat brain tissue autoradiography

Previous P2X7 autoradiography studies on wild type rat brains by Able *et al.* and Lord *et al.* with [^{3}H]A-804598 and [^{3}H]JNJ-54232334, respectively, showed discordant binding profiles. The former displayed heterogeneous binding, with hot spots in the colliculus, hypothalamus, olfactory nucleus and thalamus.[67] However, in a later study with P2X7 receptor blockade, hippocampal and cortical binding was attributed to non-specific binding.[231] Instead, autoradiography with the second tritiated compound showed ubiquitous binding with very low

non-specific binding.[231] Somewhat in accordance to the latter study, in this work a relatively homogeneous binding was seen with [^{18}F]AFA, while patches of increased binding were found in the caudate putamen and orbital cortex. With BBG blockade the binding appeared increased, particularly in the thalamus, hypothalamus, anterior commissure and olfactory nucleus but not the colliculus. This effect was surprising, as BBG is a well-established selective blocker with 10-12 nM affinity for P2X7.[215]

A possible direct BBG-AFA interaction was investigated by HPLC. However, no reduction in AFA and BBG signature peak intensities and no appearance of new peaks after 1 h of co-incubation at 25°C were found, indicating a lack of direct interaction between the two compounds in isolation. This did not exclude positive allosteric binding to P2X7, as suggested for other P2X7 ligands by Michel *et al.*[227, 228] and Muller.[17] However, the latter is usually concentration-dependent, while in the case under discussion tracer binding was consistently higher over a range of concentrations of BBG and of the tracer. Conversely, the lack of known tracer affinity leaves the possibility of an alternative P2 receptor selectivity for AFA, in which case the observed BBG-induced patterns might have been a consequence of reduced non-specific binding to P2X7 while increasing the specific binding for the unknown target. Further experiments are required to clarify this effect. In particular, it appears necessary to analyse the receptor expression upon BBG exposure, to study the allosteric modulation potential of AFA and to investigate the tracer binding upon receptor blockade by an alternative antagonist.

1.32.2 Hypoxic ischemic mouse brain tissue autoradiography

In the hypoxic ischemic mouse model at 24 hours post-ischemia, binding was expected in the peri-infarctic region, where the P2X7 and M2 microglial expression levels are highest. In line with the expectations, [^{18}F]AFA displayed peri-infarct binding and low non-specific binding. [^{18}F]EFA presented high non-specific binding, possibly due to recognition of the quinoline moiety by proteins other than the target. Finally, [^{18}F]OFA showed poor correlation with P2X7 expression in the periphery of the infarct, while instead high peri-necrotic binding was observed. However this could be an artefact arising from the tissue lesion. The loss of target selectivity could be imputable to the decrease in SAR or to the increased H-bonding ability of [^{18}F]OFA with respect to [^{18}F]AFA.

Further complications arose with the presence of blockers. Self-blocking, but not P2X7-selective BBG blocking reduced the binding of [^{18}F]AFA, suggesting selective binding to a target other than P2X7. [^{18}F]EFA binding was reduced by BBG, suggesting P2X7 selectivity, albeit in the presence of high non-specific binding, as previously discussed. Finally, [^{18}F]OFA binding was increased by BBG, suggesting an allosteric modulation effect, similarly to that of [^{18}F]AFA.

This mixture of responses points to a variety of tracer binding modes which is in need of further scrutiny. Yet this study provided a useful starting point for further explorations. Further work should also aim to clarify the P2X7 expression levels in the ischemic tissue as well as the contralateral side by immunohistochemical staining. It must however be noted that there is uncertainty regarding the exact M1/M2 phenotype within and surrounding the infarct over time, as highlighted by the discrepant observations reported in the literature.[589, 590] This might well be because of the difficulty in studying in a living model such a mutable condition as is neuroinflammation without upsetting the microenvironment and thus the condition itself.[591]

1.33 Conclusions

In conclusion, in wild type rat brains a fairly homogeneous binding was observed for [^{18}F]AFA. This was heterogeneously increased in the presence of BBG blockade, suggesting allosteric modulation, binding to a different target or other effects which merit further inspection. In the immature HI mouse brain, [^{18}F]AFA correlated with the expected P2X7 tissue distribution at 24 h post-ischemia, whereas [^{18}F]OFA and [^{18}F]EFA displayed, respectively, low target affinity and high non-specific-binding. Thus, [^{18}F]AFA appeared as the most promising tracer in this series, albeit with limitations which call for further investigations into this scaffold.

Chapter 7

In vivo tracer evaluation

In vivo tracer evaluation

1.34 Introduction

This chapter focuses on the preliminary *in vivo* evaluation of tracer [^{18}F]EFB, the most promising candidate out of the tracer series developed.

1.34.1 *In vivo* pharmacokinetic considerations

While the pharmacokinetic parameters described in section 2.1.1 (chapter 2) provide a good description of the receptor-ligand interaction, the *in vivo* picture is complicated by the increasing complexity of the system. Preclinically, the tracer undergoes absorption (except when injections are intravenous), distribution, metabolism and excretion (ADME); the nonspecific binding is affected by the presence of biomolecules in plasma and non-target tissues, metabolites can form and the studies are not necessarily being conducted under true equilibrium conditions as free and bound ligand concentrations change over time.[592]

A frequently used model to interpret and quantify *in vivo* tracer distribution is the two tissue-compartment model. Compared to the model adopted for *in vitro* tracer quantitation (chapter 2) in the two-tissue model (Figure 103), the plasma is treated as a separate compartment from the tissue of interest. The latter is divided into a free + non-specific binding compartment and a specific binding compartment. This model can be exploited to calculate the binding potential given that the free tracer in arterial plasma is assumed equal to the free tracer within the target tissue at equilibrium, which is a reasonable assumption for drugs that passively diffuse across tissue barriers.[333] However, it is not always practical to sample the tracer in arterial plasma over time due to logistic difficulties. Hence, often the binding potential is more conveniently calculated from the specific to non-displaceable tissue tracer ratio at a unique equilibrium time point (the time point of maximal specific binding, calculated with respect to a reference background region). The binding potential calculated from this method is called “non-displaceable binding potential” (BP_{ND}) and is treated as an estimate of the true BP, as the non-displaceable tracer in the tissue actually represents only a fraction of the true free plasma concentration, and the reference region is only an estimate of the background in the region of interest.[333, 593]

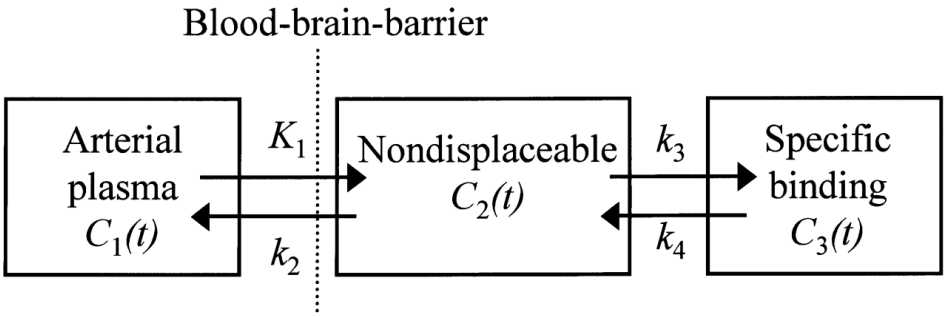

Figure 103 Two-tissue compartment model

Another difference *in vivo* is the presence of endogenous ligands that might lower the total number of binding sites available. Thus, instead of B_{MAX}, one should refer to the total receptor concentration as a combination of available (B_{AVAIL}) and unavailable ($B_{UNAVAIL}$) binding sites.[592] Furthermore, the concept of volume of distribution (V_D) has been adopted from clinical pharmacology. In the context of *in vivo* imaging, the volume of distribution (V_T) is defined as the ratio of the concentration of radiotracer in plasma (in kBq/mL) to that within a target organ volume (in kBq/cm^3), expressed in mL/cm^3. In other terms, it represents the volume of plasma that would be required to account for the radioligand in the target organ volume. V_T is the sum of free tracer volume of distribution (V_F), that of the specifically bound tracer (V_S) and that of the non-specifically bound tracer (V_{NS}).[594]

Additionally, *in vivo* it is necessary to take into account not only the concentration of tracer, but also its specific activity, as low specific activity can now lead to saturation of the target sites, with consequent non-specific binding increase and alteration of the signal readout. The challenge that the radiochemist faces here is that unless the specific activity is high, the overall mass of tracer becomes significant and could saturate the target. In a study carried out by Hume *et al.*,[595] when maximal receptor occupancy for an *in vivo* imaging experiment is constrained to 1%, a variable specific activity/radioactivity ratio threshold was estimated depending on the tracer binding affinity (Figure 104). For example, to image dopamine D_2 receptors in rat brains with a tracer such as ^{3}H-raclopride (B_{max} = 0.0235 pmol/mg; K_d = 1 nM)[596] at 50 GBq/umol, a limit of 2.5 MBq of activity are injectable in a rat (Figure 104b) if the constraint of ≤1% receptor occupancy is to be achieved.

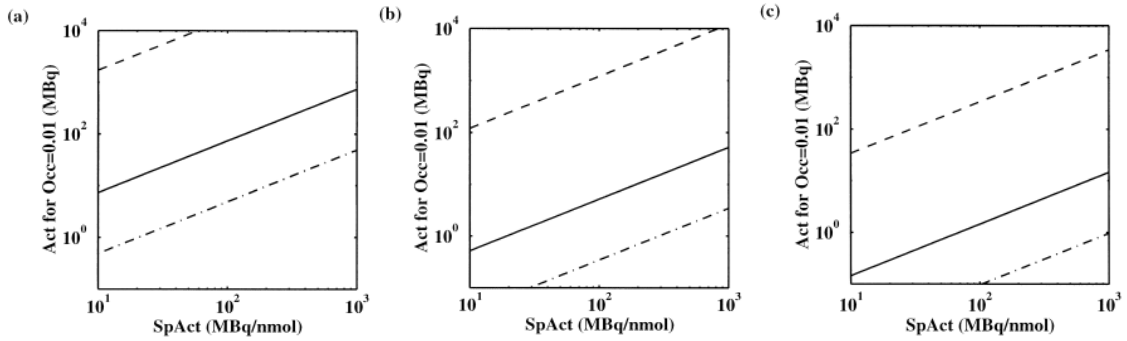

Figure 104 *In vivo* limits of radioactivity as a function of specific activity

1.34.2 An LPS rodent model for P2X7 tracer validation

In order to perform *in vivo* evaluation of [^{18}F]EFB, we employed a simple inflammatory rodent model consisting of a wild type rat with an intraperitoneal lipopolysaccharide (LPS) challenge.

Intraperitoneal injections of the bacterial endotoxin LPS are known to induce even at low dosage a lasting neuroinflammatory response.[597] On a symptomatic level, in rodents it leads to a sickness behaviour, mild loss of appetite, depressive-like symptoms, moderate piloerection, social withdrawal and a hunched back.[598] At a biochemical level, LPS was found to raise the levels of most inflammatory markers in the blood, including TNF-α, NF-κβ and IL-1β.[599] Brain cortex expression of IL-1β, IL-6, toll like receptors (TLRs) and glial fibrillary acidic protein (GFAP) are upregulated within 4 h, suggesting that glial activation and cortical inflammation quickly follow systemic inflammatory episodes,[600, 601] often outlasting them.[602]

Upon reaching the CNS, LPS is known to loosen the BBB and affect some of its normal functions, enabling the spread of inflammation into the brain through endothelial cell-mediated microglial activation and *via* brain infiltration of blood-based inflammatory cells.[603, 604] The specific routes by which LPS might cause brain inflammation have not been fully clarified. However, BBB leakage is known not to occur until an LPS concentration threshold of 3 mg/kg has been reached,[605] while even at more moderate concentrations microglia activation is observable.[606]

To determine the time point of maximal inflammation, the dose of LPS administered was found to be important. It can range between 0.002-10 mg/kg, causing microglia to become activated after 3 hours, reaching full activation between 8h and 2 days post-injection. However, several studies used a regular injection regimen to maintain a constant level of inflammation, as detailed

in a systematic review by Hoogland *et al.*[607] Also, several reported that systemic LPS-induced neuroinflammation was not associated with neurotoxicity, causing instead a somewhat milder yet detectable insult.[608, 609]

Despite the certain inflammatory consequences of LPS administration, it is important to note that there is yet only one study showing direct evidence of LPS inducing P2X7-overexpression in rodent models. This is an immunohistochemical study by Choi *et al.* where 24 h post-injection with 0.5 mg/kg LPS rats displayed moderate P2X7 overexpression, whereas this became strong with a 5 mg/kg dose.[610] Moreover, three studies carried out in P2X7$^{-/-}$ rodent models provide indirect evidence of P2X7 by reporting downregulation of pathways downstream of the receptor, as measured by IL-1β secretion (ELISA, PCR)[90, 99] or pleasure feeling (sucrose preference).[159] Additionally, P2X7 is known to be tightly correlated with LPS and with inflammation, as discussed in chapter 1. P2X7 is also known to mediate LPS downstream inflammatory signalling[115, 611-613] and vice versa, LPS modulates some of P2X7's functions.[614]

1.34.3 Aims

The work presented in this chapter aimed to characterise *in vivo* [^{18}F]EFB. In particular, we sought to determine:

- The *in vivo* distribution and kinetic profile of the tracer
- The extent by which it is able to cross the BBB
- How well it is cleared from the body and by which routes
- Whether it can discriminate inflamed from normal tissues

1.35 Methods

1.35.1 Animals

Female BALB/C mice from Harlan UK Ltd. underwent imaging at 10-12 weeks of age. Alternatively, male Sprague-Dawley rats of 240-270 g were bought from Charles River Laboratories International, Inc. and used within 90 days. The animals were housed under pathogen-free conditions in a temperature- and humidity-controlled environment and given access to food and water ad libitum. All experimental procedures were performed after over a

week of acclimatisation in the new environment and in accordance with the Animals (Scientific Procedures) Act 1986, Amendment Regulations 2012 and approved by the local ethics committee. Project licence: Licence holder – Prof Reza Razavi, PPL 70/8230 and Dr Diana Cash, PPL 70/8480. Personal Licence: Licence holder: Enrico Fantoni, PIL 70/3001. All experiments were carried out in the Rayne Institute, St. Thomas' Hospital, King's College London between 2015 and 2016.

1.35.2 Treatment regimen

300-9000 GBq/μmol, 0.2-5 MBq [^{18}F]EFB were administered to control mice without any further pre-treatment. Rats were pre-treated with an intraperitoneal injection of 0.5 mg/kg at 0.5 mg/mL LPS (Lipopolysaccharides from Escherichia coli 0111:B4 L2630, Sigma Aldrich) or with 1 mL/kg sterile saline solution 24 hours prior to scanning.

1.35.3 Radiotracer administration for scanning

Dynamic PET imaging of all mice, 3 LPS and 3 control rats was performed under isoflurane anaesthesia. The oxygen was kept at 1 L/min flow rate with isoflurane levels of 5% for induction and termination, while maintenance was carried out with a 1 L/min oxygen flow and an isoflurane rate of 1.5-3% with constant breathing and temperature monitoring. The saline-dissolved reformulated radiotracer was injected in 0.2-5 MBq and high specific activity *via* tail vein injection (mice) or cannulation (rats) and followed by 0.02-0.05 mL (mice) or 0.1-0.2 mL saline flush (rats).

1.35.4 PET/CT acquisition and quantitative image analysis

PET/CT scans were acquired via the Nuclide software with a Mediso NanoPET/CT scanner with lithium yttrium orthosilicate: cerium (LYSO:Ce) crystals of size 1.12 mm x 1.12 mm x 13 mm, within the energy window of 400-600 keV, coincidence detection ratio 1-5 and voxel resolution of 0.30 x 0.30 x 0.30 mm^{3}.[615] CT scanning was performed immediately before or after the PET scans with X-ray energy of 45 KVp, 360 projections and 0.25 x 0.25 x 0.21 mm^{3} voxel size. The datasets were resolved by dynamic fine reconstructions using the single-slice rebinning, ordered subset expectation minimisation (SSRB-OSEM 3D) algorhythm with coincidence detection ratio

1-5 (1-3 in mice) and decay correction to the time of injection. Additionally, attenuation and scatter corrections were carried out. Binning was performed in incremental time units of 1 to 60 min size (mice, 5 x 1 min, then 1 x 10 min, 1 x 15 min, 1 x 30 min, 1 x 60 min) or 5 to 30 min size (rats, 3 x 5 min, then 1 x 15 min, 1 x 30 min). All reconstructed datasets were analysed with VivoQuant 1.21 (InviCRO, LLC, Boston, USA), which enables PET/CT co-registration, alignment, image pre-processing to determine the concentration or MBq of uptake by tissue, the demarcation of regions of interest (ROIs) and colour scaling. ROI activity quantification was then corrected for background noise and binding was expressed as %ID/g, as calculated with reference to the injected activity dose at the time of injection and the ROI size in mm^3. Mouse brain binding was blood-volume-corrected. The latter is an experimentally calculated theoretical adjustment where blood represents 5.8% of the total brain volume and it only partially reflects the true blood-independent brain binding.[616] Binding was also expressed as organ-to-plasma ratio, both background corrected and where the plasma ROI was drawn on the coronary artery. All data are presented as mean ± SEM unless otherwise stated.

1.35.5 Biodistributions

Immediately after imaging, the animals were culled by terminal anaesthesia and cervical dislocation. The animals were dissected and organs and body fluids were collected for gamma counting (LKB Wallac 1282) and weighed. A counts-to-Becquerel standard curve was made for ^{18}F so as to enable conversion between the two units. The radiotracer binding in each organ was expressed as %ID/g, where %ID was the percent ratio of the measured organ radioactivity to the total administered dose. The latter was defined as the MBq injected to the animals, decay corrected to the start of counting. The resultant biodistribution data were used to validate the PET scan quantification methodology as well as to assess the routes of elimination of the tracer.

1.35.6 Statistical analysis

Data are expres[615]sed as means ± SEM from three independent replicates unless otherwise indicated. Statistical analysis of the %ID/g variation in the PET scans and biodistributions was performed with GraphPad Prism 5.0 (San Diego, USA) as a parametric two-way ANOVA test

with Bonferroni post-test, unless otherwise specified in the figure captions. * indicates P<0.01; **, P<0.005; ***, P<0.001. Where unspecified, no significance was found.

1.36 Results

1.36.1 Model validation

An LPS injection regimen is known to increase IL-1β at 24 hours post-injection and to induce a 5-10% weight loss by 24 hours. In our hands, the LPS-treated rats also showed significant weight loss after 24 hours, indicative of effectiveness of the treatment. This was accompanied by a strong upregulation of microglia in the brain (Figure 106), a decrease in sucrose preference and locomotor activity.

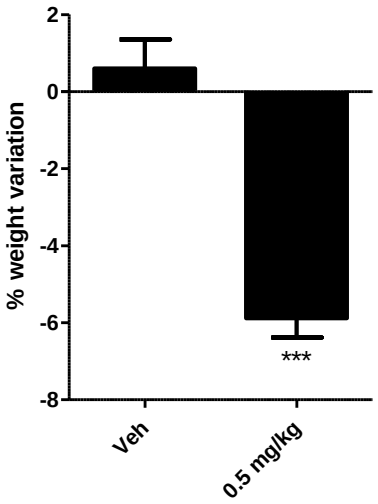

Figure 105 Percent weight variation 24 hours post-treatment in LPS treated versus saline-injected control rats

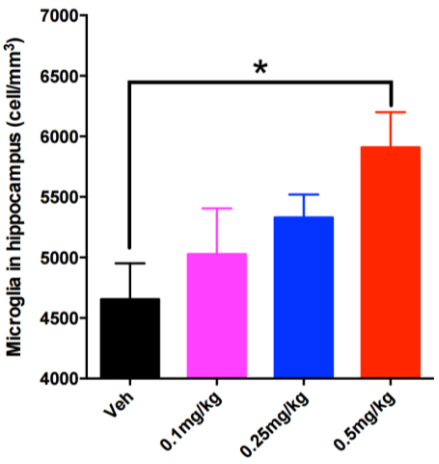

Figure 106 Number of hippocampal microglia dose response to increasing concentrations of LPS at 24 h post-injection

1.36.2 *In vivo* distribution and kinetic profile of [^{18}F]EFB

In order to determine the distribution profile of [^{18}F]EFB, whole-body wild type mouse imaging was performed (Figure 110, representative scan at the 7.5 min time point). The graphs in Figure 107 show that in all mouse CNS regions tracer uptake is maximal at 3±0.5 min post tracer administration, suggesting rapid BBB penetration. The tracers then washed off from the CNS, reaching baseline values after 2 hours. Note that CNS clearance was confounded by fast tracer excretion from the blood, which contributed to CNS concentrations remaining about an order of magnitude lower than in blood (Figure 107).

Figure 108 depicts the organ-to-blood partition over time. This draws the attention on the fact that the partition appears to slightly increase over time, suggesting a different rate of excretion between the two tissues, hence some degree of tracer CNS retention.

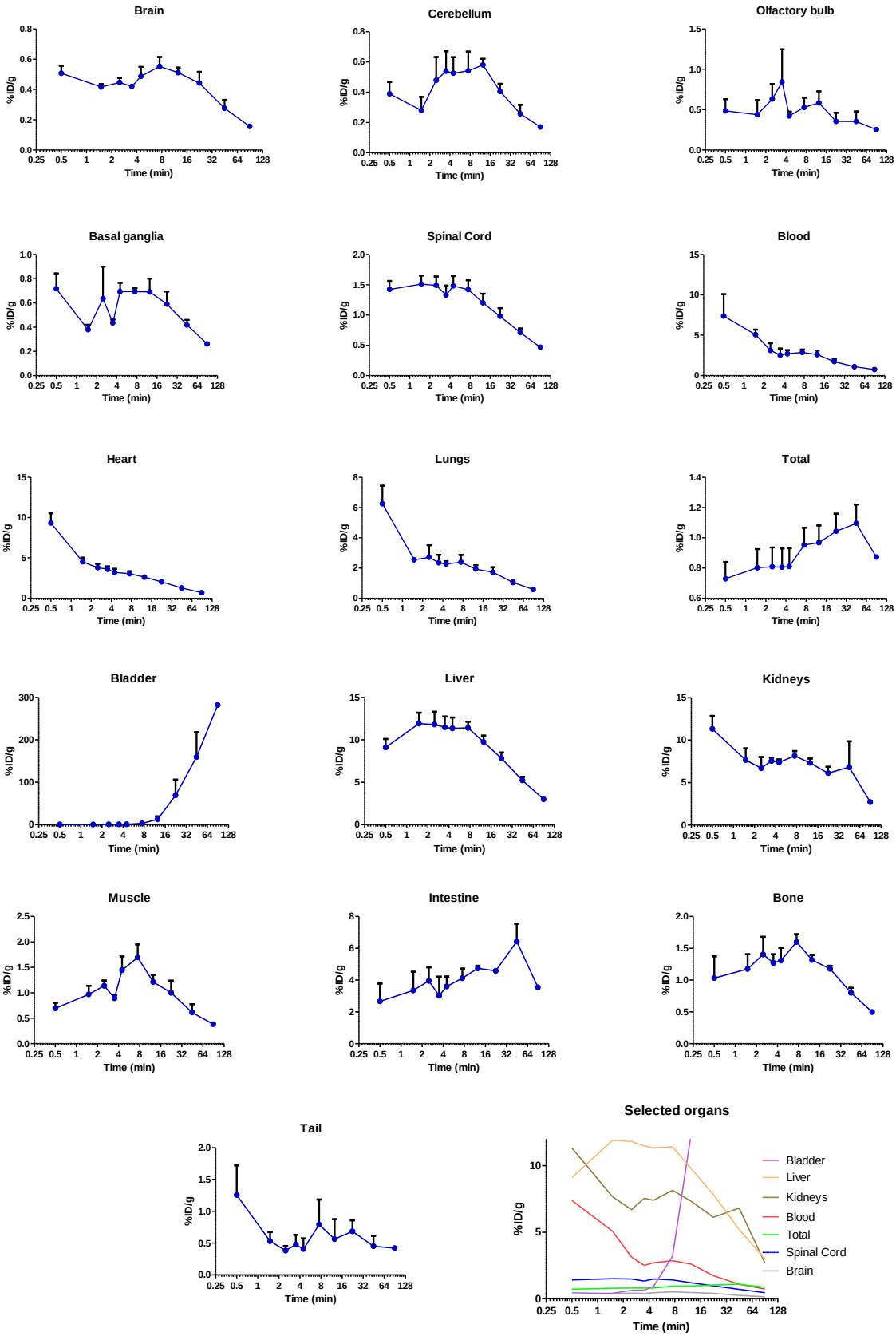

Figure 107 Whole-body BALB/C WT mouse longitudinal tracer uptake between 0 and 90 min

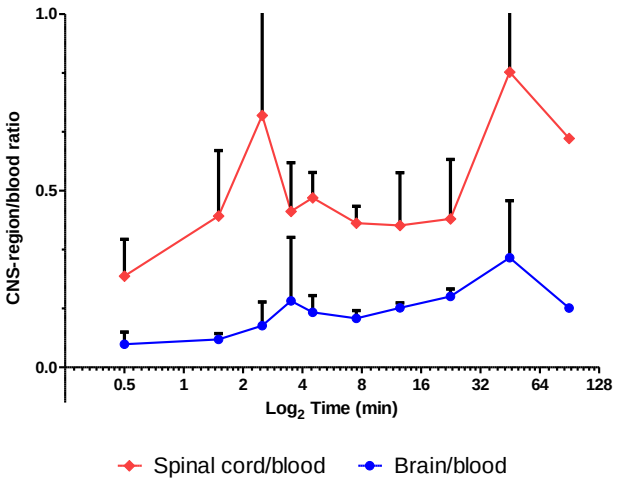

Figure 108 Longitudinal CNS-region-to-blood ratios of [^{18}F]EFB from 0 to 90 min post tracer administration

Blood and heart followed a similar exponential clearance, possibly due to the difficulty in sampling the heart ROI with exclusion of blood. Liver and kidney uptake was particularly elevated at the early time points, indicating fast metabolism and excretion of the tracer. Excretion appeared to be only partially intestinal while the large majority of tracer was removed *via* the urine and to the bladder. This was further confirmed in the biodistribution studies (Figure 109). Here, only marginal yet significant uptake was found in the CNS at the earlier time point. Finally, bone uptake was marginal and readily decreased over time, suggesting a lack of metabolic defluorination of the radiotracer.[618]

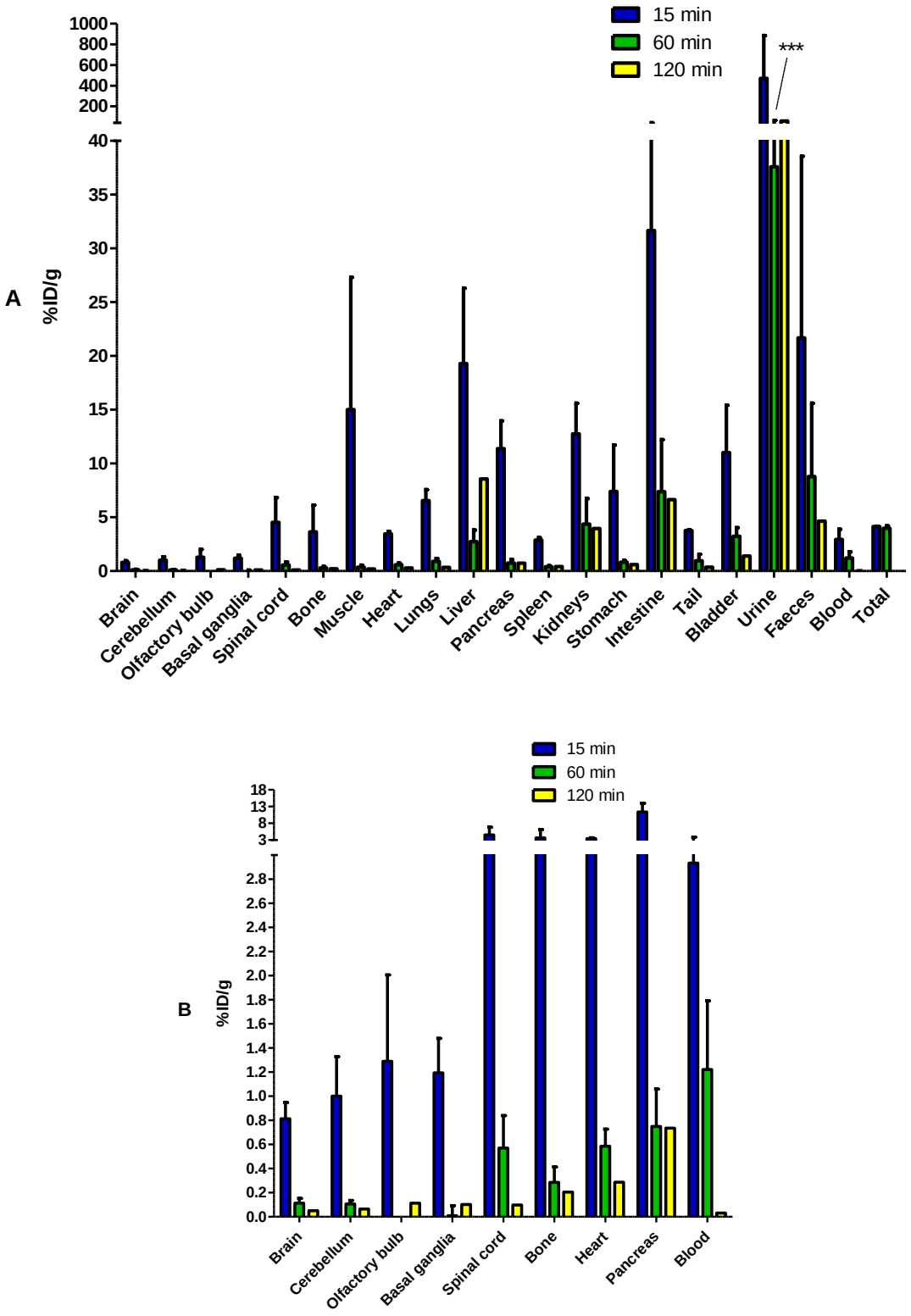

Figure 109 Biodistribution of [^{18}F]EFB in WT BALB/C mice

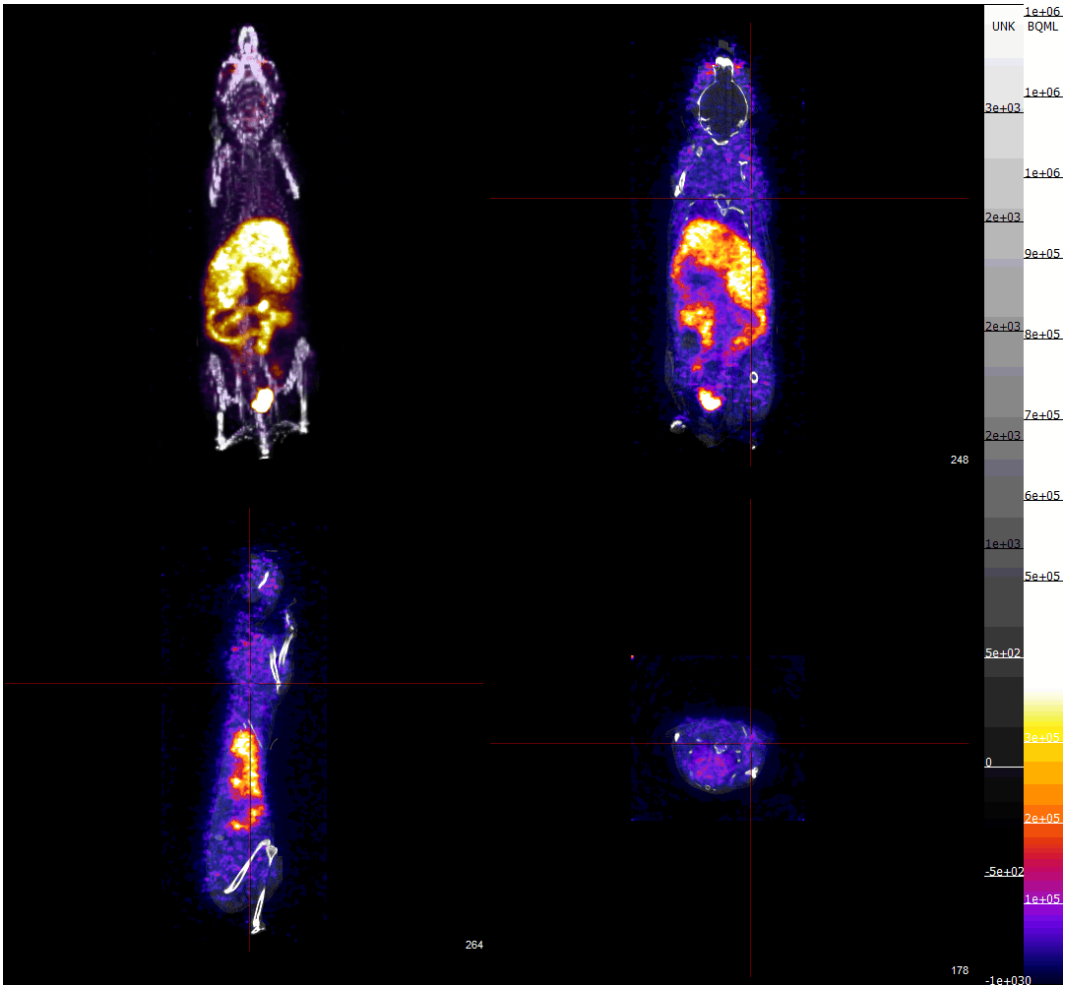

Figure 110 Representative female WT BALB/C mouse PET/CT scan of [^{18}F]EFB at 7.5 min

1.36.3 [^{18}F]EFB correlation to inflammation

Evaluation of [^{18}F]EFB as an inflammation-dependent tracer was performed by comparison of wild type and 0.5 mg/kg LPS-pre-treated Sprague-Dawley rats *via* quantitative PET imaging and biodistribution analysis. However, the scanning of rats could not be performed as a whole-body acquisition, as the field of view of the scanner was restricted to the upper body (Figure 113).

Rat longitudinal uptake profiles (Figure 111) revealed a slower wash out in all organs compared to mouse, characteristic of the reduced metabolic rate. In fact, the blood concentration remained relatively stable around 0.1 %ID/g. The CNS uptake stayed between 0.05-0.1 %ID/g for the spinal cord, while it reached a maximum of 0.02-0.07 %ID/g in the whole brain, the olfactory bulb, the cerebellum and the basal ganglia. These percentages correlate very well with the terminal biodistribution (Figure 112), demonstrating that the methodology adopted for PET quantification was reliable. Moreover, the significant mean binding found in the spinal cord of

the LPS injected rats was consistent with the P2X7 expression hotspot in spinal cord grey matter found by Able *et al.*[67]

Additionally, LPS-treated rats demonstrated a statistically significant mean increase in tracer binding compared to untreated rats. This could reflect increased P2X7 expression which, even with moderate BBB permeability, could be captured by the tracer.

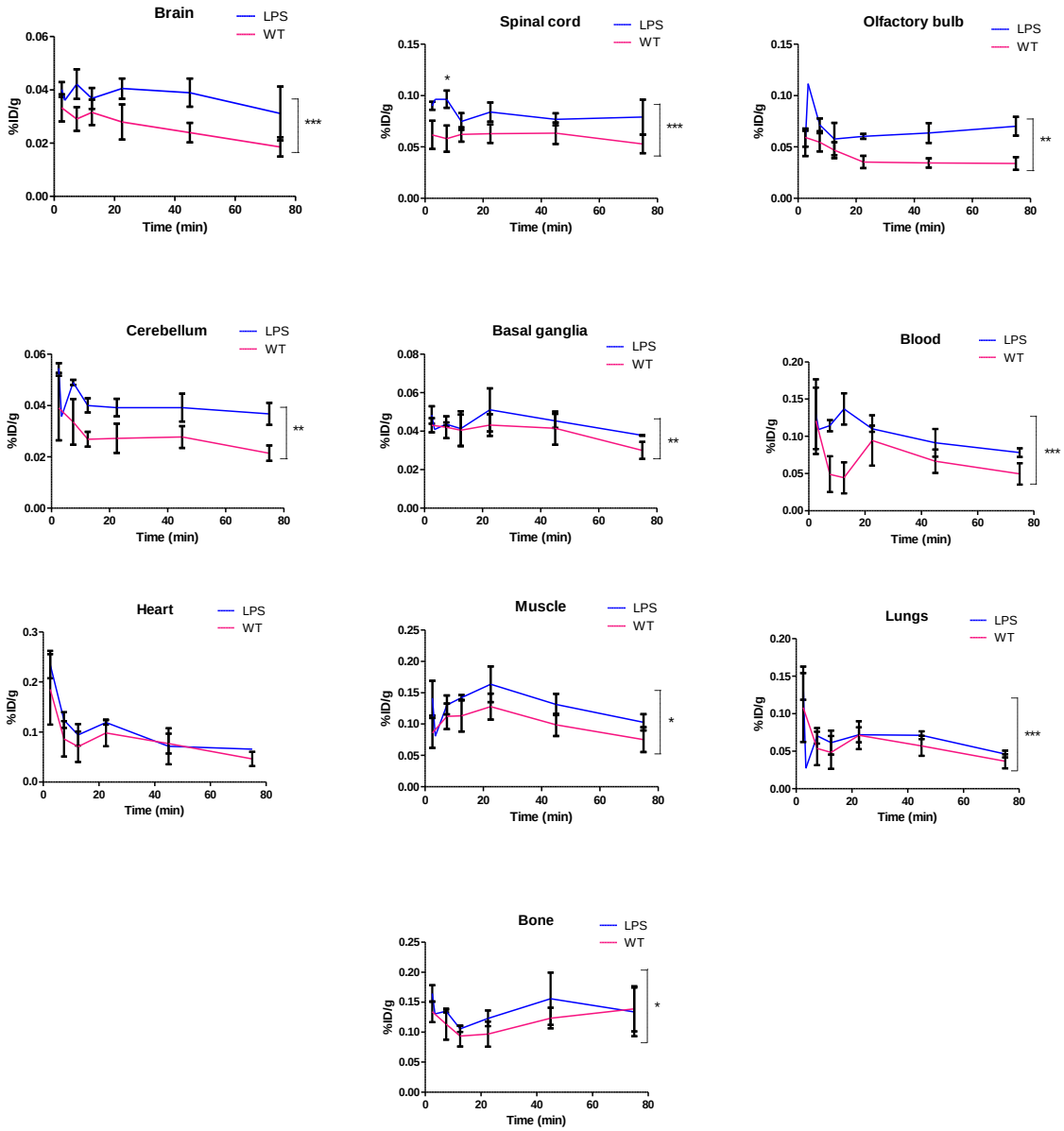

Figure 111 In vivo uptake of [^{18}F]EFB in 24 h post-LPS injection and control rats

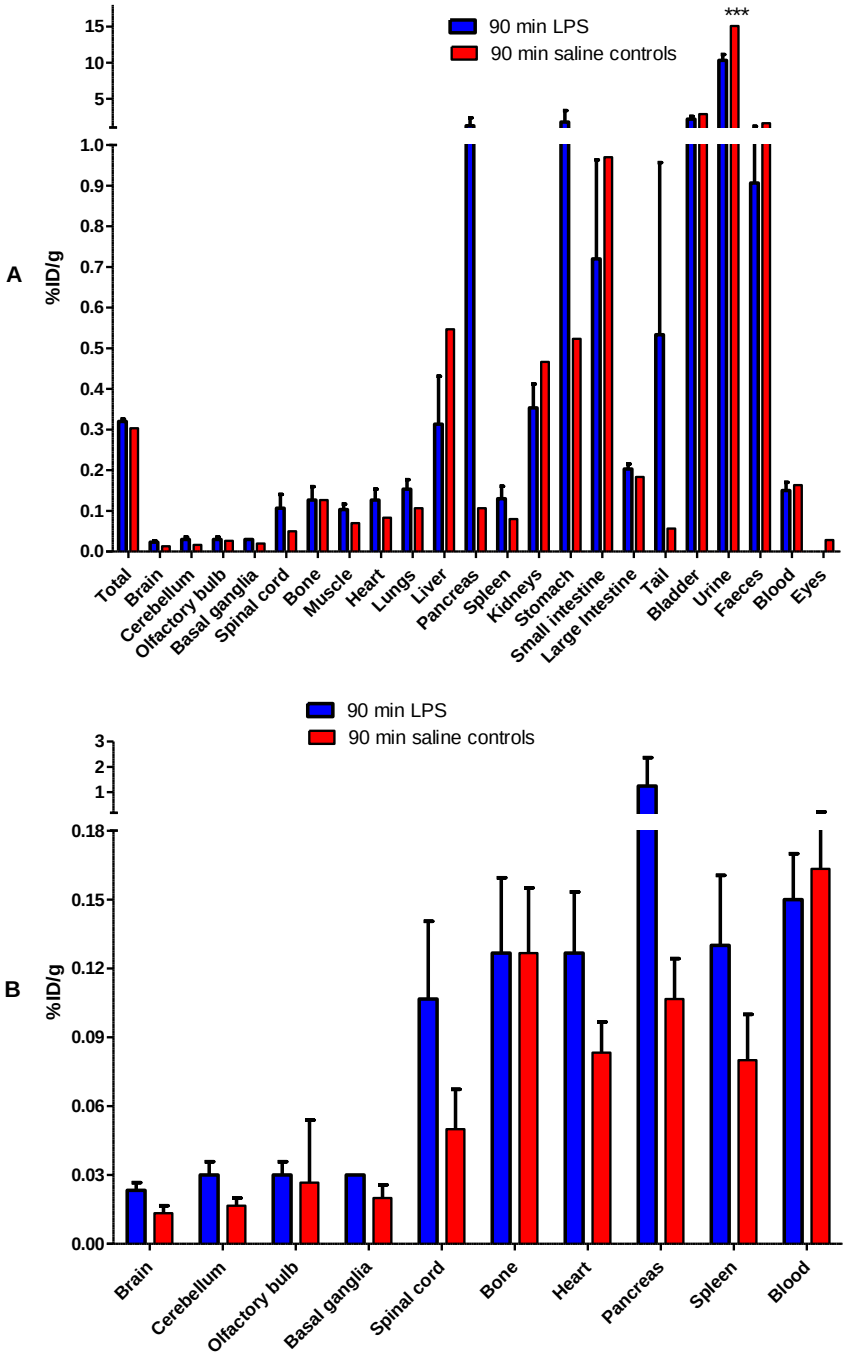

Figure 112 Biodistribution of [^{18}F]EFB at 90 min post-injection in LPS and saline injected rats

Furthermore, organ-to-blood partition plots (Figure 114) lost statistical significance between treatments due to a low relative binding in the brain compared to the blood.

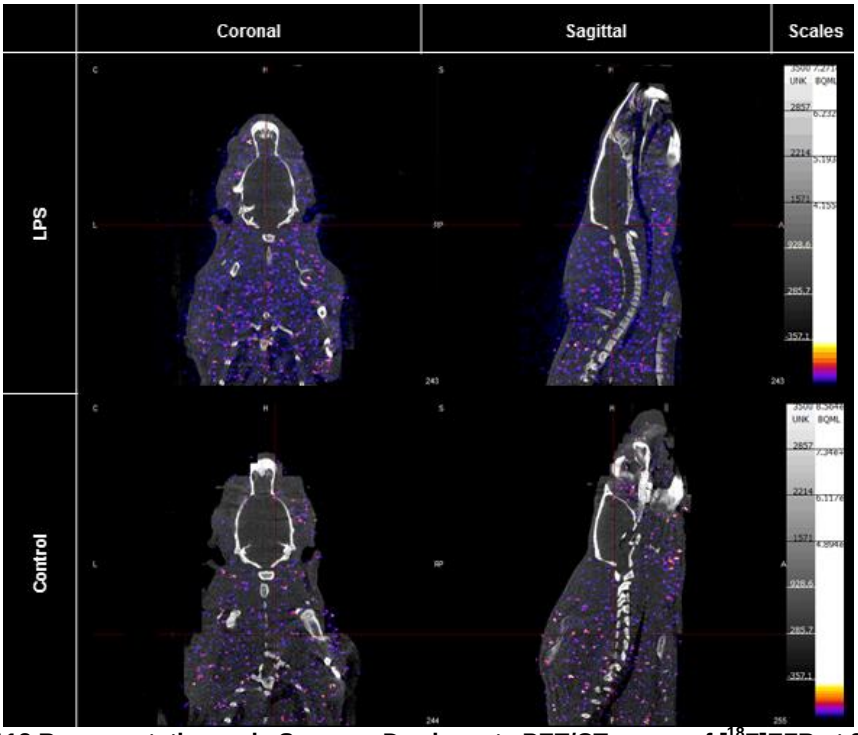

Figure 113 Representative male Sprague-Dawley rats PET/CT scans of [^{18}F]EFB at 22.5 min

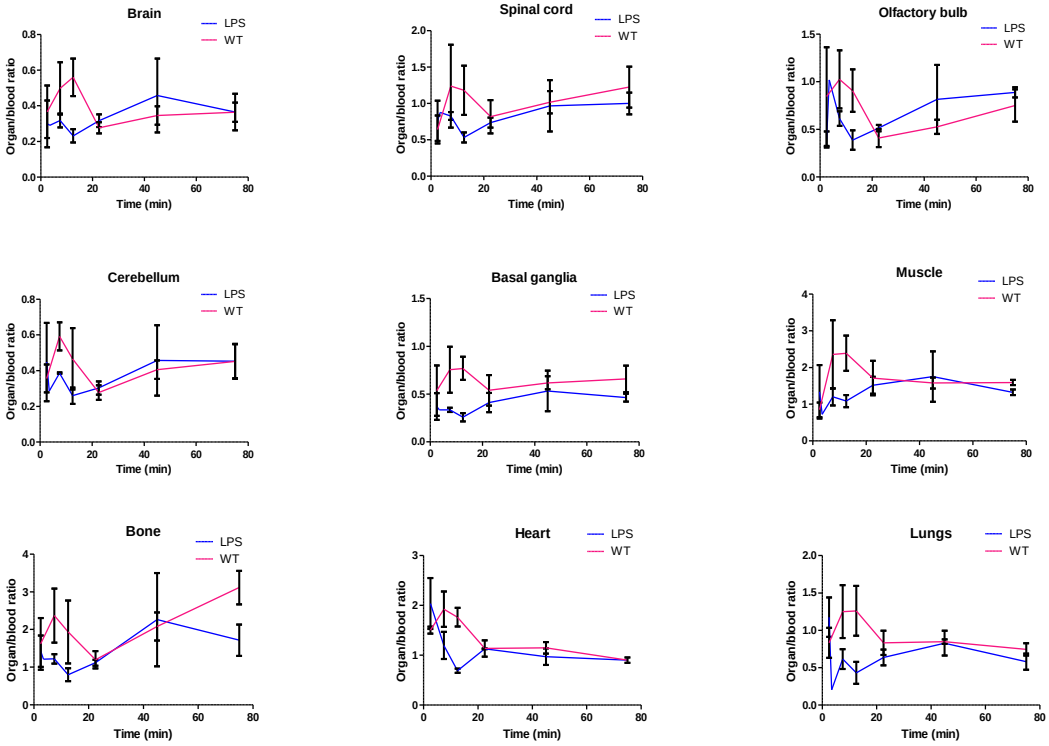

Figure 114 *In vivo* longitudinal organ-to-blood ratios of [^{18}F]EFB in 24 h post-LPS and 1 h post-BBG injections and control rats

1.37 Discussion

In this chapter it's been shown that [^{18}F]EFB exhibits some but not all of the desired features for a novel tracer targeting P2X7.

[^{18}F]EFB was quickly absorbed and distributed in both animals and excreted predominantly *via* the urinary route. In mice this was visible by comparison of the early time points, where tracer uptake was mostly in the circulation, with the later time points, where the tracer was transferred to the urine and bladder. In rats, this was less evident due to the imaging being limited to the upper body, yet it could be understood from the biodistribution, where high first pass elimination appeared likely. The transient high uptake in the mouse liver suggested some degree of metabolism of the tracer, meaning that EFB could also be have been broken down to a more hydrophilic form which then would undergo urinary excretion. This tracer excretion profile is desirable in that it allows fast removal of the radioactivity, minimising the exposure to harmful radiation. Conversely, it reduces the longitudinal bioavailability of the radiotracer, limiting the amount able to cross the BBB.

The mean longitudinal binding of [^{18}F]EFB was significantly higher in LPS compared to untreated rats. Thus, the tracer appeared promising in recognising inflammation in the CNS. However, individual time points failed to reach a significant difference, suggesting that increasing replication would be necessary. This was also linked to the limited sensitivity achievable with the low radioactivity levels at which the scans had to be performed given the limitations inherent to the lengthy radiosynthesis of [^{18}F]EFB (at times 0.2-0.5 MBq at start of scan). Nevertheless, the low radioactivity matched with the specific activity >300 GBq/µmol, far exceeding the required approximately >40 GBq/µmol for *in vivo* receptor imaging,[619] meant that less non-specific binding could be expected as a consequence of the lower receptor occupancy.[595] On the other hand, the lack of statistical significance in individual time points following radiotracer administration might be a result of high binding variation within the ROIs, possibly because of heterogeneous receptor upregulation within the tissues. Besides, significance might only be achievable at the later time points, as steady state conditions take over. Finally, the lack of a full validation of the tracer's receptor-specificity gave an extra degree of uncertainty when attempting a complete interpretation of this dataset. Thus, further work to clearly validate the target(s) of this tracer and to enable its quantitative pharmacokinetic and bioavailability profiling is required.

In the rat, the CNS showed limited and stable binding at 0.02-0.1 %ID/g at all time points. Several factors might have influenced this. The tracer might have limited BBB permeability, or

be subject to brain efflux *via* trans-barrier pumps, such as the P-glycoprotein (P-gp). Tracer metabolism might be so fast as to prevent all but marginal absorption of the original compound in the brain. Either way, <0.1 CNS %ID/g is too low for clinical use. Conversely, the mild [^{18}F]EFB brain retention highlights that there is scope for further exploration of the cyanoguanidine scaffold. In particular, radiometabolite analysis could reveal important information regarding *in vivo* molecular alterations. A future structural modification strategy should take the latter into account as well as including further LogP reductions in adherence with the modified Lipinski rule-of-5 to improve on the compound's solubility.

Moreover, there are inherent limitations to the chosen experimental animal model. Firstly, P2X7 upregulation has not been verified for the CNS or the rest of the body. This affects the ability to predict where to expect increased binding, despite the LPS insult is known to elicit inflammation systemically and centrally. Since P2X7 is much more highly expressed in the CNS than peripherally, it is reasonable to expect a much higher accuracy of detection of its upregulation in the CNS, while peripherally the overexpression might go unnoticed. Secondly, the model lacks an internal reference region against which to compare the increased binding. This is particularly due to the ubiquitous expression of the receptor. Further work would need to be oriented at immunohistologically staining control and inflamed tissues with a P2X7 antibody and correlating these with tracer binding by autoradiography. Additionally, the animal model would need to be further characterised in terms of its relative P2X7 receptor abundance by PCR or western blotting. Metabolite analysis and kinetic modelling could provide further insights into the pharmacokinetic factors responsible for the observed binding trends.

1.38 Conclusions

This work served as a preliminary study to assess the distribution and pharmacokinetics of [^{18}F]EFB in an *in vivo* model of inflammation. The tracer showed a promising distribution and excretion profile and the potential to distinguish inflamed from healthy CNS tissues. However, the lack of an individual time point at which the tracer could distinguish P2X7 expression variations points primarily towards the need for further characterisation of the tracer for its selectivity against P2X7, as well as the need for further replication with higher radioactivity levels for enhanced PET scan sensitivity. Secondly, the low overall CNS binding of the tracer

highlights that the LPS model and control are insufficiently characterised and might not differ enough in P2X7 expression for tracer binding differences to be noticeable.

Future work should thus be oriented towards resolving these critical questions, as well as exploring alternatively radiolabelled scaffolds to enable enhanced brain penetration and target binding.

Chapter 8

Final remarks

Final remarks

The development of a novel PET tracer targeting P2X7 has the potential to offer both new insight into the role of this receptor in health and disease, as well as to provide an alternative tool to image neuroinflammation. Only rarely PET tracers are developed to assist drug discovery. Yet important financial and scientific gains can arise from them and lead to profitable non-invasive diagnostics.

In this work, four new ^{18}F tracers based on the A-804598 molecular structure and targeting P2X7 have been described. In order to incorporate the ^{18}F label while lowering the parent scaffold's LogP for enhanced BBB permeability, three tracers (collectively referred to as [^{18}F]XFA) were designed to feature a cyclotriazole ring with a pendant ^{18}F label. The [^{18}F]XFA tracers presented different aryl functionalities: a hydrophobic quinoline, a less bulky phenyl ring and a hydrophilic phenol. A fourth compound ([^{18}F]EFB) closely resembling the parent scaffold, was directly radiofluorinated on a mildly electron-rich phenyl ring.

All compounds were docked by molecular modelling to the P2X7 receptor's binding pocket and their affinity was assessed quantitatively, delivering promising SAR predictions. Moreover, a set of physicochemical properties were investigated computationally, suggesting a suitable biological profile for the library of tracers.

The synthesis of the tracer precursors and reference standards was carried out successfully *via* the development of a novel route comprising in particular a step-wise trisubstituted guanidine synthesis and a copper alkyne azide cycloaddition. The overall yields were moderate, particularly due to the limited purification process success in the final synthetic steps. Nevertheless, the synthesis resulted adequate for the development and evaluation of all radiolabelled compounds.

Radiolabelling of [^{18}F]XFA was carried out with copper alkyne azide cycloadditions. [^{18}F]EFB was indirectly labelled by nucleophilic substitution followed by a two-step functional interconversion process. The resulting tracers were produced as outlined in Table 22 and their identity confirmed by HPLC analysis. The long synthetic times were partly due to the multiple steps involved in the radiolabelling procedures and the extensive purification processes. For [^{18}F]EFA, improvements were made with the SPE and HPLC-optimised purification procedure.

Table 22 Radiosynthetic parameters for the library of tracers developed

Tracer	RCP	D.C. RCY	Synthesis time (min)	SA (GBq/μmol)
[^{18}F]EFA	>99%	4-26%	160	>10
[^{18}F]AFA	>99%	10-42%	210	0.5-61
[^{18}F]OFA	>99%	5-9%	260	5-9
[^{18}F]EFB	>99%	3-5%	210	>300

However, further work remains necessary to translate these developments to the other compounds of the series. Byproduct formation and the presence of an alcohol group in [^{18}F]OFA caused the yields to remain moderate. Full characterisation of the byproducts could provide useful avenues for the further improvement of the radiolabelling processes. While the specific activity of [^{18}OFA] is low for receptor imaging *in vivo*, [^{18}F]AFA and [^{18}F]EFA are within an acceptable range, whereas that of [^{18}F]EFB is excellent.

Evaluation of the tracers was performed with a range of biological techniques with the triple aim of providing multiple quantitative and qualitative evaluation platforms with different complexities for the P2X7 tracers, to explore the value of each model and to establish benchmark methods for validating future tracers.

In cellulo, all compounds were assessed by radioligand binding and calcium influx functional assays. The former was ineffective at elucidating the affinity of the tracers due to low signal-to-noise ratio, probably imputable to low receptor expression. However, this work serves as a starting point and inspiration for the future validation of tracers aiming to visualise microglial polarisation states. The calcium influx assay showed selectivity of [^{18}F]EFB but not of the [^{18}F]XFA series for the target. The former has been found to have a K_i of 0.85 nM, 36.1 nM and 547 nM at human, rat and mouse P2X7 receptors, respectively, while in all other instances the affinity is >0.1 mM.

In vitro tissue autoradiography was used to provide a preliminary binding profile of the [^{18}F]XFA series in the native inflamed tissue setting of the hypoxic ischemic mouse. [^{18}F]AFA stood out as the tracer displaying the least non-specific binding and which best correlated with the expected P2X7 distribution in tissues. However, the atypical response to receptor blockade rendered the

tracer affinity to P2X7 complex to interpret, prompting further studies. [^{18}F]EFA presented high non-specific binding accompanied by a suitable P2X7-blockade-induced binding reduction. Finally, [^{18}F]OFA correlated poorly with the expected P2X7 expression profile and did not appear specific for P2X7. All in all, these results pointed to some advantages in the use of the immature HI mouse model as a native tissue platform to assess P2X7 tracers. Future work will be focused on the P2X7 immunohistochemical staining of the tissues for full corroboration of the results. In both *in vitro* assays, receptor blockade by BBG repeatedly resulted in abnormal [^{18}F]XFA binding patterns. Potentially, this points to a positive allosteric effect and calls for further elucidations.

In vivo wild type mouse and LPS rat PET scanning, coupled with *ex vivo* biodistribution served to assess the potential of [^{18}F]EFB as PET tracer. The tracer was able to distinguish inflamed from healthy CNS tissues. Its distribution and pharmacokinetic profile appeared promising as indicated by the good rate of excretion accompanied by some degree of retention in the target organs. However, the overall rat CNS binding was 0.02-0.1 %ID/g, fairly low for CNS imaging, while the peripheral binding would be in a much more suitable range to progress this molecule. Whether the limited CNS binding was due to low receptor expression levels of P2X7 in the chosen rodent model or whether the transport across the BBB was restricted remains to be clarified.

Besides the need for further characterisation of the tracer with respect to its P2X7 selectivity and metabolite formation, this compound provided new and important information regarding the amenability of diaryl-cyanoguanidine scaffolds for *in vivo* P2X7 imaging. The limited BBB-permeability of [^{18}F]EFB and of the previously published cyanoguanidine [^{11}C]A-740003,[216] as well as the apparent lack of target affinity of the [^{18}F]XFA tracers, rather than being suggestive of a bio-incompatibility of the cyanoguanidine scaffolds, point to the need of carefully altering their physicochemical properties to achieve permeability with retention of the target affinity. This was previously achieved, among others, by the Hooker group at Harvard University.[339] A possible next step in this direction could be a radiofluorinated or radiocarbonated version, respectively of the amide-functionalised compounds p-EFC and EFC2 (as discussed in chapter 2), Both in fact displayed higher hydrophilicity than [^{18}F]EFB whilst modifying more moderately than [^{18}F]EFA the parent molecular structure. Moreover, further tracer improvements could

benefit from additional *in silico* and *in vitro* predictions, thus enabling more rapid trial-and-error than traditional radiotracer development methods allow. Among them, LC/MS/MS showed potential as a method to instruct structural modifications to apply to poorly BBB-penetrant tracers,[620] while additional computational estimates could be carried out.[373] However, it is common for these tests to inaccurately predict tracer binding,[621] as was partly the case in this study. This was certainly partially imputable to gaps in knowledge of the full P2X7 receptor 3D structure, which await advancements in the field of X-ray crystallography. While computational tools remain a useful aid in the initial scaffold selection, as a series of compounds are radiolabelled and tested *in vivo*, insightful trends can arise that can guide future success.

On top of achieving the characterisation of four new radiotracers, this project was novel in many other aspects. Firstly, in that it added to the scientific field new and improved synthetic organic methods for the production of novel organic molecules. It also provided further applications for the incorporation of radioactive fluorine using current radiochemical techniques, building upon the existing knowledge surrounding “click” radiofluorinations, boronic ester aromatic fluorinations and multi-step fluorinations with the fluorobenzyl amine synthon. Moreover, it opened new avenues for the study of P2X7 ligands with the exploration of a range of biological assays and models, emphasising the strengths and limitations of each.

To image P2X7 means to enable the detection of the onset and progression of numerous important diseases presenting an inflammatory component. Research into novel radiotracers is especially important in this historical period, characterised by a shift towards preventative patient management strategies and a race towards personalised medicine.[622]

Bibliography

1. A. N. Drury and A. Szent-Györgyi, *The Journal of Physiology*, 1929, **68**, 213-237.
2. G. Burnstock and C. Kennedy, *General pharmacology*, 1985, **16**, 433-440.
3. C. Kennedy, *Archives internationales de pharmacodynamie et de therapie*, 1990, **303**, 30-50.
4. R. H. Hilderman, M. Martin, J. K. Zimmerman and E. B. Pivorun, *Journal of Biological Chemistry*, 1991, **266**, 6915-6918.
5. J. L. Gordon, *The Biochemical journal*, 1986, **233**, 309-319.
6. A. Surprenant, F. Rassendren*, et al.*, *Science*, 1996, **272**, 735-738.
7. G. Buell, G. Collo and F. Rassendren, *European Journal of Neuroscience*, 1996, **8**, 2221-2228.
8. C. Vial, J. A. Roberts and R. J. Evans, *Trends in Pharmacological Sciences*, 2004, **25**, 487-493.
9. S. Roger, L. Gillet*, et al.*, *Journal of Biological Chemistry*, 2010, **285**, 17514-17524.
10. M. L. Smart, B. Gu*, et al.*, *Journal of Biological Chemistry*, 2003, **278**, 8853-8860.
11. S. Ennion, S. Hagan and R. J. Evans, *Journal of Biological Chemistry*, 2000, **275**, 29361-29367.
12. J. D. Clyne, L. F. Wang and R. I. Hume, *Journal of Neuroscience*, 2002, **22**, 3873-3880.
13. N. Mehta, M. Kaur*, et al.*, *Bioorganic & medicinal chemistry*, 2014, **22**, 54-88.
14. R. Dahlquist and B. Diamant, *Acta Pharmacologica et Toxicologica*, 1974, **34**, 368-384.
15. K. A. Jacobson, M. F. Jarvis and M. Williams, *Journal of medicinal chemistry*, 2002, **45**, 4057-4093.
16. P. Pelegrin and A. Surprenant, *Purinergic Signalling*, 2009, **5**, 129-137.
17. C. E. Muller, *Current medicinal chemistry*, 2015, **22**, 929-941.
18. W. P. Schilling, W. G. Sinkins and M. Estacion, *The American journal of physiology*, 1999, **277**, C755-765.
19. R. Iglesias, S. Locovei*, et al.*, *American Journal of Physiology - Cell Physiology*, 2008, **295**, C752-C760.
20. T. Kawate, J. C. Michel, W. T. Birdsong and E. Gouaux, *Nature*, 2009, **460**, 592-598.
21. M. Hattori and E. Gouaux, *Nature*, 2012, **485**, 207-212.
22. L.-H. Jiang, j. Baldwin, S. Roger and S. Baldwin, *Frontiers in Pharmacology*, 2013, **4**.
23. E. Caseley, S. Muench*, et al.*, *International Journal of Molecular Sciences*, 2014, **15**, 13344.
24. R. Jiang, A. Taly*, et al.*, *The EMBO Journal*, 2012, **31**, 2134-2143.
25. A. Nicke, H. G. Bäumert*, et al.*, *The EMBO Journal*, 1998, **17**, 3016-3028.
26. L. Stokes, S. J. Fuller*, et al.*, *The FASEB Journal*, 2010, **24**, 2916-2927.
27. A. N. Shemon, R. Sluyter*, et al.*, *Journal of Biological Chemistry*, 2006, **281**, 2079-2086.
28. B. J. Gu, W. Zhang*, et al.*, *Journal of Biological Chemistry*, 2001, **276**, 11135-11142.
29. B. J. Gu, R. Sluyter*, et al.*, *Journal of Biological Chemistry*, 2004, **279**, 31287-31295.

30. G. Cabrini, S. Falzoni*, et al.*, *The Journal of Immunology*, 2005, **175**, 82-89.
31. S. J. Fuller, L. Stokes*, et al.*, *Purinergic Signalling*, 2009, **5**, 257-262.
32. J. S. Wiley, R. Sluyter*, et al.*, *Tissue Antigens*, 2011, **78**, 321-332.
33. A. McQuillin, N. J. Bass*, et al.*, *Molecular psychiatry*, 2009, **14**, 614-620.
34. S. Lucae, D. Salyakina*, et al.*, *Human molecular genetics*, 2006, **15**, 2438-2445.
35. N. Barden, M. Harvey*, et al.*, *American Journal of Medical Genetics Part B: Neuropsychiatric Genetics*, 2006, **141B**, 374-382.
36. B. J. Gu, R. Sluyter*, et al.*, *The Journal of biological chemistry*, 2004, **279**, 31287-31295.
37. S. L. Fernando, B. M. Saunders*, et al.*, *American Journal of Respiratory and Critical Care Medicine*, 2007, **175**, 360-366.
38. P. Nino-Moreno, D. Portales-Perez*, et al.*, *Clinical and experimental immunology*, 2007, **148**, 469-477.
39. G. Burnstock and G. E. Knight, *International review of cytology*, 2004, **240**, 31-304.
40. Y. Yu, S. Ugawa*, et al.*, *Brain research*, 2008, **1194**, 45-55.
41. S. D. Skaper, P. Debetto and P. Giusti, *The FASEB Journal*, 2010, **24**, 337-345.
42. A. Pelleg, C. M. Hurt and E. L. Hewlett, *Canadian journal of physiology and pharmacology*, 1996, **74**, 15-22.
43. G. Katchanov, J. Xu, E. S. Schulman and A. Pelleg, *Drug Development Research*, 1998, **45**, 342-349.
44. C. Barajas-Lopez, R. Espinosa-Luna and F. L. Christofi, *European journal of pharmacology*, 2000, **409**, 243-257.
45. S. E. Gabriel, M. Makhlina*, et al.*, *Journal of Biological Chemistry*, 2000, **275**, 35028-35033.
46. I. Novak, I. M. Jans and L. Wohlfahrt, *The Journal of Physiology*, 2010, **588**, 3615-3627.
47. C. H. Kim, S. S. Kim*, et al.*, *American journal of physiology. Lung cellular and molecular physiology*, 2004, **287**, L835-842.
48. C. Cario-Toumaniantz, G. Loirand, A. Ladoux and P. Pacaud, *Circulation Research*, 1998, **83**, 196-203.
49. C.-W. Chiao, R. C. Tostes and R. C. Webb, *The Journal of pharmacology and experimental therapeutics*, 2008, **326**, 864-870.
50. W. Ma, A. Korngreen*, et al.*, *Nature*, 1999, **400**, 894-897.
51. J. R. Genzen, D. Yang, K. Ravid and A. Bordey, *Cerebrospinal fluid research*, 2009, **6**, 15.
52. J. Luo, S. Lee*, et al.*, *Cell Death and Disease*, 2013, **4**, e829.
53. Q. Kong, M. Wang*, et al.*, *Purinergic Signalling*, 2005, **1**, 337-347.
54. I. P. Fairbairn, C. B. Stober, D. S. Kumararatne and D. A. Lammas, *The Journal of Immunology*, 2001, **167**, 3300-3307.
55. B. D. Humphreys and G. R. Dubyak, *The Journal of Immunology*, 1996, **157**, 5627-5637.

56. J. Dagvadorj, K. Shimada*, et al.*, *Immunity*, 2015, **42**, 640-653.
57. E. Schulze-Lohoff, C. Hugo*, et al.*, *The American journal of physiology*, 1998, **275**, F962-971.
58. G. Burnstock, *Arteriosclerosis, thrombosis, and vascular biology*, 2002, **22**, 364-373.
59. O. R. Baricordi, L. Melchiorri*, et al.*, *Journal of Biological Chemistry*, 1999, **274**, 33206-33208.
60. F. Bianco, S. Ceruti*, et al.*, *Journal of neurochemistry*, 2006, **99**, 745-758.
61. A. V. Greig, C. Linge, A. Cambrey and G. Burnstock, *The Journal of investigative dermatology*, 2003, **121**, 1145-1149.
62. B. A. N. Thompson, M. P. Storm*, et al.*, *Cellular signalling*, 2012, **24**, 770-778.
63. J. S. Wiley and B. J. Gu, *Purinergic Signalling*, 2012, **8**, 579-586.
64. N. R. Jørgensen, Z. Henriksen*, et al.*, *Journal of Biological Chemistry*, 2002, **277**, 7574-7580.
65. A. Brandao-Burch, M. L. Key*, et al.*, *Frontiers in endocrinology*, 2012, **3**, 41.
66. S. O. Suadicani, C. F. Brosnan and E. Scemes, *The Journal of Neuroscience*, 2006, **26**, 1378-1385.
67. S. L. Able, R. L. Fish*, et al.*, *British journal of pharmacology*, 2011, **162**, 405-414.
68. G. Collo, S. Neidhart*, et al.*, *Neuropharmacology*, 1997, **36**, 1277-1283.
69. S. Duan, C. M. Anderson*, et al.*, *Journal of Neuroscience*, 2003, **23**, 1320-1328.
70. G. James and A. M. Butt, *European journal of pharmacology*, 2002, **447**, 247-260.
71. A. Colomar and T. Amédée, *European Journal of Neuroscience*, 2001, **14**, 927-936.
72. S. A. Deuchars, L. Atkinson*, et al.*, *Journal of Neuroscience*, 2001, **21**, 7143-7152.
73. L. Atkinson, T. F. C. Batten*, et al.*, *Neuroscience*, 2004, **123**, 761-768.
74. Z. Deng and R. E. W. Fyffe, *Brain research*, 2004, **1020**, 53-61.
75. L. Atkinson, C. J. Milligan, N. J. Buckley and J. Deuchars, *Nature*, 2002, **420**, 42-42.
76. C. M. Anderson and M. Nedergaard, *Trends in Neurosciences*, 2006, **29**, 257-262.
77. B. Sperlagh, E. S. Vizi, K. Wirkner and P. Illes, *Progress in Neurobiology*, 2006, **78**, 327-346.
78. J. A. Sim, M. T. Young*, et al.*, *The Journal of Neuroscience*, 2004, **24**, 6307-6314.
79. G. I. Gorodeski, *Membrane Transport and Signaling*, 2012, **1**, 349-371.
80. S. Roger and P. Pelegrin, *Expert opinion on investigational drugs*, 2011, **20**, 875-880.
81. S. Roger, B. Jelassi*, et al.*, *Biochimica et Biophysica Acta - Biomembranes*, 2015, **1848**, 2584-2602.
82. B. Sperlágh and P. Illes, *Trends in Pharmacological Sciences*, 2014, **35**, 537-547.
83. R. Bartlett, L. Stokes and R. Sluyter, *Pharmacological Reviews*, 2014, **66**, 638-675.
84. D. Ferrari, C. Pizzirani*, et al.*, *The Journal of Immunology*, 2006, **176**, 3877-3883.
85. M. Solle, J. Labasi*, et al.*, *Journal of Biological Chemistry*, 2001, **276**, 125-132.
86. A. K. Clark, A. A. Staniland*, et al.*, *The Journal of neuroscience*, 2010, **30**, 573-582.
87. D. Ferrari, P. Chiozzi*, et al.*, *The Journal of experimental medicine*, 1997, **185**, 579-582.
88. C. H. Shieh, A. Heinrich*, et al.*, *Glia*, 2014, **62**, 592-607.

89. P. Pelegrin, C. Barroso-Gutierrez and A. Surprenant, *Journal of immunology*, 2008, **180**, 7147-7157.
90. R. Mingam, V. De Smedt*, et al.*, *Brain, behavior, and immunity*, 2008, **22**, 234-244.
91. L. K. Parvathenani, S. Tertyshnikova*, et al.*, *The Journal of biological chemistry*, 2003, **278**, 13309-13317.
92. S. C. Hung, C. H. Choi*, et al.*, *PloS one*, 2013, **8**, e70210.
93. R. Munoz-Planillo, P. Kuffa*, et al.*, *Immunity*, 2013, **38**, 1142-1153.
94. O. Gross, C. J. Thomas, G. Guarda and J. Tschopp, *Immunological reviews*, 2011, **243**, 136-151.
95. G. Lopez-Castejon, J. Theaker*, et al.*, *Journal of immunology*, 2010, **185**, 2611-2619.
96. C. Andrei, P. Margiocco*, et al.*, *PNAS USA*, 2004, **101**, 9745-9750.
97. A. K. Clark, R. Wodarski*, et al.*, *Glia*, 2010, **58**, 1710-1726.
98. B. J. Gu, B. M. Saunders, C. Jursik and J. S. Wiley, *Blood*, 2010, **115**, 1621-1631.
99. M. Barbera-Cremades, A. Baroja-Mazo*, et al.*, *The FASEB journal*, 2012, **26**, 2951-2962.
100. C. Cervetto, S. Alloisio*, et al.*, *Journal of neurochemistry*, 2013, **124**, 821-831.
101. M. Marcoli, C. Cervetto*, et al.*, *Journal of neurochemistry*, 2008, **105**, 2330-2342.
102. T. Fellin, T. Pozzan and G. Carmignoto, *The Journal of biological chemistry*, 2006, **281**, 4274-4284.
103. D. Ferrari, S. Wesselborg, M. K. A. Bauer and K. Schulze-Osthoff, *The Journal of Cell Biology*, 1997, **139**, 1635-1643.
104. L. Yip, T. Woehrle*, et al.*, *The FASEB journal*, 2009, **23**, 1685-1693.
105. P. Zanovello, V. Bronte*, et al.*, *Journal of immunology*, 1990, **145**, 1545-1550.
106. S. C. Chow, G. E. Kass and S. Orrenius, *Neuropharmacology*, 1997, **36**, 1149-1156.
107. M. Monif, C. A. Reid*, et al.*, *The Journal of Neuroscience*, 2009, **29**, 3781-3791.
108. O. R. Baricordi, L. Melchiorri*, et al.*, *The Journal of biological chemistry*, 1999, **274**, 33206-33208.
109. O. R. Baricordi, D. Ferrari*, et al.*, *Blood*, 1996, **87**, 682-690.
110. P. Pelegrin and A. Surprenant, *Embo j*, 2009, **28**, 2114-2127.
111. S. Apolloni, S. Amadio*, et al.*, *Disease Models & Mechanisms*, 2014, **7**, 1101-1109.
112. C. De Torre-Minguela, M. Barberà-Cremades*, et al.*, *Scientific Reports*, 2016, **6**, 22586.
113. P. Pelegrin, *British journal of pharmacology*, 2011, **163**, 908-911.
114. L. Yao, E. Kan*, et al.*, *Journal of neuroinflammation*, 2013, **10**, 1-21.
115. Y. Hu, P. L. Fisette*, et al.*, *Journal of Biological Chemistry*, 1998, **273**, 27170-27175.
116. B. Sperlagh, G. Hasko, Z. Nemeth and E. S. Vizi, *Neurochemistry international*, 1998, **33**, 209-215.
117. J. M. Kahlenberg, K. C. Lundberg*, et al.*, *The Journal of Immunology*, 2005, **175**, 7611-7622.
118. C. B. A. Grahames, A. D. Michel, I. P. Chessell and P. P. A. Humphrey, *British journal of pharmacology*, 1999, **127**, 1915-1921.

119. A. MacKenzie, H. L. Wilson*, et al.*, *Immunity*, 2001, **15**, 825-835.
120. C. A. Dinarello, *Seminars in nephrology*, 2007, **27**, 98-114.
121. M. J. Morgan and Z.-g. Liu, *Cell Research*, 2011, **21**, 103-115.
122. M. Hayakawa, H. Miyashita*, et al.*, *The EMBO Journal*, 2003, **22**, 3356-3366.
123. A. Siomek, *Acta biochimica Polonica*, 2012, **59**, 323-331.
124. R. Schreck, P. Rieber and P. A. Baeuerle, *The EMBO Journal*, 1991, **10**, 2247-2258.
125. M. Imran and I. K. Lim, *Cellular signalling*, 2013, **25**, 2400-2412.
126. J. Kakimura, Y. Kitamura*, et al.*, *The FASEB journal*, 2002, **16**, 601-603.
127. J. M. Sanz, P. Chiozzi*, et al.*, *Journal of immunology*, 2009, **182**, 4378-4385.
128. K. Fan, D. Li*, et al.*, *Journal of neuroinflammation*, 2015, **12**, 54.
129. W.-Y. Wang, M.-S. Tan, J.-T. Yu and L. Tan, *Annals of Translational Medicine*, 2015, **3**, 136.
130. G. Ramesh, A. G. MacLean and M. T. Philipp, *Mediators of Inflammation*, 2013, **2013**, 20.
131. J. M. Kahlenberg and G. R. Dubyak, *American Journal of Physiology - Cell Physiology*, 2004, **286**, C1100-C1108.
132. A. Piccini, S. Carta*, et al.*, *Proceedings of the National Academy of Sciences*, 2008, **105**, 8067-8072.
133. A. Baroja-Mazo, F. Martin-Sanchez*, et al.*, *Nature immunology*, 2014, **15**, 738-748.
134. Y. Qu, L. Franchi, G. Nunez and G. R. Dubyak, *Journal of immunology*, 2007, **179**, 1913-1925.
135. I. P. Chessell, J. P. Hatcher*, et al.*, *Pain*, 2005, **114**, 386-396.
136. J. Hughes, J. Hatcher and I. Chessell, *Purinergic Signalling*, 2007, **3**, 163-169.
137. H. E. Vries and M. Schwaninger, *Biochim Biophys Acta*, 2016, **1862**, 297–298.
138. J. G. McLarnon, J. K. Ryu, D. G. Walker and H. B. Choi, *J Neuropathol Exp Neurol*, 2006, **65**, 1090-1097.
139. H. G. Lee, S. M. Won, B. J. Gwag and Y. B. Lee, *Experimental and Molecular Medicine*, 2011, **43**, 7.
140. J. I. Diaz-Hernandez, R. Gomez-Villafuertes*, et al.*, *Neurobiology of aging*, 2012, **33**, 1816-1828.
141. K. Hensley, *Journal of Alzheimer's disease*, 2010, **21**, 1-14.
142. D. L. Krause, #252 and N. ller, *International journal of Alzheimer's disease*, 2010, **2010**.
143. A. H. Jacobs and B. Tavitian, *J Cereb Blood Flow Metab*, 2012, **32**, 1393-1415.
144. D. Krstic and I. Knuesel, *Nature reviews. Neurology*, 2013, **9**, 25-34.
145. M. Díaz-Hernández, M. Díez-Zaera*, et al.*, *The FASEB Journal*, 2009, **23**, 1893-1906.
146. D. Marcellino, D. Suárez-Boomgaard*, et al.*, *Journal of Neural Transmission*, 2010, **117**, 681-687.
147. Y. Iwamaru, T. Takenouchi*, et al.*, *PloS one*, 2012, **7**, e37896.
148. S. Apolloni, C. Parisi*, et al.*, *The Journal of Immunology*, 2013, **190**, 5187-5195.
149. C. Cervetto, D. Frattaroli, G. Maura and M. Marcoli, *Toxicology*, 2013, **311**, 69-77.

150. M. R. Bennett, *The Australian and New Zealand journal of psychiatry*, 2007, **41**, 563-571.
151. E. Setiawan, A. A. Wilson, R. Mizrahi and et al., *JAMA Psychiatry*, 2015, **72**, 268-275.
152. E. Dale, B. Bang-Andersen and C. Sánchez, *Biochemical Pharmacology*, 2015, **95**, 81-97.
153. T. J. Raedler, *Current opinion in psychiatry*, 2011, **24**, 519-525.
154. E. Boorman, G. F. Romano*, et al.*, *Psychiatric Annals*, 2015, **45**, 240-248.
155. P. Zunszain, N. Hepgul and C. Pariante, in Behavioral Neurobiology of Depression and Its Treatment, eds. P. J. Cowen, T. Sharp and J. Y. F. Lau, Springer Berlin Heidelberg, 2013, vol. 14, ch. 211, pp. 135-151.
156. K. S. Kendler, L. M. Karkowski and C. A. Prescott, *The American journal of psychiatry*, 1999, **156**, 837-841.
157. A. M. Basso, N. A. Bratcher*, et al.*, *Behavioural Brain Research*, 2009, **198**, 83-90.
158. A. A. Boucher, J. C. Arnold*, et al.*, *Neuroscience*, 2011, **189**, 170-177.
159. C. Csölle, M. Baranyi*, et al.*, *PloS one*, 2013, **8**, e66547.
160. N. Barden, M. Harvey*, et al.*, *American journal of medical genetics. Part B, Neuropsychiatric genetics*, 2006, **141b**, 374-382.
161. A. Vezzani, J. French, T. Bartfai and T. Z. Baram, *Nature reviews. Neurology*, 2011, **7**, 31-40.
162. J. N. Armstrong, T. B. Brust, R. G. Lewis and B. A. MacVicar, *The Journal of neuroscience*, 2002, **22**, 5938-5945.
163. T. Engel, A. Jimenez-Pacheco*, et al.*, *International Journal of Physiology, Pathophysiology and Pharmacology*, 2012, **4**, 174-187.
164. P. M. Rappold, E. Lynd-Balta and S. A. Joseph, *Brain research*, 2006, **1089**, 171-178.
165. T. Engel, R. Gomez-Villafuertes*, et al.*, *The FASEB journal*, 2012, **26**, 1616-1628.
166. D. Davalos, J. Grutzendler*, et al.*, *Nature neuroscience*, 2005, **8**, 752-758.
167. D. E. Kimbler, J. Shields*, et al.*, *PloS one*, 2012, **7**, e41229.
168. Y. C. Wang, Y. Cui*, et al.*, *Molecular medicine reports*, 2015, **12**, 2149-2154.
169. P. Xu, Y. Xu*, et al.*, *Brain, behavior, and immunity*, 2015, **50**, 87-100.
170. X. Wang, G. Arcuino*, et al.*, *Nature medicine*, 2004, **10**, 821-827.
171. A. Marcillo, B. Frydel, H. M. Bramlett and W. D. Dietrich, *Experimental neurology*, 2012, **233**, 687-692.
172. S. E. Browne, *Journal of neurochemistry*, 2013, **126**, 301-304.
173. C. Volonte, S. Apolloni, C. Parisi and S. Amadio, *Neuropharmacology*, 2015, DOI: 10.1016/j.neuropharm.2015.10.026.
174. S. Amadio, S. Apolloni, N. D'Ambrosi and C. Volonté, *Journal of neurochemistry*, 2011, **116**, 796-805.
175. M. Solle, J. Labasi*, et al.*, *The Journal of biological chemistry*, 2001, **276**, 125-132.
176. L. Chen and C. F. Brosnan, *The Journal of Immunology*, 2006, **176**, 3115-3126.
177. A. J. Sharp, P. E. Polak*, et al.*, *Journal of neuroinflammation*, 2008, **5**, 33.

178. I. P. Chessell, J. P. Hatcher*, et al.*, *Pain*, 2005, **114**, 386-396.
179. O. Oyanguren-Desez, A. Rodríguez-Antigüedad*, et al.*, *Cell Calcium*, 2011, **50**, 468-472.
180. B. J. Gu, J. Field*, et al.*, *Human molecular genetics*, 2015, **24**, 5644-5654.
181. F. Liu and L. D. McCullough, *Acta Pharmacologica Sinica*, 2013, **34**, 1121-1130.
182. V. C. Pimentel, F. V. Pinheiro*, et al.*, *Brain research*, 2011, **1388**, 134-140.
183. M. Domercq, A. Perez-Samartin*, et al.*, *Glia*, 2010, **58**, 730-740.
184. U. B. Eyo, S. A. Miner*, et al.*, *Neuropharmacology*, 2013, **73**, 311-319.
185. R. A. Le Feuvre, D. Brough, O. Touzani and N. J. Rothwell, *Journal of Cerebral Blood Flow & Metabolism*, 2003, **23**, 381-384.
186. H. Franke, A. Gunther*, et al.*, *J Neuropathol Exp Neurol*, 2004, **63**, 686-699.
187. F. Cavaliere, N. D'Ambrosi*, et al.*, *Neurochemistry international*, 2001, **38**, 199-207.
188. F. Cavaliere, N. D'Ambrosi*, et al.*, *Neurochemistry international*, 2001, **38**, 189-197.
189. M. Granado, S. Amor*, et al.*, *Vascular Pharmacology*, 2015, **73**, 96-103.
190. B. Wu, G.-l. Li*, et al.*, *Zhongguo Yaolixue Tongbao*, 2013, **29**, 1413-1417.
191. J. Liu, G. Li*, et al.*, *Purinergic Signal*, 2013, **9**, 463-479.
192. D. Du, M. Jiang*, et al.*, *Neuroscience letters*, 2015, **587**, 22-28.
193. J. Scholz and C. J. Woolf, *Nature neuroscience*, 2002.
194. R.-R. Ji, Z.-Z. Xu and Y.-J. Gao, *Nat Rev Drug Discov*, 2014, **13**, 533-548.
195. D. C. Broom, D. J. Matson*, et al.*, *Journal of pharmacology and experimental therapeutics*, 2008, **327**, 620-633.
196. P. Honore, D. Donnelly-Roberts*, et al.*, *Journal of pharmacology and experimental therapeutics*, 2006, **319**, 1376-1385.
197. G. Dell'Antonio, A. Quattrini*, et al.*, *Arthritis and Rheumatism*, 2002, **46**, 3378-3385.
198. S. McGaraughty, K. L. Chu*, et al.*, *Neuroscience*, 2007, **146**, 1817-1828.
199. A. K. Clark, A. A. Staniland*, et al.*, *Journal of Neuroscience*, 2010, **30**, 573-582.
200. R. E. Sorge, T. Trang*, et al.*, *Nature medicine*, 2012, **18**, 595-599.
201. P. Honore, D. Donnelly-Roberts*, et al.*, *Behav Brain Res*, 2009, **204**, 77-81.
202. A. Baroja-Mazo and P. Pelegrin, *Journal of Osteoporosis*, 2012, **2012**, 7.
203. K. A. Hillman, G. Burnstock and R. J. Unwin, *Nephron Experimental Nephrology*, 2005, **101**, e24-e30.
204. J. W. Booth, F. W. Tam and R. J. Unwin, *Clinical nephrology*, 2012, **78**, 154-163.
205. T. Muller, R. P. Vieira*, et al.*, *American journal of respiratory cell and molecular biology*, 2011, **44**, 456-464.
206. M. Tewari and P. Seth, *Ageing Research Reviews*, 2015, **24B**, 328-342.
207. B. J. Gu, W. Y. Zhang*, et al.*, *American journal of physiology. Cell physiology*, 2000, **279**, C1189-1197.
208. R. A. Worthington, M. L. Smart*, et al.*, *FEBS letters*, 2002, **512**, 43-46.
209. J. A. Barden, A. Yuksel*, et al.*, *Journal of Clinical & Cellular Immunology*, 2014, **5**, 237.
210. T. Sugiyama, *Neural Regeneration Research*, 2014, **9**, 579-581.

211. K. A. Vessey, A. I. Jobling, U. Greferath and E. L. Fletcher, *Advances in experimental medicine and biology*, 2012, **723**, 813-819.
212. T. Sugiyama, *World Journal of Diabetes*, 2014, **5**, 141-145.
213. R. Gum, B. Wakefield and M. Jarvis, *Purinergic Signalling*, 2012, **8**, 41-56.
214. D. L. Donnelly-Roberts, M. T. Namovic, P. Han and M. F. Jarvis, *British journal of pharmacology*, 2009, **157**, 1203-1214.
215. L. H. Jiang, A. B. Mackenzie, R. A. North and A. Surprenant, *Molecular pharmacology*, 2000, **58**, 82-88.
216. B. Janssen, D. J. Vugts*, et al.*, *Journal of Labelled Compounds and Radiopharmaceuticals*, 2014, **57**, 509-516.
217. C. E. Gargett and J. S. Wiley, *British journal of pharmacology*, 1997, **120**, 1483-1490.
218. M. Iwata, K. T. Ota*, et al.*, *Biological psychiatry*, 2016, **80**, 12-22.
219. A. S. Florjancic, S. Peddi*, et al.*, *Bioorganic & medicinal chemistry letters*, 2008, **18**, 2089-2092.
220. D. W. Nelson, R. J. Gregg*, et al.*, *Journal of medicinal chemistry*, 2006, **49**, 3659-3666.
221. L. Stokes, L. H. Jiang*, et al.*, *British journal of pharmacology*, 2006, **149**, 880-887.
222. A. D. Michel, S.-W. Ng*, et al.*, *British journal of pharmacology*, 2009, **156**, 1312-1325.
223. M. A. Letavic, B. Lord*, et al.*, *ACS Medicinal Chemistry Letters*, 2013, **4**, 419-422.
224. L. Abberley, A. Bebius*, et al.*, *Bioorganic & medicinal chemistry letters*, 2010, **20**, 6370-6374.
225. M. H. Abdi, P. J. Beswick*, et al.*, *Bioorganic & medicinal chemistry letters*, 2010, **20**, 5080-5084.
226. R. Romagnoli, P. G. Baraldi*, et al.*, *Bioorganic & medicinal chemistry letters*, 2004, **14**, 5709-5712.
227. A. D. Michel, L. J. Chambers*, et al.*, *British journal of pharmacology*, 2007, **151**, 103-114.
228. A. D. Michel, L. J. Chambers and D. S. Walter, *British journal of pharmacology*, 2008, **153**, 737-750.
229. D. L. Donnelly-Roberts, M. T. Namovic*, et al.*, *Neuropharmacology*, 2009, **56**, 223-229.
230. M. K. Ameriks, J. C. Rech and B. M. Savall, P2X7 modulators, 2014, *WO20160016962*.
231. B. Lord, M. K. Ameriks*, et al.*, *European journal of pharmacology*, 2015, **765**, 551-559.
232. A. Jackson and V. Morisson-Iveson, Imaging the central nervous system with purinergic p2x7 receptor binding agents, 2010, *WO2010115881A1*.
233. B. Janssen, D. Ory, S. SWilkinson and D. J. W. Vugts, Albert D., *Journal of Labelled Compounds and Radiopharmaceuticals*, 2015, **58**, S277.
234. M. Gao, M. Wang*, et al.*, *Bioorganic & medicinal chemistry letters*, 2015, **25**, 1965-1970.
235. Z. Ali, B. Laurijssens*, et al.*, *British Journal of Clinical Pharmacology*, 2013, **75**, 197-207.
236. D. Ory, S. Celen*, et al.*, *Journal of nuclear medicine*, 2016, DOI: 10.2967/jnumed.115.169995.

237. Y. Kataoka, Molecular Imaging by PET, 2010, *www.phys.org*, http://phys.org/news/2010-09-molecular-imaging-vast-world-neuroscience.html, August 2016.
238. M. Bergstrom and B. Langstrom, in Imaging in drug discovery and early clinical trials, ed. M. Rudin, Birkhauser Verlag, Progress in drug research, 2005, vol. 62, pp. 308-313.
239. O. Ivashchenko, F. van der Have*, et al.*, *Molecular imaging*, 2014, **13**.
240. A. Rahmim and H. Zaidi, *Nuclear medicine communications*, 2008, **29**, 193-207.
241. S. R. Cherry, J. A. Sorenson and M. E. Phelps, in Physics in Nuclear Medicine - Chapter 18 - Positron Emission Tomography
eds. M. E. Phelps, S. R. Cherry and J. A. Sorenson, W.B. Saunders, Philadelphia, 2012, pp. 307-343.
242. R. E. Schmitz, A. M. Alessio and P. E. Kinahan, *Washington University Imaging research laboratory Repository*, 2013, **1**, 1-16.
243. V. Bettinardi, M. Picchio*, et al.*, *The quarterly journal of nuclear medicine and molecular imaging*, 2010, **54**, 455-475.
244. K. Facey, I. Bradbury, G. Laking and L. Payne, *Health Technology Assessment*, 2007, **11**, 288.
245. B. M.-M., C. V.*, et al.*, Monographie BIPM-5, Table of radionuclides, 2004.
246. E. Hess, G. Blessing, H. H. Coenen and S. M. Qaim, *Applied radiation and isotopes*, 2000, **52**, 1431-1440.
247. G. Blessing, H. H. Coenen, K. Franken and S. M. Qaim, *International Journal of Radiation Applications and Instrumentation*, 1986, **37**, 1135-1139.
248. M. Ogawa, K. Hatano*, et al.*, *Nuclear medicine and biology*, 2003, **30**, 1-9.
249. H. Teare, E. G. Robins*, et al.*, *Chemical communications*, 2007, 2330-2332.
250. R. E. Ehrenkaufer, J. F. Potocki and D. M. Jewett, *Journal of nuclear medicine*, 1984, **25**, 333-337.
251. G. Antoni and B. Langstrom, *Handbook of experimental pharmacology*, 2008, DOI: 10.1007/978-3-540-72718-7_9, 177-201.
252. J. R. Mercer, *Journal of pharmacy & pharmaceutical sciences*, 2007, **10**, 180-202.
253. N. George, E. G. Gean*, et al.*, *CNS Drugs*, 2015, **29**, 313-330.
254. C. Nanni, S. Fanti and D. Rubello, *Journal of Nuclear Medicine*, 2007, **48**, 1577-1579.
255. T. Hara, N. Kosaka and H. Kishi, *Journal of nuclear medicine*, 1998, **39**, 990-995.
256. E. T. McKinley, G. D. Ayers*, et al.*, *PloS one*, 2013, **8**, e58938.
257. J. G. Rajendran, D. A. Mankoff*, et al.*, *Clinical cancer research*, 2004, **10**, 2245-2252.
258. H. D. Burns, K. Van Laere*, et al.*, *PNAS USA*, 2007, **104**, 9800-9805.
259. O. G. James, P. M. Doraiswamy and S. Borges-Neto, *Frontiers in Neurology*, 2015, **6**, 38.
260. R. Lewis, S. Kapur*, et al.*, *The American journal of psychiatry*, 1999, **156**, 72-78.
261. M. A. Mintun, Y. I. Sheline*, et al.*, *Biological psychiatry*, 2004, **55**, 217-224.
262. D. E. Ettlinger, D. Hausler*, et al.*, *Nuclear medicine and biology*, 2008, **35**, 475-479.

263. A. Dance, Imaging Inflammation: Can Glial PET Tracers Make a Mark?, Alzforum, www.alzforum.org/new/detail.asp?id=3133, 2012.
264. A. Ching, B. Kuhnast*, et al.*, *Insights Imaging*, 2012, **3**, 111-119.
265. C. Halldin, B. Gulyás and L. Farde, in From Morphological Imaging to Molecular Targeting, eds. M. Schwaiger, L. Dinkelborg and H. Schweinfurth, Springer Berlin Heidelberg, 2004, vol. 48, ch. 5, pp. 95-109.
266. P. M. Matthews, E. A. Rabiner, J. Passchier and R. N. Gunn, *Br J Clin Pharmacol*, 2012, **73**, 175-186.
267. J. Wang and L. Maurer, *Current topics in medicinal chemistry*, 2005, **5**, 1053-1075.
268. A. D. Gee, *British Medical Bulletin*, 2003, **65**, 169-177.
269. A. W. J. M. Glaudemans and A. Signore, *Eur J Nucl Med Mol Imaging*, 2010, **37**, 1986-1991.
270. S. Vaidyanathan, C. N. Patel, A. F. Scarsbrook and F. U. Chowdhury, *Clinical radiology*, 2015, **70**, 787-800.
271. C. Wu, F. Li, G. Niu and X. Chen, *Theranostics*, 2013, **3**, 448-466.
272. A. Roivainen and T. Yli-Kerttula, *Eur J Nucl Med Mol Imaging*, 2006, **33**, 1372-1373.
273. C. M. Matter, M. T. Wyss*, et al.*, *Arteriosclerosis, thrombosis, and vascular biology*, 2006, **26**, 584-589.
274. N. Tahara, J. Mukherjee*, et al.*, *Nature medicine*, 2014, **20**, 215-219.
275. R. Rupprecht, V. Papadopoulos*, et al.*, *Nat Rev Drug Discov*, 2010, **9**, 971-988.
276. J. K. Ryu, H. B. Choi and J. G. McLarnon, *Neurobiology of disease*, 2005, **20**, 550-561.
277. F. Chauveau, H. Boutin*, et al.*, *Eur J Nucl Med Mol Imaging*, 2008, **35**, 2304-2319.
278. B. A. Weissman, R. Brandeis*, et al.*, *Annals of the New York Academy of Sciences*, 2004, **1025**, 584-589.
279. M. Yokokura, N. Mori*, et al.*, *Eur J Nucl Med Mol Imaging*, 2011, **38**, 343-351.
280. K. Herholz, *Journal of the Neurological Sciences*, 2006, **245**, 9-13.
281. O. Gaemperli, J. Shalhoub*, et al.*, *European heart journal*, 2012, **33**, 1902-1910.
282. B. Gulyás, M. Tóth*, et al.*, *Journal of the Neurological Sciences*, 2012, **320**, 110-117.
283. S. Venneti, B. J. Lopresti*, et al.*, *The Journal of Clinical Investigation*, 2004, **113**, 981-989.
284. A. Colasanti, Q. Guo*, et al.*, *Journal of Nuclear Medicine*, 2014, **55**, 1112-1118.
285. Q. Guo, A. Colasanti*, et al.*, *Journal of nuclear medicine*, 2013, **54**, 1915-1923.
286. D. R. Owen, A. J. Yeo*, et al.*, *Journal of Cerebral Blood Flow & Metabolism*, 2012, **32**, 1-5.
287. M. A. Scarf, C. Luus*, et al.*, *Current Molecular Medicine*, 2012, **12**, 488-493.
288. D. R. Owen, R. N. Gunn*, et al.*, *Journal of nuclear medicine*, 2011, **52**, 24-32.
289. H. Boutin, K. Murray*, et al.*, *Eur J Nucl Med Mol Imaging*, 2015, **42**, 503-511.
290. A. M. Dickens, S. Vainio*, et al.*, *Journal of nuclear medicine*, 2014, **55**, 466-472.
291. Z. Fan, V. Calsolaro*, et al.*, *Journal of Nuclear Medicine*, 2016, DOI: 10.2967/jnumed.115.169078.

292. Alzforum, Meet GE-180: a PET ligand for tracking neuroinflammation, http://www.alzforum.org/news/conference-coverage/meet-ge180-pet-ligand-tracking-neuroinflammation).
293. A. C. Dupont, D. Guilloteau*, et al.*, *Médecine Nucléaire*, 2016, **40**, 72-81.
294. C. Benito, R. M. Tolón*, et al.*, *British journal of pharmacology*, 2008, **153**, 277-285.
295. N. Evens, C. Vandeputte*, et al.*, *Nuclear medicine and biology*, 2012, **39**, 389-399.
296. A. G. Horti, Y. Gao*, et al.*, *Bioorganic & medicinal chemistry*, 2010, **18**, 5202-5207.
297. A. Rominger, T. Saam*, et al.*, *Journal of nuclear medicine*, 2010, **51**, 193-197.
298. X. Li, S. Samnick*, et al.*, *EJNMMI Res*, 2012, **2**, 52.
299. M. J. Uddin, B. C. Crews*, et al.*, *Cancer Prevention Research*, 2011, **4**, 1536-1545.
300. E. F. de Vries, J. Doorduin, R. A. Dierckx and A. van Waarde, *Nuclear medicine and biology*, 2008, **35**, 35-42.
301. L. Minghetti, *J Neuropathol Exp Neurol*, 2004, **63**, 901-910.
302. D. J. Yang, J. Bryant*, et al.*, *Anti-cancer drugs*, 2004, **15**, 255-263.
303. D. Hartung, M. Schäfers*, et al.*, *Eur J Nucl Med Mol Imaging*, 2007, **34**, 1-8.
304. S. Hermann, A. Starsichova*, et al.*, *Journal of nuclear cardiology*, 2012, **19**, 609-617.
305. S. R. Lee, K. Tsuji, S. R. Lee and E. H. Lo, *The Journal of neuroscience*, 2004, **24**, 671-678.
306. J. E. Sprague, W. P. Li*, et al.*, *Nuclear medicine and biology*, 2006, **33**, 227-237.
307. S. Wagner, H.-J. Breyholz*, et al.*, *Applied Radiation and Isotopes*, 2009, **67**, 606-610.
308. Y. Kuge, N. Takai*, et al.*, *Eur J Nucl Med Mol Imaging*, 2010, **37**, 2093-2104.
309. V. Hugenberg, H. J. Breyholz*, et al.*, *Journal of medicinal chemistry*, 2012, **55**, 4714-4727.
310. V. Di Gialleonardo, A. Signore*, et al.*, *Journal of nuclear medicine*, 2012, **53**, 679-686.
311. A. Signore, A. Picarelli*, et al.*, *Nuclear medicine communications*, 2003, **24**, 305-316.
312. A. Annovazzi, E. Bonanno*, et al.*, *Eur J Nucl Med Mol Imaging*, 2006, **33**, 117-126.
313. A. Signore, M. Chianelli*, et al.*, *Journal of nuclear medicine*, 2000, **41**, 242-249.
314. C. B. Cairns, E. A. Panacek, A. H. Harken and A. Banerjee, *Academic emergency medicine*, 2000, **7**, 930-941.
315. Q. Cao, W. Cai*, et al.*, *Eur J Nucl Med Mol Imaging*, 2007, **34**, 1832-1842.
316. M. Gao, C. M. Lola*, et al.*, *Applied radiation and isotopes*, 2010, **68**, 1950-1958.
317. E. F. J. de Vries, M. Roca*, et al.*, *Eur J Nucl Med Mol Imaging*, 2010, **37**, 842-848.
318. A. Autio, S. Jalkanen and A. Roivainen, *EJNMMI Research*, 2013, **3**, 1-7.
319. M. Bhatti, P. Chapman*, et al.*, *Gut*, 1998, **43**.
320. P. T. Chapman, F. Jamar*, et al.*, *Br J Rheumatol*, 1996, **35**.
321. P. T. Chapman, F. Jamar*, et al.*, *Arthritis Rheum*, 1996, **39**.
322. F. Jamar, F. A. Houssiau*, et al.*, *Rheumatology*, 2002, **41**.
323. E. T. Keelan, A. A. Harrison*, et al.*, *Journal of nuclear medicine*, 1994, **35**.
324. A. Broisat, L. M. Riou*, et al.*, *Eur J Nucl Med Mol Imaging*, 2007, **34**.
325. M. Nahrendorf, E. Keliher*, et al.*, *JACC Cardiovasc Imaging*, 2009, **2**.

326. M. Sans, D. Fuster*, et al.*, *Eur J Gastroenterol Hepatol*, 2001, **13**.
327. A. J. Beer and M. Schwaiger, *Cancer Metastasis Rev*, 2008, **27**.
328. W. Cai, S. S. Gambhir and X. Chen, *Biotechniques*, 2005, **39**.
329. R. Haubner, *Eur J Nucl Med Mol Imaging*, 2006, **33**.
330. A. Autio, T. Ujula*, et al.*, *Eur J Nucl Med Mol Imaging*, 2010, **37**.
331. K. Jaakkola, T. Nikula*, et al.*, *The American journal of pathology*, 2000, **157**.
332. T. Ujula, S. Salomäki*, et al.*, *Molecular imaging and biology*, 2010, **12**.
333. M. Fumita and R. B. Innis, in Neuropsychopharmacology: The Fifth Generation of Progress, 2000, pp. 411-425.
334. S. Patel and R. Gibson, *Nuclear medicine and biology*, 2008, **35**, 805-815.
335. E. C. Hulme and M. A. Trevethick, *British journal of pharmacology*, 2010, **161**, 1219-1237.
336. E. D. Morris and E. D. London, in Quantitative Functional Brain Imaging with Positron Emission Tomography, ed. R. E. Carson, Academic Press, 1998, ch. VII, 61, pp. 407-414.
337. J. Singh, R. C. Petter, T. A. Baillie and A. Whitty, *Nat Rev Drug Discov*, 2011, **10**, 307-317.
338. P. M. Matthews, E. A. Rabiner, J. Passchier and R. N. Gunn, *British Journal of Clinical Pharmacology*, 2012, **73**, 175-186.
339. G. C. Van de Bittner, E. L. Ricq and J. M. Hooker, *Accounts of Chemical Research*, 2014, **47**, 3127-3134.
340. A. Bhattacharya, Q. Wang*, et al.*, *British journal of pharmacology*, 2013, **170**, 624-640.
341. C. A. Lipinski, F. Lombardo, B. W. Dominy and P. J. Feeney, *Advanced Drug Delivery Reviews*, 1997, **23**, 3-25.
342. R. N. Waterhouse, *Molecular imaging and biology*, 2003, **5**, 376-389.
343. H. Pajouhesh and G. R. Lenz, *NeuroRx*, 2005, **2**, 541-553.
344. S. A. Hitchcock and L. D. Pennington, *Journal of medicinal chemistry*, 2006, **49**, 7559-7583.
345. V. W. Pike, *Trends in Pharmacological Sciences*, 2009, **30**, 431-440.
346. P. Brust, J. van den Hoff and J. Steinbach, *Neuroscience bulletin*, 2014, **30**, 777-811.
347. H. U. Shetty, S. S. Zoghbi*, et al.*, *Eur J Nucl Med Mol Imaging*, 2007, **34**, 667-678.
348. S. Osman, C. Lundkvist*, et al.*, *Nuclear medicine and biology*, 1996, **23**, 627-634.
349. E. Briard, S. S. Zoghbi*, et al.*, *Journal of medicinal chemistry*, 2008, **51**, 17-30.
350. A. K. Brown, Y. Kimura*, et al.*, *Journal of nuclear medicine : official publication, Society of Nuclear Medicine*, 2008, **49**, 2042-2048.
351. E. Arstad, unpublished work, "Click" fluorine-18 labelling of small molecules for the synthesis of PET tracers, *Positron emission tomography technology and application - KCL course*, 2013.
352. S. S. Zoghbi, H. U. Shetty*, et al.*, *Journal of nuclear medicine*, 2006, **47**, 520-527.

353. K. Hashimoto, M. Kojima*, et al.*, *International Journal of Radiation Applications and Instrumentation. Part B. Nuclear Medicine and Biology*, 1986, **13**, 79-80.
354. J. S. Fowler, A. P. Wolf*, et al.*, *Journal of neurochemistry*, 1988, **51**, 1524-1534.
355. D. N. Tipre, S. S. Zoghbi*, et al.*, *Journal of nuclear medicine*, 2006, **47**, 345-353.
356. A. Matusch, P. T. Meyer*, et al.*, *Nuclear medicine and biology*, 2006, **33**, 891-898.
357. H. Sun, H. Dai, N. Shaik and W. F. Elmquist, *Adv Drug Deliv Rev*, 2003, **55**, 83-105.
358. A. Tsuji, *NeuroRx*, 2005, **2**, 54-62.
359. H. Davson and M. B. Segal, Physiology of the CSF and Blood Brain Bariers, CRC-Press, 1995.
360. T. J. Raub, *Molecular pharmaceutics*, 2006, **3**, 3-25.
361. G. Lacan, A. Plenevaux*, et al.*, *Eur J Nucl Med Mol Imaging*, 2008, **35**, 2256-2266.
362. S. Syvanen, O. Lindhe*, et al.*, *Drug metabolism and disposition*, 2009, **37**, 635-643.
363. N. Tournier, W. Saba*, et al.*, *The AAPS journal*, 2013, **15**, 1082-1090.
364. L. Di, E. H. Kerns*, et al.*, *European journal of medicinal chemistry*, 2003, **38**, 223-232.
365. K. Cohen-Kashi Malina, I. Cooper and V. I. Teichberg, *Brain research*, 2009, **1284**, 12-21.
366. K. Valkó, *Journal of Chromatography A*, 2004, **1037**, 299-310.
367. A. Patabendige, R. A. Skinner and N. J. Abbott, *Brain research*, 2013, **1521**, 1-15.
368. M. Hitzl, S. Drescher*, et al.*, *Pharmacogenetics*, 2001, **11**, 293-298.
369. A. Stewart, J. Steiner*, et al.*, *Clinical cancer research*, 2000, **6**, 4186-4191.
370. S. M. Witherspoon, D. L. Emerson*, et al.*, *Clinical cancer research*, 1996, **2**, 7-12.
371. M. Yamazaki, W. E. Neway*, et al.*, *The Journal of pharmacology and experimental therapeutics*, 2001, **296**, 723-735.
372. H. C. Helms, M. Hersom*, et al.*, *The AAPS journal*, 2014, **16**, 1046-1055.
373. L. Zhang, A. Villalobos*, et al.*, *Journal of medicinal chemistry*, 2013, **56**, 4568-4579.
374. D. Schwab, H. Fischer*, et al.*, *Journal of medicinal chemistry*, 2003, **46**, 1716-1725.
375. B. Feng, J. B. Mills*, et al.*, *Drug Metabolism and Disposition*, 2008, **36**, 268-275.
376. M. R. Kilbourn, M. R. Pavia and V. E. Gregor, *International journal of radiation applications and instrumentation. Part A, Applied radiation and isotopes*, 1990, **41**, 823-828.
377. F. Fuchtner, S. Preusche*, et al.*, *Nuklearmedizin. Nuclear medicine*, 2008, **47**, 116-119.
378. K. Suzuki, T. Yamazaki, M. Sasaki and A. Kubodera, *Radiochimica Acta*, 2000, **88**, 211.
379. K. Müller, C. Faeh and F. Diederich, *Science*, 2007, **317**, 1881-1886.
380. J. Wang, M. Sánchez-Roselló*, et al.*, *Chemical reviews*, 2014, **114**, 2432-2506.
381. A. Duatti, *Nuclear medicine and biology*, 2013, **40**, 871-872.
382. B. K. Park, N. R. Kitteringham and P. M. O'Neill, *Annual review of pharmacology and toxicology*, 2001, **41**, 443-470.
383. M. R. Kilbourn, *Nuclear medicine and biology*, 2013, **40**, 956-958.
384. M. Blau, W. Nagler and M. A. Bender, *Journal of nuclear medicine*, 1962, **3**, 332-334.

385. T. Yamazaki, T. Taguchi and I. Ojima, in Fluorine in Medicinal Chemistry and Chemical Biology, ed. I. Ojima, John Wiley & Sons, Ltd, 2009, vol. 1, pp. 1-46.
386. D. E. Ponde, C. S. Dence*, et al.*, *Journal of Nuclear Medicine*, 2007, **48**, 420-428.
387. H.-J. Park, C. H. Kim*, et al.*, *Journal of Nuclear Medicine*, 2013, **54**, 1263-1269.
388. N. Vasdev, P. Seeman*, et al.*, *Nuclear medicine and biology*, 2007, **34**, 195-203.
389. A. Perez-Medrano, D. L. Donnelly-Roberts*, et al.*, *Journal of medicinal chemistry*, 2009, **52**, 3366-3376.
390. W. A. Carroll, A. Perez-Medrano*, et al.*, P2X7 antagonists for treating neuropathic pain, 2004, *US20040980674*.
391. M. J. Morytko, P. Betschmann*, et al.*, *Bioorganic & medicinal chemistry letters*, 2008, **18**, 2093-2096.
392. P. Betschmann, B. Bettencourt*, et al.*, *Bioorganic & medicinal chemistry letters*, 2008, **18**, 3848-3851.
393. H. Gunosewoyo and M. Kassiou, *Expert opinion on therapeutic patents*, 2010, **20**, 625-646.
394. D. Dal Ben, M. Buccioni*, et al.*, *European journal of medicinal chemistry*, 2015, **89**, 561-580.
395. G. Morris and M. Lim-Wilby, in Molecular Modeling of Proteins, ed. A. Kukol, Humana Press, 2008, vol. 443, ch. 19, pp. 365-382.
396. H. M. Berman, J. Westbrook*, et al.*, *Nucleic Acids Research*, 2000, **28**, 235-242.
397. S. D. Guile, L. Alcaraz*, et al.*, *Journal of medicinal chemistry*, 2009, **52**, 3123-3141.
398. A. K. Ghose and G. M. Crippen, *Journal of Chemical Information and Computer Sciences*, 1987, **27**, 21-35.
399. V. N. Viswanadhan, A. K. Ghose, G. R. Revankar and R. K. Robins, *Journal of Chemical Information and Computer Sciences*, 1989, **29**, 163-172.
400. Molinspiration, logP - octanol-water partition coefficient, http://www.molinspiration.com/services/logp.html, (accessed 30 March 2016).
401. P. Ertl, B. Rohde and P. Selzer, *Journal of medicinal chemistry*, 2000, **43**, 3714-3717.
402. J. P. Stewart, *Journal of Computer-Aided Molecular Design*, 1990, **4**, 1-103.
403. W. D. Cornell, P. Cieplak*, et al.*, *Journal of the American Chemical Society*, 1995, **117**, 5179-5197.
404. G. M. Morris, R. Huey*, et al.*, *Journal of Computational Chemistry*, 2009, **30**, 2785-2791.
405. G. M. Morris, D. S. Goodsell*, et al.*, *Journal of Computational Chemistry*, 1998, **19**, 1639-1662.
406. T. A. Halgren, *Journal of Computational Chemistry*, 1996, **17**, 490-641.
407. T. A. Halgren, *Journal of Computational Chemistry*, 1999, **20**, 720-748.
408. M. Glaser and E. G. Robins, *Journal of Labelled Compounds and Radiopharmaceuticals*, 2009, **52**, 407-414.
409. C. Mamat, T. Ramenda and F. R. Wuest, *Mini-Reviews in Organic Chemistry*, 2009, **6**, 21-34.

410. M. Glaser and E. Årstad, *Bioconjugate Chemistry*, 2007, **18**, 989-993.
411. O. Tietz, S. K. Sharma*, et al.*, *Organic & Biomolecular Chemistry*, 2013, **11**, 8052-8064.
412. R. W. Turner, *Synthesis*, 1975, **1975**, 332-332.
413. P. C. Unangst, D. T. Connor*, et al.*, *Journal of medicinal chemistry*, 1994, **37**, 322-328.
414. Y. Dai, Y. Guo*, et al.*, *Journal of medicinal chemistry*, 2005, **48**, 6066-6083.
415. A. Buschauer, R. Mohr and W. Schunack, *Archiv der Pharmazie*, 1995, **328**, 349-358.
416. T. Hashimoto, S. Harusawa*, et al.*, *Journal of medicinal chemistry*, 2003, **46**, 3162-3165.
417. K. S. Atwal, S. Z. Ahmed and B. C. O'Reilly, *Tetrahedron Letters*, 1989, **30**, 7313-7316.
418. J. K. Choi, Y. S. Jeong*, et al.*, Novel thiourea derivatives and the pharmaceutical compositions containing the same, 2002, *WO2002016318*.
419. P. W. Manley, U. Quast, H. Andres and K. Bray, *Journal of medicinal chemistry*, 1993, **36**, 2004-2010.
420. C. D. Smith, *Sel. Org. React. Database (SORD)*, 2008, no pp. given.
421. R. Altenbach, H. Bai*, et al.*, Potassium channel openers, 2002, *WO2002062762A2*.
422. G. Evindar, Novel Approaches to Synthesis of Nitrogen Containing Heterocycles, Thesis (Ph.D.) - University of Toronto, 2004.
423. A. Perez-Medrano, D. L. Donnelly-Roberts*, et al.*, *Journal of medicinal chemistry*, 2009, **52**, 3366-3376.
424. R. Berg and B. F. Straub, *Beilstein J. Org. Chem.*, 2013, **9**, 2715-2750.
425. V. V. Rostovtsev, L. G. Green, V. V. Fokin and K. B. Sharpless, *Angewandte Chemie International Edition*, 2002, **41**, 2596-2599.
426. V. O. Rodionov, V. V. Fokin and M. G. Finn, *Angewandte Chemie International Edition*, 2005, **44**, 2210-2215.
427. V. O. Rodionov, S. I. Presolski*, et al.*, *Journal of the American Chemical Society*, 2007, **129**, 12705-12712.
428. L. Jin, D. R. Tolentino, M. Melaimi and G. Bertrand, *Science Advances*, 2015, **1**, e1500304.
429. G. R. Fulmer, A. J. M. Miller*, et al.*, *Organometallics*, 2010, **29**, 2176-2179.
430. Z. P. Demko and K. B. Sharpless, *Organic Letters*, 2001, **3**, 4091-4094.
431. M. S. Haka, M. R. Kilbourn, G. Leonard Watkins and S. A. Toorongian, *Journal of Labelled Compounds and Radiopharmaceuticals*, 1989, **27**, 823-833.
432. B. L. Finkelstein, E. A. Benner*, et al.*, *Bioorganic & medicinal chemistry*, 2002, **10**, 599-613.
433. T. Yamada, Y. Nobuhara*, et al.*, *Journal of medicinal chemistry*, 1983, **26**, 373-381.
434. S. Beaudoin, H. Finlay*, et al.*, Cycloalkyl inhibitors of potassium channel function, 2003, *WO 2003063797*.
435. S. Beaudoin, H. Finlay*, et al.*, Heterocyclo inhibitors of potassium channel function, 2003,

436. J. H. Beynon, J. A. Hopkinson and A. E. Williams, *Organic Mass Spectrometry*, 1968, **1**, 169-187.
437. H. L. Yale and E. R. Spitzmiller, *Journal of Heterocyclic Chemistry*, 1976, **13**, 443-448.
438. P. Betschmann, W. A. Carroll*, et al.*, Piperazines as p2x7 antagonists, 2008, *WO2008005368A2*.
439. J. H. Yen, Sulfide precipitation of heavy metals from aqueous solutions, 1994, *US5338460A*.
440. M. G. Loudon, in Organic Chemistry, Oxford University Press, 4th edition edn., 2002, pp. 165–168.
441. V. V. Rostovtsev, L. G. Green, V. V. Fokin and K. B. Sharpless, *Angewandte Chemie*, 2002, **41**, 2596-2599.
442. R. N. Butler, W. J. Cunningham, A. G. Coyne and L. A. Burke, *Journal of the American Chemical Society*, 2004, **126**, 11923-11929.
443. M. K. Singh, R. Tilak*, et al.*, *European journal of medicinal chemistry*, 2013, **63**, 635-644.
444. M. M. Heravi, H. Hamidi and V. Zadsirjan, *Current Organic Synthesis*, 2014, **11**, 647-675.
445. K. B. Kellogg and G. H. Cady, *Journal of the American Chemical Society*, 1948, **70**, 3986-3990.
446. S. Forsback and O. Solin, *Radiochimica Acta*, 2015, **103**, 219-226.
447. J. Bergman and O. Solin, *Nuclear medicine and biology*, 1997, **24**, 677-683.
448. E. Lee, A. S. Kamlet*, et al.*, *Science*, 2011, **334**, 639-642.
449. H. Teare, E. G. Robins*, et al.*, *Angewandte Chemie International Edition*, 2010, **49**, 6821-6824.
450. K. Hamacher and H. H. Coenen, *Applied Radiation and Isotopes*, 2002, **57**, 853-856.
451. P. A. Schubiger, L. Lehmann, M. Friebe and D. J. Yang, *Journal of Nuclear Medicine*, 2007, **48**, 1750.
452. G. Angelini, M. Speranza, A. P. Wolf and C. Y. Shiue, *Journal of Fluorine Chemistry*, 1985, **27**, 177-191.
453. B. de Bruin, B. Kuhnast*, et al.*, *Bioconjug Chem*, 2005, **16**, 406-420.
454. B. Kuhnast, B. de Bruin*, et al.*, *Bioconjug Chem*, 2004, **15**, 617-627.
455. G. Tang, X. Tang and X. Wang, *Journal of Labelled Compounds and Radiopharmaceuticals*, 2010, **53**, 543-547.
456. B. Shen, D. Löffler*, et al.*, *Journal of Labelled Compounds and Radiopharmaceuticals*, 2010, **53**, 113-119.
457. T. M. Moore, M. R. Akula, L. Collier and G. W. Kabalka, *Applied Radiation and Isotopes*, 2013, **71**, 47-50.
458. M. Attiná, F. Cacace and A. P. Wolf, *Journal of Labelled Compounds and Radiopharmaceuticals*, 1983, **20**, 501-514.

459. M. S. Berridge, C. Crouzel and D. Comar, *Journal of Labelled Compounds and Radiopharmaceuticals*, 1985, **22**, 687-694.
460. F. Cacace, M. Speranza, A. P. Wolf and J. S. Fowler, *Journal of Labelled Compounds and Radiopharmaceuticals*, 1981, **18**, 1721-1730.
461. S. Telu, J. H. Chun*, et al.*, *Organic & Biomolecular Chemistry*, 2011, **9**, 6629-6638.
462. E. M. Billaud, A. Maisonial-Besset*, et al.*, *European journal of medicinal chemistry*, 2015, **92**, 818-838.
463. M. Tredwell and V. Gouverneur, *Angewandte Chemie*, 2012, **51**, 11426-11437.
464. N. Lazarova, F. G. Siméon*, et al.*, *Journal of Labelled Compounds and Radiopharmaceuticals*, 2007, **50**, 463-465.
465. G. Tang, W. Zeng, M. Yu and G. Kabalka, *Journal of Labelled Compounds and Radiopharmaceuticals*, 2008, **51**, 68-71.
466. H. H. Coenen, in PET Chemistry, eds. P. A. Schubiger, L. Lehmann and M. Friebe, Springer Berlin Heidelberg, 2007, vol. 64, ch. 2, pp. 15-50.
467. J. D. Way, M. Wang*, et al.*, *Nuclear medicine and biology*, 2014, **41**, 660-669.
468. F. R. Wuest, A. Hohne and P. Metz, *Organic & Biomolecular Chemistry*, 2005, **3**, 503-507.
469. F. R. Wüst and T. Kniess, *Journal of Labelled Compounds and Radiopharmaceuticals*, 2004, **47**, 457-468.
470. T. A. Forngren, Yvonne; Lamm, Bo; Långström, Bengt, *Acta Chemica Scandinavica*, 1998, **52**, 475-479.
471. E. Marrière, J. Rouden, V. Tadino and M.-C. Lasne, *Organic Letters*, 2000, **2**, 1121-1124.
472. Z. Gao, V. Gouverneur and B. G. Davis, *Journal of the American Chemical Society*, 2013, **135**, 13612-13615.
473. M. S. Yusubov, D. Y. Svitich, M. S. Larkina and V. V. Zhdankin, *Arkivoc*, 2013, **i**, 364-395.
474. A. F. Brooks, J. J. Topczewski*, et al.*, *Chemical Science*, 2014, **5**, 4545-4553.
475. J.-H. Chun and V. W. Pike, *The Journal of Organic Chemistry*, 2012, **77**, 1931-1938.
476. E. A. Merritt and B. Olofsson, *Angewandte Chemie International Edition*, 2009, **48**, 9052-9070.
477. N. Satyamurthy and J. R. Barrio, No-carrier-added nucleophilic [F-18] fluorination of aromatic compounds, 2011, *WO2010117435A3*.
478. J. Cardinale, J. Ermert, S. Humpert and H. H. Coenen, *RSC Advances*, 2014, **4**, 17293-17299.
479. B. H. Rotstein, N. A. Stephenson, N. Vasdev and S. H. Liang, *Nat Commun*, 2014, **5**.
480. N. Satyamurthy and J. R. Barrio, Nucleophilic fluorination of aromatic compounds, 2010,
481. M. Kovac, S. Mavel and M. Anderluh, *Current Organic Chemistry*, 2013, **17**, 2921-2935.

482. D. W. Kim, H.-J. Jeong, S. T. Lim and M.-H. Sohn, *Nuclear Medicine and Molecular Imaging*, 2010, **44**, 25-32.
483. S. Preshlock, M. Tredwell and V. Gouverneur, *Chemical reviews*, 2016, **116**, 719-766.
484. M. Tredwell, S. M. Preshlock*, et al.*, *Angewandte Chemie International Edition*, 2014, **53**, 7751-7755.
485. K. Sander, T. Gendron*, et al.*, *Sci. Rep.*, 2015, **5**.
486. L. Mu, C. R. Fischer*, et al.*, *European Journal of Organic Chemistry*, 2012, **2012**, 889-892.
487. L. Lehmann, T. Stellfeld*, et al.*, Triaryl-sulphonium compounds, kit and methods for labeling positron emitting isotopes, 2010,
488. J.-H. Chun, C. L. Morse, F. T. Chin and V. W. Pike, *Chemical communications*, 2013, **49**, 2151-2153.
489. A. S. Kamlet, C. N. Neumann*, et al.*, *PloS one*, 2013, **8**, e59187.
490. E. Lee, J. M. Hooker and T. Ritter, *Journal of the American Chemical Society*, 2012, **134**, 17456-17458.
491. A. J. Hoover, M. Lazari*, et al.*, *Organometallics*, 2016, **35**, 1008-1014.
492. H. Ren, H.-Y. Wey*, et al.*, *ACS Chemical Neuroscience*, 2014, **5**, 611-615.
493. C. N. Neumann, J. M. Hooker and T. Ritter, *Nature*, 2016, **534**, 369-373.
494. B. Beuthien-Baumann, K. Hamacher, F. Oberdorfer and J. Steinbach, *Carbohydrate research*, 2000, **327**, 107-118.
495. F. Dollé, F. Hinnen*, et al.*, *Journal of Labelled Compounds and Radiopharmaceuticals*, 2006, **49**, 687-698.
496. J. Marik and J. L. Sutcliffe, *Tetrahedron Letters*, 2006, **47**, 6681-6684.
497. M. Pretze, D. Pietzsch and C. Mamat, *Molecules*, 2013, **18**, 8618-8165.
498. D. Zeng, B. M. Zeglis, J. S. Lewis and C. J. Anderson, *Journal of Nuclear Medicine*, 2013, **54**, 829-832.
499. T. Reiner and B. M. Zeglis, *Journal of labelled compounds & radiopharmaceuticals*, 2014, **57**, 285-290.
500. J. C. Knight, S. Richter*, et al.*, *Organic & Biomolecular Chemistry*, 2013, **11**, 3817-3825.
501. R. D. Carpenter, S. H. Hausner and J. L. Sutcliffe, *ACS Medicinal Chemistry Letters*, 2011, **2**, 885-889.
502. V. Hugenberg, H.-J. Breyholz*, et al.*, *Journal of medicinal chemistry*, 2012, **55**, 4714-4727.
503. A. Haslop, L. Wells*, et al.*, *Molecular pharmaceutics*, 2014, **11**, 3818-3822.
504. L. Frullano, C. Catana*, et al.*, *Angewandte Chemie International Edition*, 2010, **49**, 2382-2384.
505. L. S. Campbell-Verduyn, L. Mirfeizi*, et al.*, *Angewandte Chemie International Edition*, 2011, **50**, 11117-11120.
506. B. M. Zeglis, K. K. Sevak*, et al.*, *Journal of nuclear medicine*, 2013, **54**, 1389-1396.
507. H. Struthers, B. Spingler, T. L. Mindt and R. Schibli, *Chemistry*, 2008, **14**, 6173-6183.

508. D. E. Lee, J. H. Na*, et al.*, *Molecular pharmaceutics*, 2013, **10**, 2190-2198.
509. H. L. Evans, L. Carroll, E. O. Aboagye and A. C. Spivey, *Journal of Labelled Compounds and Radiopharmaceuticals*, 2014, **57**, 291-297.
510. W. J. McBride, R. M. Sharkey and D. M. Goldenberg, *EJNMMI Research*, 2013, **3**, 36-36.
511. R. Schoffelen, R. M. Sharkey*, et al.*, *Molecular cancer therapeutics*, 2010, **9**, 1019-1027.
512. W. J. McBride, R. M. Sharkey*, et al.*, *Journal of nuclear medicine*, 2009, **50**, 991-998.
513. E. Benedetto, M. Tredwell*, et al.*, *Chemical Science*, 2013, **4**, 89-96.
514. J. J. Topczewski, T. J. Tewson and H. M. Nguyen, *Journal of the American Chemical Society*, 2011, **133**, 19318-19321.
515. C. Hollingworth, A. Hazari*, et al.*, *Angewandte Chemie*, 2011, **123**, 2661-2665.
516. T. J. A. Graham, R. F. Lambert*, et al.*, *Journal of the American Chemical Society*, 2014, **136**, 5291-5294.
517. M. S. Berridge, M. P. Franceschini, E. Rosenfeld and T. J. Tewson, *The Journal of Organic Chemistry*, 1990, **55**, 1211-1217.
518. N. Okamura, S. Furumoto*, et al.*, *Journal of Nuclear Medicine*, 2013, **54**, 1420-1427.
519. X. Huang, W. Liu*, et al.*, *Journal of the American Chemical Society*, 2014, **136**, 6842-6845.
520. T. S. Mourne, Suggested strategy for HPLC method development, 2013, http://www.mournetrainingservices.co.uk/training_resources.html, 12 August 2016.
521. I. Koslowsky, J. Mercer and F. Wuest, *Organic & Biomolecular Chemistry*, 2010, **8**, 4730-4735.
522. E. Galante, B. Schoultz, M. Koepp and E. Årstad, *Molecules*, 2013, **18**, 5335.
523. D. Zhou, W. Chu*, et al.*, *Nuclear medicine and biology*, 2012, **39**, 1175-1181.
524. N.-N. Su, Y. Li*, et al.*, *Res Chem Intermed*, 2013, **39**, 759-766.
525. J. I. Sarmiento-Sanchez, A. Ochoa-Teran and I. A. Rivero, *Arkivoc*, 2011, **2011**, 177-188.
526. C. Bouillon, A. Meyer*, et al.*, *The Journal of Organic Chemistry*, 2006, **71**, 4700-4702.
527. O. L. P. De Jesus, E. W. Kovacs*, et al.*, Selective radiolabeling of biomolecules, 2008, *WO2009080561A1*.
528. D. Zhou, W. Chu*, et al.*, *Tetrahedron Letters*, 2015, **56**, 952-954.
529. M. Glaser, J. Goggi*, et al.*, *Bioorganic & medicinal chemistry letters*, 2011, **21**, 6945-6949.
530. L. Iddon, J. Leyton*, et al.*, *Bioorganic & medicinal chemistry letters*, 2011, **21**, 3122-3127.
531. L. Li, X. Shao*, et al.*, *ACS Med Chem Lett*, 2015, **6**, 548-552.
532. A. Mossine, E. Cole*, et al.*, *Journal of Labelled Compounds and Radiopharmaceuticals*, 2015, **58**, S325.
533. T. Andreani, Y. Jin*, et al.*, *Synthetic Communications*, 2008, **38**, 3834-3839.

534. J. Way and F. Wuest, *Nuclear medicine and biology*, 2013, **40**, 430-436.
535. N. Turkman, A. Shavrin*, et al.*, *Nuclear medicine and biology*, 2012, **39**, 593-600.
536. J. O. Osby, S. W. Heinzman and B. Ganem, *Journal of the American Chemical Society*, 1986, **108**, 67-72.
537. B. Fleiss, V. Chhor*, et al.*, *Developmental neuroscience*, 2015, **37**, 363-375.
538. A. Henn, S. Lund*, et al.*, *Altex*, 2009, **26**, 83-94.
539. A. Karperien, H. Ahammer and H. Jelinek, *Frontiers in Cellular Neuroscience*, 2013, **7**.
540. S. Gordon, *Nat Rev Immunol*, 2003, **3**, 23-35.
541. V. Chhor, T. Le Charpentier*, et al.*, *Brain, behavior, and immunity*, 2013, **32**, 70-85.
542. T. Kielian, *Journal of neurochemistry*, 2016, **136**, 5-9.
543. R. M. Ransohoff and V. H. Perry, *Annual review of immunology*, 2009, **27**, 119-145.
544. M. Devices, Fura-2 QBT Calcium Kit, www.moleculardevices.com/reagents-supplies/assay-kits/gpcr-assays/fura-2-qbt-calcium-kit www.moleculardevices.com/reagents-supplies/assay-kits/gpcr-assays/fura-2-qbt-calcium-kit, (accessed 02/2016).
545. M. Nobile, I. Monaldi*, et al.*, *FEBS letters*, 2003, **538**, 71-76.
546. A. C. Hung and S. H. Sun, *Cellular signalling*, 2002, **14**, 83-92.
547. W. Paneka, H. Jijon*, et al.*, *Journal of Neuroscience*, 2001, **21**, 7135-7142.
548. A. D. Garbo, S. Alloisio and M. Nobile, *Physical Biology*, 2012, **9**, 026001.
549. A. D. Hibell, K. M. Thompson*, et al.*, *The Journal of pharmacology and experimental therapeutics*, 2001, **296**, 947-957.
550. A. D. Michel, R. Kaur, I. P. Chessell and P. P. A. Humphrey, *British journal of pharmacology*, 2000, **130**, 513-520.
551. R. H. Mitchell and B. I. Goldstein, *Journal of the American Academy of Child and Adolescent Psychiatry*, 2014, **53**, 274-296.
552. R. Rizzuto, M. Brini*, et al.*, *Current Biology*, 1995, **5**, 635-642.
553. A. Morelli, P. Chiozzi*, et al.*, *Molecular Biology of the Cell*, 2003, **14**, 2655-2664.
554. S. Falzoni, M. Munerati*, et al.*, *J Clin Invest*, 1995, **95**, 1207-1216.
555. C.-S. Tham, F.-F. Lin*, et al.*, *International Journal of Developmental Neuroscience*, 2003, **21**, 431-443.
556. D. L. Donnelly-Roberts and M. F. Jarvis, *British journal of pharmacology*, 2007, **151**, 571-579.
557. Z. Xie, T. E. Morgan, I. Rozovsky and C. E. Finch, *Experimental neurology*, 2003, **182**, 135-141.
558. H. K. Hamalainen, J. C. Tubman*, et al.*, *Analytical biochemistry*, 2001, **299**, 63-70.
559. Y.-H. Feng, L. Wang*, et al.*, *American journal of physiology. Cell physiology*, 2005, **288**, C1342-C1356.
560. G. Lopez-Castejón, A. Baroja-Mazo and P. Pelegrín, *Cellular and Molecular Life Sciences*, 2010, **68**, 3095-3107.
561. X.-J. Zhang, G.-G. Zheng*, et al.*, *Sheng Li Xue Bao*, 2005, **57**, 193-198.

562. R. Raouf, A.-J. Chabot-Doré*, et al.*, *Neuropharmacology*, 2007, **53**, 496-504.
563. F. Bianco, M. Fumagalli*, et al.*, *Brain Research Reviews*, 2005, **48**, 144-156.
564. R. F. Zanin, E. Braganhol*, et al.*, *PloS one*, 2012, **7**, e31205.
565. A. Melani, S. Amadio*, et al.*, *Journal of cerebral blood flow and metabolism*, 2006, **26**, 974-982.
566. T. Suzuki, I. Hide*, et al.*, *The Journal of neuroscience*, 2004, **24**, 1-7.
567. E. Adinolfi, M. G. Callegari*, et al.*, *Molecular Biology of the Cell*, 2005, **16**, 3260-3272.
568. I. P. Chessell, A. D. Michel and P. P. A. Humphrey, *British journal of pharmacology*, 1998, **124**, 1314-1320.
569. S. Lazareno and N. J. Birdsall, *British journal of pharmacology*, 1993, **109**, 1110-1119.
570. U. S. F. a. D. A. (FDA), Guidance for Industry. Drug Interaction Studies - Study Design, Data Analysis, and Implications for Dosing and Labeling. , *Clinical Pharmacology*, 2006.
571. Y.-C. Cheng and W. H. Prusoff, *Biochemical Pharmacology*, 1973, **22**, 3099-3108.
572. E. G. Solon, *Expert opinion on drug discovery*, 2007, **2**, 503-514.
573. A. Rogers, Techniques of autoradiography, Elsevier, Amsterdam, 3rd edn., 1979.
574. D. J. Mujsce, M. A. Christensen and R. C. Vannucci, *Pediatric research*, 1990, **27**, 450-453.
575. S. O. Algra, K. M. Groeneveld*, et al.*, *Journal of neuroinflammation*, 2013, **10**, 24.
576. G. Stoll, S. Jander and M. Schroeter, *Prog Neurobiol*, 1998, **56**, 149-171.
577. M. Gelderblom, F. Leypoldt*, et al.*, *Stroke; a journal of cerebral circulation*, 2009, **40**, 1849-1857.
578. M. Schroeter, S. Jander*, et al.*, *Stroke; a journal of cerebral circulation*, 1997, **28**, 382-386.
579. M. Schilling, M. Besselmann*, et al.*, *Experimental neurology*, 2003, **183**, 25-33.
580. P. Ferrazzano, V. Chanana*, et al.*, *CNS & neurological disorders drug targets*, 2013, **12**, 338-349.
581. J. R. Weinstein, I. P. Koerner and T. Moller, *Future neurology*, 2010, **5**, 227-246.
582. C. Benakis, L. Garcia-Bonilla, C. Iadecola and J. Anrather, *Front Cell Neurosci*, 2014, **8**, 461.
583. Y. Ma, J. Wang, Y. Wang and G. Y. Yang, *Prog Neurobiol*, 2016, **In press**.
584. D. Yanagisawa, Y. Kitamura*, et al.*, *Biological and Pharmaceutical Bulletin*, 2008, **31**, 1121-1130.
585. W. Zeng, Y. Tong*, et al.*, *Molecular Medicine Reports 5*, 2012, **5**, 1357-1361.
586. L.-Y. Wang, W.-Q. Cai*, et al.*, *Glia*, 2009, **57**, 307-319.
587. J. E. Rice, R. C. Vannucci and J. B. Brierley, *Annals of Neurology*, 1981, **9**, 131-141.
588. G. Paxinos and C. Watson, The Rat Brain in Stereotaxic Coordinates, Academic Press, 4th edition edn., 1998.
589. C. Perego, S. Fumagalli and M. G. De Simoni, *Journal of neuroinflammation*, 2011, **8**, 174.

590. X. Hu, P. Li*, et al.*, *Stroke; a journal of cerebral circulation*, 2012, **43**, 3063-3070.
591. S. Fumagalli, C. Perego*, et al.*, *Frontiers in Neurology*, 2015, **6**, 81.
592. W. C. Eckelman, M. R. Kilbourn and C. A. Mathis, *Nuclear medicine and biology*, 2009, **36**, 235-237.
593. L. Farde, L. Eriksson, G. Blomquist and C. Halldin, *Journal of cerebral blood flow and metabolism*, 1989, **9**, 696-708.
594. R. B. Innis, V. J. Cunningham*, et al.*, *Journal of cerebral blood flow and metabolism*, 2007, **27**, 1533-1539.
595. S. P. Hume, R. N. Gunn and T. Jones, *European journal of nuclear medicine*, 1998, **25**, 173-176.
596. C. Kohler, H. Hall, S. O. Ogren and L. Gawell, *Biochemical Pharmacology*, 1985, **34**, 2251-2259.
597. S. T. Anderson, S. Commins, P. N. Moynagh and A. N. Coogan, *Brain, behavior, and immunity*, 2015, **43**, 98-109.
598. S. Biesmans, T. F. Meert*, et al.*, *Mediators of Inflammation*, 2013, **2013**, 14.
599. L. Qin, X. Wu*, et al.*, *Glia*, 2007, **55**, 453-462.
600. H. Noh, J. Jeon and H. Seo, *Neurochemistry international*, 2014, **69**, 35-40.
601. H. A. Silverman, M. Dancho*, et al.*, *Molecular medicine*, 2014, **20**, 601-611.
602. H. Q. Fu, T. Yang*, et al.*, *PloS one*, 2014, **9**, e106331.
603. C. Schmitt, N. Strazielle and J. F. Ghersi-Egea, *Journal of neuroinflammation*, 2012, **9**, 187.
604. H.-K. Jeong, I. Jou and E.-h. Joe, *Exp Mol Med*, 2010, **42**, 823-832.
605. W. A. Banks, A. M. Gray*, et al.*, *Journal of neuroinflammation*, 2015, **12**, 223.
606. R. Sankowski, S. Mader and S. I. Valdés-Ferrer, *Frontiers in Cellular Neuroscience*, 2015, **9**.
607. I. C. Hoogland, C. Houbolt*, et al.*, *Journal of neuroinflammation*, 2015, **12**, 114.
608. K.-A. Ji, M.-S. Yang*, et al.*, *Glia*, 2007, **55**, 1577-1588.
609. H. Matsumoto, Y. Kumon*, et al.*, *Journal of Neuroscience Research*, 2007, **85**, 994-1009.
610. H. B. Choi, J. K. Ryu, S. U. Kim and J. G. McLarnon, *The Journal of neuroscience*, 2007, **27**, 4957-4968.
611. J. J. Watters, J. A. Sommer*, et al.*, *Drug Development Research*, 2001, **53**, 91-104.
612. C.-W. Chiao, R. C. Tostes and R. C. Webb, *Journal of pharmacology and experimental therapeutics*, 2008, **326**, 864-870.
613. C. W. Chiao, J. E. da Silva-Santos*, et al.*, *Clinical science*, 2013, **125**, 131-141.
614. E. Leiva-Salcedo, C. Coddou*, et al.*, *Mediators of Inflammation*, 2011, **2011**, 1-12.
615. I. Szanda, J. Mackewn*, et al.*, *Journal of nuclear medicine*, 2011, **52**, 1741-1747.
616. B. P. Chugh, J. P. Lerch*, et al.*, *Neuroimage*, 2009, **47**, 1312-1318.
617. D. Cash and C. Simmons, unpublished work, Characterisation of a 0.5 mg/kg LPS rat model of neuroinflammation, 2016.

618. T. R. Sykes, T. J. Ruth and M. J. Adam, *International journal of radiation applications and instrumentation. Part B, Nuclear medicine and biology*, 1986, **13**, 497-500.
619. Y. Liu and M. J. Welch, in Molecular imaging of small animals, ed. H. Zaidi, Springer, 2014, vol. 1, pp. 281-283.
620. E. M. Joshi, A. Need*, et al.*, *ACS Chemical Neuroscience*, 2014, **5**, 1154-1163.
621. Y. J. Seo, Y. Kang*, et al.*, *ACS Chemical Neuroscience*, 2014, **5**, 588-596.
622. A. Herranz and A. Ruibal, *Biomarkers journal*, 2015, **1**, 1-3.

The true delight is in the finding out rather than in the knowing.

Isaac Asimov